UNIVERSIDADE FEDERAL DE MINAS GERAIS
Instituto de Geociências
Programa de Pós-Graduação em Geologia

Silas Santos Salgado

Geologia da Serra de Buritirama e Gênese de suas Mineralizações Manganesíferas

N° 50

BELO ORIZONTE
DATA (20/07/2020)

Silas Santos Salgado

Geologia da Serra de Buritirama e Gênese de suas Mineralizações Manganesíferas

Tese apresentada ao Programa de Pós-Graduação em Geologia do Instituto de Geociências da Universidade Federal de Minas Gerais como requisito parcial à obtenção do título de Doutor em Geologia Econômica e Aplicada.

Orientação: Prof. Dr. Fabrício de A. Caxito

Coorientação: Profa. Dra. Rosaline C. F. e Silva

Belo Horizonte
2020

S164g Salgado, Silas Santos.
2020 Geologia da Serra de Buritirama e gênese de suas mineralizações manganesíferas [manuscrito] / Silas Santos Salgado. – 2020.
152 f., enc.: il. (principalmente color.)

Orientador: Fabrício de Andrade Caxito.
Coorientadora: Rosaline Cristina Figueiredo e Silva.
Tese (doutorado) – Universidade Federal de Minas Gerais, Instituto de Geociências, 2020.
Área de concentração: Geologia Econômica e Aplicada.
Bibliografia: f. 89-104.
Inclui anexos.

1. Geologia estratigráfica – Teses. 2. Petrologia – Pará – Teses. 3. Geoquímica – Pará – Teses. 4. Tempo geológico – Teses. I. Caxito, Fabrício de Andrade. II. Figueiredo e Silva, Rosaline Cristina. III. Universidade Federal de Minas Gerais. Instituto de Geociências. IV. Título.

CDU: 551.7(811.5)

Ficha catalográfica elaborada por Graciane Aparecida de Paula – CRB6 3404

UNIVERSIDADE FEDERAL DE MINAS GERAIS

PROGRAMA DE PÓS-GRADUAÇÃO EM GEOLOGIA

FOLHA DE APROVAÇÃO

Geologia da Serra de Buritirama e Gênese de suas Mineralizações Manganesíferas

SILAS SANTOS SALGADO

Tese submetida à Banca Examinadora designada pelo Colegiado do Programa de Pós-Graduação em GEOLOGIA, como requisito para obtenção do grau de Doutor em GEOLOGIA, área de concentração GEOLOGIA ECONÔMICA E APLICADA.

Aprovada em 20 de julho de 2020, pela banca constituída pelos membros:

Prof. Fabrício de Andrade Caxito - Orientador
UFMG

Prof. Gustavo Melo
UFOP

Prof. Carlos Alberto Spier
The University of Queensland

Prof. Hermínio Arias Nalini Júnior
UFOP

Profa. Flávia Cristina Silveira Braga
UEMG

Belo Horizonte, 20 de julho de 2020.

AGRADECIMENTO

A presente tese representa uma longa trajetória onde diversas pessoas contribuíram para que eu pudesse alcançar o estágio final. Tentei demonstrar minha gratidão ao apoio recebido durante todo este percurso, já sabendo que se torna difícil recordar-me de todos neste momento. Assim, peço desculpas pelos nomes que eventualmente me esqueça.

Ao orientador Fabrício Caxito (Boni), a quem eu conheço desde os idos de 2004 e foi fundamental para o início, meio e fim deste trabalho. Muito obrigado grande Boni. A coorientadora Rosaline Figueiredo e Silva que sempre demonstrou uma grande boa vontade e acessibilidade para os debates e alinhamentos que culminaram neste trabalho final. Aos professores Gabriel Uhlein, Alexandre Uhlein, Tiago Amâncio, Mahyra Tedeschi, Ivo Dussin, Alexandre Chaves que sempre me apoiaram em todas as eventuais demandas. Aos profissionais do CPMTC Hélvio, Carlão, Jonhy, Igor, dentre outros que deram todo apoio técnico em diversas atividades. Os profissionais que trabalham no instituto de geociências, especialmente ao William da pós-graduação, sempre muito solícito. Agradeço a toda galera da pós, que sempre meu ajudou demais quando precisei de uma força. Valeu geologada! Agradeço também os professores e profissionais da UFOP Glaúcia Queiroga, Marco Paulo, Ana Alkmim, Cristiano Lana, Gustavo Melo e Morgado. Agradeço ao Felipe Tavares (CPRM) pelas produtivas conversas que tivemos. Ao Conselho Nacional de Desenvolvimento Científico e Tecnológico (CNPq).

A empresa Mineração Buritirama, agradeço via os profissionais João Araújo, Michel Fontes, Jorge Batista, Afonso Petta, Denis Tibúrcio, Flávia Moller, Paulo Henrique, Raquel Coelho, Thomás Clara, Maurício, Fátima, Leo, Ferraz, Divino, Elder, Carlos, Raul, Casemiro, Carol, Amanda, Chicuta, aos japas, Claudinei, dentre tantos outros que insentivaram o presente trabalho e com os quais tive o prazer de conviver durante o tempo em que trabalhei na empresa.

A minha esposa, Marcelle Alves, por sempre me apoiar durante toda esta jornada e entender os motivos pelos quais permaneci desperto durante as madrugadas e em casa durante os fins de semana.
Por fim, agradeço à minha família, gente de enorme coração.

“Se no caminho dele havia uma pedra, no meu existem muitas e, elas ainda falam uma linguagem única, que os geólogos tentam decifrar” (S. S. Salgado, 2020)

RESUMO

A Formação Buritirama localiza-se ao longo da serra homônima no extremo norte do domínio Carajás, próximo ao contato com o dóminio Bacajá, na porção sudeste do Cratón Amazonas. Consiste em uma estrutura NW-SE com 40 km de extensão e 3 km de largura e é constituída, ao longo de sua seção tipo, por quatro zonas de empurrão que individualizam três unidades estratigráficas: i) Unidade Inferior, composta por ortoquartzitos, rochas carbonato-silicáticas (Di+Cal+Phl+Pl+K-Fds+Qtz) e mármores dolomíticos (Cal+Dol); ii) Unidade Intermediária, formada por mármores manganesíferos (Kut+Sps+Rdn+Kan+Pym+Hya+Mn-Phl) e rochas carbonato-silicáticas manganesíferas (Mn-cal+Mn-Di+Mn-Phl+Pl+K-Fds), ambas amplamente hidrotermalizadas devido à intrusão de diques e sills de pegmatíticos e diabásio e; iii) Unidade Superior, constituída essencialmente por quartzito e quartzo-mica xisto seguido por rochas carbonato-silicáticas. O embasamento local é formado por ortognaisses migmatíticos (Complexo Xíngu) e pelo metagranito Buritirama. A configuração estrutural da Formação Buritirama registra o evento compressional transamazônico responsável pelo transporte de massa de NE para SW e individualizado nas seguintes fases deformacionais: i) D1 (compressiva dúctil) constitui-se a partir de cisalhamento simples de baixo ângulo marcado por dobras intrafoliais (F1) com uma foliação plano-axial penetrativa (S1) paralela ao bandamento composicional (Bn). S1 é dobrado em dobras isoclinais (F2) vergentes para SW. Uma segunda foliação metamórfica penetrativa (S2) é identificada na região de charneira das dobras F2. S2 ocorre normalmente paralela a S1//Bn e mergulha para NE com um máximo modal de 025/30. Dobras abertas e suaves (F3) representam a última expressão desta fase; ii) D2 (compressiva rúptil) é representada por falhas reversas e retro-cavalgamentos que dão origem a um quarto padrão de dobramentos (F4) marcados por planos axias vergentes para NE; iii) D3 (extensional rúptil), representa o sistema de falhas normais conjugadas. Dados geoquímicos do metagranito Buritirama indicaram sua afinidade metaluminosa, calcio-alcalina, ferroana e o classificam como um granito anorogênico (A2). Sua idade de cristalização de 2549 ± 5,9 Ma (U-Pb) é semelhante à reportada para outros granitos presentes na porção norte do domínio Carajás. Dados geocronológicos (U-Pb) de zircões detríticos extraídos de quartzitos associados às unidades Inferior e Superior indicam uma importante contribuição de fontes Arqueanas (idades > 2,5 Ga) à bacia Buritirama, mas também registram idades Siderianas e até Riacianas. Padrões geoquímicos como anomalias negativas de La, Ce e altas razões Y/Ho (> 48), em conjunto a valores isotópicos positivos de $\delta^{13}C$ (+ 3,18‰ to + 4,96‰ V-PDB), sugerem uma natureza marinha para os mármores dolomíticos. As rochas carbonáticas manganesíferas apresentam anomalias positivas de Eu e correlação positiva Eu vs. Mn, o que em conjunto a valores isotópicos predominantemente negativos de $\delta^{13}C$ (- 2,56‰ to + 0,15‰ V-PDB), indicam uma origem marinha hidrothermal e uma natureza diagenética para os carbonatos, kutnohorita e Mn-calcita. Em síntese, o conjunto de dados obtidos para a Formação Buritirama suportam sua interpretação como uma plataforma continental posicionada no limite norte do bloco Carajás, com aporte de sedimentos do referido bloco e, subordinadamente, de um arco magmático Riaciano localizado a nordeste (bloco Bacajá). Os valores positivos de $\delta^{13}C$ obtidos em mármores dolomíticos são interpretados como uma expressão da Excursão Isotópica Lomagundi e sugerem a conexão da bacia Buritirama com um oceano global. Os estágios iniciais de abertura da bacia Buritirama provavelmente vinculam-se ao magmatismo anorogênico do final do Neoarqueano (~2,55 Ga), enquanto seu fechamento é atribuído à amalgamação entre os blocos Carajás e Bacajá, durante a orogênese Transamazônica (~2,06 Ga). A idade máxima deposicional da bacia considerando o zircão detrítico mais novo datado foi de 2,18 Ga, mas a população mais jovem ocorre em ~2,3 Ga. As mineralizações manganesíferas carbonáticas associadas constituíram-se a partir de um processo com multi-estágios, envolvendo: i) precipitação de nódulos de manganês em condições oxidantes e deposição no fundo oceânico; ii) redução dos óxidos de manganês (Mn^{4+} para Mn^{2+}) via atividade microbiana; iii) formação diagenética dos carbonatos manganesíferos via reação entre Mn^{2+} e CO_3^{2-} (orgânico e marinho). O depósito da Formação Buritirama apresenta idade e gênese semelhante aos depósitos de Serra do Navio (Amapá) e Nsuta (Gana), e são correlacionados ao longo do sistema orogênico Birimiano-Transamazonas, que abrange o oeste africano e o norte brasileiro.

Palavras-Chave: Manganês, Buritirama, Lomagundi, Carajás, Bacajá

ABSTRACT

The Buritirama Formation crops out along the homonymous ridge at the extreme northern of Carajás domain, close to the contact with the Bacajá domain, in the southeastern portion of the Amazon Craton. Consist of 40 km long, ca. 3 km wide NW-SE trending structure arranged in four imbricated trusts that individualize three stratigraphic unit: Inferior Unit, composed of orthoquartzite, carbonate-silicate rocks (Di+Cal+Phl+Pl+K-Fds+Qtz) and dolomitic marbles (Cal+Dol); ii) Intermediate Unit, formed by Mn-marbles (Kut+Sps+Rdn+Kan+Pym+Hya+Mn-Phl) and Mn-carbonate-silicate rocks (Mn-cal+Mn-Di+Mn-Phl+Pl+K-Fds), both widely hydrothermalized by sills and dykes of pegmatite and diabase intrusions; iii) Upper Unit, composed of quartzite, quartz-mica schist and carbonate-silicate rocks. The local basement is formed by the Xingu Complex (gneiss-migmatitic) and the Buritirama metagranite. The Buritirama Formation structural framework records the Transamazonian compressional event responsible to the mass transport from NE to SW that is individualized in three deformational phases: i) D1 (compressional ductile) is product of a low angle shear and marked by rootless intra-folial folds (F1) and a penetrative axial-plane foliation (S1) parallel to the metamorphic banding (Bn). S1 is folded into isoclinal folds (F2) verging to SW. A second axial-plane foliation (S2) is recognized in the F2 hinge zone. S2 is usually parallel to S1//Bn and dips preferentially to NE with modal maximum at 025/30. Gentle upright folds (F3) are the last expression of this phase; ii) D2 (compressional brittle) is characterized by reverse and back-thrust faults that give rise to the fourth fold pattern marked by axial-plane verging to NE; D3 (extensional brittle) represents a system of conjugated normal faults. Geochemical data of the Buritirama metagranite points to a metaluminous, calc-alkaline and ferroan affinity and classify this rock as an anorogenic granite (A2). Its crystallization age of 2549 ± 5.9 Ma (U-Pb) has been also reported to other granites presented at the northern part of the Carajás domain. Detrital zircon ages (U-Pb) from quartzites of Inferior and Upper Unit suggest the contribution of Archean (> 2.5 Ga) sources for the Buritirama basin, but also record Siderian and Rhyacian ages. Geochemical patterns and negative anomalies of La, Ce and high ratios Y/Ho (>48), couple with positive isotopic values of $\delta^{13}C$ (+ 3,18‰ to + 4,96‰ V-PDB), suggest a marine nature for the dolomitic marbles. The carbonate-rocks show positive Eu anomalies and a positive correlation between Eu vs. Mn, that couple with mostly negative $\delta^{13}C$ (- 2,56‰ to + 0,15‰ V-PDB) values suggest a hydrothermal marine origin and a diagenetic nature for the carbonates kutnohorite and Mn-calcite. In conclusion, the dataset obtained for the Buritirama Formation supports its interpretation as a continental platform located at the northern border of the Carajás block, with input of detrital sediments from this block, and minor contributions from a Rhyacian magmatic arc settled to the north-eastern (Bacajá block). The positive $\delta^{13}C$ values from dolomitic marbles are understood as an expression of the Lomagundi Isotopic Excursion and suggest the connection between the Buritirama basin and a global ocean. Early stages of the base opening are probable linked to the late Neoarchean anorogenic magmatism (~2.55 Ga), while the close of the basin is attributed to the amalgamation between the Carajás and Bacajá blocks, during the Transamazonian Orogen (~2.06 Ga). The maximum depositional age based on a single detrital zircon was defined at 2.18 Ga, while the youngest population occur at c.a. 2.3 Ga. The Mn-carbonatic mineralization formed by a multi-stage process involving: i) Mn-nodules formation over oxic conditions followed by their deposition on the ocean bottom; ii) bacterially mediated reduction of Mn-oxides (Mn^{4+} to Mn^{2+}); iii) diagenetic formation of (Ca)Mn-carbonates by reactions between Mn^{2+} and CO_3^{2-} (organic and inorganic bicarbonate). The Mn-Buritirama deposit is similar in age and genesis to the Serra do Navio (Amapá) and Nsuta (Gana). These Mn-deposits deposits and were probably correlated along the Birimian (western Africa) and Transamazonian orogen (northern Brazil).

Keywords: Manganese, Buritirama, Lomagundi, Carajás, Bacajá

LISTAS DE SIGLAS E ABREVIATURAS

BF – *Buritirama Formation*
BSE – *Backscattered Electron*
Cal – Calcita
Cb – Carbonatos
CBS – *Carbonate-Silicate Rocks*
CCS – *Calc-Silicate Rocks*
CL – *Cathodoluminescence*
Dps – Diopsídio
EPMA – *Electron Probe Microanalyzer*
Fds – Feldspato
Hya – Hialofano
ICP-OES - *Induced Coupled Plasma - Optical Emission Spectroscopy*
IM - *Impure Marbles*
IU – *Intermediate Unit*
Kan – Kanoita
Kut – Kutnohorita
LMic – *Microscopy and Microanalysis Laboratory*
LU – Lower Unit
Mc – Microclínio
MC-ICP-MS – *Multicollector Inductively Coupled Plasma Mass Spectrometer*
MM – *Manganesiferous Marbles*
MTG – Metagranito Buritirama
PAAS – *Post-Archean Australian shale*
Phl – Flogopita
Pl – Plagioclásio
Pym – Piroxmanguita
Qtz – Quartzo
Rdn – Rodonita
SGS – SGS Laboratório Geosol
Sps – Espessartita
UU – *Upper Unit*
V-SMOW – *Vienna Standard Mean Ocean Water*
WDS – *Wavelength Dispersive Spectrometers*

SUMÁRIO

1. INTRODUÇÃO

A presente tese "Geologia da Serra de Buritirama e Gênese de suas Mineralizações Manganesíferas" abrange os trabalhos de cunho geológico desenvolvidos entre os anos de 2017 e 2020 na Formação Buritirama, ao longo da serra homônima, localizada no município de Marabá, porção sudeste do Estado do Pará. A Serra de Buritirama, em um contexto geológico-geotectônico, encontra-se posicionada na porção sudeste do Cráton Amazônico, mais especificamente no limiar de contato entre os domínios Bacajá (a norte) e Carajás (a sul; Figura 2.1). É composta por metassedimentos químicos e siliciclásticos (Supergrupo Rio Itacaiúnas) que hospedam importantes mineralizações manganesíferas oxidadas e carbonáticas. O minério de manganês oxidado é atualmente lavrado e comercializado exclusivamente pela empresa Mineração Buritirama S.A. e, segundo o último Anuário Mineral Brasileiro, elaborado pela Agência Nacional de Mineração (ANN), em 2017 a Mina de Buritirama representou 33% da produção nacional de manganês. À parte dos estudos apresentados neste documento, os últimos trabalhos científicos desenvolvidos especificamente na Formação Buritirama são da década de setenta. Questões como a estratigrafia e a idade da Formação Buritirma, sua conexão com os domínios Carajás e Bacajá, sua estruturação tectônica, a gênese de suas mineralizações, dentre outros aspectos, permaceram em aberto nos últimos quarenta anos.

Considerando este panorama, a presente tese contemplam novos dados geológicos, estruturais, petrográficos, geoquímicos e geocronológicos da Formação Buritirama e, em parte, de suas rochas encaixantes (metagranito Buritirama). Tais informações culminaram na: i) caracterização petrográfica dos litotipos da Formação Buritirama suportada por análises via difração de raio-x, microscópio óptico de luz transmitida e refletida, microscópio eletrônico de varredura (MEV) e microssonda; ii) determinação do empilhamento tectono-sedimentar que estrutura a Formação Buritirama; iii) determinação das fases deformacionais dúcteis e rúpteis registradas na Formação Buritirama; iv) datação (U-Pb) e determinação de aspectos geoquímicos do metagranito Buritirama, que compõem o embasamento da Formação Buritirama; v) determinação das idades máximas e mínimas depositionais da Formação Buritirama via datação (U-Pb) de zircões detríticos e análise da proveniência dos principais aportes sedimentares da bacia; vi) análise geoquímica e isotópica (carbono e oxigênio) das rochas de natureza carbonática que compõem a Formação Buritirama e a proposição de um modelo metalogenético para suas mineralizações carbonáticas manganesíferas.

1.1. Localização

A Serra de Buritirama localiza-se na porção centro sul do município de Marabá, Pará, entre as coordenadas geográficas 50°03’ e 50°18’ (longitude oeste) e 5°28’ e 5°39’ (latitude sul). Está inserida na bacia do rio Itacaiúnas, dista 140 km da sede de Marabá (PA) e cerca de 100 km do município de Parauapebas (PA; Figura 1.1). Consiste em um alto topográfico orientado na direção NW-SE, estruturado por cristas de quartzito que alcançam altitudes entre 250-400 m (Anderson et al. 1974).

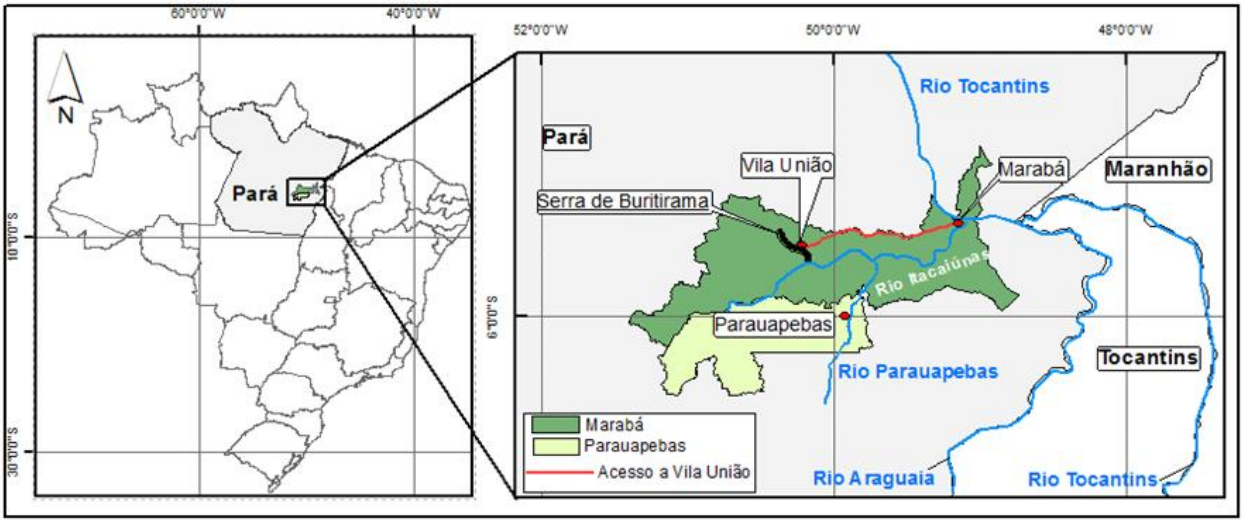

Figura 1.1 - Localização da Serra de Buritirama em relação aos município de Marabá e Parauapebas, e aos estados do Pará, Maranhão e Tocantins.

1.2. Objetivos e Justificativas

Os estudos desenvolvidos na Formação Buritirama, ao longo da serra homônima, tiveram como principais objetos:

i. Determinar a estratigrafia da Formação Buritirama (contatos de base e topo), realizar a caracterização petrográfica de suas principais litologias, detalhar a geologia estrutural da área e sugerir um possível ambiente deposicional para os metassedimentos. O único trabalho que versa sobre a estratigrafia e sugere um ambiente deposicional para os litotipos aflorantes ao longo da Serra de Buritirama foi realizado por Peters et al. (1977);

ii. Determinar a idade mínima e máxima deposicional via a datação (LA-ICP-MS; U-Pb) de zircões detríticos em quartzitos;

iii. Realizar a caracterização geoquímica e isotópica das rochas carbonática da Formação Buritirama,

bem como a proposição de um modelo metalogenético para os carbonatos manganesíferos;

iv. Avaliar o posicionamento geotectônico da Formação Buritirama com relação aos domínios Bacajá e Carajás. Apesar da Serra de Buritirama ser uma peça chave na determinação deste limite, a mesma vem sendo vinculada a ambos os domínios;

v. Caracterização geoquímica e geocronológica do metagranito Buritirama;

2. EVOLUÇÃO DO CONHECIMENTO GEOLÓGICO

2.1. Geologia Regional

O Cráton Amazônico possui uma dimensão de aproximadamente 4.500.000 Km², abrange os países Brasil, Guiana Francesa, Guiana, Suriname, Venezuela, Colômbia e Bolívia. Constitui uma das mais importantes estruturas pré-cambrianas da Plataforma Sul-Americana. Basicamente, é composto por núcleos arqueanos circundados de orógenos paleo e mesoproterozóicos estabilizado a cerca de 1.0 Ga (Figura 2.1). Atuou como zona de antepaís durante o desenvolvimento da Província Tocantins (Almeida et al. 1976, 1981, 2000; Brito Neves & Cordani, 1991; Cordani et al. 2000).

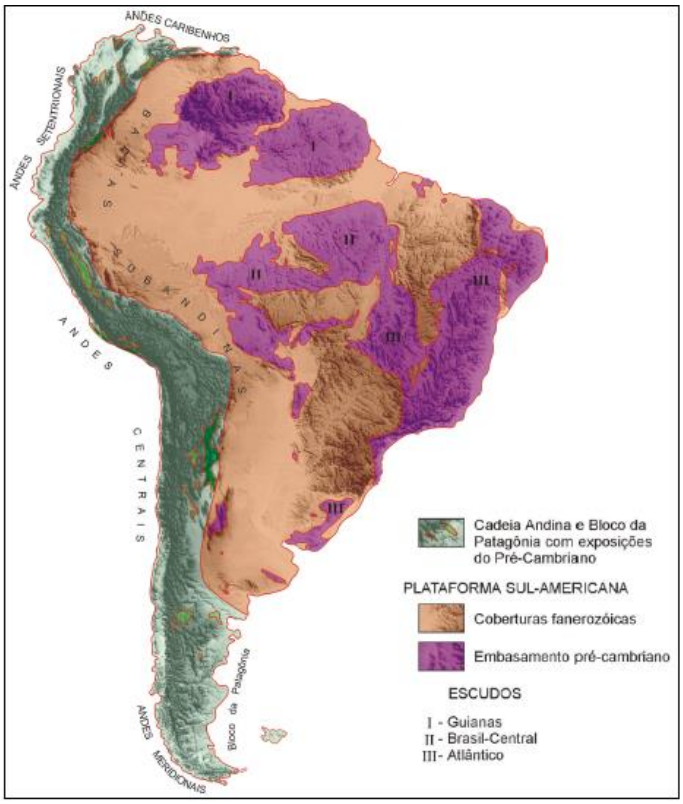

Figura 2.1 – Escudos pré-cambrianos da plataforma sul-americana e coberturas fanerozóicas. Destaque para os escudos das Guianas e do Brasil Central ou Guaporé, que compõem o Cráton Amazônico (Almeida et al. 1976; Schobbenhaus & Brito Neves, 2003).

Diferentes modelos de compartimentação do Cráton Amazônico têm sido propostos por diversos autores ao longo das últimas décadas, como Cordani et al. (1979); Hasui & Almeida, (1985); Costa & Hasui, (1997); Tassinari & Macambira, (1999; 2004); Santos et al. (2000); Santos, (2003); Tassinari et al. (2000), sendo estes trabalhos baseados principalmente em dados geocronológicos, estruturais, geofísicos e de geoquímica isotópica. Um ponto importante, visto como um consenso entre os diferentes modelos, é o entendimento do Cráton Amazônico como uma unidade estruturada por núcleos arqueanos (microcontinentes) formados por terrenos granito-*greenstone* e gnaisse-migmatíticos, contornados por sucessivas faixas móveis e arcos magmáticos proterozóicos (2,2-1,95 Ga). O desenvolvimento de orógenos colisionais entre 1,95-1,00 Ga, associados a provável subducção de uma litosfera oceânica, teriam levado a acreção de uma massa continental a oeste (Laurentia).

Vasquez & Rosa-Costa (2008) em trabalho realizado pelo Serviço Geológico do Brasil (CPRM) onde apresentam o mapa geológico do Estado do Pará, adota-se a proposta de Santos (2003), modificada, no qual o Cráton Amazônico é dividido nas seguintes províncias tectônicas/geocronológicas: Carajás (3,0-2,5 Ga); Transamazonas (2,2-1,9 Ga); Tapajós-Parima (2,0-1,8 Ga); Amazônia Central (1,9-1,8 Ga); Rondônia-Juruena (1,8-1,5 Ga); Rio Negro (1,8-1,5 Ga) e Sunsás (1,4-1,0 Ga). As províncias tectôno/geocronológicas ainda foram compartimentadas por Santos et al. (2003) em onze domínios tectônicos (Figura 2.2), a partir de critérios como geocronologia, associações litológicas, *trends* estruturais, assinaturas geofísicas e, consequentemente, sua evolução geológica.

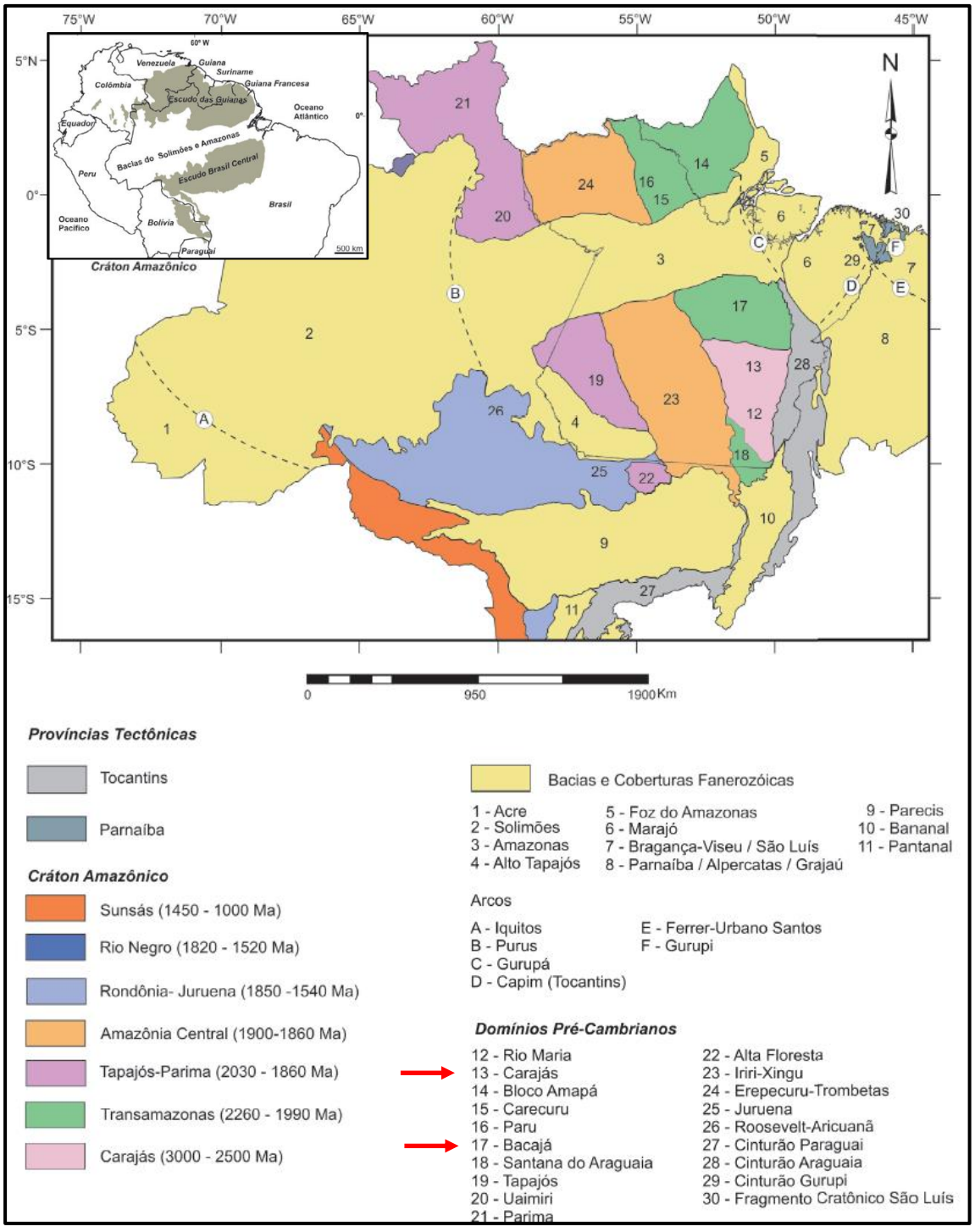

Figura 2.2 – Províncias Tectônicas do Cráton Amazônico (Vasquez & Rosa-Costa, 2008 e respectivas referências).

2.2. Histórico de Exploração Mineral

A história dos trabalhos geológicos desenvolvidos na Serra de Buritirama iniciou-se em 1967 com a descoberta de ocorrências manganesíferas no local por uma equipe coordenada pelo geólogo Erasto Boretti de Almeida. A descoberta se deu durante uma campanha de exploração realizada pela Companhia Meridional de Mineração (subsidiária da United States Steel). A referida empresa, em projeto coordenado pelo geólogo Gene E. Tolbert, identificou as formações ferríferas da Província Mineral de Carajás no mesmo ano (Dyer 1972; 1973).

Os trabalhos de pesquisa realizados pela Companhia Meridional de Mineração na Serra de Buritirama se estenderam até 1979 e individualizaram a serra em cinco alvos principais, sendo estes de sudeste para noroeste os corpos B4, B5, B6, B7 e B8 (Figura 2.3). A partir de 1979, a Mineração Colorado Ltda. assumiu as atividades de pesquisa, realizando uma campanha de sondagem exclusivamente nos alvos B4 e B5, o que culminou em um relatório final de pesquisa protocolado junto ao DNPM (Departamento Nacional de Produção Mineral) no ano de 1982 (Andrade et al. 1986).

Em meados da década de oitenta, dados provenientes de levantamentos geofísicos magnetométricos terrestre e aéreo desenvolvidos no Projeto Brasil-Canadá-Folha SB-22-X-C-V contribuíram no aumento do conhecimento geológico sobre serra, sendo as anomalias geofísicas detectadas pela pesquisa vinculadas à quartzitos ferruginosos.

A partir de meados dos anos oitenta, até o início dos anos dois mil, as atividades na Serra de Buritirama permanecerem relativamente paralisadas. Entre os anos de 2000 a 2005, após a aquisição das concessões de lavra, a empresa Mineração Buritirama S.A iniciou o desenvolvimento de novas pesquisas na região que culminaram na elaboração de um Relatório de Reavaliação de Reservas no ano de 2005. No ano de 2008 uma nova campanha de sondagem abrangendo todos os alvos foi realizada, o que por sua vez possibilitou a confecção de um novo Relatório de Reavaliação de Reservas no ano de 2009. Atualmente, a Mineração Buritirama S.A desenvolve suas atividades de lavra exclusivamente nos corpos B5 e B4 (Figura 2.3), mas detém as concessões dos demais alvos. Segundo o último anuário mineral fornecido pela Agência Nacional de Mineração (ANM), no ano de 2019 a Mina Buritirama forneceu 36% do manganês produzido no Brasil sendo a maior fonte brasileira do metal neste ano (ANM, 2018).

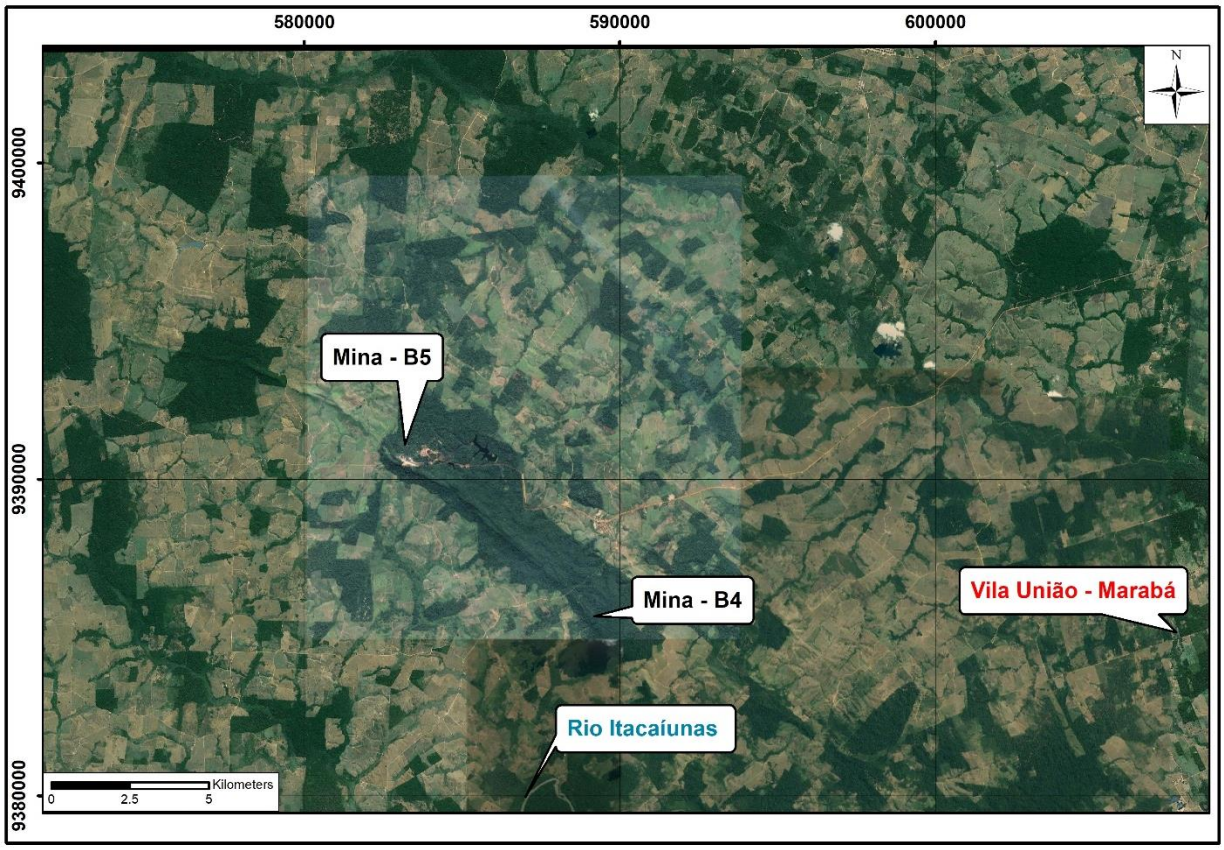

Figura 2.3 – Localização das minas B4 e B5 ao longo da Serra de Buritirama. Destaque para o Rio Itacaiúnas e o distrito de Vila União.

2.3. Evolução das Propostas Estratigráficas para a Formação Buritirama

Em uma perspectiva da evolução do conhecimento geológico, as rochas aflorantes na Serra de Buritirama foram inicialmente correlacionadas às rochas presentes nas serras do Cinzento, Misteriosa, Sereno, Arqueada, Seringa, Andorinhas e Carajás. Todas estas unidades, por sua vez, são interpretadas como sequências metassedimentares arqueanas do Grupo Grão Pará, o qual se sobrepõe ao Complexo Xingu (Figura 2.4; Beisegel et al. 1973; Gomes et al. 1975).

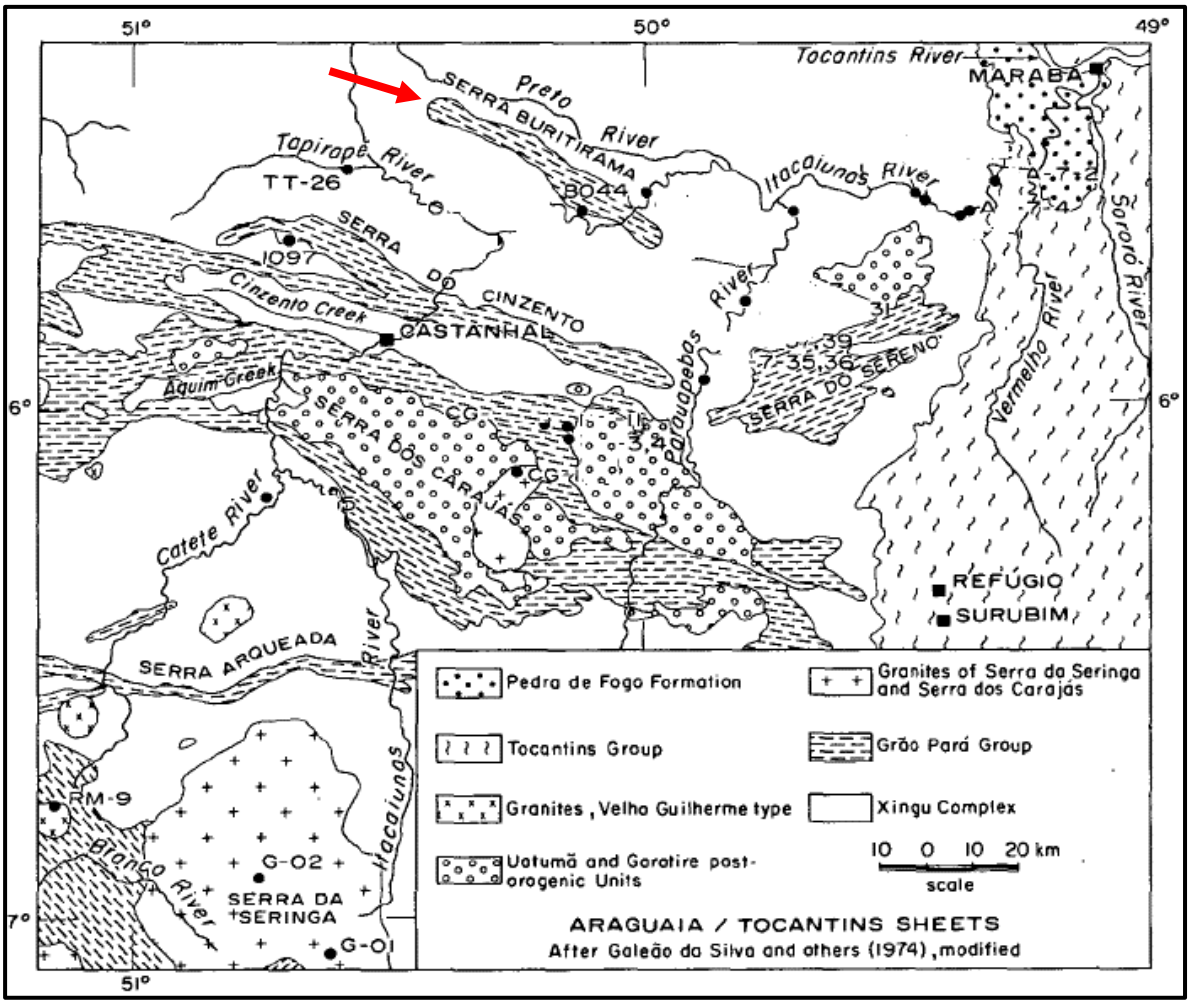

Figura 2.4 – Mapa geológico proposto para a região da Serra de Carajás por Gomes et al. (1975). Destaque para a Serra de Buritirama indicada pela seta vermelha.

DOCEGEO (1988) propõe a criação do Supergrupo Rio Itacaiúnas, que individualiza associações de rochas vulcano-sedimentares entendidas como de idade Arqueana nos grupos (Figura 2.5): Igarapé Salobo, Igarapé Pojuca, Grão-Pará (Formações Parauapebas e Carajás), Igarapé Bahia e Buritirama. Tais unidades apresentam distintos graus metamórficos e registram diferentes intensidades deformação e estruturação tectônica.

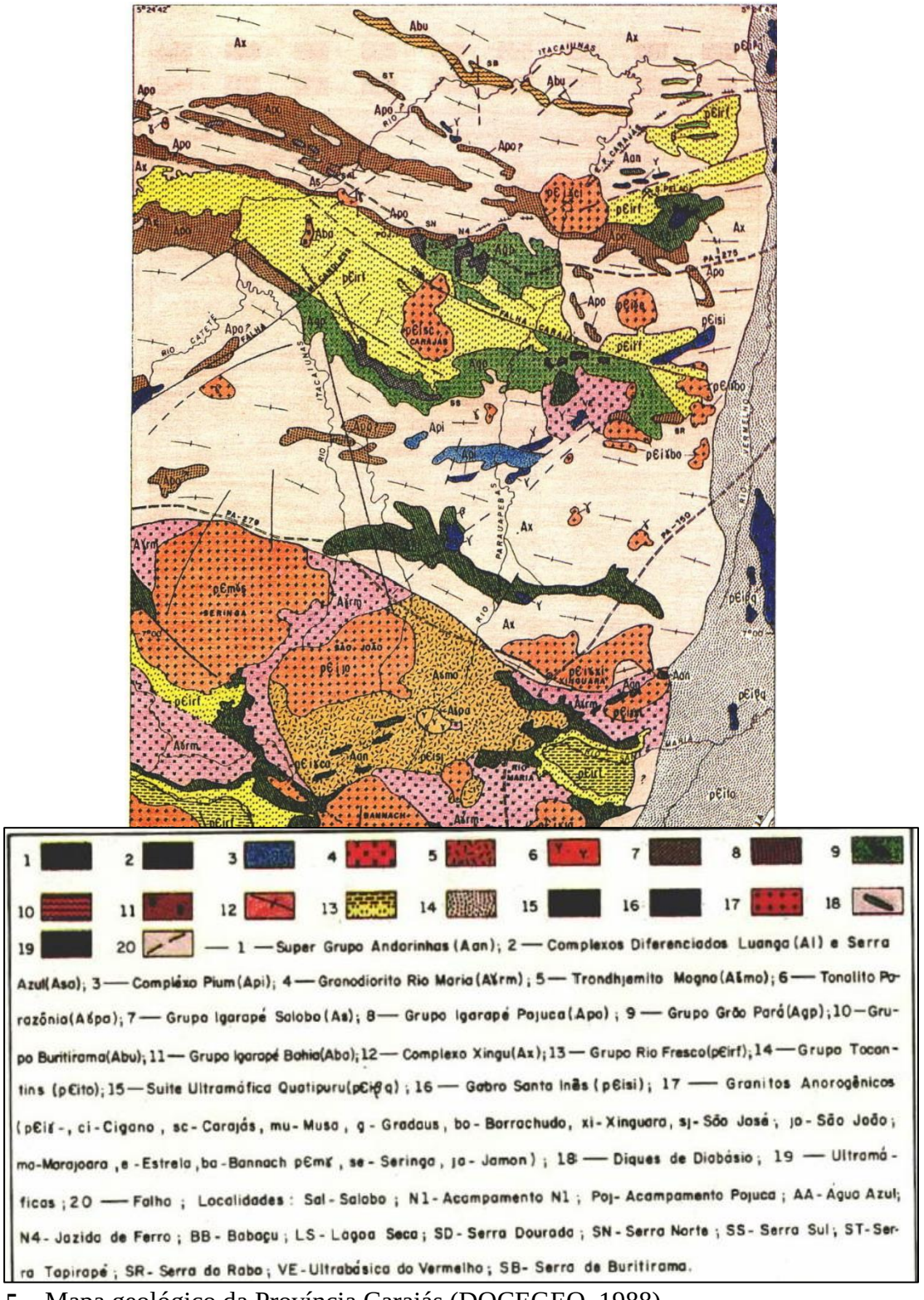

Figura 2.5 – Mapa geológico da Província Carajás (DOCEGEO, 1988).

Já nos anos dois mil Vasquez & Rosa-Costa (2008) propõem que duas formações, Buritirama e Tapirapé, constituam o então criado Grupo Vila União (Figura 2.7). Neste mesmo trabalho o Grupo Vila União é interpretado como parte integrante da unidade Greenstone Belts Arqueanos do Domínio Bacajá e posicionado acima do Complexo ortoderivado Cajazeiras (2942 ± 4 Ma).

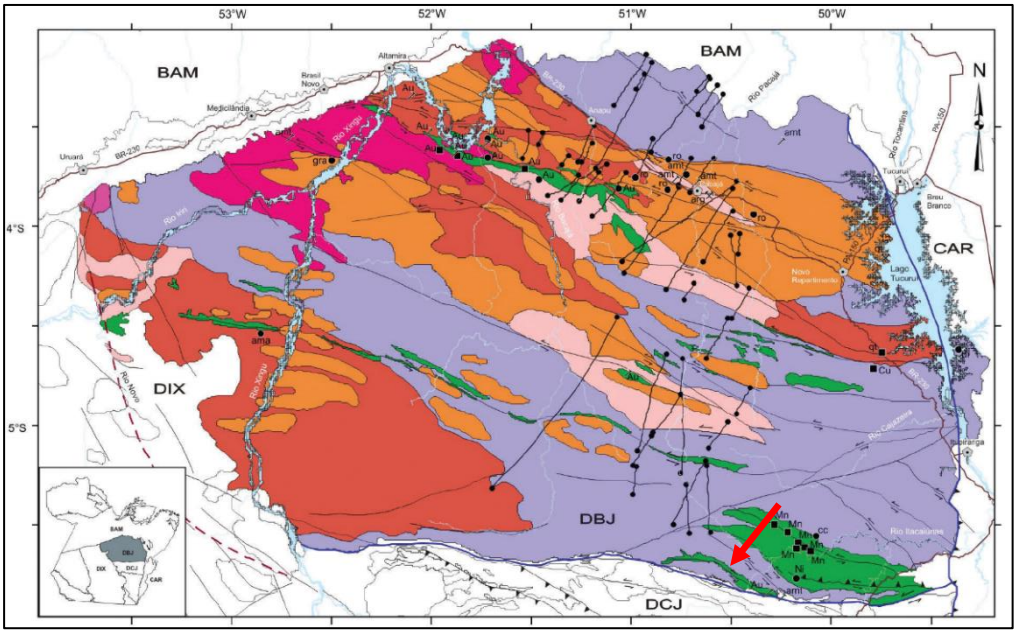

Associações Tectônicas do Domínio Bacajá

PP3γ — *Suíte Plutônica Pós-orogênica* - granitóide orosiriano que pode representar um pulso magmático tardio do Ciclo Transamazônico ou um reflexo de antepaís da Orogênese Cuiú-Cuiú. Granodiorito Sant'Ana (1986 Ma).

Orógeno Riaciano do Ciclo Transamazônico (Arcos de Ilha/Magmático e Colisão Continental)

PP2γ3 — *Suítes Plutônicas Tardi a Pós-colisionais* - granitóides e charnockitos riacianos (2086-2069 Ma) relacionados ao relaxamento crustal posterior à colisão transamazônica. Suítes intrusivas Arapari e João Jorge.

PP2γ2 — *Suítes Plutônicas Sin a Tardicolisionais* - granitóides e charnockitos riacianos (2114-2094 Ma) relacionados ao clímax da colisão continental (ca. 2,1 Ga). Complexo Bacajaí, Granito Canaã, Granodiorito Babaquara.

PP2γ1 — *Suítes Plutônicas Pré-colisionais* - granitóides de arcos de ilha e magmáticos riacianos (2215-2133 Ma) colididos durante o Ciclo Transamazônico. Tonalito Brasil Novo, granodioritos Oca e Belo Monte, Monzogranito Piranhaquara e Metatonalito Tapiranga.

Fragmentos Arqueanos e Siderianos Retrabalhados no Riaciano

APPgn — *Associação Granito-gnáissico-migmatítica Arqueana/Paleoproterozóica* - ortognaisses migmatíticos com protólitos arqueanos a siderianos (2671-2338 Ma) e leucossomas riacianos (2195 Ma). Ortognaisses Pacajá e Uruará, Metonalito Rio Bacajá.

APPgb — *Greenstone Belts Arqueano/Paleoproterozóicos* - seqüências metavulcano-sedimentares neoarqueanas a siderianas. Grupo Vila União, Seqüência Três Palmeiras (2359 Ma), Rochas Supracrustais 1.

APPgl — *Associação Granulítica Arqueana/Paleoproterozóica* - granulitos com protólitos (3009-2597 Ma) de fontes detríticas (3135-2475 Ma) arqueanas e siderianas, e metamorfismo granulítico riaciano (2109-2064 Ma), com charnockitos associados. Complexo Cajazeiras, Ortogranulito Máfico Rio Preto, Granulito Novolândia, Paragnaisse Ipiacava.

DIX - Domínio Iriri-Xingu
DBJ - Domínio Bacajá
DCJ - Domínio Carajás
BAM - Bacia do Amazonas
CAR - Cinturão Araguaia

Diques máficos

Figura 2.6 – Mapa geológico do Domínio Bacajá. A Serra de Buritirama encontra-se inserida na unidade *Greenstone Belts* Arqueanos e sua localização está indicada pela seta vermelha.

A Formação Tapirapé (Oliveira et al. 1994) ocupa a base do Grupo Vila União, localiza-se a sul da Formação Buritirama, com a qual estabelece contato tectônico. É constituída essencialmente por rochas de composição máfico-ultramáfica, como hornblenda-anfibólio, plagioclásio-actinolita xisto e plagioclásio-clorita xisto. De forma subordinada estão presentes cherts e formações ferríferas (Figura 2.7).

Tavares et al. (2018) e Araújo & Sousa (2018) retomam a interpretação da Formação Buritirama como uma unidade pertencente ao Domínio Carajás, mas mantem sua idade Arquena.

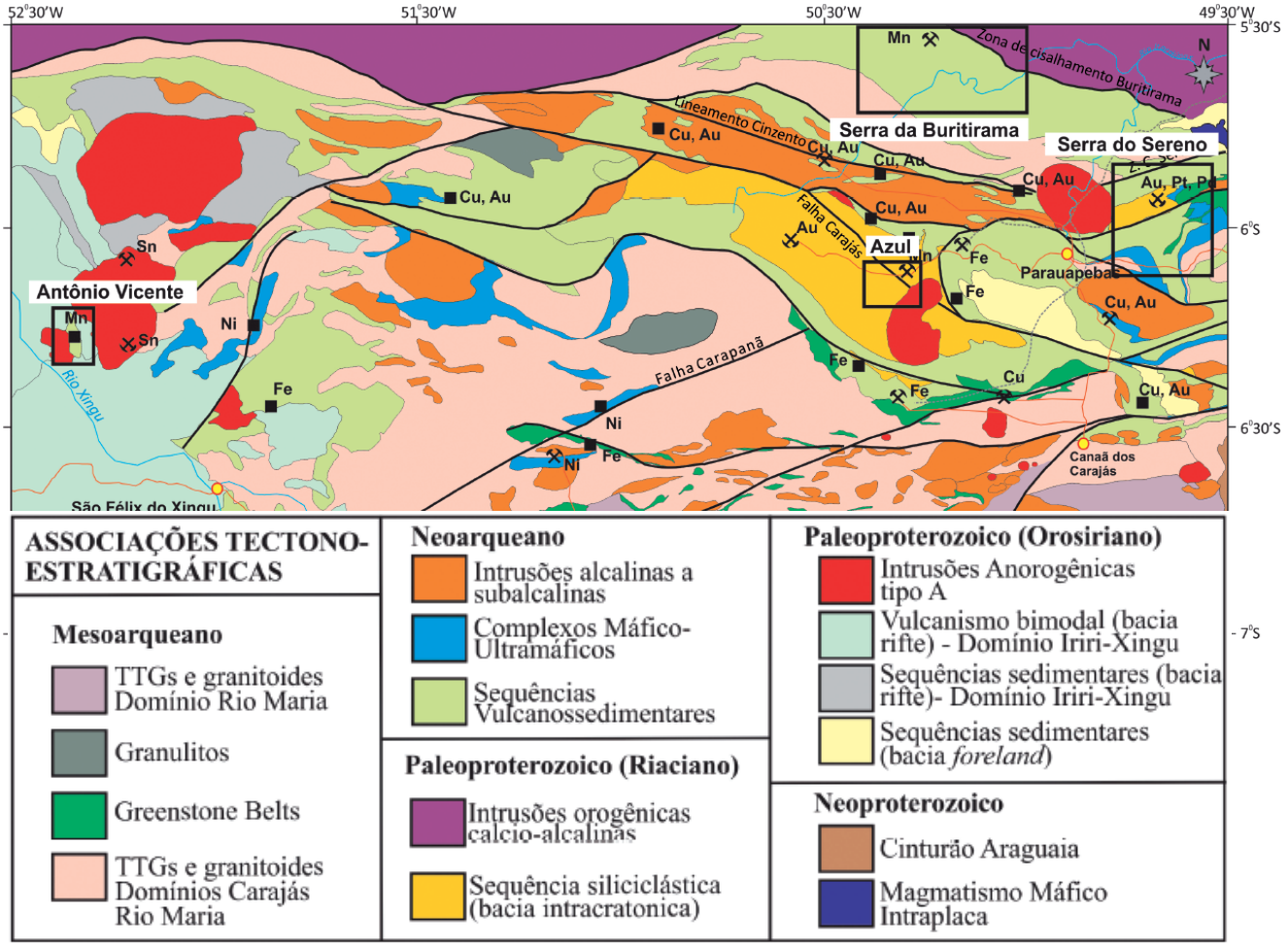

Figura 2.7 – Mapa geológico do domínio Carajás com destaque para os principais depósitos de manganês (Araújo & Sousa, 2018).

2.4. Geologia da Formação Buritirama

A Formação Buritirama, objeto de estudo do presente projeto, ocupa o topo do Grupo Vila União e hospeda o depósito de manganês da Serra de Buritirama. É interpretada por Peters et al. (1977) como uma sequência depositada em uma plataforma marinha rasa, onde o manganês seria proveniente do intemperismo de rochas continentais.

Anderson et al. (1974), a partir do mapeamento geológico e da análise de testemunhos de sondagem realizados no corpo B5, apresenta um mapa geológico e uma estratigrafia para a Serra de Buritirama (

Figura **2.8**), que é subdividida da base para o topo em: quartzito sericítico, calco-xisto com intercalações de mármore, mármores com a intercalação de calco-xistos, protominérios de manganês e quartzito sacaroidal. Os autores ainda propõem a presença de três litotipos especificamente para as

porções superficiais do terreno (acima do limite do intemperismo), sendo estes: calco-xisto intemperizado, xistos alterados com impregnações de manganês e minério de manganês epigenéticos.

As principais paragêneses minerais que constituem as rochas encaixantes foram definidas como (Peters et al. 1977): piroxênio diopsídico + flogopita + calcita + dolomita; diopsídio + flogopita + granada; tremolita + flogopita + K-feldspato + calcita + dolomita; diopsídio + quartzo; diopsídio + tremolita + calcita + dolomita + quartzo; biotita + granada + quartzo + K-feldspato + andalusita. Esfênio, apatita e turmalina constituem acessórios comuns.

No que se refere aos protominérios, destacam-se as seguintes rochas e paragêneses (Peters et al. 1977; Bello, 1978): mármores calco-silicáticos (clinopiroxênio + Mn-calcita + Mn-flogopita); xistos calco-silicáticos (manganofilita + Johannsenita + Mn-carbonatos); piroximanguita mármores compostos pelo intercrescimento entre diversos carbonatos (rodocrosita) associado com grandes cristais de piroximanguita e espessartita; alabandita-tefroita-rodocrosita mármore que contêm como acessório piroximanguita e hausmannita; braunita-mangano calcita mármore (intercrescimento entre braunita e mangano calcita).

A Formação Buritirama, até o momento, não possui dados geocronológicos. A idade arqueana inferida para esta unidade foi sugerida por Gomes et al. (1975) após obter uma idade de 1961±31 Ma (método K-Ar) para um anfibolito coletado nas imediações da serra. Vasquez & Rosa-Costa (2008) obtém uma idade de 2942 ± 4 Ma (método Pb-Pb) para o Complexo Cajazeiras, considerado o embasamento da Formação Buritirama, e optam por manter a idade arqueana previamente proposta. Valarelli et al. (1978) através de estudos da paragênese mineral e de inclusões fluidas indicam que o metamorfismo da sequência sedimentar de Buritirama ocorreu em fácies anfibolito baixo, com temperatura e pressão em torno de 550°C e 1,5 kbar respectivamente.

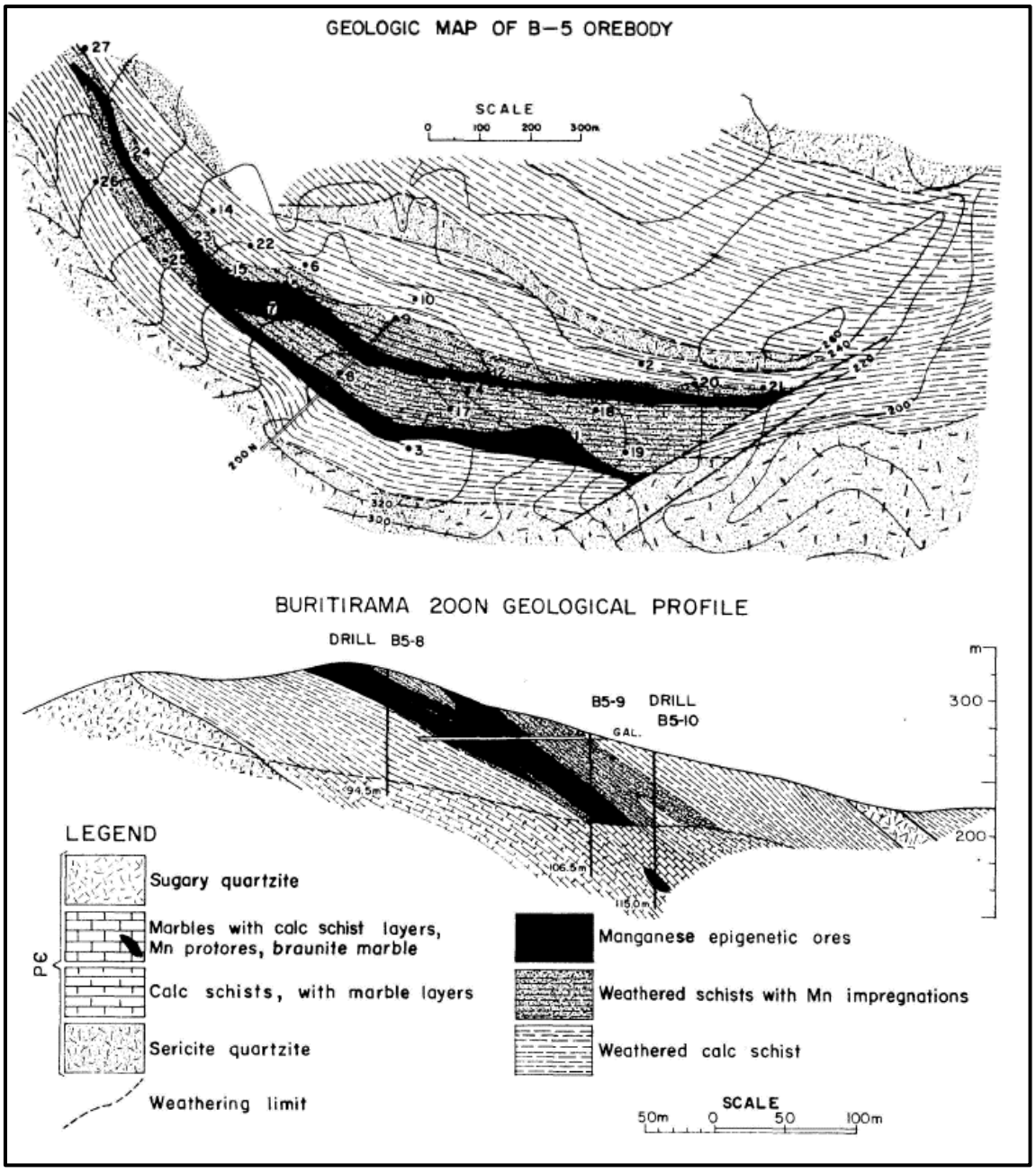

Figura 2.8 – Mapa Geológico da Serra de Buritirama e perfil geológico apresentando a estratigrafia da serra (Anderson et al. 1974; Peters et al. 1977).

2.5. Entendimento do Trabalho

O doutorado foi estruturado na forma de três artigos. O primeiro artigo "Stratigraphy, Petrography and Tectonics of the Manganese-Bearing Buritirama Formation, Northern Carajás Domain, Amazon Craton" foi publicado no "Brazilian Journal of Geology" no ano de 2019 e contempla a petrografia, química mineral, tectonoestratigrafia e geologia estrutural da Formação Buritirama. O segundo artigo "Provenance of the Buritirama Formation Reveals the Paleoproterozoic Assembly of the Bacajá and

Carajás Block (Amazon Craton) and the Chronocorrelation of Mn-Deposits in the Transamazonian/Birimian System of Northern Brazil/West Africa" foi publicado no "Journal of South American Earth Sciences" no ano de 2019 e contempla dados geocronológicos provenientes de zircões detríticos dos quartzitos da Formação Buritirama e dados geocronológicos e geoquímicos do metragranito Buritirama. O terceiro artigo "Genesis of the Mn-Carbonate Rocks and Dolomitic Marbles of the Buritirama Formation, Carajás Domain (Amazon Craton): Implication for a Metallogenetic Mn-Model and a Record of the Lomagundi Isotopic Excursion" foi submetido a "Ore Geology Review" e está em fase de revisão. Tal artigo contempla dados de química mineral, geoquímicos e isotópicos das rochas carbonáticas da Formação Buritirama. As principais conclusões obtidas a partir dos três trabalhos estão condensadas no item 6.

3. ARTIGO I - STRATIGRAPHY, PETROGRAPHY AND TECTONICS OF THE MANGANESE-BEARING BURITIRAMA FORMATION, NORTHERN CARAJÁS DOMAIN, AMAZON CRATON

- Autores: Silas Santos Salgado, Fabrício de Andrade Caxito, Glaucia Nascimento Queiroga, Marco Paulo de Castro
- Publicado no *Brazilian Journal of Geology – Volume 49 - 2019*

3.1. Abstract

The Buritirama Formation (BF) occurs at the extreme north of the Carajás Province, close to the contact with the Bacajá domain, in the southeastern portion of the Amazon Craton (Brazil). The BF consists of a 40 km long, ca. 3 km wide NW-SE trending structure arranged in four imbricated thrusts that individualize three main stratigraphic units. The Lower Unit is composed of orthoquartzite followed by carbonate-silicate rocks. The Intermediate Unit hosts a supergene manganese ore deposit formed by weathering of kutnohorite-rich marble. Quartzite/mica-quartz schist followed by carbonate-silicate rocks make up the Upper Unit. The local basement is constituted by orthogneiss-migmatite (Xingu Complex) and the Buritirama metagranite. Mineral chemistry data and metamorphic textures record a high consumption of carbonate and quartz to produce clinopyroxenes. The structural assemblage of the BF records mass transport from NE to SW and the following deformational phases: D1 (compressional ductile), D2 (compressional brittle) and D3 (extensional brittle). The BF is interpreted as part of a platformal depositional system positioned at the border of the Carajás domain, which was probably

inverted, deformed and metamorphosed during the Transamazonian event (ca. 2.1 Ga), in a deformation belt related to the amalgamation between the Carajás and Bacajá domains.

3.2. Introduction

The Carajás province (3000-2500 Ma) is the oldest part of the Amazon craton and it is located in the southeastern Pará state, north of Brazil (Santos et al. 2000; Santos 2003). It comprises one of the largest mineral provinces of the world (Carajás Mineral Province) hosting world-class deposits of iron, copper, and gold (DOCEGEO 1988; Grainger et al. 2008). Based on geochronological data, the province was subdivided into the essentially Neoarchean Carajás domain (northern portion) and the Mesoarchean Rio Maria domain (southern portion; Gibbs et al. 1986; Machado et al. 1991; Santos et al. 2003; Vasquez and Rosa-Costa 2008; Dall'Agnol et al. 2013).

The Carajás domain is bordered to the west by Iriri-Xingu domain (1992–1860 Ma; Semblano et al. 2016), to the east by the Neoproterozoic/Cambrian (Brasiliano) Araguaia Belt (850–500 Ma; Herz et al. 1989; Moura and Gaudette 1993; Alvarenga et al. 2000), and to the north by the Bacajá domain (Transamazonas Province - 2600-2070 Ma; Vasquez 2006; Besser 2012). The limits among these geotectonic units are still poorly understood, but especially the northern boundary between the Carajás and Bacajá domains was subject to different interpretations in the last years (Ricci et al. 2003; Faraco et al. 2005; Vasquez and Rosa-Costa 2008; Costa et al. 2016).

The Buritirama Formation, at the homonymous ridge, consist of a ca. 40 km long and ca. 3 km wide NW-SE trending structure that plays a key role in this context, since it stands right in the border zone between the Carajás and Bacajá domains and was variably interpreted as a member of both terrains (Vasquez and Rosa-Costa 2008; Costa et al. 2016; Tavares 2015). This formation is also noteworthy because it hosts supergene Mn deposits with resources estimated at 18.6 Mt (Andrade et al. 1986) and mined by Buritirama Company since 2000.

Considering the lack of information about the Buritirama Formation, the aim of this paper is to provide the first systematic structural and stratigraphic framework of this unit coupled with new petrographic and mineral chemistry data. We present preliminary insights in an attempt to elucidate the meaning of the Buritirama Formation in the amalgamation between the Carajás and Bacajá blocks.

3.3. Geological Setting

The Amazon Craton (Almeida et al. 1976; Almeida et al. 1981) is the largest cratonic unit of the South American platform with an area of 4.500.000 Km² spreading through Brazil, French Guyana,

Guyana, Suriname, Venezuela, Colombia and Bolivia. It is formed by Archean nuclei composed of greenstone belts and gneiss-migmatitic terrains (TTG) surrounded by Proterozoic orogenic belts (Almeida et al. 2000; Brito Neves and Cordani 1991; Cordani et al. 2000). Based on geochronological, geophysical, structural, geochemical and isotopic data several authors have proposed different compartmentalization models for the Amazon Craton over the years (e.g. Hasui and Almeida, 1985; Costa and Hasui, 1997; Tassinari and Macambira, 1999; 2004; Santos et al. 2000; Santos, 2003; Vasquez and Rosa-Costa 2008). Here, we assume the latest compilation model provided by Vasquez and Rosa-Costa (2008) in the Geological Map of Pará State (Figure 3.1).

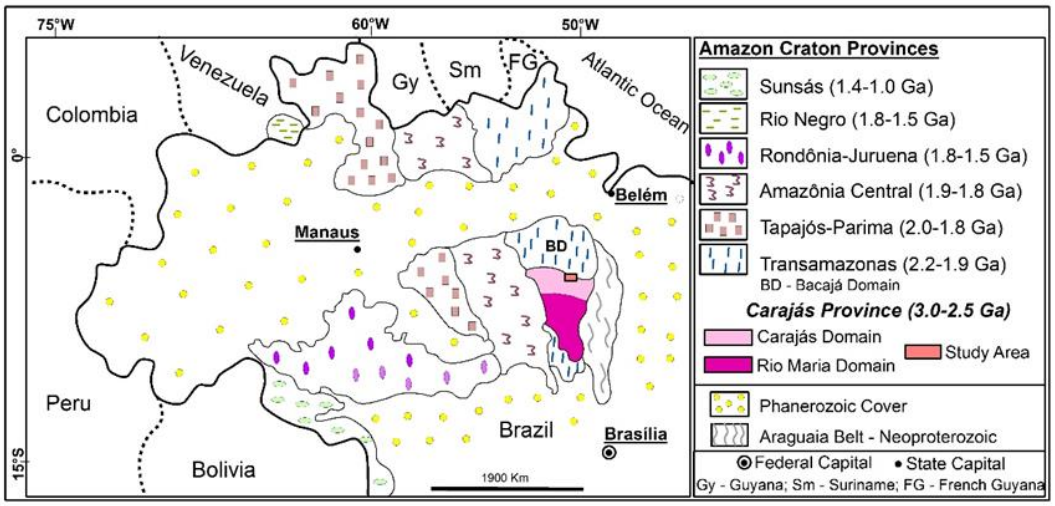

Figure 3.1 – Tectonic provinces of the Amazon Craton (Vasquez and Rosa-Costa 2008) showing location of the study area at the border between the Carajás (Archean) and Bacajá (Paleoproterozoic) domains.

Following works developed by Santos (2003), Vasquez and Rosa-Costa (2008) individualized seven main tectonic provinces in the Amazon Craton: Carajás (3.0-2.5 Ga; Carajás and Rio Maria domains); Transamazonas (2.2-1.9 Ga); Tapajós-Parima (2.0-1.8 Ga); Amazônia Central (1.9-1.8 Ga); Rondônia-Juruena (1.8-1.5 Ga); Rio Negro (1.8-1.5 Ga) and Sunsás (1.4-1.0 Ga). In this scenario, the northern segment of the Carajás domain is composed of three main geochronological units (Figure 3.2; Vasquez and Rosa-Costa 2008; Costa et al. 2016):

Mesoarchean Unit – It is represented by the TTG (Tonalite-Trondhjemite-Granodiorite) gneiss-migmatitic sequence of the Xingu Complex (Silva et al. 1974; Cordani et al. 1984) dated at 3.0-2.85 Ga (Machado et al. 1991; Pidgeon et al. 2000; Delinardo 2014). In its southern border, it is thrusts upon metavolcano-sedimentary groups related to Itacaíunas Supergroup through the Cinzento Shear Zone.

Neoarchean Unit – In the eastern part of the Carajás domain, it represented by the Rio Novo greenstone belt (Araújo and Maia 1991), genetically related to mafic-ultramafic rocks comprising the Luanga Complex (Suita 1988; Ferreira Filho et al. 2007), dated at 2763 ± 6 Ma (U-Pb; Machado et al.

1991). In the central part of the Carajás domain, the Neoarchean unit consists of the A-type calc-alkaline Igarapé-Gelado metagranite dated at 2731 ± 26 Ma (Pb-Pb; Barbosa 2004) and limited by the Carajás lineament to the south.

The Itacaiúnas Supergroup (DOCEGEO 1988) represents the major Neoarchean unit and is formed by the correlate metavolcano-sedimentary groups Igarapé Salobo, Igarapé Bahia, Igarapé Pojuca, Rio Novo and the Grão-Pará group (Vasquez and Rosa-Costa 2008). The Grão-Pará group is represented by basalt-gabbro and andesite (Parauapebas Formation; Meireles et al. 1984; Araújo and Maia 1991) and the giant iron deposits comprising the Carajás Formation (Beisiegel et al. 1973; Macambira 2003). These rocks were dated around 2.77-2.50 Ga (Wirth et al. 1986; Macambira et al. 1996; Trendall et al. 1998) and were probably deposited in a continental rift setting (Gibbs et al. 1986; DOCEGEO 1988; Macambira 2003; Martins 2017).

The Igarapé Salobo, Igarapé Bahia, Igarapé Pojuca and Rio Novo groups are metavolcano-sedimentary units (DOCEGEO 1988) that are distinguished by distinct structural pattern and metamorphic grade (Winter 1994; Siqueira 1996; Pinheiro 1997), but being temporally related (ca. 2.70 Ga; Machado et al. 1991; Tallarico et al. 2005).

The Buritirama ridge (Anderson et al. 1974; Peters et al. 1977; Bello 1978) has been inserted in different lithostratigraphic settings, being linked to the Buritirama group (Itacaiúnas Supergroup – Carajás Domain; DOCEGEO 1988) and the Buritirama Formation (Vila União group – Bacajá Domain; Vasquez and Rosa-Costa 2008). Both interpretations have connected the Buritirama ridge with distinct tectonic provinces and stratigraphic hierarchy, despite none of these works are supported by specifically studies on the Buritirama unit. Considering that, based on the above-mentioned authors and the new geological data presented in this paper, we assumed the Buritirama ridge as part of the Buritirama Formation (Vila União group), but belonging to the Itacaiúnas Supergroup (Carajás Domain). The Vila União group also includes the poorly understood Tapirapé Formation (Oliveira et al. 1994) that comprehend metabasalts and talc-schist (Figure 3.2).

The Buritirama Formation (BF) is located at the northern part of Carajás domain and hosts important manganese mineralization associated with carbonate-silicate rocks and marbles. It was interpreted as deposited in a shallow platform basin and later metamorphosed during the Transamazonic event (ca. 2.0-2.2 Ga) at amphibolite conditions (ca. 550°C; Peters et al. 1977). Despite no geochronological data are available for this unit, the Neoarchean age assumed comes from previously interpretations (e.g. DOCEGEO 1988; Vasquez and Rosa-Costa 2008; Tavares 2015).

Paleoproterozoic Unit – It is represented by clastic continental sedimentary rocks of the Caninana Formation (maximum age 2.1 Ga – U-Pb; Pereira 2009). The Paredão Group (Oliveira et al.

1994) and the Águas Claras Formation (Araújo et al. 1988) have been also assumed to be of Paleoproterozoic age (Tavares et al. 2018). Anorogenic sienogranites and monzogranites (Serra dos Carajás Suite) dated at 1.88 Ga also belong to this unit (Machado et al. 1991; Dall'Agnol et al. 2005).

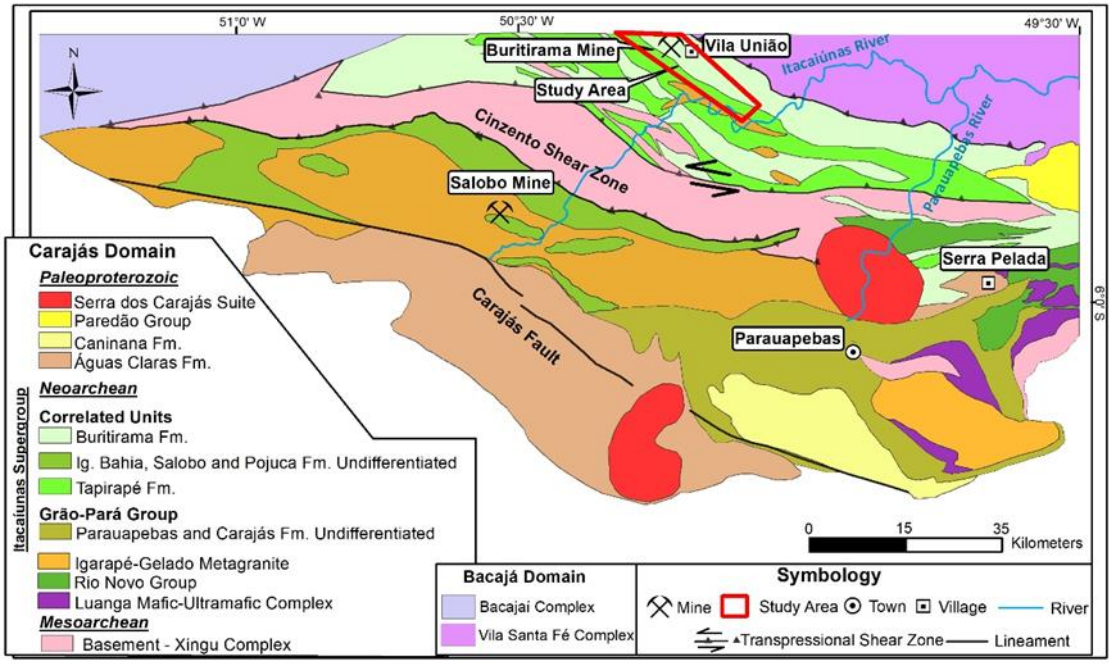

Figure 3.2 – Geological map of the northern Carajás Domain (modified from Costa et al. 2016) presenting the study area (red polygon) near Vila União.

3.4. Materials and Methods

Field work was conducted in the Buritirama ridge, in order to constrain its lithology, stratigraphy and structural geology. To build up the Buritirama stratigraphy, 21 borehole cores (supplied by Buritirama Mineração) combined with field data were employed. Unweathered samples were selected for the preparation of fifty-five polished thin section that were used in the petrographic characterization and mineral chemistry analyses.

Metacarbonate and associated rocks were classified according to the scheme proposed by Rosen et al. (2007). Non-carbonate rocks were informally called silicate rocks or referred to their respective protoliths (e.g. quartzite, metagranite).

Electron Microprobe Analysis (EMPA) were performed in a JEOL JXA-8230 superprobe, equipped with five wavelength dispersive spectrometers (WDS), at the Microscopy and Microanalysis Laboratory (LMic) of the Department of Geology, Universidade Federal de Ouro Preto, Brazil. Six different crystals were used: thallium acid phthalate on H type spectrometer (TAPH in WDS 1), thallium acid phthalate (TAP in WDS 2), lithium floride on H type spectrometer (LIFH in WDS 3), pentaerythritol

on H type spectrometer (PETH in WDS 3); pentaerythritol (PETL in WDS 5) and lithium fluoride (LIFL in WDS 5). The JEOL EMPA software Ver.3.0.1.16 package was used to perform the calibration, overlap correction and quantification. Operating conditions were 15kV accelerating voltage, 20nA beam current and 5 µm beam diameter. The work distance on EMPA is fixed at 11 mm with no variation during the analysis. The following standards were used for calibration: anorthoclase (Na), CaF_2 (F), quartz (Si), corundum (Al), olivine (Mg), magnetite (Fe), scapolite (Cl), $BaSO_4$ (Ba), fluor-apatite (P, Ca), strontianite (Sr), ilmenite (Ti), chromite (Cr), microcline (K) and MnO_2 (Mn). Counting time for Ba, Sr and P was set at 30s at peak and 15s at background while for Na, F, Si, Al, Mg, Fe, Cl, Cr, Ti, Ca, Mn and K was set at 10s at peak and 5s at background. The major spectral interferences were corrected during the standard analysis and during the quantification. Lα X-ray was used for Ba and Sr while Kα X-ray was used for the other elements. The standard deviation for each element was: Na (1%), F (1.05%), Si (0.29%), Al (0.45%), Mg (0.46%), Fe (0.4%), Cl (0.97%), Ba (0.29%), P (0.61%), Sr (0.68%), Ti (0.29%), Cr (0.54%), Ca (0.25%), K (0.49%) and Mn (0.43%).

3.5. Results

3.5.1. Geology of the Buritirama Formation

The BF outcrops in the homonymous ridge along a 40 km long NW-SE structure and shows variable thickness (max. around 900 m). It dips predominantly at 30° to northeast. The Itacaiúnas River defines its southeast border where the ridge ends in an anticlinal structure with the Buritirama metagranite in its core. To the southwest it is thrusts over the Xingu Complex orthogneisses (Carajás Domain) and to the northeast, a quartz, iron-rich shear zone marks the contact between the BF and an the probably Bacajá domain (Figure 3.3A and Figure 3.3B).

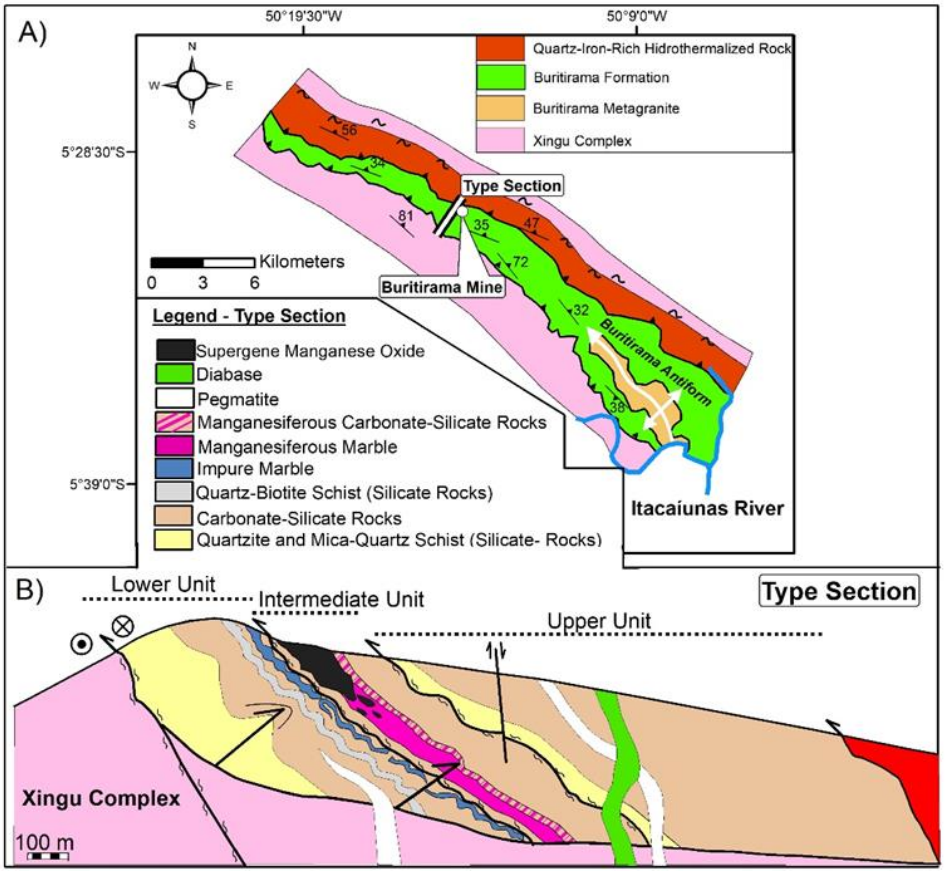

Figure 3.3 – A) Geological map of the Buritirama ridge (for location see Figure 3.2); and B) type section of the Buritirama Formation showing the individualized Lower, Intermediate and Upper units.

3.5.2. Stratigraphy

The stratigraphy of the BF type section is marked by four imbricated thrusts that individualize three main metamorphic units (Figure 3.3B and Figure 3.4): Lower Unit (LU); Intermediate Unit (IU), and Upper Unit (UU). Based on fieldwork combined with borehole logging, each unit was separated according to the dominant lithotypes: silicate rocks, carbonate-silicate rocks, calc-silicate rocks and impure marbles. It is important to emphasize that these lithotypes are strongly intercalated throughout the sequence, thus we will always refer to the predominant lithotype.

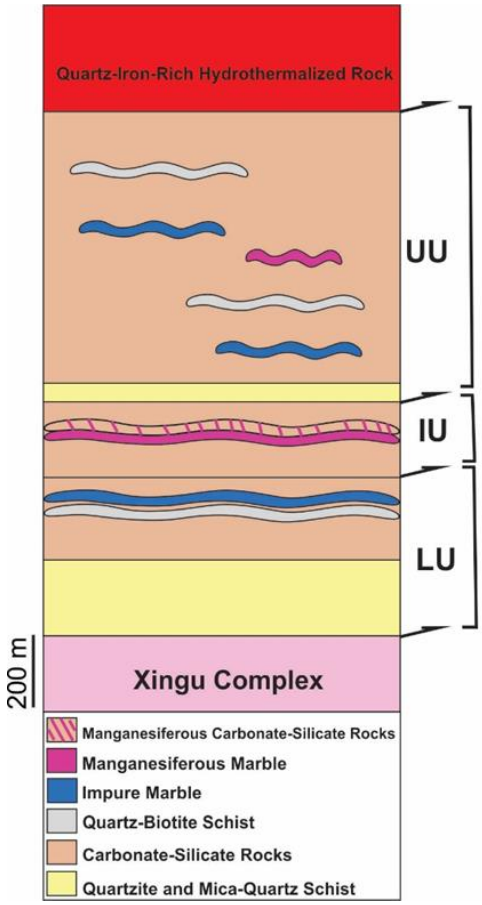

Figure 3.4 – Tectonic-stratigraphic column of the BF in its type-section.

Lower Unit (LU) – It is represented by a thick (approx. 200 m) rock package made up of orthoquartzite and minor mica-quartz schist that are followed mainly by carbonate-silicate rocks (Mc±Phl±Cb+Di paragneiss; Figure 3.5A; mineral abbreviations according to Whitney and Evans 2010, described at the figure caption). Near the uppermost contact, layers of silicate rocks (Alm±Cum±Pl+Qz+Bt schist) and impure marble (Di+Phl+Cb marble) occur (Figure 3.5B and Figure 3.5C). A strike-slip dextral shear zone set in orthogneiss-migmatite of the Xingu Complex bounds the basal contact and, in this area, the BF records its highest dipping (approx. 75°NE; Figure 3.5D).

Intermediate Unit (IU) – The supergene manganese ore deposit is hosted in this unit (up to 70 m thick) and is formed by weathering of kutnohorite-rich marble (Figure 3.5E and Figure 3.5F). Manganesiferous marble (ca. 20 m thick) grades to Mn-rich carbonate-silicate rocks (Mn-Cal±Mn-Di+Phl paragneiss/schist) and silicate rocks (Qz+Pl+Bt Schist). Mylonitic textures present in the basal contact define a ductile thrust upon the LU.

Upper Unit (UU) – It is very similar to the LU. At the base, sheared quartzite (minor) and mica-quartz schist record a ductile thrusting upon IU. A thick layer of carbonate-silicate rocks intercalated with minor lenses of silicate rocks and impure marbles (occasionally Mn-rich) comes next. The

uppermost contact is defined by hydrothermalized rocks rich in quartz, iron oxide (Figure 3.5G) and related to a compressional shear zone that has been impressed on the Xingu Complex.

A deformed alkaline porphyritic granite (Buritirama metagranite) composed essentially of perthitic-Mc, Qtz, Pl, Bt and Mag was recognized near the Itacaíunas River and comprises the local basement of the BF (Figure 3.5H). Undeformed sills and dikes of pegmatite and later diabase cut the ridge (Figure 3.5I).

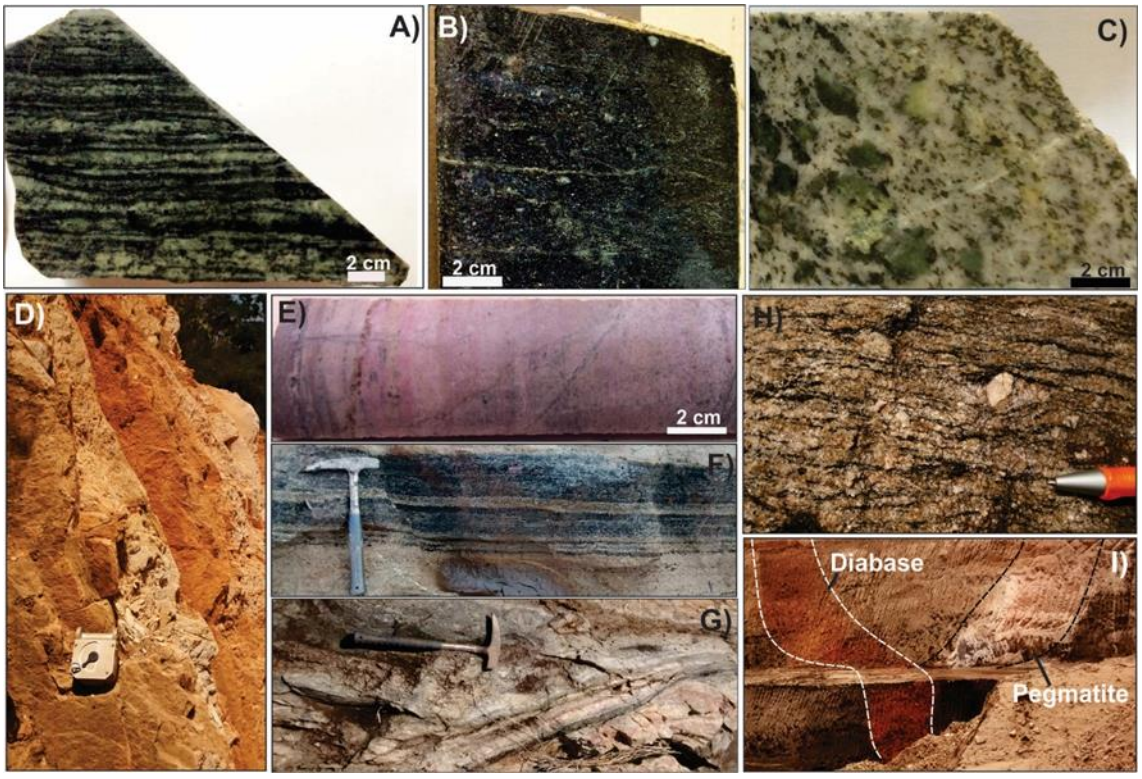

Figure 3.5 – General aspects of BF lithotypes. A) Mc±Cb±Phl+Di paragneiss (carbonate-silicate rock); B) Alm±Cum±Pl+Qz+Bt schist (silicate rock); C) Tr+Phl+Cb marble (impure marble); D) steeply dipping quartzite present at the base of BF; E) kutnohorite-marble (manganesiferous marble); F) layers of Mn-oxide (kutnohorite-marble protolith) and clay minerals (carbonate-silicate rock protolith) intercalated; G) hydrothermalized rock rich in quartz and magnetite (Xingu Complex); H) sheared porphyritic granite (Buritirama Metagranite); I) a diabase dike cross-cutting a pegmatite dike, both intensely weathered.

3.5.3. Petrography

Based on visually estimated modal mineralogy, the metamorphic rocks of the BF were classified as impure marble, carbonate-silicate rocks, calc-silicate rocks and silicate rocks. Manganesiferous varieties were also recognized. These group of rocks record two main penetrative fabrics (metamorphic banding and schistosity) depending on the greater or lesser amount of carbonates/pyroxenes in relation to phyllosilicates (e.g. phlogopite-biotite). The banding occurs preferentially in carbonate-silicate rocks,

whereas silicate rocks show greater contents of phyllosilicates and, therefore, a conspicuous schistosity.

Carbonate-Silicate Rocks (CBS) – It is the main lithotype of the BF and consists of dark and greenish rocks with seriate, nematoblastic, lepidoblastic and/or granoblastic fabrics. It is composed of diopside (40–30 %vol), calcite (40–15 %vol), phlogopite (35–15 %vol) and microcline (<15 %vol). Quartz, plagioclase and spessartine (syn and post-tectonic) are subordinate. The rocks commonly show a prominent metamorphic banding (< 1.5 cm; Figure 3.6A) defined by intercalation of diopside and phlogopite-carbonate layers.

Diopside occurs as large poikiloblastic and porphyroblast (less common) crystals up to 1.5 cm, containing inclusions of all above-mentioned minerals. Calcite/dolomite is present as subhedral medium-grained crystals with straight boundaries and triple junctions. Phlogopite occurs as anhedral medium-grained tabular crystals. Microcline hardly shows its typical twinning, exhibits expressive modal variation and usually occurs as inclusions in diopside (Figure 3.6B). Carbonate-silicate rocks change into a manganesiferous variety (MCBS) by the introduction of manganese in the structure of minerals: Mn-Diopside, Mn-calcite/Kutnohorite and Mn-phlogopite.

Calc-Silicate Rocks (CCS) – This class of rocks shares many similarities with carbonate-silicate rocks, like fabrics, colour and mineralogy. Nevertheless, they differ by the low abundance of carbonates and phlogopite.

Impure Marbles (IM) – It is present mainly in the lower unit and is formed essentially by coarse-grained crystals (up to 2.5 mm) of calcite and dolomite (>50 %Vol) arranged in a polygonal fabric (granoblastic; Figure 3.6C). Tabular, fine to medium-grained crystals of phlogopite are oriented and locally exhibit deformational structures (e.g. kink bands). Poikiloblastic diopside crystals bearing inclusions of carbonates, phlogopite and minor quartz and microcline are present. Secondary tremolite commonly replaces diopside.

Apatite, titanite, magnetite and sulphides are the main accessory minerals in impure marbles and carbonate-silicate rocks.

Manganesiferous Marbles (MM) – It is restricted to the intermediate unit and is composed of kutnohorite/Mn-calcite (> 50 %Vol), spessartine (30–10 %Vol), kanoite (~15 %Vol), Mn-phlogopite (<15 %Vol) and rhodonite (<10 %Vol; Figure 3.6D). Medium-grained carbonates occur with typical polygonal fabric. Euhedral, fine-grained (~0.05 mm) spessartine crystals are distributed throughout the rock. Kanoite (Kan; rare Mn-clinopyroxene) occurs as medium to coarse-grained poikiloblastic crystals and bears kutnohorite inclusions. Oriented subhedral crystals of carbonate-bearing rhodonite are also present. Mn-phlogopite exhibit its typical tabular habit. It is important to note that all above minerals were recognized by microprobe analyses. Quartz, microcline, apatite, sulphides and barite are present

as minor minerals. MM represents the proto-ore, later overprinted by supergene processes giving rise to Mn-oxides (Figure 3.6E).

Silicate Rocks (SR) –Three main lithologies (orthoquartzite, biotite schist and mica-quartz schist) represent this class. Orthoquartzite and biotite schist occur mainly in the LU, while mica-quartz schist was also recognized in the UU. Orthoquartzite is formed by anhedral, medium to coarse-grained crystals of quartz, characterized by conspicuous dynamic recrystallization fabric (subgrains and interlobate grain boundaries). Minor muscovite and magnetite are present. Biotite schist (Figure 3.6F) shows a prominent lepidoblastic fabric and is composed essentially of biotite (>50 %Vol), quartz (30-10 %Vol), plagioclase (30-5 %Vol), cummingtonite (<10 Vol%), microcline (<10 %Vol) and almandine (<5 %Vol). Ilmenite, zircon, titanite and sulphides occur as accessory minerals.

Mylonitic fabrics as pressure shadows and S-C foliations are present close to the main shear zones and remarkable post-tectonic features such as annealing and overgrown minerals are ubiquitous in all studied units. Evidence of retrometamorphic processes like uralitization, chloritization, sericitization and saussuritization is also observed.

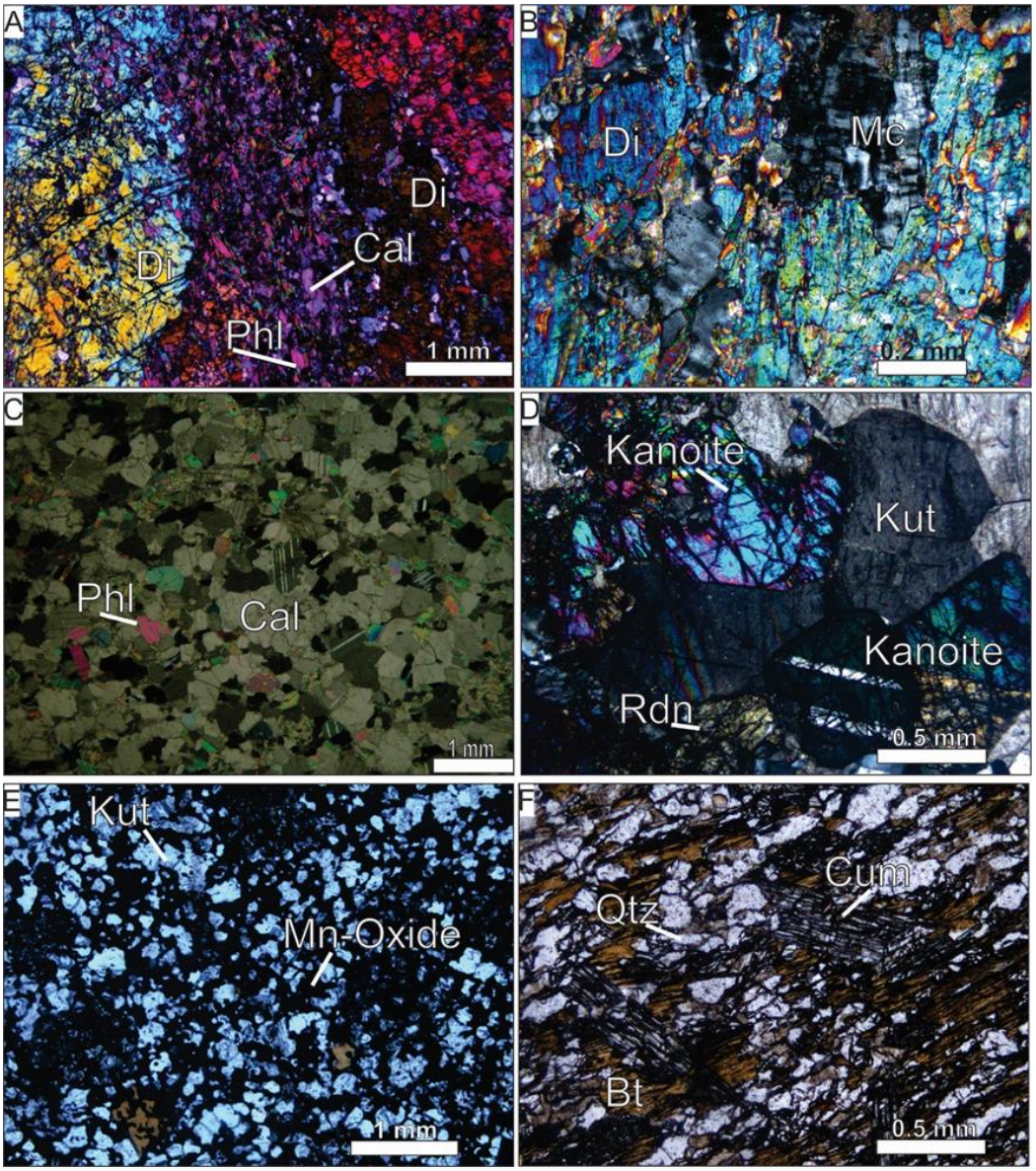

Figure 3.6 – Petrographic aspects of rocks from the BF under the microscope (crossed polarizers, except F); A) banded Mc-Phl-Cal-Di paragneiss; B) poikiloblast of diopside bearing microcline inclusion (carbonate-silicate rocks); C) impure marble showing typical granoblastic fabric; D) kanoite, kutnohorite and rhodonite present in manganesiferous marble; E) manganese oxides formed by kutnohorite weathering; F) cummingtonite-quartz-biotite schist.

3.5.4. Mineral Chemistry

Chemical compositions were determined for carbonate, pyroxene, garnet, feldspar, pyroxenoid, amphibole and mica that occur in the main BF lithotypes (Appendix 1A to 1G).

Carbonate – Calcite (Figure 3.7A) occurs mainly in CBS and IM (normally surrounding phlogopite crystals). Kutnohorite and Mn-calcite are present in different samples of MM and record a Mn-enrichment trend. Dolomite is restricted to IM, however, high grades of Mg are also reported in kutnohorite ($MgCO_3$ up to 20 Mol%).

Pyroxene – Diopside, Mn-diopside and kanoite are present in CBS, CCS and MM, respectively. These minerals show a clear Mn-enrichment trend, from diopside to kanoite (Figure 3.7B).

Garnet – It is mainly represented by the end-members spessartine and almandine (Figure 3.7C). Spessartine occurs in MM and shows mole fraction of pyrope and grossular below 10 %. In CCS the grossular mole fraction in spessartine reaches up to 30 %. Almandine is restricted to silicate rocks and contains up to 45 Mol% of grossular and pyrope, the former being dominant.

Feldspar – Microcline is the main feldspar present in CBS and IM. Ba-rich microcline (up to 5 wt% of BaO) also occurs in these rocks. Andesine with intergrowth of labradorite (anorthite mole fraction up to 52%) and anorthoclase (K-Fds mole fraction up to 24%) was recognized the SR (Figure 3.7D).

Pyroxenoid – It is represented by rhodonite crystals present exclusively in MM (Figure 3.7E). Rhodonite is characterized by high $MgSiO_3$ contents (up to 30 Mol%).

Amphibole – Tremolite, cummingtonite and Mn-cummingtonite (Figure 3.7F) are present in IM, SR and CCS, respectively.

Micas – Phlogopite occurs in CBS and MM while Mn-phlogopite is present in the manganesiferous varieties of these rocks. Biotite is restricted to SR (Figure 3.8).

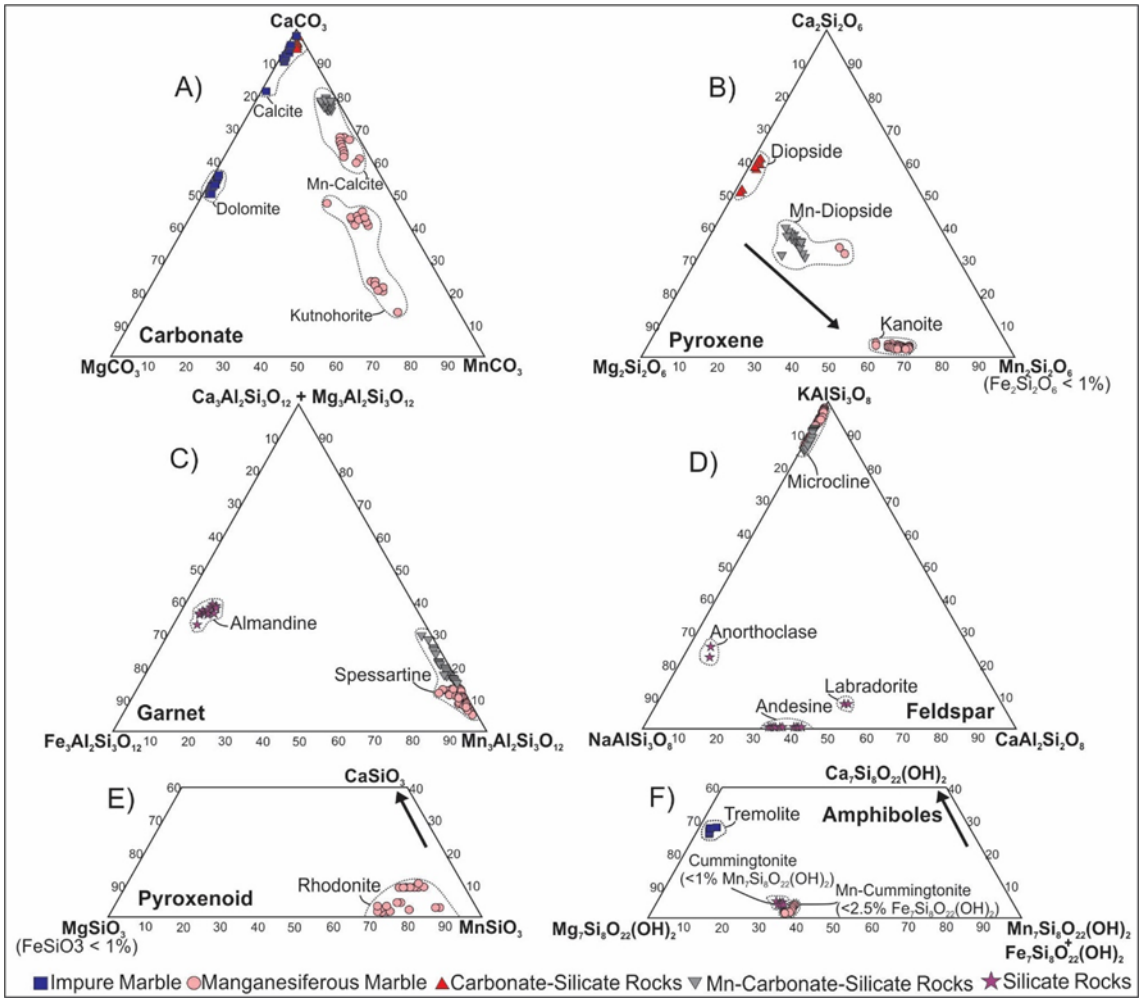

Figure 3.7 – Ternary diagrams showing the mineral composition of A) carbonates (Goldsmith and Graf 1960); B) pyroxenes (Morimoto 1988); C) garnets (modified from Klein and Duthow 2007); D) feldspars (Deer et al. 1992); E) piroxenoid (Peacor et al. 1978); F) amphiboles (Klein and Duthow 2007) for different lithologies of BF.

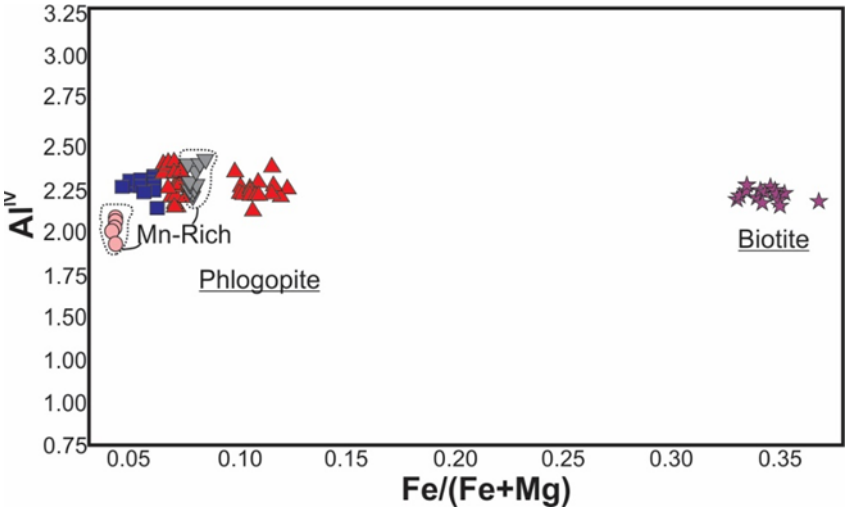

Figure 3.8 – Binary diagram (based on Deer et al. 1992) showing mica composition of BF. Legend in the Figure 3.7.

3.5.5. Structural Geology

The structural framework of the Buritirama ridge is the result of polyphasic deformation divided in three main phases.

Phase D1 – It starts with earlier formed rootless intrafolial folds (F1) and a penetrative axial-plane foliation (S1) parallel to metamorphic banding (Bn; Figure 3.9A). S1 is folded into isoclinal folds (F2; Figure 3.9B) verging to SW with hinge dipping to NW and NE. A second penetrative axial-plane foliation (S2; Figure 3.9C) is recognized in the F2 hinge zone. S2 is usually parallel to S1//Bn and dips preferentially to NE with modal maximum at 025/30 (Figure 3.9D). Down-dip and slightly oblique mineral stretching lineation (Ls), formed by quartz and mica, occurs on the S2 plane. Ls dips chiefly to NE with parallel/sub-parallel trend to F2 hinge (Figure 3.9E). Sinistral shear folds related to steep S2 are present in the basal boundary of the BF.

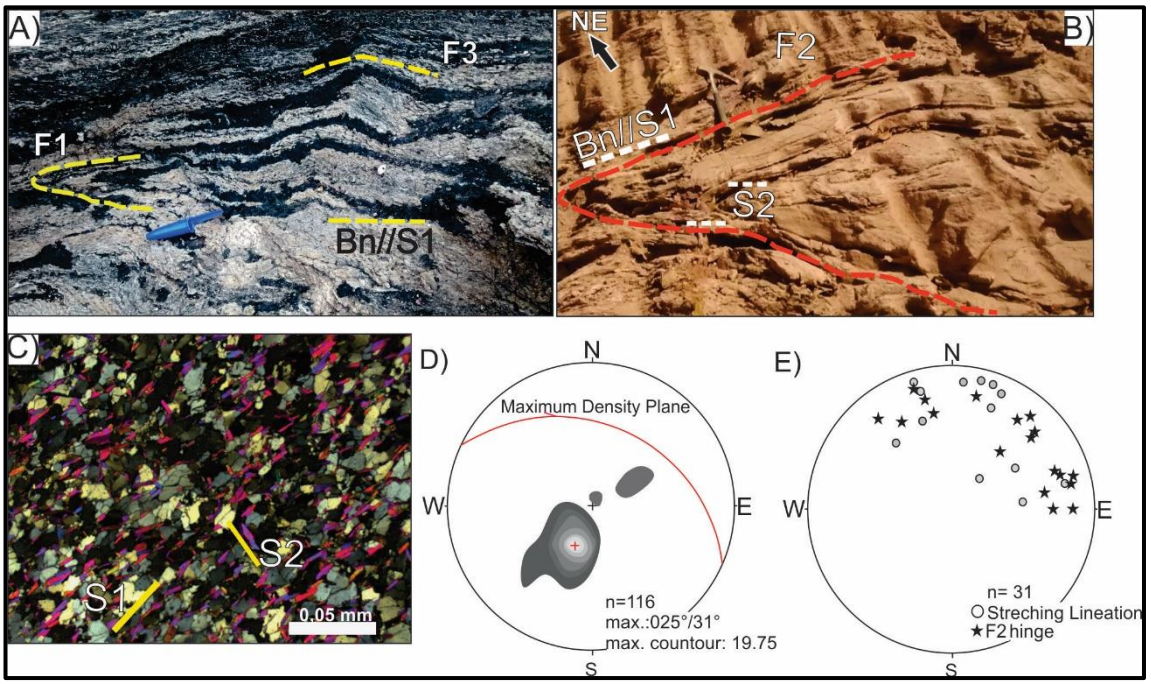

Figure 3.9 – Structural features of phase D1. A) Intrafolial fold (F1) and Bn parallel to S1; B) isoclinal folds (F2) with axial-plane foliation (S2); C) photomicrograph exhibiting the relationship between S1 and S2 (marked by muscovite) in the hinge-zone of F2 fold-pattern; D) equal area lower hemisphere projection showing S1//S2//Bn distribution; E) equal area lower hemisphere projection showing distribution of stretching lineation and F2-hinge.

Narrow branches of ductile shear zones distinguished by mylonitic rocks (S-C foliation and mantled porphyroclasts are easily recognizable; Figure 3.10A) cross the ridge parallel to S2, overprinting F2 folds and recording a tectonic transport towards SW. The imbricated thrusts that build the ridge are broken apart in minor segments by transfer shear zones (Figure 3.10B).

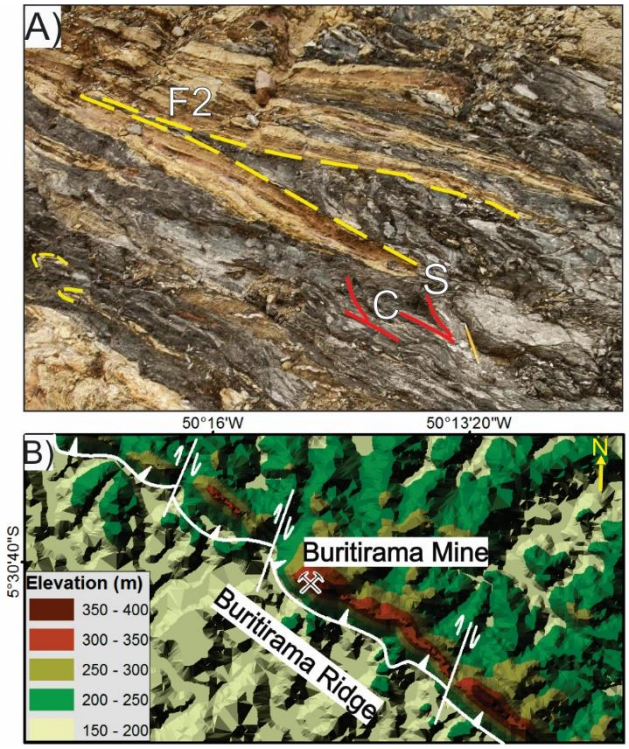

Figure 3.10 – Shear zones related to phase D1. A) F2-fold pattern transposed by ductile reverse shear zone; B) Digital elevation model of the Buritirama ridge (NW-SE) split by transfer faults (NE-SW) in different sections.

Gentle upright folds (F3) with horizontal hinges plunging at a low angle to NW and SE (Figure 3.11A and Figure 3.11B) represent the last expression of the D1 phase. The superimposed F2 and F3 folds constitute two types of interference folds, which depend on the interception angle between the hinges. When F2 and F3 hinges are parallel, Type 3 (Ramsay and Huber, 1987) interference pattern forms (Figure 3.11C). However, the rotation of F2-hinges detected in some areas of the BF causes interception of F3-hinges at a high angle, constituting a Type 2 (mushroom; Ramsay and Huber, 1987) pattern (Figure 3.11D). Sheath folds are also present, locally, within the shear zones.

Phase D2 – It is characterized by brittle reverse and back-thrust faults verging to SW and NE, respectively. Reverse surfaces occur rather along the lithological transitions or oblique to them and dips ca. 40° (Figure 3.12A). Back-thrusting give rise to fault-propagation folds gathered in the F4 pattern. F4 consists of open to close folds with hinge plunging at low angles to NW (Figure 3.12B and Figure 3.12C). It is coaxial to the F3-folds pattern.

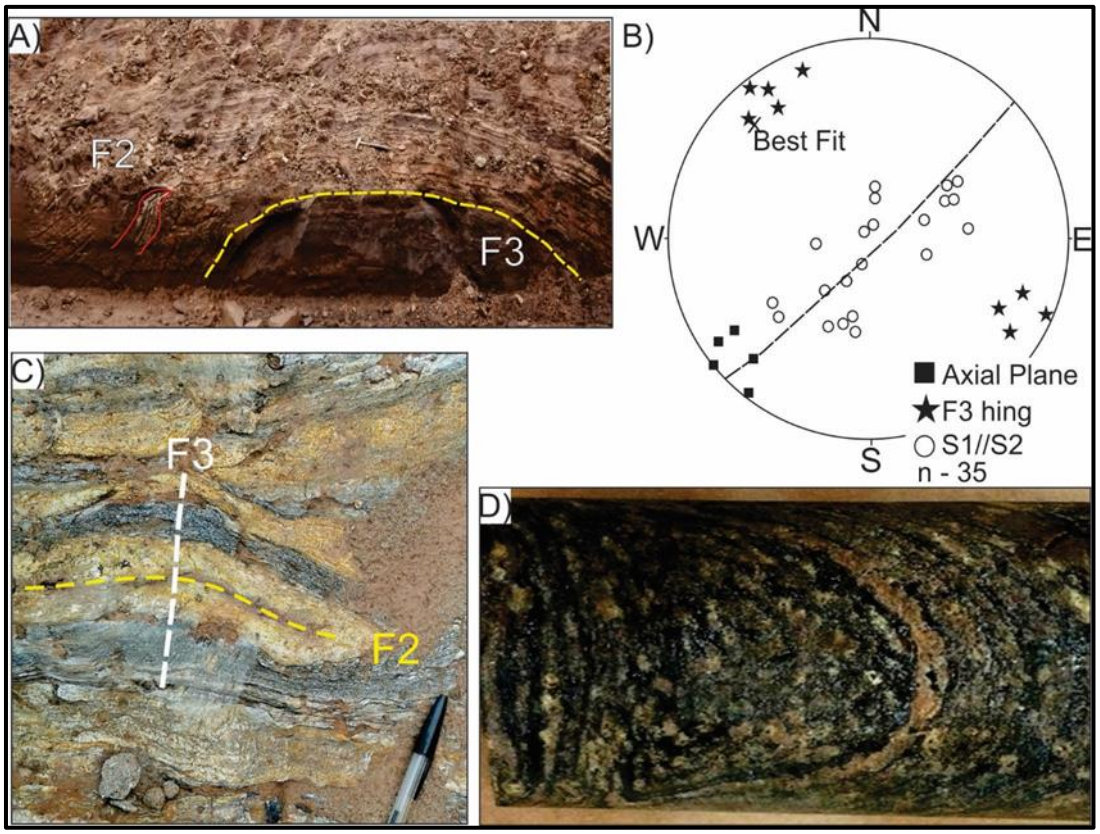

Figure 3.11 – Structural features of phase D1. A) Gently upright F3 fold; B) equal area lower hemisphere projection showing the main structures of F3 pattern; C) superimposed F2 and F3 folds giving rise to type 3; and D) type 2 (mushroom) interference patterns (borehole diameter of 9.8 cm).

Phase D3 – It represents an essentially brittle and extensional regime characterized by conjugated normal faults that, despite significant angular variation, can be represented by the two modal maximum at 141/87 and 254/87 (Figure 3.13A and Figure 3.13B).

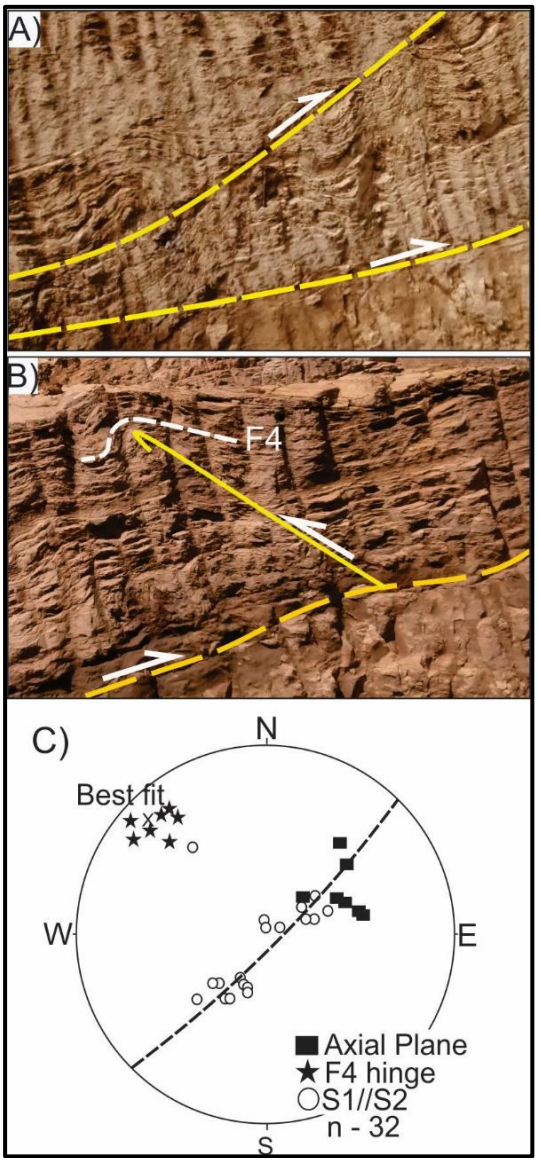

Figure 3.12 – Structural features of phase D2. A) Reverse faults; B) back-thrusting associated to F4 folds pattern; C) equal area lower hemisphere projection showing the main structures of F4 pattern.

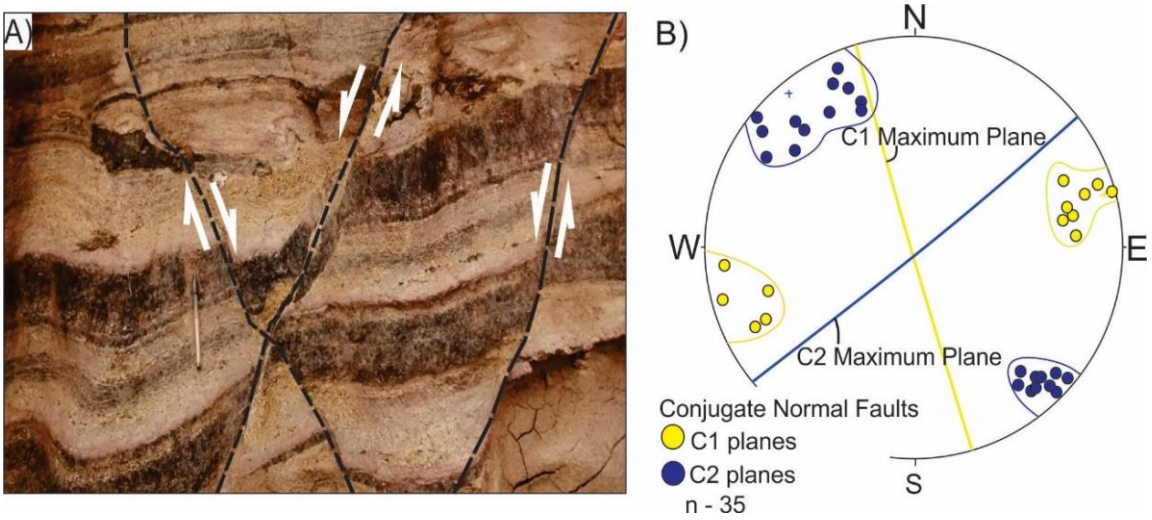

Figure 3.13 – Structural features of phase D3. A) Normal faults impressed in manganesiferous saprolite; B) equal area lower hemisphere projection showing the normal conjugate planes C1 and C2.

3.6. Discussion

3.6.1. Mineral Paragenesis, Metamorphic Reactions and Protoliths of Metamorphic Rocks

The mineral paragenesis of the BF are compiled in the Figure 3.14. Carbonates textures and chemistry data from IM, MM, CCS and CBS suggest that these minerals were consumed by metamorphic reactions, producing silicate phases. Diopside and Mn-diopside probably formed by reactions involving dolomite and Mn-calcite, respectively (Reactions 1 and 2). Rhodonite is restricted to kutnohorite-bearing rocks and the expressive Mg content in both minerals corroborates its genetic relation (Reaction 3). Kanoite is for the first time reported in Brazil and it is normally recognized in Mn deposits (Kobayashi 1977; Dasgupta et al. 1990). Diopside, Mn-diopside and kanoite compositions point to solid solution reactions (Brown et al. 1980) as is also the case for calcite, Mn-calcite and kutnohorite. The very low abundance of quartz and its occurrence as inclusions or relict crystals indicate it was probably consumed in the mentioned reactions.

$2MgCaCO_3 + 4SiO_2 = 2CaMgSi_2O_6 + CO_2$ **(Reaction 1)**
Dolomite + Quartz = Diopside + Carbon Dioxide
$2(CaMn)_{1-x}Mg_xCO_3 + 4SiO_2 = 2(CaMn)_{1-x}Mg_xSi_2O_6 + CO_2$ **(Reaction 2)**
Mg-Kutnohorite + Quartz = Mn-Diopside + Carbon Dioxide
$Mn_{1-(x+y)}Ca_xMg_yCaCO_3 + SiO_2 = Mn_{1-(x+y)}Ca_xMg_ySiO_3 + CO_2$ **(Reaction 3)**
Kutnohorite + Quartz = Rhodocrosite +

Microcline and phlogopite have also a large distribution in BF lithotypes. In some samples, the occurrence of microcline exclusively as inclusions in pyroxene coupled with phlogopite overgrowth texture indicates a reaction probably involving dolomite (Carbon Dioxide Reaction 4). Despite of the previous reactions, marked essentially by decarbonatization process, water is required for phlogopite formation (Kretz and Garrett 1979; Sanford 1980) and could derive from dehydration reactions (metamorphic grade increasing) or external sources.

$3MgCaCO_3 + KAlSi_3O_8 + H2O = KMg_3AlSi_3O_{10}(OH)_2 + 3CaCO_3 + 3CO_2$ **(Reaction 4)**
Dolomite + Microcline + Water = Phlogopite + Calcite + Carbon Dioxide

A low-amphibolite metamorphic grade has been previously indicated for the BF (Peters et al. 1977; Valarelli et al. 1978), which is also pointed out by diopside, Mn-diopside, kanoite and calcite, Mn-calcite and kutnohorite solid solutions (Brown et. 1980; Capitani et al. 1981). The Paleoproterozoic

metamorphic age (2.1 Ga; Transamazonic event; Costa et al. 2016) recorded in the basement nearby the Buritirama ridge can also be tentatively attributed to the age of metamorphism of the BF (Macambira et al. 2009).

The mineral paragenesis and metamorphic reactions described for carbonate-silicate rocks and impure marbles indicated that both group of rocks represent metamorphic product of marls and/or silt-argillaceous limestones, probably compose mainly of carbonates (calcite, Mn-calcite, dolomite and kutnohorite), quartz, K-feldspar and phlogopite (Roy 1972; Ferry 1976; Ferry 1983; Stanford, 1980; Yardley 1989; Bucher and Grapes 2011).

Minerals/ Rock Groups	CBS	MCBS	IM	MM	SR
Calcite	■		■		
Dolomite			■		
Mn-Calcite		■		■	
Kutnohorite		■		■	
Rhodonite				■	
Diopside	■		■		
Mn-Diopside		■			
Kanoite				■	
Cummingtonite					■
Mn-Phlogopite		■		■	
Phlogopite	■		■		
Biotite					■
Microcline	■	■			■
Almandine					■
Spessartine				■	
Quartz					■
Muscovite					■

CBS - Carbonate-Silicate Rock; MCBS - Manganesiferous Carbonate-Silicate Rock; IM - Impure Marble; MM - Manganesiferous Marble; SR - Silicate Rock

Figure 3.14 – Mineral paragenesis of BF lithotypes.

3.6.2. Structural Evolution

The structural assemblage of the BF records an essentially Transamazonic-age compressional event (Gomes et al. 1975; Costa et al. 2016) responsible for mass transport from NE to SW that is summarized in the following phases (Figure 3.15):

• D1 – It is the earlier phase and marked by a low-angle (ca. 30°) ductile simple shear deformation

related to S1, S2 and Bn formation and for the development of fold generations F1, F2 and F3. Bn is mainly controlled by protolith compositional variation as suggested by thin (<1 cm) metamorphic banding but can be also related to porphyroblast deformation. D1 gave rise to ductile reverse shear zones verging to SW and responsible for the thrust stacking of the BF.

A dextral strike-slip shear zone impressed in the Xingu Complex (basement) hampered the SW-verging mass transport creating a sharp foliation (dip deflection) at the BF basal contact and contributing to back-thrust development. Shear folds recognized in the lower quartzite point out to sinistral reactivation of that system;

• D2 – represents the beginning of the brittle tectonic regime that is characterized by reverse and back-thrust faults. Fault-propagation folds (F4) verging to NE and related to back-thrust faults formed at this time;

• The final stage D3 comes up after the contractional forces have ceased and is recognized by the presence of conjugate normal faults. NE-SW diabase dykes cutting the ridge indicate that transfer faults were probably later reactivated as normal faults.

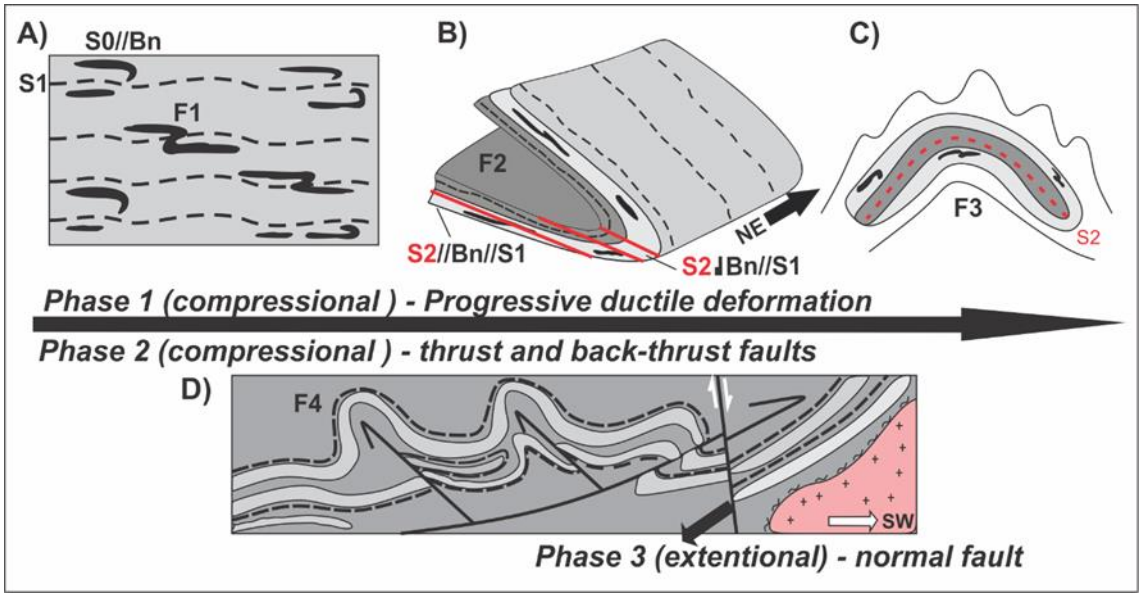

Figure 3.15 – Structural evolution of the BF. Progressive ductile deformation A) starting with intrafolial folds associated to Bn//S0 transposition and S1; B) Reclined fold F2 with the S2 axial plane verging; C) vertical upright F3 fold ; D) Brittle regime marked by a reverse fault, back-thrust faults and F4 verging to NE.

3.6.3. Depositional Setting

The lithotypes of the BF are metamorphic rocks with no preserved sedimentary features that could be used to infer a specific depositional environment. However, marls and limestones are commonly related to a marine platformal system which is also suggested for the BF by: i) the basal orthoquartzite, often connected to transitional environments; ii) the presence of significant grades of Ba registered by

barite (IM) and Ba-rich feldspar; iii) high Mn/Fe fractionation recorded by the substitution of Fe by Mn in mineral structure and the very low abundance of iron oxide (Force and Cannon, 1988; Maynard 2010); iv) the similarities between Buritirama mineralization and host-rocks associated with platformal-interpreted manganesiferous deposits such as the Sausar and Sandur groups (India) and Franceville Group (Gabon; Roy, 2006); v) the most accepted depositional model for manganesiferous carbonates formation assume a platformal sub-oxic/anoxic environment (Force and Cannon, 1988; Okita et al. 1988; Maynard 2010).

3.6.4. Tectonic Considerations

The new data presented in this paper suggests that the BF at the homonymous ridge is part of a compressional orogenic system develop during the Transamazonic cycle (~2.1 Ga; Macambira et al. 2007; Cordani et al. 1984; Gomes et al. 1975; Costa el al. 2016) in response to amalgamation between the Carajás and Bacajá blocks (Macambira et al. 2009). Tectonic features of this orogenic event are strongly impressed in the BF and have also been documented in the inner part of the Carajás domain (Pereira 2009; Tavares 2015) breaking the paradigm of restricted Archean deformation for this area (Machado et al. 1991; Pinheiro and Holdsworth 2000). Detrital zircons dated in a paragneiss, located about 25 km north of the Buritirama ridge, suggest a provenance likely derived from the Carajás domain and corroborate the presence of an Archean-Paleoproterozoic basin for this area (Macambira et al. 2007). A probable foreland basin (Caninana Formation) has been also related to the later stages of this collisional system (Pereira 2009). Considering the BF as formed in a platformal setting at the border of the Carajás domain, two different tectonic frameworks can be proposed: I) the BF represents an ensialic platform related to an aborted rift or ii) the BF represents a continental platform connected to an oceanic basin (Figure 3.16). Geochronological and isotopic studies are being conducted in order to clarify this issue.

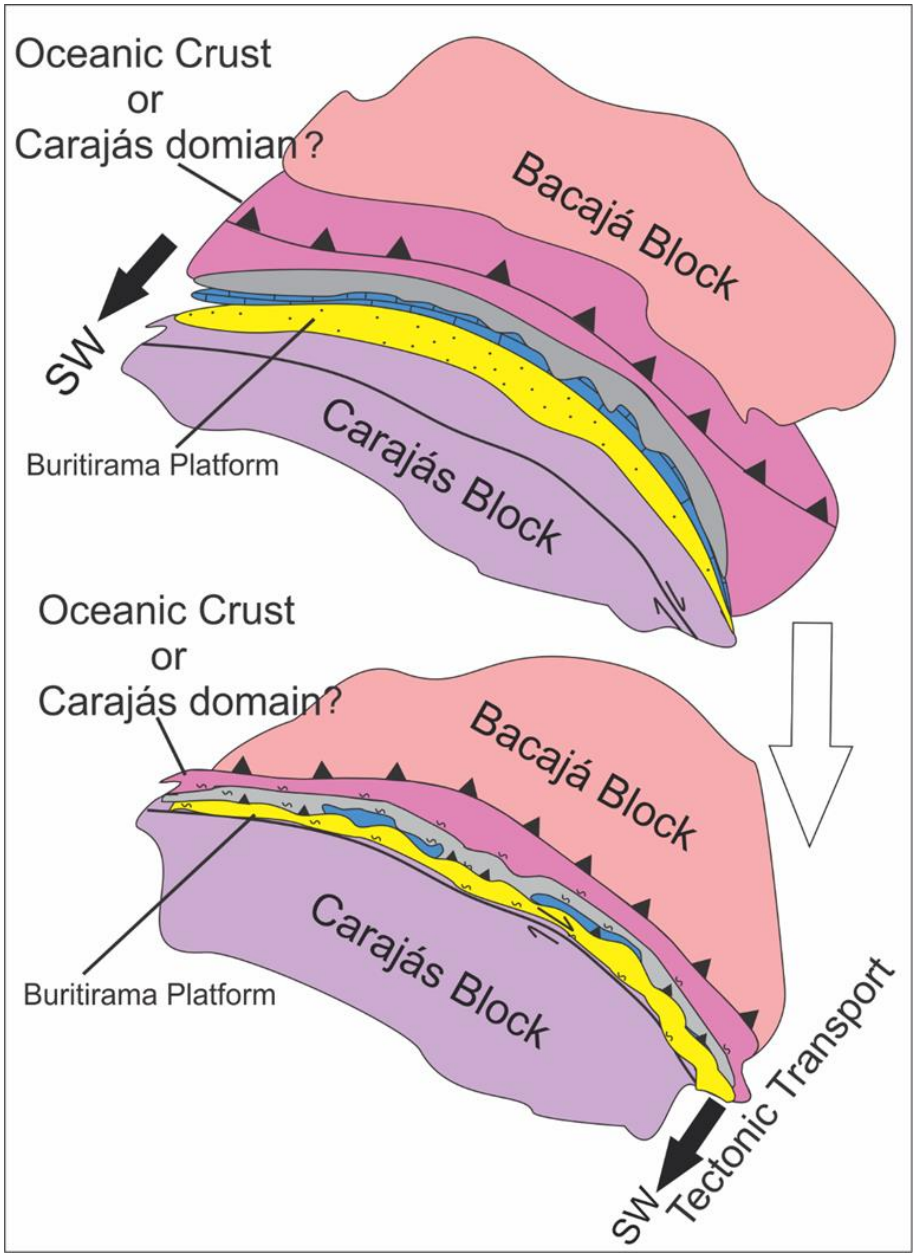

Figure 3.16 – Schematic tectonic models for evolution of the BF in the border zone between the Bacajá and Carajás blocks. In this model, the BF represents an Archean / Paleoproterozoic continental platform of the northern Carajás Block connected to an oceanic basin, which was closed during the Paleoproterozoic Transamazonic Orogeny, when the Carajás and Bacajá blocks collided and amalgamated, causing metamorphism and thrusting of the BF over the Carajás block (lower plate) to the southwest.

3.7. Conclusions

The BF along the homonymous ridge consists of four imbricated reverse shear zones that individualize three main metamorphic units: Lower Unit (LU; mainly siliciclastic and carbonate-silicate rocks); Intermediate Unit (IU; mainly carbonate-silicate rocks and manganesiferous marbles), and Upper Unit (UU; mainly carbonate-silicate rocks). The supergene Mn-deposit is formed by weathering of

kutnohorite-rich marble and restricted to the IU. The BF basement is composed of orthogneiss of the Xingu Complex and the Buritirama metagranite. A dextral strike-slip shear zone impressed in the Xingu Complex bounds the basal contact while the uppermost contact is defined by a quartz-iron rich hidrothermalized rock.

The BF lithotypes record an abundant presence of carbonate minerals (calcite, dolomite and kutnohorite) that combined with quartz, phlogopite and K-feldspar were probably a major constituent of marls and impure limestones protoliths. In addition, the minerals paragenesis recognized in the BF have been interpreted as a metamorphic product of such sedimentary rocks, normally related to a platformal environment.

The BF is interpreted as part of a platformal depositional system positioned at the border of the Carajás domain, which was probably inverted, deformed and metamorphosed during the Transamazonian event (~2.1 Ga), in a deformation belt related to the amalgamation between the Carajás and Bacajá blocks.

3.8. Acknowledgments

This work was greatly facilitated by Buritirama Mineração that allowed the access to borehole cores and mapping areas. The authors acknowledge João Araújo, Jorge Baptista and Maurício Soares, all members of Buritirama Mineração, and Felipe Tavares from Brazilian Geological Survey (CPRM). Analytical facilities of CPTMC (Centro de Pesquisa Manoel Teixeira da Costa), IGC-UFMG, and of LMIc (Laboratório de Microscopia e Microanálises) integrated to the Ouro Preto Federal University provided additional support for this research. Fabrício Caxito and Glaucia Queiroga are Fellow of the Brazilian Research Council (CNPq) and acknowledges for the support received. The original manuscript was greatly improved after constructive and helpful comments and suggestions by two anonymous reviewers.

4. ARTIGO II – PROVENANCE OF THE BURITIRAMA FORMATION REVEALS THE PALEOPROTEROZOIC ASSEMBLY OF THE BACAJÁ AND CARAJÁS BLOCK (AMAZON CRATON) AND THE CHRONOCORRELATION OF MN-DEPOSITS IN THE TRANSAMAZONIAN/BIRIMIAN SYSTEM OF NORTHERN BRAZIL/WEST AFRICA

- Autores: Silas Santos Salgado, Fabrício de Andrade Caxitoa, Rosaline Cristina Figueiredo e Silva, Cristiano Lana
- Publicado no *Journal of South American Earth Science – Volume 96 - 2019*

4.1. Abstract

The Mn-bearing Buritirama Formation along the homonymous ridge consists of a 40 km long by ca. 3 km wide NW-SE trending unit that limits the northern border of the Archean Carajás domain with the Paleoproterozoic Bacajá domain in the southeastern Amazon Craton. The Buritirama Formation type section is arranged in four imbricated thrusts that individualize three main stratigraphic units: Lower Unit, Intermediate Unit and Upper Unit. Detrital U-Pb zircons ages from the Lower Unit and Upper Unit record the prevalence of Neoarchean populations, suggesting the Carajás block as the main sedimentary source for the Buritirama basin. However, minor Paleoproterozoic populations attributed to the Bacajá block are also recognized, defining a maximum depositional age at ca. 2186 Ma. The anorogenic Buritirama metagranite occurs at the local basement, represents a probable precursor stage of the Buritirama rift and yielded a Concordia age of 2549 ± 5.9 Ma (U-Pb).

Supported by these new geochronological data, a framework model for the evolution of the Buritirama basin is proposed. Contrary to previous interpretations, the basin was active until at least the Rhyacian, representing a platformal setting fringing the northern margin of the Carajás block. A regional metamorphic event (ca. 2.06 Ga) records the closure of the basin during the Transamazonian Orogeny and the amalgamation of the Bacajá and Carajás blocks. The depositional age bracketed in between 2.3-2.1 Ga links the Buritirama Mn deposit (southeastern Amazon Craton) with those of Serra do Navio (Amapá Block, northeastern Amazon Craton) and Nsuta (West African Craton), suggesting: (i) widespread chronocorrelation of Mn-bearing sequences in the continental-scale Rhyacian Transamazonian / Birimian orogenic system, and (ii) formation of the primary carbonate ores under the influence of a major global manganese deposition episode.

4.2. Introduction

The oldest provinces of the Amazon Craton are located in the southeastern Pará state, Brazil, including the Carajás and Rio Maria domains or blocks (Archean, mainly 3.0-2.5 Ga) and the Bacajá domain (part of the Transamazonas Province of mainly 2.2-2.0 Ga; Santos, 2003; Vasquez and Rosa-Costa, 2008). The processes that led to the amalgamation of the Carajás and Bacajá blocks are still not well resolved, but preliminary geochronological and structural data suggest continental collision during the Transamazonian orogenic cycle (ca. 2.1-2.0 Ga; Macambira et al. 2009; Tavares et al. 2018; Salgado et al. 2019a). Determining the location of the suture zone in collisional systems can yield critical information about the patterns of sedimentation, deformation, and magmatism in both blocks involved

in the continental collision. Besides, sedimentary basins located at the margins of convergent terrains could provide insights on the relations between meaningful magmatic events in both areas (Condie, 2016). In this sense, the Buritirama Formation (BF), at the homonymous ridge, stands right in the inferred suture zone between the Bacajá and Carajás blocks (Oliveira et al. 2017) and was previously interpreted as a probable Paleoproterozoic passive margin basin (Salgado et al. 2019a). This paleogeographical setting makes the Buritirama Formation a key unit for understanding the geodynamic evolution of both the Carajás and Bacajá domains and the crustal evolution of the southeastern Amazon Craton.

In this paper, we present the first systematic detrital zircon U-Pb study of the Buritirama Formation along with unpublished U-Pb and geochemical data for the Buritirama metagranite, which composes the local basement. Based on the novel geochronological dataset, we discuss the possible sedimentary provenance areas for the Buritirama basin, its maximum depositional age, and geological evolution of the Carajás and Bacajá blocks. Most importantly, the new geochronological data suggests a chronostratigraphic link with similar manganese-bearing units in the Paleoproterozoic Bacajá Domain of the southeastern Amazon Craton (Buritirama deposit), in the Amapá Block of the northeastern Amazon Craton (Serra do Navio deposit; Chisonga et al. 2012), both located within the 2.1-2.0 Ga Transamazonian Orogen, and with the Nsuta deposit located within the Birimian orogen of the West African Craton (Mücke et al. 1999). The Birimian Orogen is regarded as the counterpart of the Transamazonian system in ancient paleogeographic configurations related to the Atlantica Supercontinent (Rogers, 1996; Kuleshov, 2011; Grenholm, 2019).

4.3. Geological Setting

The southeastern portion of the Amazon Craton (Almeida et al. 1976; 1981) is composed of the Archean Carajás and Rio Maria domains (Carajás Province – 3.0-2.5 Ga) and the Paleoproterozoic Bacajá domain (Transamazonas Province – 2.2-2.0 Ga; Figure 4.1A; Santos, 2003; Vasquez and Rosa-Costa, 2008). The Buritirama Formation has been interpreted as belonging to the northern part of the Carajás domain (Costa et al. 2016; Salgado et al. 2019a), and according to Bouguer anomalies would compose part of the suture zone with the Bacajá block (Oliveira et al. 2017).

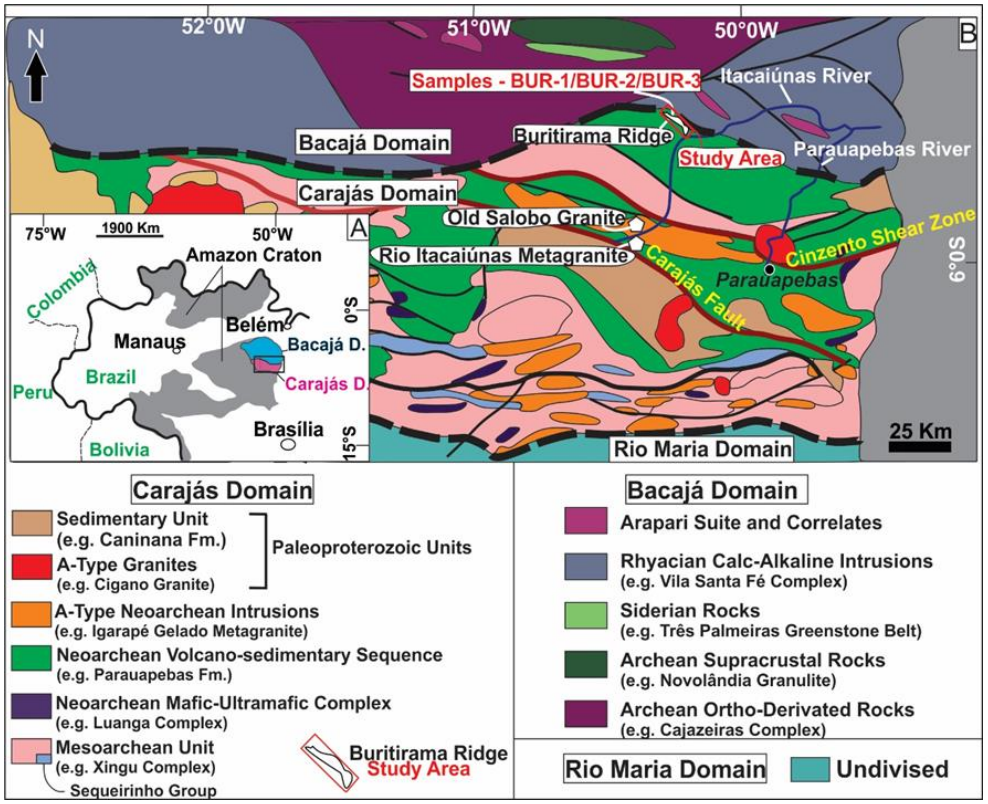

Figure 4.1 – A) Schematic tectonic map of part of the Amazon craton exhibiting the location of the Carajás and Bacajá domains (Santos, 2003); B) Simplified geological map of the Carajás domain and part of Bacajá domain (Vasquez and Rosa-Costa, 2008; Feio et al. 2013; Tavares et al. 2018).

4.3.1. Carajás Domain

The northern segment of the Carajás domain is formed by five main tectonostratigraphic and geochronological units (Figure 4.1B; Vasquez and Rosa-Costa, 2008; Costa et al. 2016; Tavares et al. 2018):

(i) Mesoarchean Basement Units and Metavolcano-Sedimentary Sequence – Represented chiefly by TTG (Tonalite-Trondhjemite-Granodiorite) gneiss-migmatite units of the Xingu Complex (Silva et al. 1974; Cordani et al. 1984) dated at ca. 3.0-2.85 Ga (Machado et al. 1991; Pidgeon et al. 2000; Delinardo, 2014). The Sequeirinho metavolcano-sedimentary sequence (2968 ± 15; U-Pb; Moreto et al. 2014; Moreto et al. 2015), the mafic orthogranulites of the Xicrim-Cateté complex (3002 ± 14; U-Pb; Pidgeon et al. 2000; Vasquez and Rosa-Costa, 2008) and the Cruzadão metagranite (2857 ± 8 Ma; Feio et al. 2013) represent the other members of this unit.

(ii) Neoarchean Mafic-Ultramafic Complexes – Comprise the Luanga Complex (Suita, 1988; Ferreira Filho et al. 2007), dated at 2763 ± 6 Ma (U-Pb; Machado et al. 1991) and correlated mafic-ultramafic intrusions.

(iii) A-Type Neoarchean Granites – Consist of the Igarapé-Gelado metagranite (2731 ± 26 Ma; Pb-Pb; Barbosa, 2004) and correlated units, such as the Estrela granite (2763 ± 7 Ma; Pb-Pb; Barros et

al. 2004) and the Plaquê granite (2736 ± 24; U-Pb; Avelar et al. 1999). A second younger and minor set of Neoarchean A-type granites is represented by the Old Salobo granite (2573 ± 2; U-Pb; Machado et al. 1991; Lindenmayer et al. 1994) and the Rio Itacaiúnas granite (2560 ± 37; U-Pb; Souza et al. 1996; Figure 4.1B). Some world-class IOCG mineralizations are related to this unit (Xavier et al. 2012).

(iv) Neoarchean Metavolcano-Sedimentary Units / Itacaiúnas Supergroup – This is the major unit of the Carajás domain (Figure 4.1B), comprising the Grão Pará Group, which includes the Parauapebas Formation at the bottom (Meireles et al. 1984; Araujo and Maia, 1991) and the overlapping Carajás Formation (Beisiegel et al. 1973; Macambira, 2003). U-Pb ages of zircon crystals from volcanic rocks of both formations are at ca. 2.75 Ga (Wirth et al. 1986; Macambira et al. 1996; Trendall et al. 1998). Those rocks have been related to a continental rift setting (Gibbs et al. 1986; DOCEGEO, 1988; Macambira, 2003; Martins et al. 2017). The Carajás Formation is known for hosting giant iron ore mineralization (Figueiredo e Silva et al. 2013). The metavolcano-sedimentary Igarapé Bahia, Igarapé Salobo and Igarapé Pojuca groups (DOCEGEO, 1988; Machado et al. 1991; Tallarico et al. 2005) consist of correlated units also included in the Itacaiúnas Supergroup and distinguished by the metamorphic grade and structural patterns. The age of the metavolcano-sedimentary rocks of the Rio Novo Group (Hirata et al. 1982; Oliveira et al. 1994) is contentious (DOCEGEO, 1988; Machado et al. 1991; Costa et al. 2016), but following Vasquez and Rosa-Costa (2008) we consider its deposition during the Neoarchean.

The Buritirama ridge (Anderson et al. 1974, Peters et al. 1977, Bello 1978) has been inserted in different lithostratigraphic settings, with the outcropping metasedimentary rocks individualized both as the Buritirama Group (Itacaiúnas Supergroup — Carajás Domain; DOCEGEO 1988) and the Buritirama Formation (Vila União Group — Bacajá Domain; Vasquez & Rosa-Costa 2008). Both interpretations have connected the Buritirama ridge with distinct tectonic provinces and stratigraphic hierarchy, despite none of these works are supported by specific studies on the Buritirama unit. Considering that, based on the above-mentioned authors, Salgado et al. (2019a) and the new geological data presented in this paper, we assume the metasedimentary rocks of the Buritirama ridge as part of the Buritirama Formation (Vila União Group), but belonging to the Itacaiúnas Supergroup (Carajás Domain). The Buritirama Group also includes the poorly understood Tapirapé Formation that comprehends metabasalts and talc-schist (Oliveira, 1994).

(v) Paleoproterozoic Sedimentary Units and Anorogenic Granites – Represented by clastic continental sedimentary rocks of the Caninana Formation (maximum depositional age at ca. 2.0 Ga – detrital zircon U-Pb; Pereira, 2009) and the probably Paleoproterozoic Paredão Group (Oliveira et al.

1994) and Águas Claras Formation, which has also a marine portion (Araújo et al. 1988; Nogueira, 1995; Mougeot et al. 1996; Fabre et al. 2011; Tavares et al. 2018). Anorogenic syenogranites and monzogranites (Serra dos Carajás Suite; Figure 4.1B) dated at 1.88 Ga also belong to this unit (Machado et al. 1991; Dall'Agnol et al. 2005).

4.3.2. Bacajá Domain

Geological information about the Bacajá domain is rather scarce when compared to the adjacent Carajás domain and very few works cover the boundary between such domains (Cordani et al. 1984; Macambira et al. 2003; 2009; Santos, 2003). In general, the Bacajá domain is described as an essentially Paleoproterozoic block with expressive crustal growth during the Transamazonian Orogeny (2.1-2.0 Ga), also responsible for reworking older Archean remnants. Based on Vasquez et al. (2008), Vasquez and Rosa-Costa (2008), Macambira et al. (2009), Costa et al. (2016) and Tavares et al. (2018), the central-southern part of the Bacajá domain is composed of the following geochronological units (Figure 4.1B):

(i) Archean Ortho-Derived Rocks – Represented by orthogranulites and orthogneisses of the Cajazeiras Complex (Faraco et al. 1996b) dated at 2942 ± 4 Ma (Pb-evaporation; Vasquez and Rosa-Costa, 2008). The Pacajá migmatite-gneiss and the Rio Preto mafic granulite represent Neoarchean components with ages around 2.67 and 2.62 Ga, respectively (Vasquez and Rosa-Costa, 2008; Macambira et al. 2004). The Rio Preto granulite crops out ca. 15 Km to the north of the Buritirama ridge and was related to an island arc environment (Oliveira et al. 1994).

(ii) Archean Supracrustal Rocks – Composed of kinzigites, mafic granulites and potassic paragneisses included in the Novolândia Granulite Complex (Ricci, 2006a). These rocks are linked to a metavolcano-sedimentary sequence metamorphosed at 2064 ± 4 Ma (U-Pb monazite; Macambira et al. 2007) with an inferred Mesoarchean protolith.

(iii) Siderian Rocks – Represented by units correlated to the Três Palmeiras greenstone belt (2359 ± 3 Ma; Pb-evaporation; Macambira et al. 2004). The metavolcano-sedimentary Três Palmeiras sequence has been related to an island arc environment (Jorge João et al. 1987; Macambira et al. 2009). Siderian crystallization ages of ca. 2.44 Ga are also reported for quartz-monzodioritic gneisses located at the northern part of the Bacajá domain (Santos, 2003; Macambira et al. 2009).

(iv) Rhyacian Calc-Alkaline Intrusions – Composed of tonalitic orthogneiss and granodioritic rocks, both showing metatexite and diatexite structures (Tavares and Silva, 2013). Such rocks are included in the Vila Santa Fé Complex and provided crystallization and metamorphic ages around 2.1-2.09 Ga and 2.09-2.06 Ga, respectively (Macambira et al. 2007; Tavares and Silva, 2013).

(v) Arapari Suite – Consists of deformed batholiths and stocks related to a charnokitic and

charno-enderbitic suite (Ricci and Costa, 2004; Ricci et al. 2006b), dated at ca. 2.08 Ga (Santos, 2003; Vasquez et al. 2008).

4.1.3. The Buritirama Formation

The Buritirama Formation (Anderson et al. 1974; Peters et al. 1977; Bello, 1978; Salgado et al. 2019a) along the homonymous ridge consists of a 40 km long by ca. 3 km wide NW-SE trending unit, located at the extreme north of the Carajás domain and arranged in four imbricated thrusts that individualize three main stratigraphic units (Figure 2; Salgado et al. 2019a). The Lower Unit (LU) is composed of quartzite/mica-quartz schist followed by carbonate-silicate rocks. The Intermediate Unit (IU) hosts a supergene manganese ore deposit formed by weathering of hydrothermalized kutnohorite-marble (Salgado et al. 2019a). The Upper Unit (UU) is composed of quartzite/mica-quartz schist followed by carbonate-silicate rocks. These rocks are thrust upon the local basement formed by orthogneiss-migmatite attributed to the Xingu Complex and the Buritirama metagranite (Salgado et al. 2019a). The uppermost contact is defined by iron-quartz rich hydrothermalized rocks. The BF has been interpreted as a part of a platformal depositional system positioned at the border of the Carajás block (Salgado et al. 2019a), which was probably inverted, deformed and metamorphosed during the Transamazonian event (ca. 2.1 Ga).

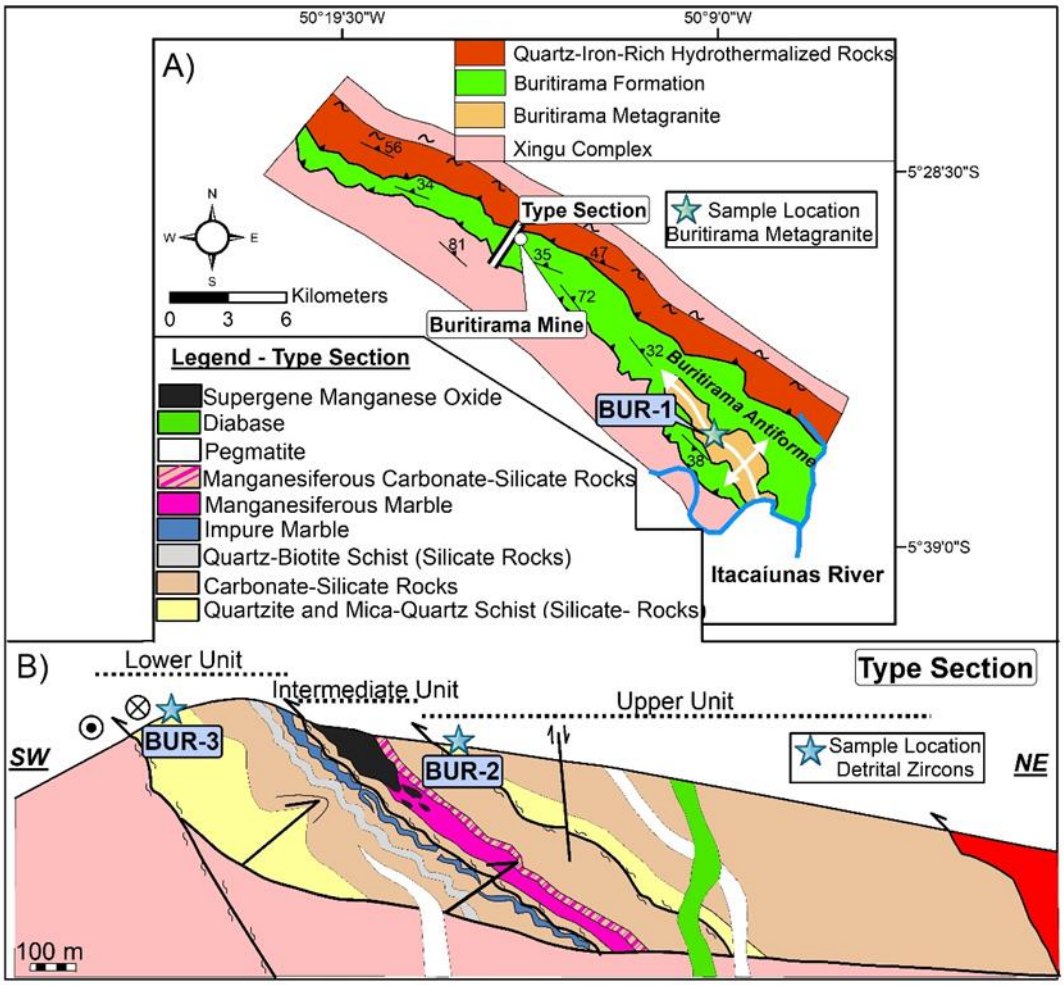

Figure 4.2 – A) Geological map of the Buritirama ridge (for location see Figure 4.1B) presenting the location of sample BUR-1 (5°34'58.69''S/50°09'58.77''W); and B) Buritirama Formation type section showing the individualised Lower, Intermediate and Upper units (Salgado et al. 2019a). Samples BUR-3 (5°30'53.41''S/50°14'55.26''W) and BUR-2 (5°30'44.80''S/50°14'49.93''W) come from the Lower and Upper units, respectively.

4.4. Materials and Methods

Fieldwork was conducted along the Buritirama ridge to collect unweathered and representative quartzite samples of the Buritirama Formation (samples BUR-2 and BUR-3) and of the Buritirama metagranite (samples BUR-3 and MTG-01 to MTG-04). Zircon crystals were recovered from samples BUR-1, BUR-2, and BUR-3 and submitted to U-Pb isotopic analysis, carried out at the Department of Geology (DEGEO), Universidade Federal de Ouro Preto (UFOP), Brazil. The zircon extraction technique makes use of a jaw crusher, milling, manual panning, heavy liquids separation, hand-picking under a binocular microscope and mounting on 25 mm epoxy (SpeciFix) mounts, and was carried out both at the SEPURA – Mineral Separation Laboratory of the CPMTC-IGC-UFMG, and at DEGEO-UFOP. Mounts were polished and imaged using cathodoluminescence (CL) and backscattered electron

(BSE) detectors in a JEOL 6510 Scanning Electron Microscope hosted at DEGEO-UFOP.

U-Pb analyses were carried out in a ThermoScientific Neptune Plus Multicollector Inductively Coupled Plasma Mass Spectrometer (MC-ICP-MS). For the full U-Pb analytical procedures followed in this study and machine parameters, see Lana et al. (2017). Results were corrected for common lead content by measuring the 202Hg and 204total (Pb + Hg) in the blank and then subtracting both from the zircon analysis on a ratio-by-ratio basis.

The most suitable location for the analytical U–Pb spots was considered recognizing areas without inclusions, fractures and preferably displaying clear internal textures of recrystallization/crystallization (e.g., magmatic growth). Dark areas (U-rich) in the CL images were avoided to prevent probably Pb-loss zones. U-Pb calculated ages, Concordia diagrams, probability density curves and histograms were made using Isoplot 3.6 (Ludwig, 2008).

Whole-rock chemical analyses of four samples of the Buritirama metagranite (MTG-01 to MTG-04) were carried out at SGS Geosol Laboratories (SGS), Vespasiano, Brazil, and started with the crushing and pulverization of ca. 400 g of homogeneous and unweathered samples. The analysis followed the induced coupled plasma (ICP) routine at SGS Geosol Laboratories. Major oxides elements were analysed by Induced Coupled Plasma - Optical Emission Spectroscopy (ICP-OES), and trace elements by ICP-MS. The accuracy and precision were better than 10% and the confidence level is at 95%.

4.5. Results

4.5.1. Lithogeochemistry of the Buritirama Metagranite

The Buritirama metagranite (Salgado et al. 2019a) crops out at the core of an anticlinal structure (near the Itacaiúnas River; Figure 4.1B) as an elliptical and sheared stock bearing stretched microcline porphyries and showing a steeply NW-SE metamorphic foliation (ca. 70° dip). It consists of a black-white-pinkish rock composed essentially by perthitic microcline, biotite, quartz, plagioclase and magnetite.

Four samples of the Buritirama metagranite (MTG-1 to MTG-4) were analyzed for major and trace element data (Appendix 2). Geochemical data available for two samples from the late Neoarchean Old Salobo granite (ca. 2.57 Ga; Lindenmayer, 1990) and twenty-eight samples from the earlier Neoarchean Planalto and Estrela granite suites (ca. 2.7 Ga; Barros et al. 2009; Feio et al. 2012; 2013) are plotted for comparison in all diagrams.

The contents of SiO_2 (70-73 wt%), TiO_2 (<1 wt%), Al_2O_3 (~12 wt%), Fe_2O_3 (~5 wt%), MnO (<1 wt%), MgO (<1 wt%), CaO (~1.7 wt%), Na_2O (~2.91 wt%), K2O (~5 wt%) and P_2O_5 (<1 wt%) display

small variation. The values of Mg# are around 0.14. Based on the aluminosity index (Shand, 1947; Maniar and Piccoli, 1989), modified alkali-lime index (MALI) and on the ferroan/magnesian classification (Frost et al. 2001), the Buritirama metagranite is defined as a metaluminous (Figure 4.3A), calc-alkaline (Figure 4.3B) and ferroan granite (Figure 4.3C), respectively.

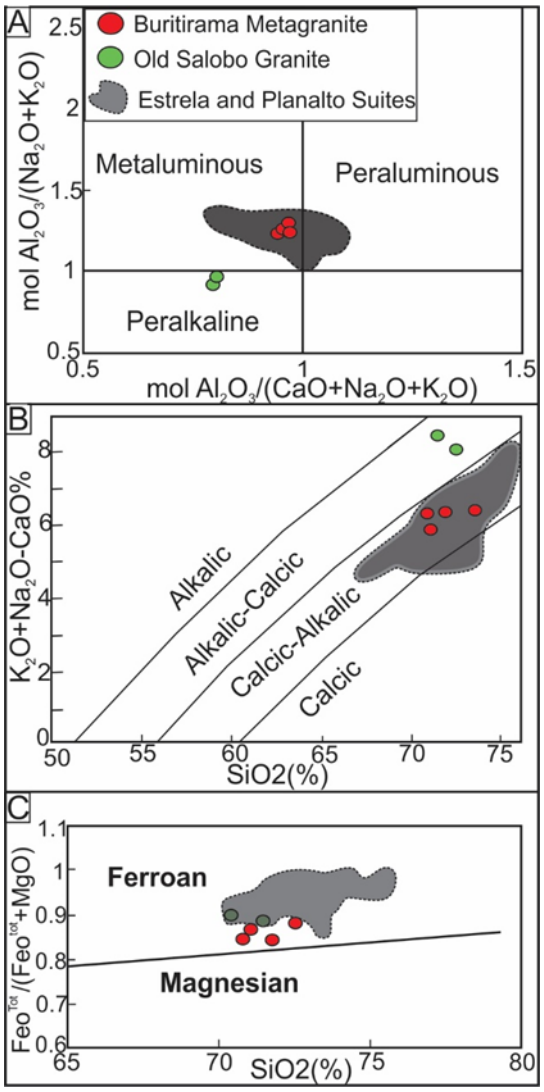

Figure 4.3 – Lithogeochemical classification of Buritirama Metagranite samples including data from the Old Salobo granite and Estrela-Planalto suites plotted for comparison (Lindenmayer, 1990; Barros et al. 2009; Feio et al. 2012; 2013). A) Aluminosity index (Shand, 1947; Maniar and Piccoli 1989); B) modified alkali-lime index (MALI) and; C) ferroan/magnesian classification (Frost et al. 2001).

The trace element contents are shown in primitive-mantle normalized spidergrams (Figure 4.4A; normalization values from Sun and McDonough, 1989). The Buritirama metagranite displays overall LILE (Large Ion Lithophile Elements)-enriched patterns, except for negative Sr anomalies, probably related to feldspar fractionation. The HFSE (High Field Strength Elements) present distinct behaviors, where elements normally associated with iron-oxides such as Nb, Ta and Ti display a depleted-pattern

while zircon-related elements like Zr, Hf and Th present high concentrations (Nielsen and Beard, 2000; Hoskin and Schaltegger, 2004). The negative anomalies of P are attributed to apatite fractionation.

The REE (Rare Earth Elements) values were normalized to the C1 chondrite (Sun and McDonought, 1989) and are shown in multi-element diagrams (Figure 4.4B). The ∑REE (Total Rare Earth Elements) are distributed from 255 ppm to 871 ppm. The La_N/Yb_N (7–30), La_N/Sm_N (3–9) and GdN/YbN (1.6–1.9) ratios display a strong enrichment-pattern of LREE (Light Rare Earth Elements) coupled with a nearly flat pattern of HREE (Heavy Rare Earth Elements). The Eu anomalies (Eu/Eu*) values are negative and about 0.37.

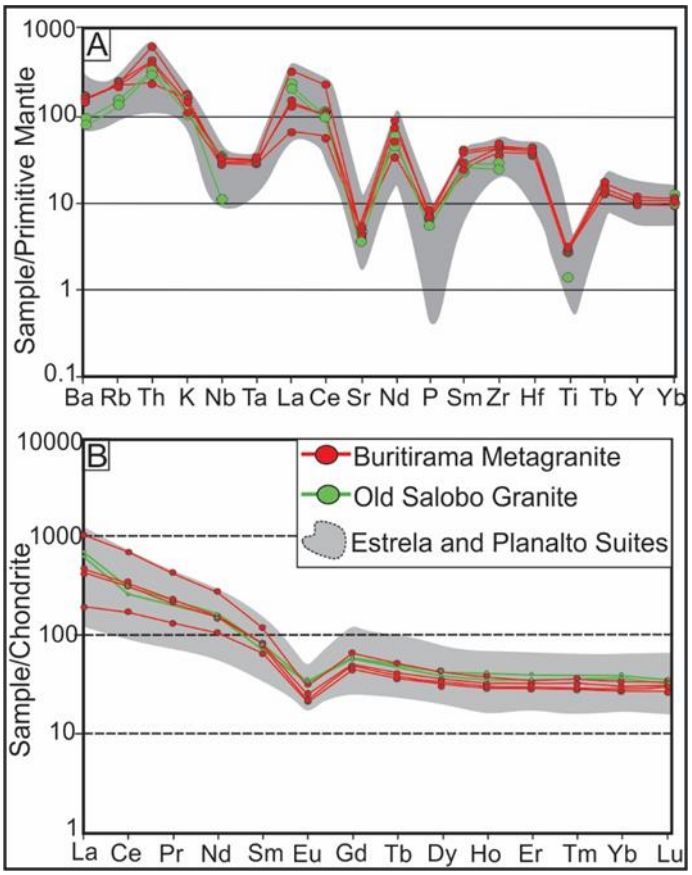

Figure 4.4 – Multi-element spidergram normalised to the Primitive Mantle (McDonough and Sun, 1995); B) chondrite-normalised rare earth elements patterns (Sun and McDonough, 1989) of samples from the Buritirama Metagranite. Samples from the Old Salobo granite and Estrela-Planalto suites are plotted for comparison (Lindenmayer, 1990; Barros et al. 2009; Feio et al. 2012; 2013).

Pearce et al. (1984) proposed a tectonic discrimination diagram for granites based on concentrations of Nb and Y (HFSE). In this diagram, the Buritirama metagranite samples (Figure 4.5A) cluster in the within-plate granites field (A-type granites). Whalen et al. (1987) suggested the relationship between Zr and the Ga/Al ratio to distinguish A-type I and S type granites. This assumption considers essentially the low mobility of Ga in anhydrous magmas. Whalen's diagram is presented in Figure 4.5B,

where the Buritirama metagranite samples plot in the anorogenic field. Following Eby (1992), samples clustered in the anorogenic fields of Pearce and Whalen diagrams can be classified as A1 or A2 granites. The A1 group is understood as representing mantle-source affinity magmas while A2 granites are derived from the continental crust or underplated crust involved in previous orogenic cycles. All of the Buritirama metagranite samples plot within the A2 field (Figure 4.5C).

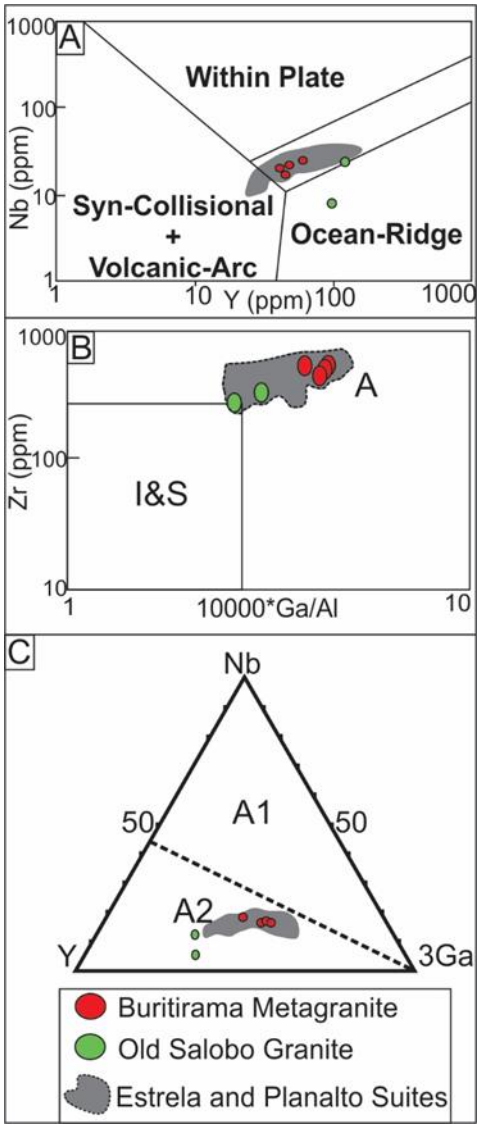

Figure 4.5 – Discrimination diagrams for A) tectonic interpretation of granitic rocks (Pearce et al. 1984); B) I-S and A-type granites (Whalen et al. 1987); C) A1 and A2 anorogenic granites (Eby, 1992) of Buritirama Metagranite. Samples from the Old Salobo granite and Estrela-Planalto suites are plotted for comparison (Lindenmayer, 1990; Barros et al. 2009; Feio et al. 2012; 2013).

4.5.2. U-Pb Geochronology of the Buritirama Metagranite

Zircon crystals extracted from sample BUR-1 of the Buritirama metagranite (Figure 4.2; Figure 4.6A) are clear euhedral-subhedral prisms (100–500 μm long), bearing a typically igneous internal

zoning and predominantly 2:1 length/width ratios (Figure 4.7). Twenty-three spots were analyzed for U-Pb isotopes and presented high Th/U ratios typical of zircons crystallized from igneous melts (0.95–1.77; Rubatto et al. 2002; Appendix 3A). Such crystals yielded a Concordia age of 2549 ± 5.9 Ma (all uncertainties are reported at the 2σ level), which is interpreted as the magmatic crystallization age of the Buritirama metagranite (Figure 4.7). Two probably inherited zircon crystals yielded Concordant ages of 2769 ± 17 Ma and 2884 ± 17 Ma.

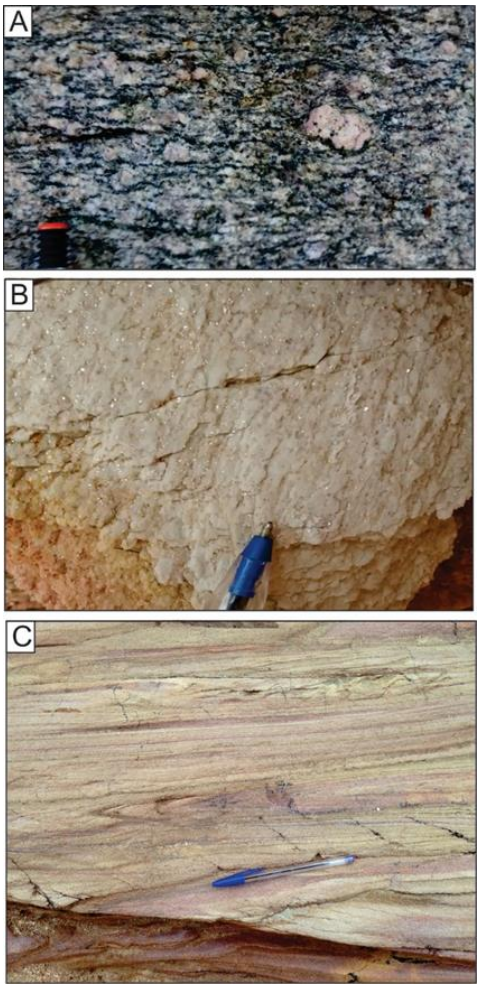

Figure 4.6 – A) Buritirama Metagranite (BUR-1); B) Lower Unit quartzite (BUR-3) and C) Upper Unit quartzite (BUR-2).

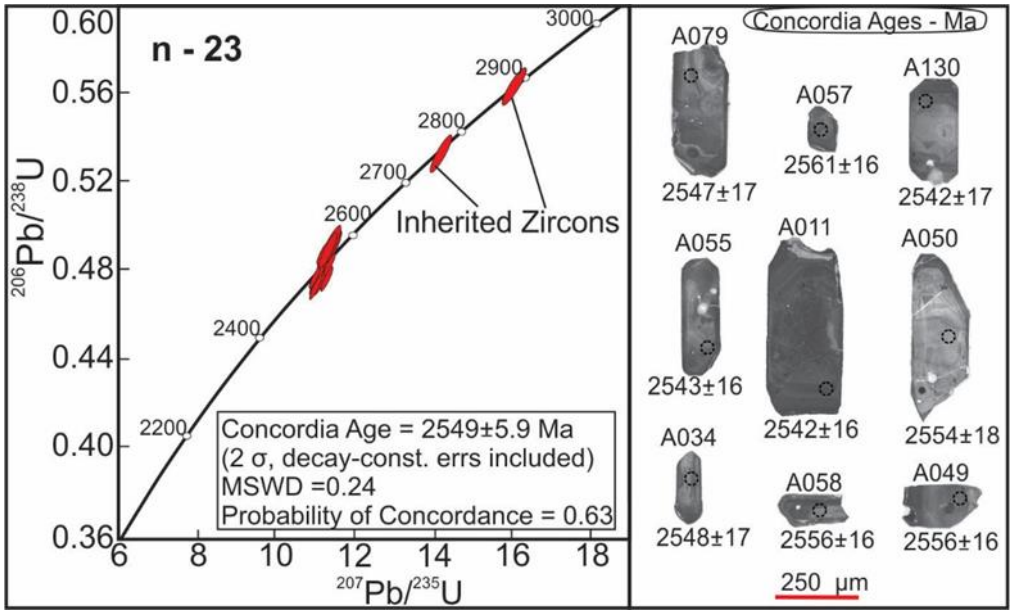

Figure 4.7 – Left: LA-ICP-MS U-Pb Concordia diagram with twenty-three zircon crystals from sample BUR-1 (Buritirama metagranite). Right: cathodoluminescence images of representative zircons grains analysed from sample BUR-1.

4.5.3. Detrital Zircon U-Pb Geochronology

Detrital zircons grains were extracted from two siliciclastic rocks (quartzite) collected in the Lower Unit (sample BUR-3) and the Upper Unit (sample BUR-2) of the Buritirama Formation (Figure 4.2; Figure 4.6B). Samples BUR-3 and BUR-2 provided 140 and 82 zircon grains from which 80 and 46, respectively, yielded a maximum discordance of 10% and low common lead abundance (predominantly <0.01%; Appendix 3B and Appendix 3B of the supplementary material). Only the latter are discussed below. Most of the crystals are euhedral-subhedral prisms bearing igneous internal zoning (Figure 4.8). All of the ages quoted below are $^{207}Pb/^{206}Pb$ ages, except for the Concordia ages.

4.5.3.1. Sample BUR-3

The histogram and probability density curve for spots analyzed in detrital zircon grains of sample BUR-3 display a predominance of Neoarchean sources with peaks around 2714 Ma (39%) and 2535 Ma (37%; Figure 4.8). Mesoarchean populations show a peak at ca. 2908 Ma (18%) and sparse ages near 3125 Ma. The oldest grain yielded an Eoarchean Concordia age of 3673 ± 21 Ma. A smaller Paleoproterozoic population comprises exclusively Siderian grains with the youngest age at ca. 2347 Ma.

4.5.3.2. Sample BUR-2

The histogram and probability density curve for spots analyzed in detrital zircon grains of sample

BUR-2 display a similar spectrum to BUR-3 and record the prevalence of Neoarchean sources with peaks around 2680 Ma (41%) and 2522 Ma (24%; Figure 4.8). The Mesoarchean population spreads along 2900-2800 Ma with a peak about 2841 Ma (17%). Paleoarchean ages are represented by just two grains dated ca. 3443 Ma and 3525 Ma. The majority of Paleoproterozoic grains are Siderian, however, two Rhyacian grains dated ca. 2272 Ma and 2186 Ma were identified, providing an important constraint on the maximum age of sedimentation of the Buritirama Formation.

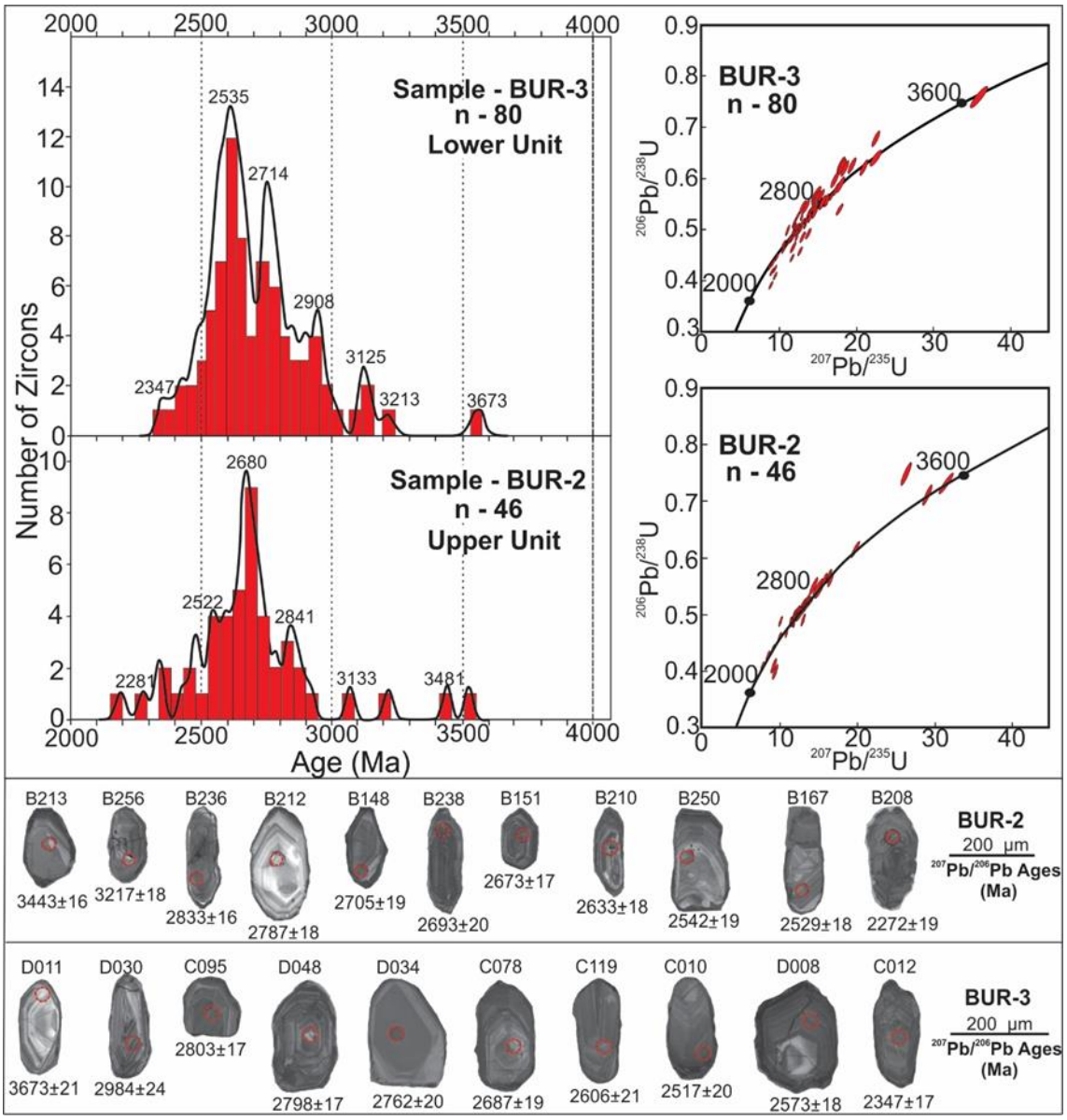

Figure 4.8 – Left: Frequency histogram and probability density curves from samples BUR-3 and BUR-2. Only ages greater than 89% concordant were plotted. Right: Concordia diagrams from detrital zircons of each sample. Bottom: cathodoluminescence images of representative zircon grains analysed for samples BUR-2 and BUR-3.

4.6. Discussion

4.6.1. The Late Archean Magmatic Event in the Northern Carajás Domain

The late Neoarchean crystallization age (2549 ± 5.9 Ma) yielded by the Buritirama metagranite is similar to other ages reported for A-type granites in the northern Carajás domain, such as the Old Salobo granite (2573 ± 2 Ma; U-Pb; Machado et al. 1991; Lindenmayer et al. 1994) and the Rio Itacaiúnas granite (2560 ± 37 Ma; U-Pb; Souza et al. 1996). It is also in the age range of IOCG (Iron-Oxide-Copper and Gold) mineralization grouped in the Northern Copper Belt (e.g., Salobo deposit; Réquia et al. 2003; Silva et al. 2005; Tallarico et al. 2005; Xavier et al. 2012; Moreto et al. 2015). Such intrusions are likely connected to the same Neoarchean magmatic-hydrothermal event impressed in the northern Carajás domain.

Inherited zircon crystals (ca. 2.88 Ga and 2.77 Ga) detected in the Buritirama metagranite are probably correlated to the Xingu Complex and the Carajás Formation country rocks, respectively, reinforcing its emplacement in the Carajás block.

The Buritirama metagranite and the Planalto and Estrela suites (PES; ca. 2.7 Ga; Barros et al. 2009; Feio et al. 2012; 2013) are marked by metaluminous, calc-alkaline and ferroan geochemistry affinities (Figure 4.3), while the Old Salobo granite record alkali-calcic and peralkaline composition. All those groups of rocks display corresponding patterns of trace elements (Figure 4.4A) and REE (Figure 4.4B), exhibiting: i) negative anomalies of Nb, Ta and, Ti probably related to iron-titanium oxide fractionation; ii) negative anomalies of Sr and Eu linked to plagioclase fractionation; iii) negative anomalies of P connected to apatite fractionation; iv) positive anomalies of Th related to the great abundance of zircon.

4.6.2. Source Areas and Maximum Depositional Age of the Buritirama Formation

The detrital zircon age spectra for the combined BUR-2 (Upper Unit) and BUR-3 (Lower Unit) samples range from the Paleoarchean to the Rhyacian with a prominent Neoarchean peak. In the diagrams of Figure 4.9, the probable source areas of the Buritirama Formation zircon crystals are compared with tectonic-magmatic events and radiometric ages recorded in the Bacajá and Carajás domains, including detrital zircon age spectra of samples from the Salobo Group (Demelo et al. 2016), the Caninana Formation (Pereira, 2009), and from a quartzite sample collected near the Itacaiúnas River and attributed to the Buritirama Formation, referred as IBF (Araújo and Sousa, 2018; Figure 4.9).

Paleoarchean zircons (3.60 Ga – 3.20 Ga) – A few Paleoarchean grains are recognized in the Buritirama Formation and can be related to old lithosphere remnants eroded or probably incorporated into the Xingu Complex and correlated units. Primary sources for those zircon crystals have not been

mapped yet in the area, so the reworking of ancient sedimentary units is also a possibility.

Mesoarchean zircons (3.20 – 2.80 Ga) – The ages between ca. 3.00 Ga and 2.80 Ga are conspicuous in spectra of all samples and can be correlated to the protoliths of the Xingu Complex (ca 3.0 Ga), and the two subsequent magmatic stages recorded in this complex at ca. 2.95 Ga and 2.85 Ga (Machado et al. 1991; Pidgeon et al. 2000; Delinardo, 2014).

Early Neoarchean zircons (2.80 – 2.70 Ga) – This is the second most abundant group of ages in the Buritirama Formation and is strongly recorded in the Caninana Formation. This age range corresponds to the ages yielded by the bimodal volcanic rocks of Parauapebas Formation and early Neoarchean A-type granites (e.g., Estrela Suite), both connected to the Carajás rift (Machado et al. 1991; Trendall et al. 1998; Galarza and Macambira, 2002).

Middle Neoarchean zircons (2.70 – 2.60 Ga) – This is the main group of ages in the Buritirama Formation. Ages about 2.68-2.61 Ga have been reported in the Carajás domain and are probably linked to sparse and late-stage magmatic pulses of the Carajás rift (Trendall et al. 1998; Galarza and Macambira, 2002; Tallarico et al. 2005; Reis, 2017). The Pacajá Orthogneiss (ca. 2.67 Ga) and the Rio Preto Granulite (ca. 2.62 Ga; Vasquez and Rosa-Costa, 2008; Macambira et al. 2004) could have contributed to the Neoarchean peak, suggesting the participation of the Bacajá domain as a minor provenance area for the Buritirama Formation.

Late Neoarchean zircons (2.60 – 2.50 Ga) – This peak is conspicuously impressed in the Buritirama Formation, as well as in the IBF, and was recognized in the Caninana Formation as a single detrital grain. This age range is connected to A-type granites (e.g., Buritirama metagranite and Old Salobo) and IOCG mineralization in the northern Carajás domain. Late Neoarchean ages have been poorly documented in the Bacajá domain.

Siderian zircons (2.50 – 2.30 Ga) – The ages around 2.44 Ga and 2.35 Ga are present in the Buritirama Formation and were reported exclusively in the Bacajá domain for the Três Palmeiras greenstone belt and a quartz-monzodioritic gneiss, respectively (Vasquez et al. 2008; Macambira et al. 2009).

Rhyacian zircons (2.30 – 2.05 Ga) – Represented by two detrital zircon grains with crystallization ages around 2.27 Ga and 2.18 Ga (sample BUR-2) and can be related to the Transamazonian orogenic system developed in the Bacajá domain. An expressive population of Rhyacian detrital zircons was recognized in the Caninana Formation that also bears a few Orosirian grains.

The youngest consistent population of detrital zircons of the Buritirama Formation cluster around 2365 Ma; however, the age of the younger crystal ca. 2.18 Ga is assumed as the maximum depositional

age.

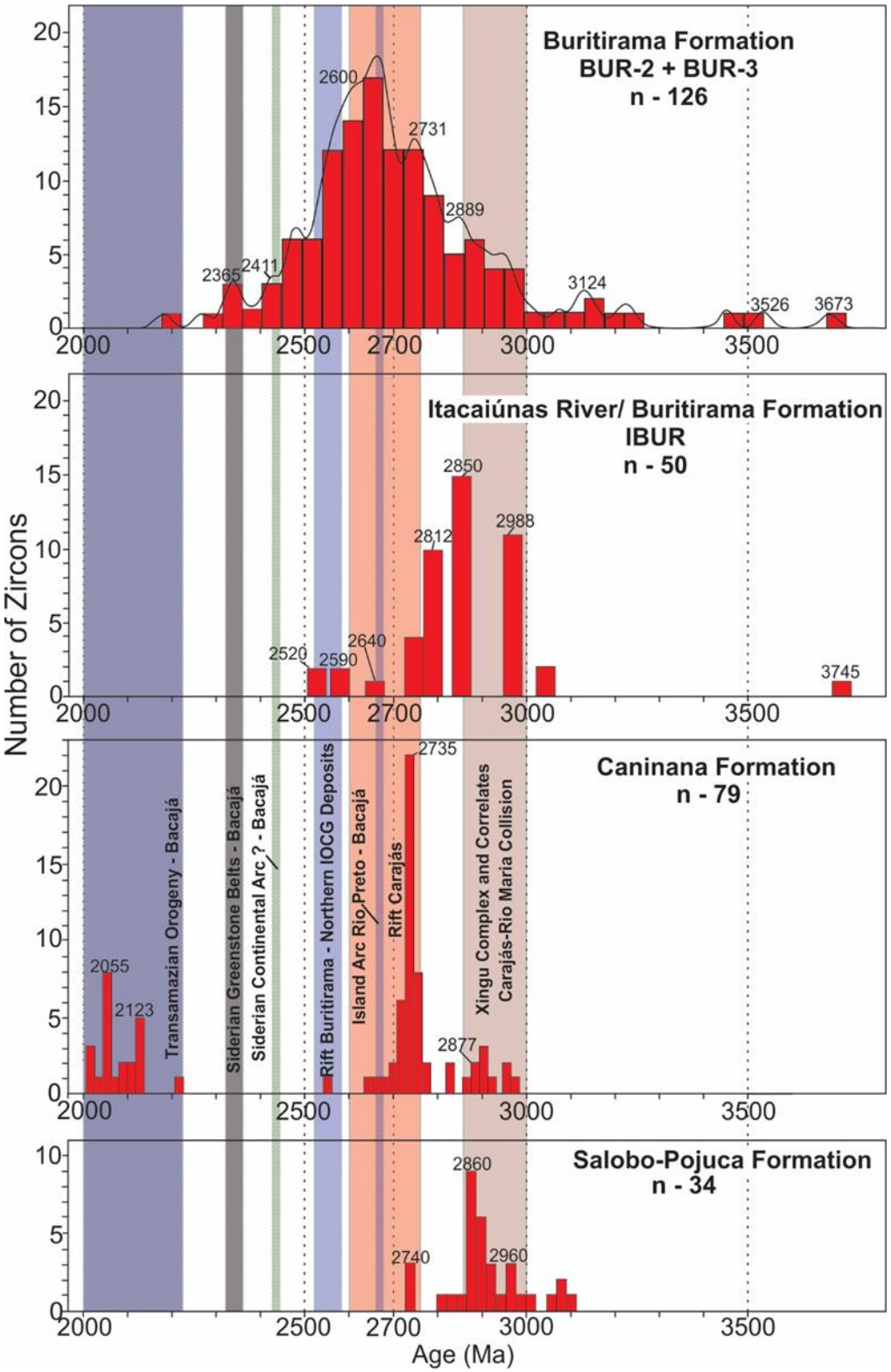

Figure 4.9 – Frequency histogram and probability density curves from samples BUR-3 and BUR-2 grouped. Other frequency histograms from Buritirama Formation (Itacaiúnas River – IBUR), Caninana Formation and Salobo Formation are presented for comparison. The main tectonic-magmatic events and ages recognised in the Carajás and Bacajá domains are shown to contrast probable provenance areas.

4.6.3. Evolution of the Buritirama Basin and Implications for the Carajás/Bacajá Amalgamation

The early stages of basin opening in the northern Carajás block (Figure 4.10) can be related to the emplacement of late Neoarchean A-type granites (e.g., Buritirama metagranite – ca. 2.55 Ga) and the world-class IOCG mineralization grouped in the Carajás Northern Copper Belt (Xavier et al. 2012; Moreto et al. 2015). Both processes were probably controlled by extensional reactivation of major NW-SE shear zones during the late Neoarchean (Tavares et al. 2018). In this model, the Transamazonian event (ca. 2.1 Ga), strongly recorded at the northern boundary of the Carajás domain, could be responsible for the reactivation of normal faults related to the former rift setting in a compressional regime.

During the second stage of opening (Figure 4.10), the Buritirama basin evolved to a passive margin setting characterized by a carbonate platform with impure marbles (limestone) and carbonate-silicate rocks (marls; Salgado et al. 2019a). The development of the Buritirama basin into an evolved or aborted rift is unsure, however, the high grade of manganese in the Buritirama carbonate rocks combined to the elevate Mn/Fe ratios probably reflects connection of the platformal basin to a distal mid-ocean ridge (source of Mn-hydrothermal fluids).

Geochronological data from the Carajás rift further south point out to a main magmatic stage at ca. 2.77-2.70 Ga, however, it probably persisted on a smaller scale until ca. 2.61 Ga (Lindenmayer et al. 1994; Trendall et al. 1998; Galarza and Macambira, 2002; Tallarico et al. 2005; Reis, 2017). These broad age spectra coupled with ages related to the late Neoarchean magmatic and hydrothermal event (ca. 2.55 Ga) represent the dominant zircon populations in the Buritirama Formation detrital age spectra, suggesting that the Carajás domain acted as the main sedimentary source for the Buritirama basin. In this context, the Buritirama basin may represent a superimposed and/or laterally related rift to the older Carajás basin. The transpressional event at 2.6 Ga is based mainly on data from the Carajás Fault area (Pinheiro and Holdsworth 2000) and lack further tectonic and geochronological evidence in both the Cinzento Shear Zone and in the northern boundaries of the domain (Tavares 2015).

In this arrangement, the Rhyacian and Siderian zircon ages recovered from the Buritirama quartzites (BUR-2 and BUR-3) suggest the approaching of a possible Transamazonian Magmatic Arc installed further northeast (Bacajá block), since that such magmatic ages have not yet been reported in the Carajás domain. An important shift in sedimentary provenance of the basin is indicated by the Rhyacian grains, which are restricted to the upper unit of Buritirama Formation (sample BUR-2). The Buritirama passive margin, which started after ca. 2.5 Ga with sources from the Carajás domain to the south, would thus initiate to be fed by a Transamazonian arc developed in the Bacajá block to the north

at ca. 2.3-2.1 Ga.

The amalgamation between the Bacajá and Carajás blocks during the Transamazonian orogeny marks the inversion and deformation of the Buritirama basin. Tectonic features from this collision are probably impressed in the whole northern Carajás Domain. The metamorphic age of ca. 2.06 Ga (Tavares and Silva, 2013) recorded in the Buritirama basement rocks is assumed as the minimum depositional age for the basin.

Regarding this framework, we can assume that the Buritirama Formation: (i) records a basinal system that evolved loosely during ca. 400 Ma (Figure 4.10), from a rift basin into a marine platform on the northern passive margin of the Carajás block, and then finally to a syn-orogenic basin between ca. 2.18 and 2.06 Ga; (ii) this platformal basin was probably linked to an oceanic basin and a Rhyacian magmatic arc (Bacajá Domain) located further northeast of this system; (iii) this basin was closed and subsequently deformed and metamorphosed during the amalgamation of the Bacajá and Carajás blocks (Transamazonian Orogen – ca. 2.06 Ga; Figure 4.10; Tavares et al. 2018). Those interpretations are supported by gravimetric Bouguer anomalies, which suggest the Buritirama Formation occupies the suture zone between two blocks of distinct density and crustal structure, corresponding to the Carajás and Bacajá blocks (Oliveira et al. 2017).

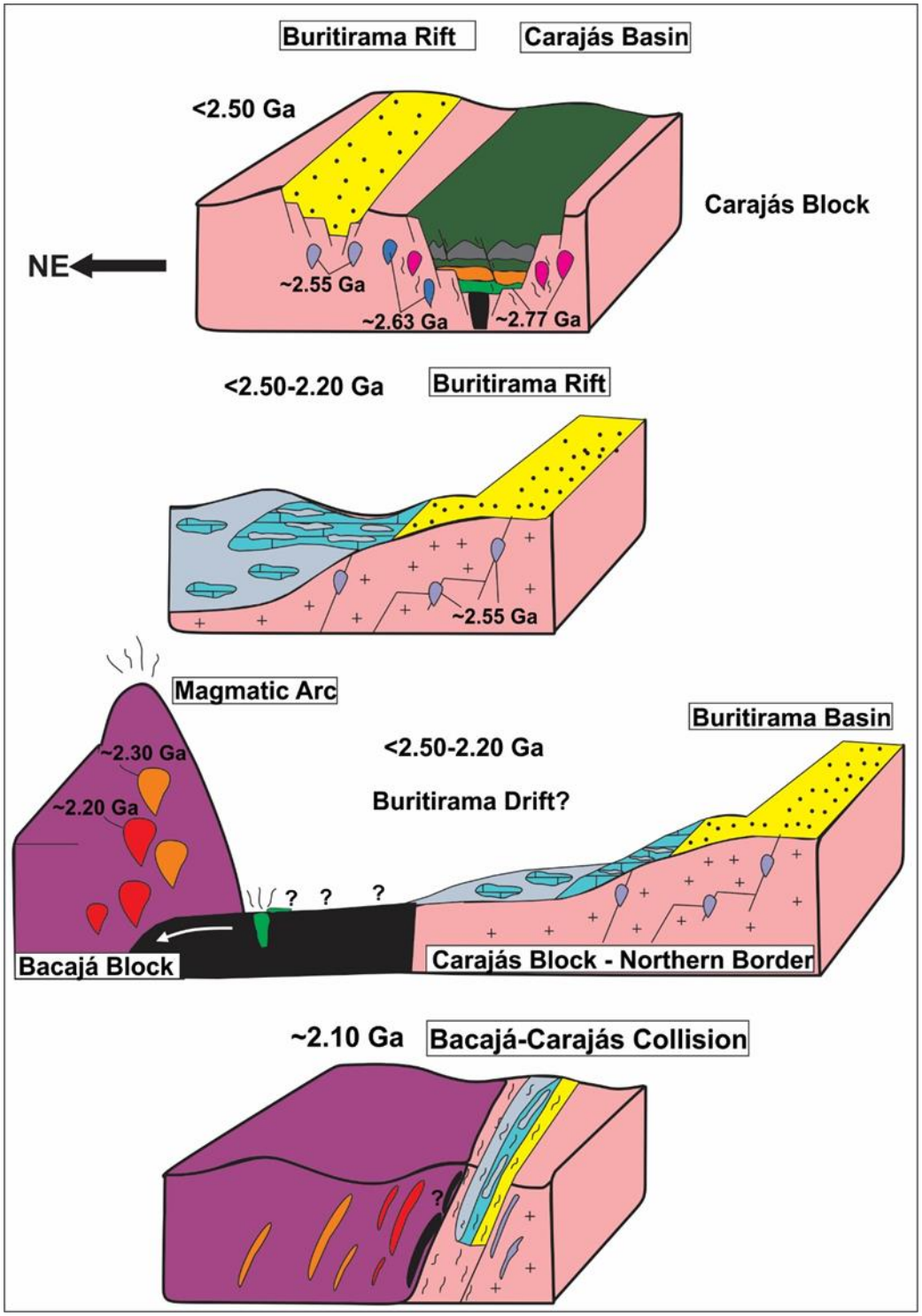

Figure 4.10 – Schematic cartoon representing the evolution of Buritirama basin in the context of Carajás and Bacajá blocks. See text for further details.

4.6.4. Linking the Manganese Deposits of the Transamazonian/Birimian Orogenic System

The West African Craton is composed of Archean blocks sutured by the extensive Birimian accretionary-collisional orogenic system, developed around 2.27-1.96 Ga (Grenholm, 2019 and references therein). The Paleoproterozoic Birimian Orogen of the southern West African Craton is

broadly coeval with the Transamazonian Orogen of the northeastern Amazon Craton (e.g., Bacajá and Amapá blocks). Those two major orogenic tracts are thought to represent a contiguous system which joined the Archean blocks of the Amazon and West African cratons and culminated in the assembly of the Paleoproterozoic Atlantica supercontinent (Rogers, 1996), which includes crustal domains now present in Africa, South America, Eastern Europe and North China (Figure 4.11; Kuleshov, 2011; Grenholm, 2019).

The Mn deposits of the Serra do Navio (Amapá Block) and Nsuta (Birimian Supergroup) have been interpreted as laterally and temporally correlative units in the Transamazonian and Birimian Orogens, respectively (Chisonga et al. 2012). Based on recent geochronological, petrographic and stratigraphic data, we reinforce and enlarge the Transamazonian track system to include the Buritirama Formation at the southern border of the Bacajá domain, in the southeastern Amazon Craton (Figure 4.11).

The metasedimentary rocks present at the Buritirama (Peters et al. 1977; Salgado et al. 2019a), Serra do Navio (Nagell 1962; Chisonga et al. 2012) and Nsuta (Hirdes and Davis, 1998; Mücke et al. 1999) deposits are all thought to have been formed at ca. 2.3-2.1 Ga, which fits in the proposed major and widespread global manganese deposition episode (Maynard, 2010). The metallogenic model proposed for those deposits considers that Mn-oxides formed through the weathering of impure marbles and carbonate-silicate rocks composed of rhodochrosite, kutnohorite, Mn-calcite, spessartine, rhodonite, and Mn-pyroxenes/amphiboles. Formation of Mn-silicate phases seems to be primarily controlled by metamorphic reactions involving the consumption of carbonate minerals present in limestone and marl protoliths (Kleinschrot et al. 1993; Bucher and Grapes, 2011; Salgado et al. 2019a).

Despite the similarities between the primary protores, distinct preliminary paleogeographical models have been proposed for each deposit considering mainly the lithological association. Graphitic schist (carbonaceous sediments) and pyroclastic rocks are reported in the Serra do Navio deposit, which is connected to a proximal intra-arc environment (Chisonga et al. 2012), while the volcanic rocks in the Nsuta deposit are probably associated with a platform break setting (Mücke et al. 1999). High Mn/Fe ratios and widespread carbonate rocks suggest a shallow platformal environment for the Buritirama Formation (Salgado et al. 2019a). The manganese concentrations in all carbonate-ores are linked to a primary submarine volcanogenic source.

Considering this configuration, we assume here that the Buritirama, Serra do Navio and Nsuta manganiferous sediments were probably interconnected at ca. 2.3 Ga in a system embracing an archipelago of juvenile arcs and platformal settings developed at the margins of ancient Archean blocks, from ca. 2.5 Ga to ca. 2.1 Ga, similarly to the archipelago model of Grenholm (2019) or the Birimian system. Hydrothermal activity in the mid-ocean ridges developed in the oceanic domains separating the

Archean blocks and the juvenile arcs was very important in furnishing metal-rich fluids which were then transported to shallow marine waters and deposited as manganese-rich passive margin sequences fringing the Archean cratons. The blocks that composed this system (island arcs of the archipelago and Archean blocks bearing manganese-rich passive margins) were later agglutinated during the collisional phase of the Transamazonian/Birimian Orogeny, leaving records preserved as manganese deposits in both the Amazon and West African counterparts of the Rhyacian orogenic system.

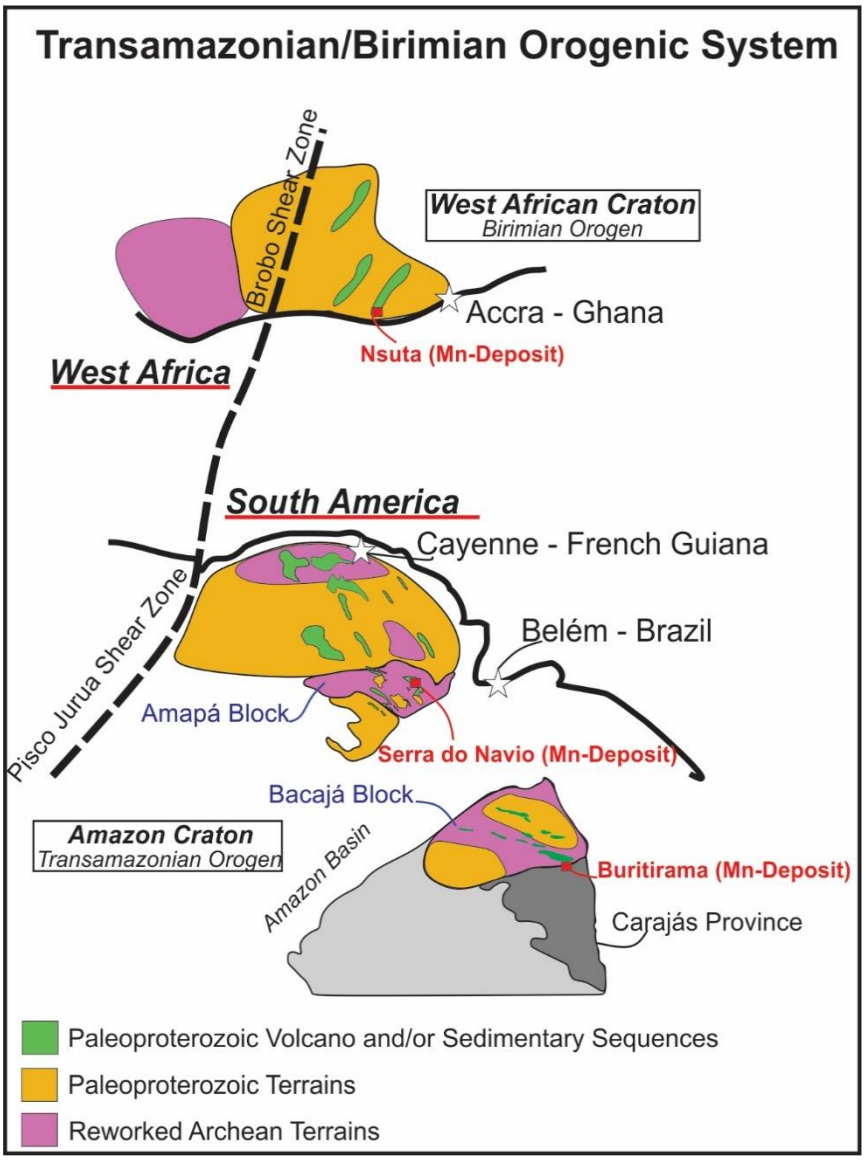

Figure 4.11 – Configuration of the West African Craton and Amazon Craton (Transamazonian-Birimian System; modified from Grenholm, 2019 and references therein) showing the Mn-deposits of Buritirama, Serra do Navio and Nsuta.

4.7. Conclusions

The Buritirama Formation along the Buritirama ridge represents part of a platformal basin on the

northern border of the Carajás block, which loosely evolved during ca. 400 Ma, from ca. 2.5 to 2.1 Ga from a rift basin into a marine platform, likely connected to an oceanic basin further North.

The precursor stage of the Buritirama rift is recorded by the A-type Buritirama metagranite, presented at the local basement and dated at ca. 2.5 Ga. Ages around 2.5 Ga have been reported in the northern Carajás domain for the Old Salobo granite, the Rio Itacaiúnas granite and related IOCG mineralization (Northern Copper Belt), indicating a wide magmatic and hydrothermal event at this period. The trace element patterns of the Buritirama metagranite are very similar to other late and early Neoarchean granites in the Carajás domain, suggesting the link of these rocks with two superimposed or laterally-related rift systems.

Detrital zircon age spectra for samples of the Buritirama Formation display the main populations at 2.7-2.5 Ga, indicating that the Carajás block acted as the main sedimentary source for the basin. However, distinct Paleoproterozoic zircon populations and a maximum depositional Rhyacian age at ca. 2.18 Ga are recorded in the Upper Unit of the Buritirama Formation, suggesting that the basin received a minimum amount of detritus from the Transamazonian Magmatic Arc installed in the Bacajá domain to the Northeast. Contrary to previous studies, a Paleoproterozoic age is for the first time reported for the Buritirama Formation, constraining the deposition of its upper part between 2.18 and 2.06 Ga.

The metamorphic event dated at the local basement (ca. 2.06 Ga) provides a minimum depositional age for the basin and records its closure, deformation and metamorphism during the Transamazonian Orogeny, which culminated in the amalgamation between the Bacajá and Carajás blocks.

The Buritirama Formation is thus a very important unit for understanding the geodynamic evolution of the southeastern Amazonian Craton, as it defines the suture zone between the major Bacajá and Carajás blocks and records an important provenance shift indicating a complete plate tectonics cycle at the northern margin of the Carajás block during the Archean / Paleoproterozoic transition. The evolution from a rift to a passive margin and then possibly to a syn-orogenic setting influenced the deposition of Mn-rich sediments, with metal-rich fluids probably transported from a deep oceanic basin into the platformal setting of the Buritirama Formation, forming the important and economic Mn deposits of the area.

In a global framework, the new geochronological data suggest chronocorrelation between the Paleoproterozoic Buritirama (Carajás-Bacajá blocks of the southeastern Amazon Craton), Serra do Navio (Amapá Block of the northeastern Amazon Craton) and Nsuta (West African Craton), all of them related to a major global manganese deposition period at ca. 2.3-2.1 Ga. A model is proposed where all of those sequences were interconnected during their development in the Archean-Paleoproterozoic

transition, in a system involving an archipelago of juvenile magmatic arcs separating Archean blocks fringed by manganese-bearing passive margin sequences. During the collisional phase of the Transamazonian / Birimian Orogeny those crustal blocks were all amalgamated, causing deformation and metamorphism of the manganese-bearing sequences and ultimately the formation of the Paleoproterozoic Atlantica Supercontinent at ca. 2.0 Ga.

4.8. Acknowledgments

This work was supported by Buritirama Mineração and the authors acknowledge João Araújo, Jorge Baptista and Michel Fontes, all members of this Company, for the support received. Analytical facilities of CPTMC (Centro de Pesquisa Manoel Teixeira da Costa), IGC-UFMG, and of Laboratório de Geoquímica Isotópica integrated to the Universidade Federal de Ouro Preto provided laboratory support for this research. FAC, RCFC and CL are Fellows of the Brazilian Scientific Council (CNPq) and acknowledge for the support received. The original manuscript was greatly improved after constructive and helpful comments and suggestions by two anonymous reviewers.

5. ARTIGO III – GENESIS OF THE Mn-CARBONATE ROCKS AND DOLOMITIC MARBLES OF THE BURITIRAMA FORMATION, CARAJÁS DOMAIN (AMAZON CRATON): IMPLICATION FOR A METALLOGENETIC Mn-MODEL AND A RECORD OF THE LOMAGUNDI ISOTOPIC EXCURSION

- Autores: Silas Santos Salgado, Fabrício de Andrade Caxito, Rosaline Cristina Figueiredo e Silva, Gabriel Jubé Uhlein, Leonardo Brandão Nogueira, Hermínio Arias Nalini Júnior, Ramon de Oliveira Aranda
- Em revisão no *Ore Geology Reviews*

5.1. Abstract

The Mn-bearing Buritirama Formation is composed of clastic and chemical metasedimentary rocks representing a Rhyacian platformal basin (ca. 2.18–2.06 Ga) that limits the northern border of the Archean-Paleoproterozoic Carajás domain with the Paleoproterozoic Bacajá domain in the southern Amazon craton, northern Brazil. The Buritirama Formation is individualized in three main stratigraphic units: Lower Unit, Intermediate Unit and Upper Unit. The Lower and Upper units are made up of a basal quartzite followed by carbonate-silicate rocks (marls), dolomitic marbles (limestone) and minor biotite

schist while the Intermediate Unit consists of Mn-carbonate rocks covered by a supergene Mn-oxide deposit. These rocks were deformed and metamorphosed during the Transamazonian event (ca. 2.06 Ga). Geochemical data from dolomitic marbles (Lower Unit) exhibit negative Ce anomalies, high Y/Ho ratios (c.a. 48) and ocean-like REE+Y patterns that reinforce the platformal nature of the Buritirama basin. Positive $\delta^{13}C$ values (+ 3.18‰ to + 4.96‰ V-PDB) detected on dolomitic marbles are understood as an expression of the Lomagundi Carbon Isotopic Excursion. The Lomagundi Event has been reported also within the Carajás domain for the Mn-bearing Águas Claras Formation, which is here correlated to the Buritirama Formation in a Rhyacian framework. The metallogenesis of Mn-carbonate rocks was evaluated based on redox-sensitive trace elements (e.g. Zn and Ni), PAAS-normalized REE+Y patterns and $\delta^{13}C$ values (- 2.56‰ to + 0.15‰ V-PDB) that point out to the classical multistage redox-controlled Mn-model involving: i) a primary hydrothermal source; ii) microbially-mediated reduction of Mn-oxides at the ocean bottom and; iii) reactions between Mn^{2+} and CO_3^{2-} (organic and marine derived) giving rise to diagenetic Mn-carbonates.

5.2. Introduction

The Buritirama Formation (BF) is composed of clastic and chemical metasedimentary rocks representing a Rhyacian platformal basin (ca. 2.18–2.06 Ga) that limits the northern border of the Archean-Paleoproterozoic Carajás domain with the Paleoproterozoic Bacajá domain, in the southeastern Amazon Craton, northern Brazil (Peters et al. 1977; Santos, 2003; Vasquez and Rosa-Costa, 2008; Tavares et al. 2018; Salgado et al. 2019a, 2019b). The basin was closed, deformed and metamorphosed during the Transamazonian event (ca. 2.06 Ga; Tavares and Silva, 2013), but its lifespan is still unclear. The early opening stages are probable recorded by the emplacement of late Archean A-type granites (ca. 2.55 Ga) in the northern part of the Carajás domain and linked to the world-class Iron-Oxide-Copper and Gold (IOCG) deposits in this area (Machado et al. 1991; Lindenmayer et al. 1994; Souza et al. 1996; Xavier et al. 2012; Moreto et al. 2015).

The oxide and carbonate Mn-mineralization present along the Buritirama ridge was first discovered in 1967 by the Companhia Meridional de Mineração (U.S. Steel subsidiary), which in the same year recognized the remarkable iron deposits of the Carajás Metallogenetic Province (e.g. N5W; Dyer, 1972; Anderson et al. 1974). Currently, the Buritirama Mn-deposit is explored by the company Mineração Buritirama and represented in 2017 the major Brazilian Mn-source (ANM, 2018). Despite its significance, the Mn-deposit and its host-rocks had not yet been systematically evaluated until the recent studies developed by Salgado et al. (2019a, 2019b).

Salgado et al. (2019a) individualize the BF along its type section in three main units: Lower Unit (LU), Intermediate Unit (IU) and Upper Unit (UU). The LU and UI are composed of a basal quartzite followed by carbonate-silicate rocks, dolomitic marbles and minor biotite schist while the IU hosts the oxide-carbonated Mn-deposit. In this paper, we present the first geochemical, C and O isotopic data for the carbonate-silicate rocks (LU), dolomitic marbles (LU) and Mn-carbonate rocks (IU) of BF. The petrography presented by Salgado et al. (2019a) is revisited in the light of the protolith rocks and metamorphic process. The hydrothermal system partially settled on Mn-carbonate rocks (protore) will be addressed in further works.

The novel dataset reinforce the platformal nature of the Buritirama carbonates and suggests it is linked to the Paleoproterozoic Lomagundi Carbon Isotopic Excursion (Schidlowski et al. 1976; Karhu and Holland 1996; Bekker et al. 2003; Canfield et al. 2013; Lyons et al. 2014). Such event has been documented within the Carajás domain for the Águas Claras Formation (Bekker et al. 2017) indicating a Paleoproterozoic framework involving both units (Costa et al. 2016; Tavares et al. 2018). Besides, a multistage metallogenetic model for the Buritirama Mn-deposit is proposed and compared to the previous correlated Rhyacian Nsuta (Ghana; Kleinschrot et al. 1993; Beukes et al. 2016; Mücke and Olobaniyi, 2017) and Serra do Navio deposits (North Brazil; Chisonga et al. 2012), all of them encompassing the Transamazonian-Birimian system (Salgado et al. 2019b).

5.3. Geological Setting

The southeastern portion of the Amazon Craton (Almeida et al. 1976, 1981) is composed of the Archean-Paleoproterozoic Carajás and Rio Maria domains (Carajás Province – 3.0–2.1 Ga) and the Paleoproterozoic Bacajá domain (Transamazonas Province – 2.2–2.0 Ga; Figure 1A; Santos, 2003; Vasquez and Rosa-Costa, 2008). The BF is interpreted as belonging to the northern part of the Carajás domain (Costa et al. 2016; Salgado et al. 2019b), and according to Bouguer anomalies would compose part of the suture zone with the Bacajá block (Oliveira et al. 2017).

5.3.1. Carajás Domain

Five main tectonostratigraphic and geochronological units (Figure 5.1B; Vasquez and Rosa-Costa, 2008; Costa et al. 2016; Tavares et al. 2018) form the northern segment of the Carajás domain:

(i) Mesoarchean Basement Units and Metavolcano-Sedimentary Sequence – Represented chiefly by TTG (Tonalite-Trondhjemite-Granodiorite) gneiss-migmatite units of the Xingu Complex (Silva et al. 1974; Cordani et al. 1984) dated at ca. 3.0–2.85 Ga (Machado et al. 1991; Pidgeon et al.

2000; Delinardo, 2014). The Sequeirinho metavolcano-sedimentary sequence (2968 ± 15; U-Pb; Moreto et al. 2014; Moreto et al. 2015), the mafic orthogranulites of the Xicrim-Cateté complex (3002 ± 14; U-Pb; Pidgeon et al. 2000; Vasquez and Rosa-Costa, 2008) and the Cruzadão metagranite (2857 ± 8 Ma; Feio et al. 2013) represent the other members of this unit.

(ii) Neoarchean Mafic-Ultramafic Complexes – Comprise the Luanga Complex (Suita, 1988; Ferreira Filho et al. 2007), dated at 2763 ± 6 Ma (U-Pb; Machado et al. 1991) and correlated mafic ultramafic intrusions.

(iii) A-Type Neoarchean Granites – Consist of the Igarapé-Gelado metagranite (2731 ± 26 Ma; Pb-Pb; Barbosa, 2004) and correlated units, such as the Estrela granite (2763 ± 7 Ma; Pb-Pb; Barros et al. 2004), Plaquê granite (2736 ± 24; U-Pb; Avelar et al. 1999) among others (Marangoanha et al. 2019). A second younger and minor set of Neoarchean A-type granites is represented by the Old Salobo granite (2573 ± 2; U-Pb; Machado et al. 1991; Lindenmayer et al. 1994), the Rio Itacaiúnas granite (2560 ± 37; U-Pb; Souza et al. 1996; Figure 5.1B) and the GT-46 granite (Toledo et al. 2019). Some world-class IOCG mineralization are related to this unit (Xavier et al. 2012).

(iv) Neoarchean Metavolcano-Sedimentary Units/Itacaiúnas Supergroup – This is the major unit of the Carajás domain (Figure 1B), comprising the Grão Pará Group, which includes the Parauapebas Formation at the bottom (Meireles et al. 1984; Araújo and Maia, 1991) and the overlapping Carajás Formation (Beisiegel et al. 1973; Macambira, 2003). U-Pb ages of zircon crystals from volcanic rocks of both formations are at ca. 2.75 Ga (Wirth et al. 1986; Macambira et al. 1996; Trendall et al. 1998). Those rocks have been related to a continental rift setting (Gibbs et al. 1986; DOCEGEO, 1988; Macambira, 2003; Martins et al. 2017). The Carajás Formation is known for hosting a giant iron ore mineralization (Figueiredo e Silva et al. 2013). The metavolcanosedimentary Igarapé Bahia, Igarapé Salobo and Igarapé Pojuca groups (DOCEGEO, 1988; Machado et al. 1991; Tallarico et al. 2005) consist of correlated units also included in the Itacaiúnas Supergroup and distinguished by the metamorphic grade and structural patterns. The age of the metavolcanosedimentary rocks of the Rio Novo Group (Hirata, 1982; Oliveira et al. 1994) is contentious (DOCEGEO, 1988; Machado et al. 1991; Costa et al. 2016), but following Vasquez and Rosa-Costa (2008) we consider its deposition during the Neoarchean.

(v) Paleoproterozoic Sedimentary Units and Anorogenic Granites – Represented by clastic continental sedimentary rocks of the Caninana Formation (maximum depositional age at ca. 2.0 Ga – detrital zircon U-Pb; Pereira, 2009) and the probably Paleoproterozoic Paredão Group (Oliveira et al. 1994) and Águas Claras Formation, which has also a marine portion (Araújo et al. 1988; Nogueira, 1995; Mougeot et al. 1996; Fabre et al. 2011; Bekker et al. 2017). The Buritirama Formation has recently been considered a Paleoproterozoic unit (Salgado et al. 2019b) and will be later detailed. Anorogenic

syenogranites and monzogranites (Serra dos Carajás Suite; Figure 1B) dated at 1.88 Ga also belong to this unit (Machado et al. 1991; Dall'Agnol et al. 2005).

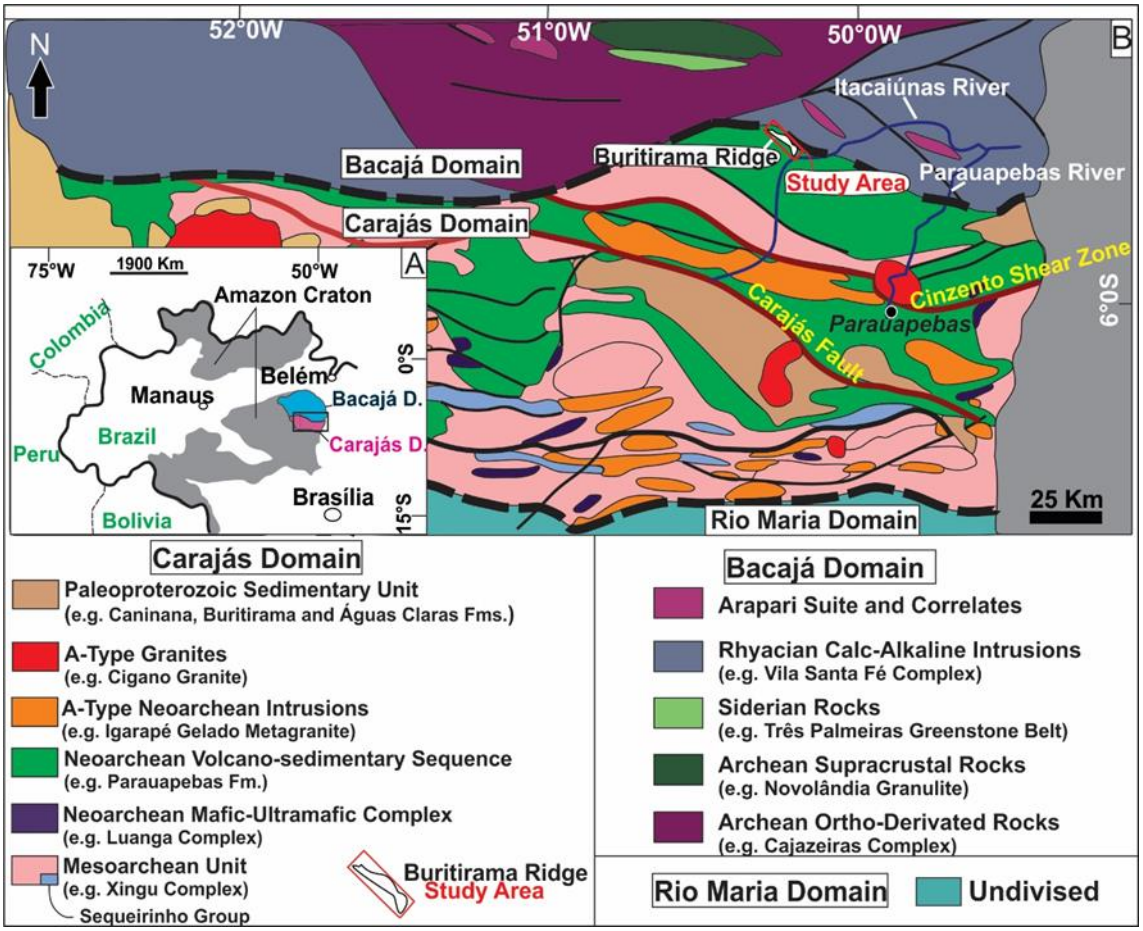

Figure 5.1 – A) Schematic tectonic map of part of the Amazon craton exhibiting the location of the Carajás and Bacajá domains (Santos, 2003); B) Simplified geological map of the Carajás domain and part of the Bacajá domain (Vasquez and Rosa-Costa, 2008; Feio et al. 2013; Tavares et al. 2018).

5.3.2. Bacajá Domain

Geological information about the Bacajá domain is rather scarce when compared to the adjacent Carajás domain and very few works cover the boundary between such domains (Cordani et al. 1984; Macambira et al. 2003, 2009; Santos, 2003). In general, the Bacajá domain is described as an essentially Paleoproterozoic block with expressive crustal growth during the Transamazonian Orogeny (2.1–2.0 Ga), also responsible for reworking older Archean remnants. Based on Vasquez et al. (2008), Vasquez and Rosa-Costa (2008), Macambira et al. (2009), Costa et al. (2016) and Tavares et al. (2018), the central-southern part of the Bacajá domain is composed of the following geochronological units (Figure 1B): (i) Archean Ortho-Derived Rocks; (ii) Archean Supracrustal Rocks; (iii) Siderian Rocks; (iv) Rhyacian Calc-Alkaline Intrusions and (v) Arapari Suite. Further information about these units is

presented in Salgado et al. (2019b) and in the cited works.

5.3.3. Buritirama Formation

The Paleoproterozoic Buritirama Formation (Anderson et al. 1974; Peters et al. 1977; Bello, 1978; Salgado et al. 2019a, 2019b) crops out along the homonymous ridge and consists of a 40 km long by ca. 3 km wide NW-SE trending unit, located at the northern border of the Carajás domain. It dips at ca. 35° to the northeast where a quartz, iron-rich shear zone defines the contact between the BF and the probable Bacajá domain (Figure 5.2). The Itacaiúnas River limits the BF southeast border while to the southwest, it is thrusted over the Xingu Complex orthogneisses (Carajás domain).

The Buritirama metasedimentary rocks have been interpreted as part of a platformal depositional system positioned at the border of the Carajás block, which was enclosed during the Rhyacian Transamazonian Orogeny (2.06 Ga; Tavares and Silva, 2013). Such SW-verging mass transport event develop a polyphasic deformation in the BF recorded by superimposed folds, back-thrusts and four ductile imbricated thrusts that individualize three main stratigraphic units (Figure 5.2; Salgado et al. 2019a).

The Lower Unit (LU) is formed by orthoquartzite, quartz-mica schist and minor iron-rich quartzite that lie over the Xingu Complex with a sharp foliation (ca. 75° to NE). Carbonate-Silicate rocks, impure marbles and minor quartz-biotite schist also occurs. The Intermediate Unit (IU) is delimited by two shear zones and hosts an oxide manganese supergene ore capping (up to 30 thickness) and its manganesiferous carbonate protolith. A hydrothermal post-metamorphic system related to acid pegmatite and later diabase intrusion is recorded over the manganesiferous rocks by veins. The Upper Unit (UU) is composed of mainly quartzite/mica-quartz schist followed by carbonate-silicate rocks, minor impure marble and quartz-biotite schist (Salgado et al. 2019a).

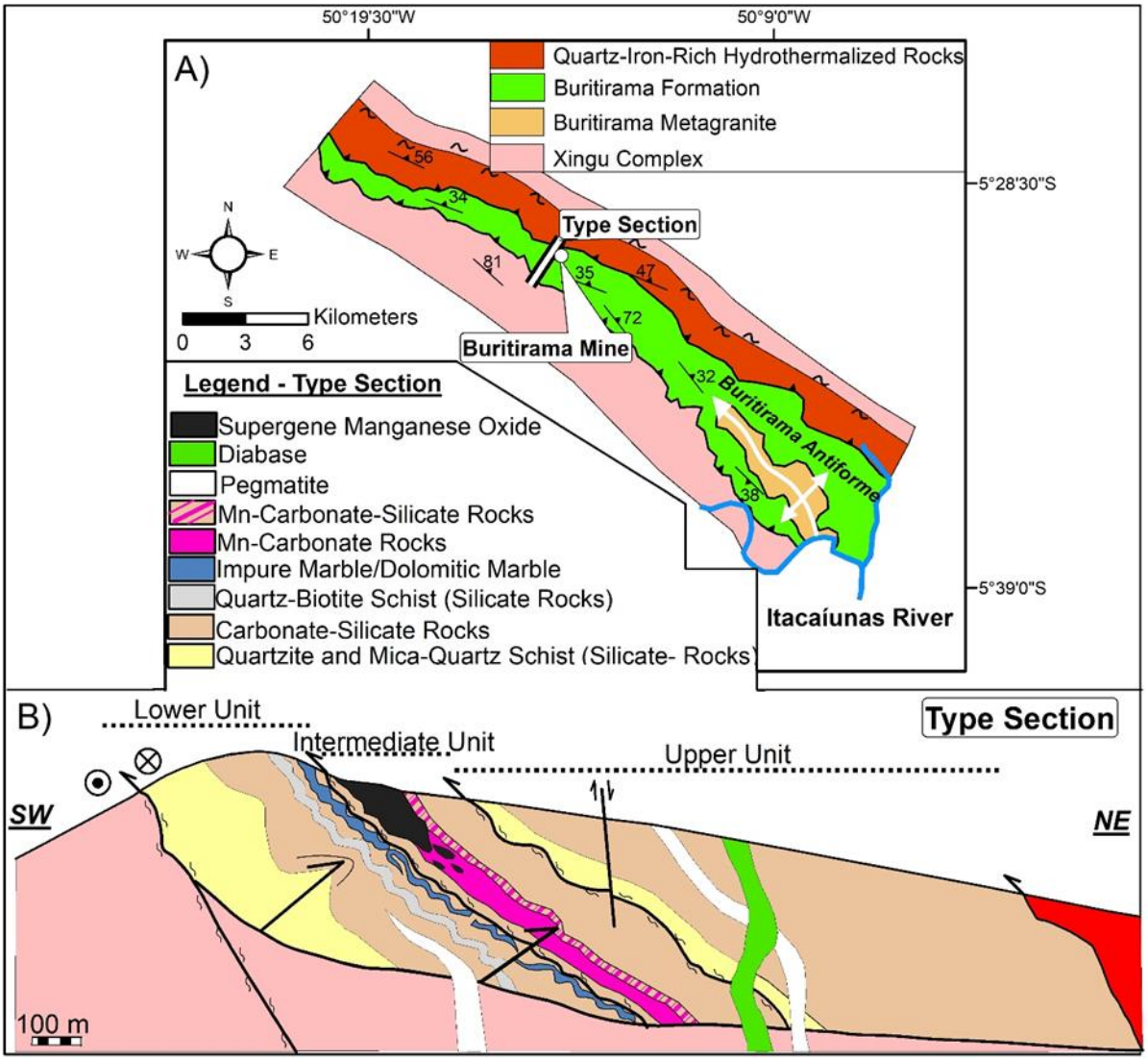

Figure 5.2 – A) Geological map of the Buritirama ridge (for location see Figure 5.1); B) Buritirama Formation type section showing the individualized Lower, Intermediate and Upper units (Salgado et al. 2019a).

5.4. Materials and Methods

The non-weathered carbonate-bearing samples of BF were collected in the LU and IU after the description of ca. 8.000 m drillcore provided by the company Mineração Buritirama S/A and executed along the Buritirama ridge. Samples were prepared for analysis in the laboratories of the CPMTC Research Center, UFMG, Brazil. The whole-rock geochemistry was carried out in twenty-three samples at SGS Geosol Laboratories (SGS), Vespasiano, Brazil, and started with the crushing and pulverization of ca. 400 g of homogeneous and unweathered samples. Major oxides elements were analysed by Induced Coupled Plasma - Optical Emission Spectroscopy (ICP-OES), and trace elements by Inductively Coupled Plasma Mass Spectrometer (ICP-MS), both housed at the SGS Geosol Laboratories. The accuracy and precision were better than 10% and the confidence level is at 95%.

Five polished thin sections were employed in the microprobe analyses performed on the

Microscopy Center of the Federal University of Minas Geras (CM-UFMG) using an Electron Probe Microanalyzer (EPMA) model JXA-8900 RL. Operating conditions were 15 kV acceleration voltage, 20 nA beam current, 1 to 5 μm beam diameter and counting time between 10 and 20 seconds. The contents of SiO_2, $Al2O_3$, Na_2O, CaO, K_2O, FeO, MgO, MnO, TiO_2, P_2O_5, CrO_2 and BaO were analyzed using natural and synthetic standards (e.g. Sanidine for SiO_2 and K_2O; Jadeite for Na_2O; Magnetite for FeO; MgO for MgO; Spessartite for MnO; Rutile for TiO_2) and ZAF matrix correction was carried out to obtain the results.

C and O isotope analyses were carried out in five samples of Mn-carbonate rocks and three samples of dolomitic marbles at the Geochemistry Laboratory (LGQa) of the Federal University of Ouro Preto - Brazil. Carbon and oxygen isotope composition from whole-rock samples were obtained by close tube reaction with orthophosphoric acid (100%) using a Thermo Finningan Delta V advance Mass Spectrometer (IRMS) coupled to GasBench II. Samples were reacted at 72 °C. The average values obtained for the standards NBS-18 (7.20‰, Coplen, 1996), NBS-19 (28.60‰; Coplen, 1996) and LSVEC (- 146 46.60‰; Coplen et al. 2006), NBS-19 (1.95‰; Coplen et al. 2006) were used to normalize the raw data in each run to the VSMOW (Vienna Standard Mean Ocean Water) and Vienna Pee Dee Belemnite Standard (VPDB) scale respectively. The external accuracy based on multi-standard measurements of NBS-19, NBS-18 and LSVEC was better than 0.2 permil for carbon and oxygen. The results are expressed in notation δ in parts per thousand (‰) in relation to VPDB.

5.5. Results

5.5.1. Petrography and Mineral Chemistry of Carbonate-bearing Rocks of Buritirama Formation

Based on visually-estimated modal mineralogy, metamorphic fabric and mineral chemistry, the carbonate-bearing rocks of the BF are individualized in impure marbles (> 50 %vol carbonates), carbonate-silicate rocks (ca. 35 %vol carbonates) and manganesiferous carbonate rocks (20-70 %vol carbonates). Banding and schistosity are the main penetrative fabric, but a post-metamorphic hypogene system, related to acid and basic intrusions, disturbs these formers patterns and affect the whole fabric. Here, we incorporate new data on the previous work developed by Salgado et al. (2019a) and focus exclusively on the metamorphic processes recorded on BF. Mineral abbreviations are according to Whitney & Evans (2010).

5.5.1.1. Carbonate-Silicate Rocks and Dolomitic Marbles

The carbonate-silicate rock is the main lithotype of the BF and consists of coarse-grained dark

and greenish rocks (Figure 5.3A) with seriate, nematoblastic, lepidoblastic and/or granoblastic fabrics. They commonly show a prominent metamorphic banding defined by diopside intercalated to phlogopite, calcite and K-feldspar bands (Figure 5.3B).

Dolomitic marbles are present mainly at the LU and composed of coarse-grained crystals (up to 2.5 mm; Figure 5.3C) of calcite (> 90% $CaCO_3$ Mol%; Salgado et al. 2019a) and dolomite (ca. 50% $MgCO_3$ Mol%; Figure 5.3D) arranged in a polygonal granoblastic fabric. Phlogopite records an incipient metamorphic foliation and poikiloblastic diopside (up to 3.0 mm) is usually replaced by tremolite. Minor quartz and K-feldspar are present.

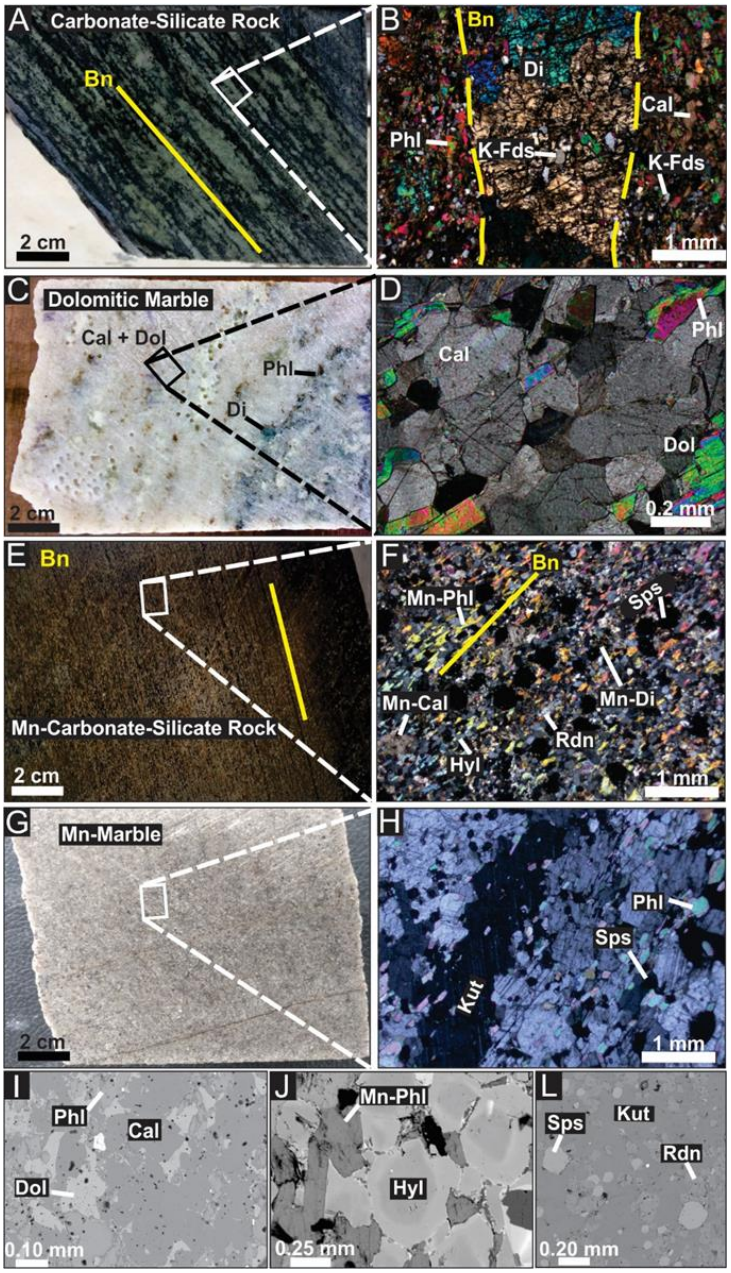

Figure 5.3 – General features of Buritirama Formation lithotypes. B, D, F and H crossed polarizer photomicrographies. I, F and G backscattered electrons image. A) and B) Greenish carbonate-silicate rock formed

by Di and Cal+Phl+K-Fds bands; C) and D) dolomitic marble compose of Cal+Dol+Phl and showing a granoblastic texture; E) and F) Mn-carbonate-silicate rock compose of Mn-Di+Mn-Cal+Mn-Phl+Sps+Rdn+Hyl; G) and H) Mn-marble comprising stretched Kut associated to fine Sps and Phl; I) Cal+Dol+Phl paragenesis in dolomitic marble; J) zoned Hyl and Mn-phl in Mn-carbonate-silicate rock; L) Kut+Sps+Rdn in Mn-marble.

5.5.1.2. Mn-Carbonate Rocks

Mn-carbonate-silicate rocks (Figure 5.3E and Figure 5.3F) and Mn-marbles (Figure 5.3G and Figure 5.3H) share the same fabric of the non-manganesiferous counterpart, but are usually medium-grained and composed of Mn-calcite (ca. 25 Mol% $MnCO_3$; Figure 5.4A), kutnohorite (ca. 50 Mol% $MnCO_3$; Figure 5.4A), Mn-diopside (up to 23 Mol% $Mn_2Si_2O_3$; Figure 5.4B), spessartine (ca. 80 Mol% $Mn_3Al_2Si_3O_{12}$; Figure 5.4C), zoned hyalophane (up to 42 Mol% $BaAlSi_3O_8$; Figure 5.3J; Figure 5.4D), rhodonite (up to 86 Mol% $MnSiO_3$; Figure 5.4E; Appendix 4A to 4D) and Mn-phlogopite (Salgado et al. 2019a). Minor apatite, barite and sulphides (e.g. pyrrhotite, chalcopyrite, sphalerite and pyrite) also occur. Stretched kutnohorite with interlobate and straight borders defines an incipient metamorphic banding on Mn-marbles (Figure 5.3H). Mn-carbonate-silicate rocks exhibit a clear banding formed by the intercalation of spessartine and rhodonite poikiloblast (up to 0.5 mm) with Mn-calcite, phlogopite and hyalophane (Figure 5.3E and Figure 5.3F).

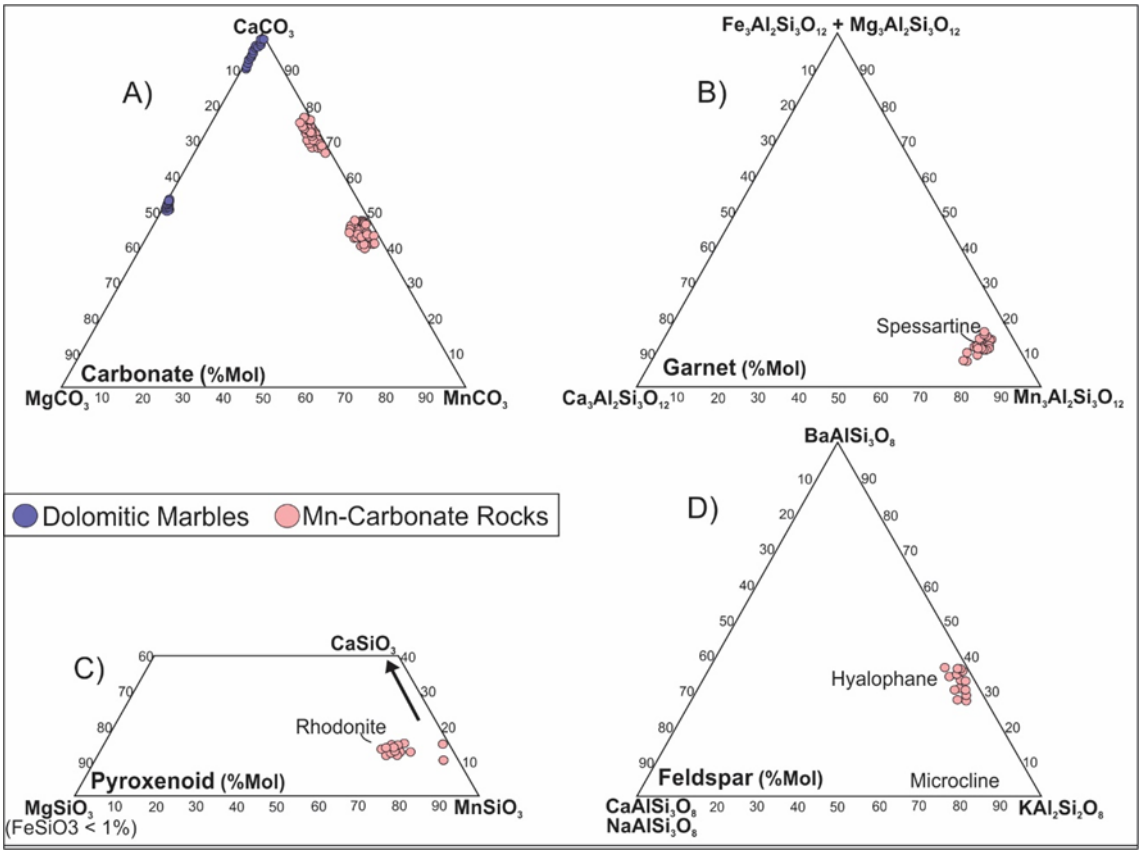

Figure 5.4 – Ternary diagrams showing the mineral composition of: A) carbonate; B) garnet; C) pyroxenoid and; D) feldspar.

5.5.2. Lithogeochemistry of Carbonate-bearing Rocks of the Buritirama Formation

Datasets for whole rock geochemistry of Mn-carbonate rocks, dolomitic marbles and carbonate-silicate rocks are presented in the Appendix 5. Two samples of Mn-carbonate-silicate rocks were individualized in the diagrams for presenting lower grades of MnO (ca. 10 wt%). Geochemistry data from Mn-carbonate rocks of Nsuta (West Congo craton; Kleinschrot et al. 1993; Beukes et al. 2016; Mücke and Olobaniyi, 2017) and Serra do Navio deposits (Tranzamazonas Province; Amazon craton; Chisonga et al. 2012) are plotted for comparison in most diagrams.

5.5.2.1. Major, Minor and Trace-Elements

The plots of MnO, Mn, SiO_2, Zr and Sc vs. major oxides and selected minor and trace elements provide the main characteristics of BF lithotypes (Figure 5.5 and Figure 5.6).

Dolomitic marbles presents the lower grades of upper continental crust elements such as Al_2O_3 (0.89–3.72 wt%; Figure 5.5A and Figure 5.5G), TiO_2 (0.01–0.15 wt%; Figure 5.5C and Figure 5.5H), Zr (lowest values around 10 ppm; Figure 5.6G), Sc (up to 3.2 ppm; Figure 5.6J) and metals as Ni (up to 50 ppm; Figure 5.6A), Mo (up to 0.58 ppm; Figure 5.6B), Zn (up to 75 ppm; Figure 5.6C) and V (up to 75 ppm; Figure 5.6F). Such rocks show the highest concentrations of CaO (26.07–30.10 wt%; Figure 5.5D) and MgO (17.30–19.70 wt%; Figure 5.5E). Specifically, the samples SS-091, SS-092 and SS-093 exhibit the lowest grades of Al_2O_5, TiO_2, Zr, Sc, SiO_2 (up to 9.43 wt%; Figure 5.5B) and the highest values of loss-on-ignition (LOI; 38.37–39.76).

Mn-carbonate rocks share similar concentrations of Al_2O_3 (up to 7.65 wt%), TiO_2 (0.49–0.70 wt%), Zr (9.90–68.5 ppm), Sc (1.7–11.7 ppm) of dolomitic marbles. Those rocks exhibit the higher contents of MnO (9.05–32.80 wt%), Ni (230–1048 ppm), Mo (3.79–1530 ppm), Zn (892–10000 ppm), Cd (1.03–29.59 ppm), Cu (4–812 ppm) and BaO (up to 1.12 wt%; Appendix 5). Cr and minor Co shows a positive correlation with Zr and Sc ($r > + 0.58$).

Carbonate-silicate rocks are marked by the higher concentrations of SiO_2 (39.39–51.30 wt%), Al_2O_3 (6.37–9.26 wt%), TiO_2 (0.23–0.34 wt%), Fe_2O_3 (1.83–3.17 wt%; Figure 5.5I), Zr (83.20–138.20 ppm) and Sc (5.00–6.80 ppm). Such rocks differ from the manganesiferous counterpart by lower concentrations of MnO (0.12–0.35 wt%), Ni (18.90–30.40 ppm), Mo (0.32–2.50 ppm), Zn (53–140 ppm) and Cd (0.07–0.36 ppm).

In general, BF lithotypes present low grades of Fe_2O_3 (up to 6.12 wt%) and similar contents of Co and V (excepting some Mn-rocks). The overall Co grades (up to 21.30 ppm) show a slightly positive correlation with Sc ($r = + 0.48$). SiO_2 exhibits a positive correlation with Al_2O_3 ($r = + 0.91$), TiO_2 ($r = + 0.77$), Zr ($r = + 0.65$) and Sc ($r = + 0.66$). Zr and Sc exhibit a scattered distribution when compared to

Ni, Mo and Zn. The higher BaO values are linked to Mn-carbonate rocks.

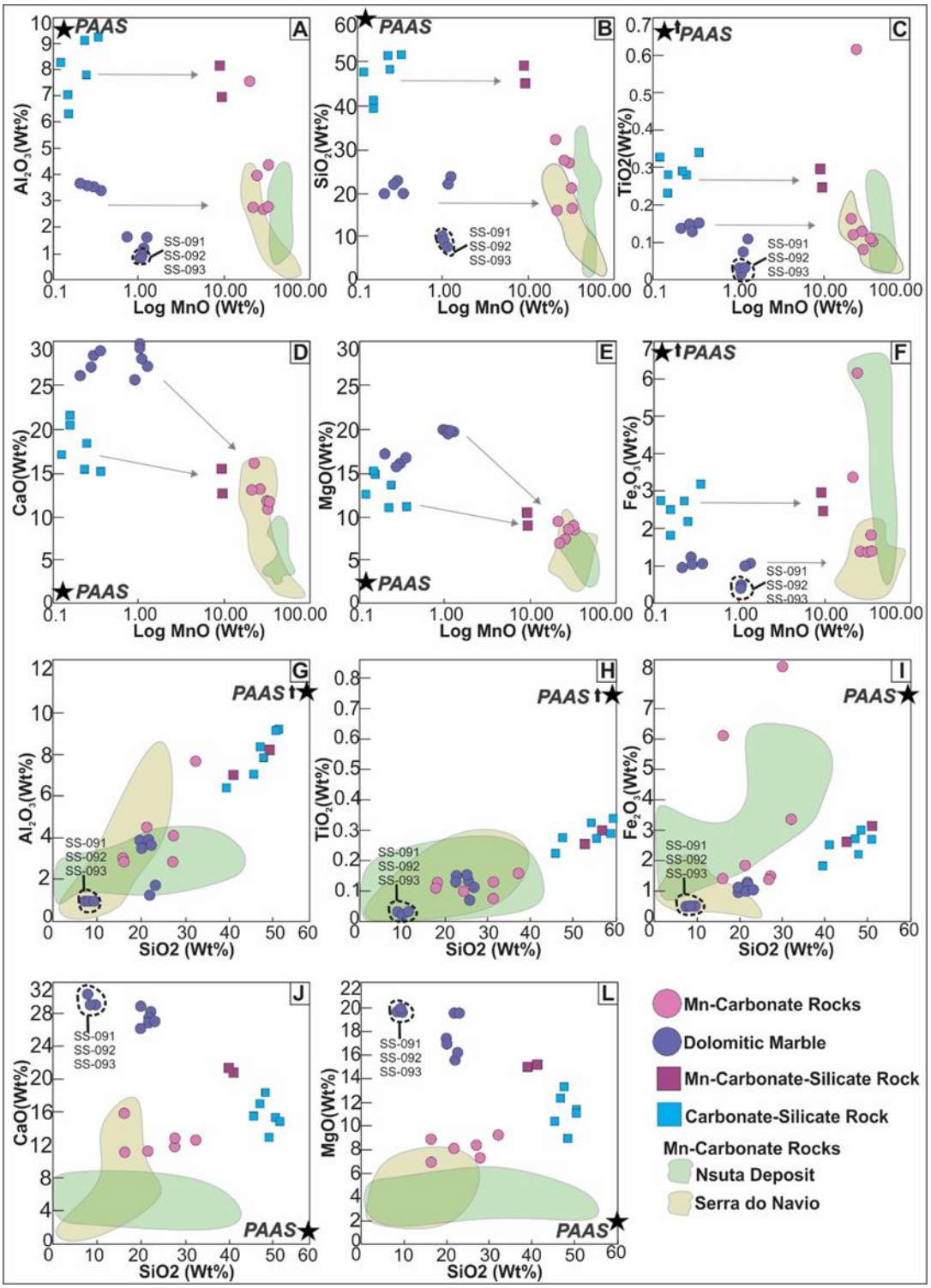

Figure 5.5 – Binary plots for major elements of Mn-carbonate rocks, Mn-carbonate-silicate rocks, dolomitic marble and carbonate-silicate rocks of Buritirama Formation. Mn-carbonate rocks from Nsuta (Kleinschrot et al. 1993; Mücke and Olobaniyi, 2017) and Serra do Navio (Chisonga et al. 2012) deposits are plotted for comparison.

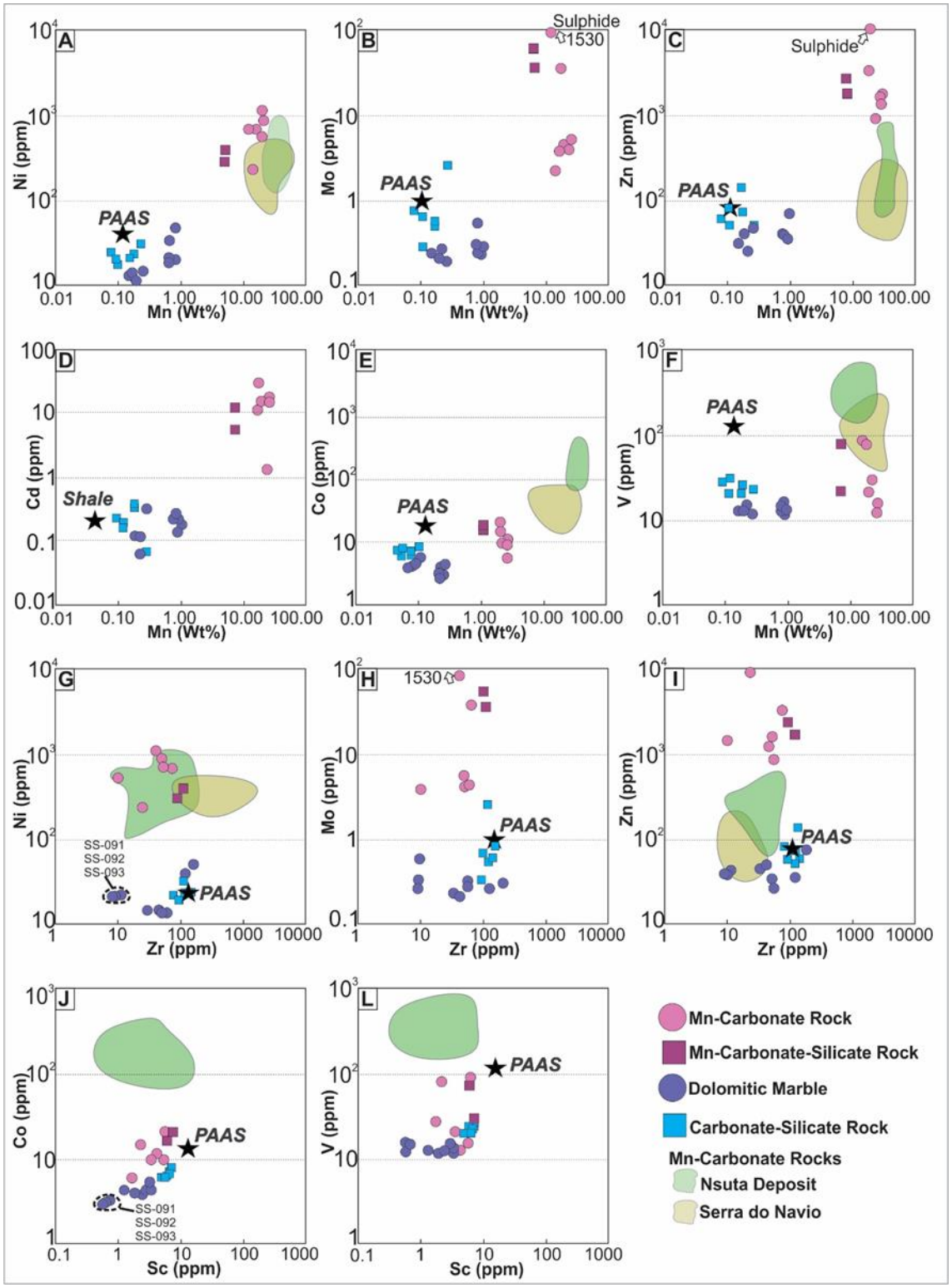

Figure 5.6 – Binary plots for Mn and trace elements of Mn-carbonate rocks, Mn-carbonate-silicate rocks, dolomitic marble and carbonate-silicate rocks of Buritirama Formation. Mn-carbonate rocks from Nsuta (Kleinschrot et al. 1993; Mücke and Olobaniyi, 2017) and Serra do Navio (Chisonga et al. 2012) deposits are plotted for comparison.

5.5.2.2. Lithogeochemistry of Carbonate-bearing Rocks of the Buritirama Formation

The Rare-Earth Elements and Y (REE+Y) PAAS-normalized patterns of BF lithotypes (Figure 5.7; Taylor and McLennan, 1985) are marked Pr_N/Yb_N (up to 1.18) and Tb_N/Yb_N (up to 1.42) ratios. Usually, positive Eu (up to 3.82), La (up to 1.85) anomalies and negative Ce/Ce* anomalies (0.16–1.00) are present.

Dolomitic marbles show the lowest concentration of ∑REE+Y (41.79–59.07 ppm) and highest Y/Ho ratio (27.71–53.65). They are characterized by Heavy Rare-Earth Elements and yttrium (HREE+Y) enrichment and positive La_N/Sm_N (0.98–1.36), La_N/Yb_N (0.75–1.72) and Tb_N/Yb_N (0.95–1.24) ratio. Positive anomalies of Eu/Eu* (1.00–1.46) and La/La* (1.09–1.41) and slightly negative anomalies of Ce (0.69–1.08) are present. Zr shows strong positive correlation with ∑REE+Y (r = + 0.89), but no correlation with Eu/Eu* anomalies (r = + 0.06). Ce/Ce* exhibits moderate positive correlations with SiO_2 (r = + 0.69), Al_2O_3 (r = + 0.88) and Sc (r = + 0.87), contrasting to the absence of correspondence between Eu/Eu* anomalies vs. SiO_2 (r = + 0.13), Al_2O_3 (r = - 0.02) and Sc (r = + 0.15).

Specifically, samples SS-091, SS-092 and SS-093 have the highest LOI (ca. 40%) and Y/Ho ratios (>48.39). They exhibit predominantly negative correlations between Ce anomalies vs. Zr (r = - 0.57), Sc (r = - 0.67), Al_2O_3 (r = - 0.42), ∑REE+Y (r = + 0.11) and Eu anomalies vs. Zr (r = - 0.86), Sc (r = - 0.92), Al_2O_3 (r = - 0.01), ∑REE+Y (r = - 0.31). Y/Ho ratio show negative correspondence with Sc (r = - 0.62), Zr (r = - 0.72) and ∑REE+Y (r = - 0.99).

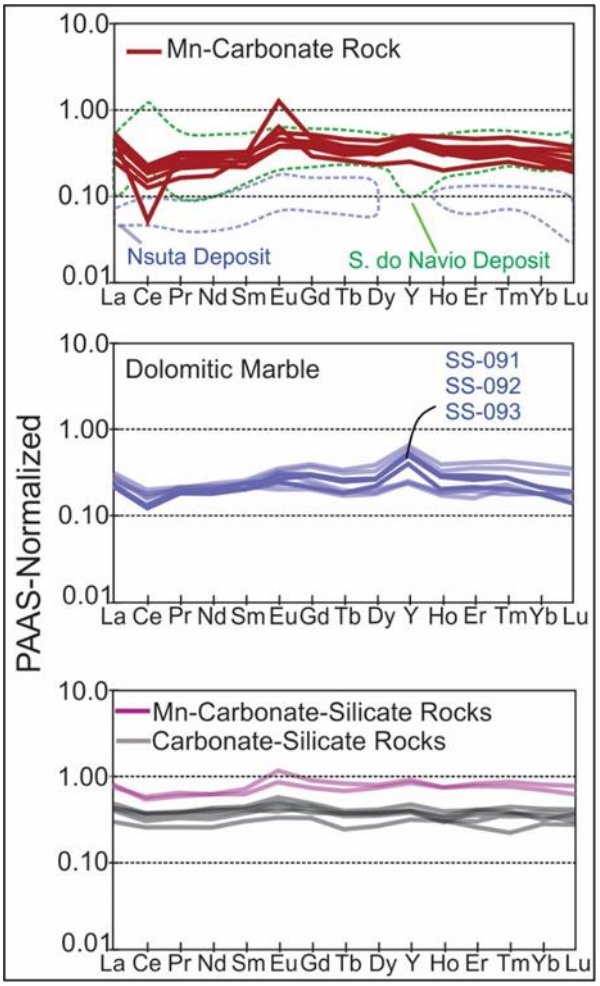

Figure 5.7 – PAAS-normalized REE+Y patterns (Taylor and McLennan, 1985) for: A) Mn-carbonate rocks; B) dolomitic marble and; C) carbonate-silicate rocks and Mn-carbonate-silicate rocks of Buritirama Formation. Mn-carbonate rocks from Nsuta (Beukes et al. 2016) and Serra do Navio (Chisonga et al. 2012) deposits are plotted for comparison.

Mn-carbonate rocks show the higher values of ∑REE+Y (65.65–145.63 ppm) associated with two samples of Mn-carbonate-silicate rocks. They are marked by HREE+Y-enrichment, similar Y/Ho (ca. 34) ratio and primarily positive La_N/Sm_N (1.05–1.91), La_N/Yb_N (0.95–1.84) and Tb_N/Yb_N (0.84–1.28) ratio. Positive anomalies of Eu/Eu* (1.26–2.20) and La/La* (0.93–1.84) are present. Ce/Ce* anomalies are mainly negative (0.69–1.07) and exhibit a slightly positive correlation with Zr (r = + 0.32). Eu/Eu* anomalies present a positive correlation with Mn (r = + 0.76), Ni (r = + 0.78), Ba (r = + 0.44), negative correlation with Fe (r = - 0.61), Al_2O_3 (r = - 0.67), Zn (r = - 0.44) and no clear correspondence with Zr (r = - 0.36) and Sc (r = - 0.26; Figure 5.8).

Carbonate-silicate rocks present similar ∑REE+Y (58.61–82.92 ppm) values to those of Mn-carbonate silicate-rocks. They are marked by slightly HREE+Y-enrichment and regular La_N/Sm_N (0.98–1.09), La_N/Yb_N (1.06–1.28) and Tb_N/Yb_N (0.87–1.18) ratios. Positive anomalies of Eu/Eu* (1.02–1.34), La/La* (0.92–1.29) and regular anomalies of Ce/Ce* (0.87–1.13) are present. Zr exhibits a slightly

positive correlation with ∑REE+Y (r = + 0.64) and is virtually independent of Eu/Eu* (r = + 0.16). MnO exhibits a slightly positive correlation with Eu/Eu* anomalies.

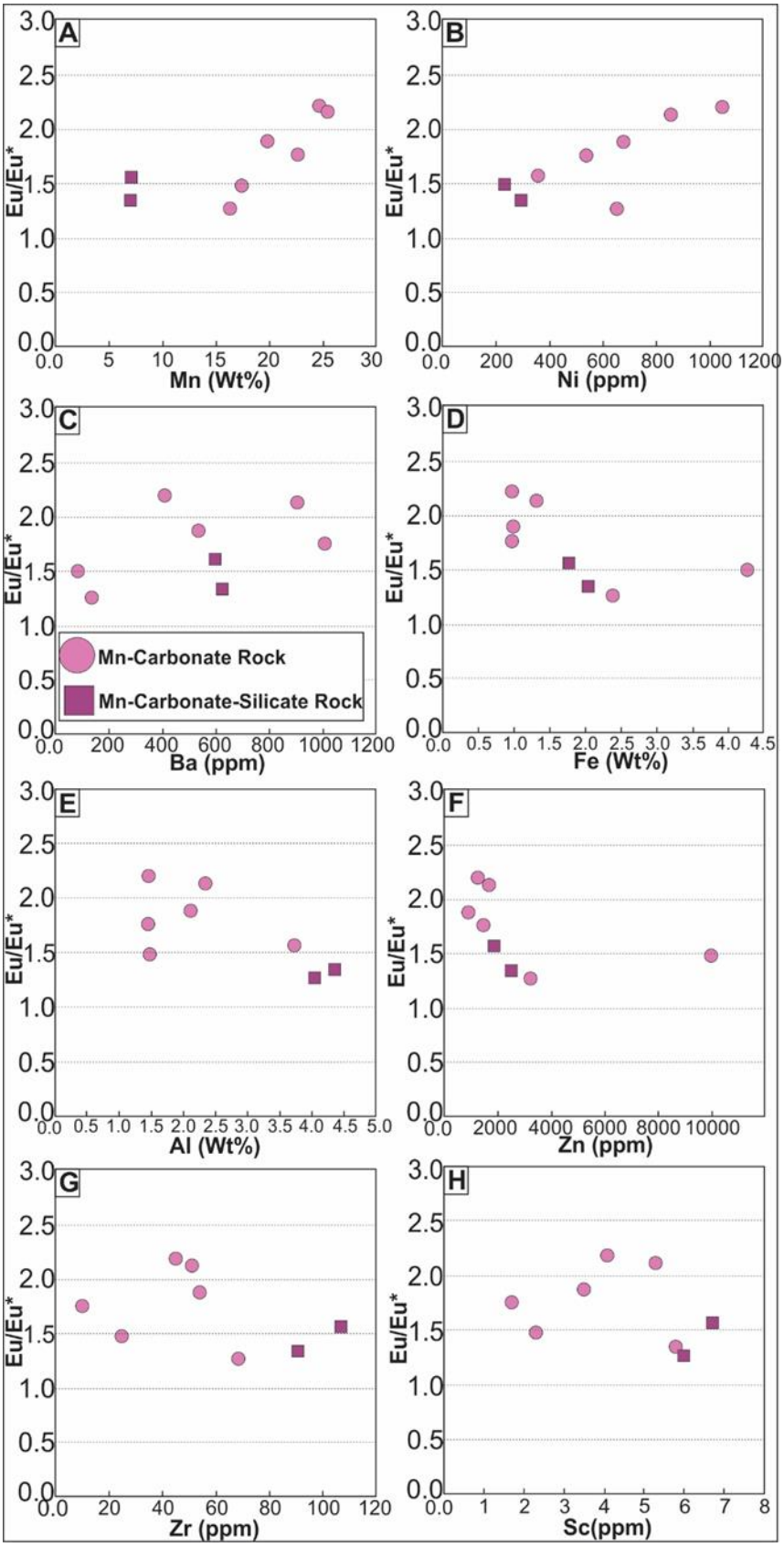

Figure 5.8 – Binary plots for Eu/Eu* vs. major and trace elements of Mn-carbonate rocks and Mn-carbonate-silicate rocks of Buritirama Formation.

5.5.3. C and O Isotopes of Dolomitic Marbles and Mn-carbonate rocks

Dolomitic marbles (samples SS-091, SS-092 and SS-093) and Mn-carbonate rocks $\delta^{13}C$ and $\delta^{18}O$ values are present in the Appendix 6 and Figure 5.9. Dolomitic marbles are distinguished by high positively fractionated $\delta^{13}C$ (+ 3.18‰ to + 4.96‰) and low $\delta^{18}O$ (- 13.54‰ to - 14.79‰). Mn-carbonate rocks exhibit predominantly negative $\delta^{13}C$ (- 2.56‰ to + 0.15‰) and low negative $\delta^{18}O$ (- 10.79‰ to - 14.74‰) values. Both present a strong negative correlation (r = - 0.79). Data from Mn-calcite and kutnohorite-marbles of Nsuta (Nyame and Beukes, 2006), Serra do Navio (Chisonga et al. 2012) and Molango (Okita and Shanks, 1992) deposits are plotted for comparison.

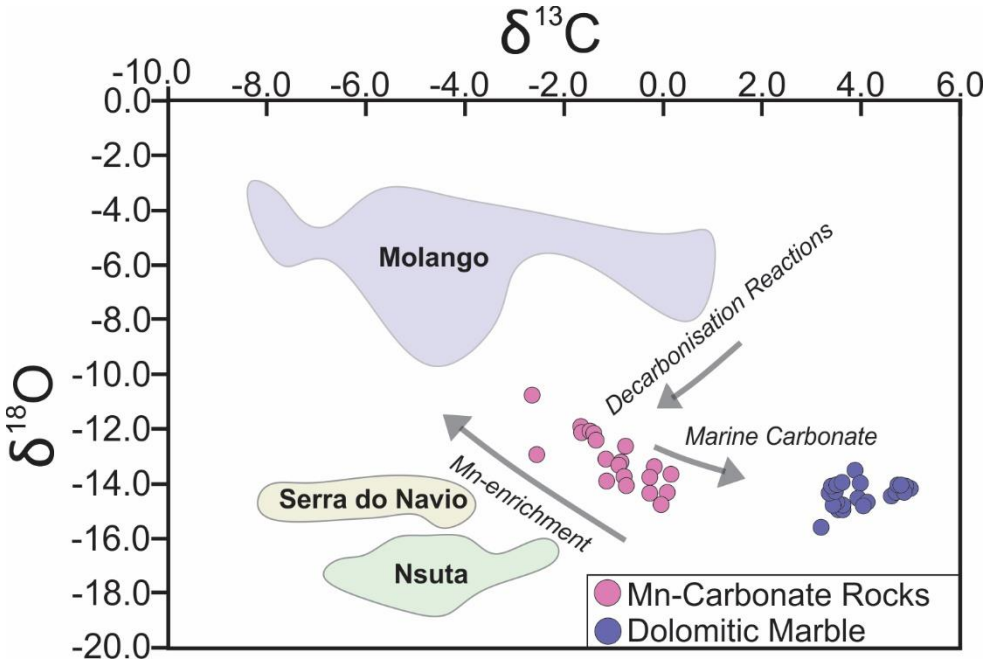

Figure 5.9 – C and O isotopes distribution for dolomitic marbles and Mn-carbonate rocks of Buritirama Formation. C and O data of Mn-calcite and kutnohorite-marbles of Nsuta (Nyame and Beukes, 2006), Serra do Navio (Chisonga et al. 2012) and Molango (Okita and Shanks, 1992) deposits are plotted for comparison.

5.6. Discussion

5.6.1. Dolomitic Marble and Carbonate-Silicate Rocks

5.6.1.1. Nature and Origin

Geochemical and isotopic data from metacarbonates (e.g. dolomitic marble) have been used as a proxy for the geochemistry of Paleoproterozoic oceans, providing valuable insights on oxygen levels and ocean-atmosphere redox conditions (Bekker et al. 2006; Canfield et al. 2013; Lyons et al. 2014). However, following this approach requires a broad understanding of the carbonate genesis and the

potential mechanisms capable to disturb primary marine signatures (Buick et al. 1998; Bekker et al. 2003; Hood et al. 2018; Nascimento et al. 2007; Melezhik et al. 2005; Bau and Alexander, 2006). Both aspects are considered below.

The Transamazonian metamorphic event established on dolomitic marbles of the BF reached temperatures up to 550 °C (Valarelli et al. 1978) originating metasomatic borders (e.g. dolomitic marble and quartz-biotite schist contact) and hydrothermal veinlets. Both features can affect the post-depositional geochemistry and isotope signatures and thus samples bearing those features were avoided during borehole sampling (Thompson et al. 1975; Ague, 2003; Ordóñez-Calderón et al. 2008). In a first attempt to detected detrital contamination, the samples were screened avoiding high modal occurrence of diopside, interpreted as formed by the reaction between marine carbonates and continental silicate minerals (Salgado et al. 2019a).

In a second stage of analysis, three samples (SS-091, SS-092 and SS-093) exhibiting the lowest content of crustal elements such as Zr (Figure 5.6G), TiO2 (Figure 5.5H), Sc (Figure 5.6J), SiO2 (Figure 5.5I) and Al_2O_3 (Figure 5.5A) were tracked. The samples SS-091, SS-092 and SS-093 record modern-seawater REE+Y pattern (Bau and Moller, 1997; Bau and Alexander, 2006; Liu et al. 2019) as high Y/Ho ratios (> 48.39), low concentrations of ∑REE+Y, HREE+Y-enrichment, positive anomalies of La and slightly negative anomalies of Ce (Figure 5.7; Appendix 5). Confronting ∑REE+Y, Ce/Ce*, Eu/Eu*and Y/Ho vs. HFSE, TiO_2 and Al_2O_3, minor influence of crustal sediments is recognized, supporting the application of these rocks as proxies.

Ce negative anomalies and high Y/Ho ratios recorded in the Buritirama dolomitic marbles are typical signatures of modern oxic shallow-waters (German et al. 1990; Bau and Moller, 1997) while positive Eu/Eu* anomalies and high contents of MnO (up to 1.25 wt%) suggest the influence of hydrothermal vents over the protoliths of these rocks (Figure 5.8; Derry and Jacobsen, 1990; Von Damm, 1990). The fractionation of Ce and Ho into the oceans is attributed to the sorption and sinking of both elements by Fe-Mn oxyhydroxides (Bau and Koschinsky, 2009). Such process developed over the transition between oxic to anoxic waters in a stratified ocean model that probably reflect the Buritirama basin.

Carbonate-silicate rocks from BF have been previous reported as a metamorphic product of marls (Salgado et al. 2019a) and record substantial amounts of crustal sediments, primary expressed by the broad mineral assemblage (Ca, Dol, Di, Phl, K-Fds, Qz and Pl). They contrast to dolomitic marbles by higher concentrations of continental source elements (e.g. Zr, Th, Al_2O_3), lower Y/Ho ratios and a flat REE+Y pattern (Figure 5.5, Figure 5.6 and Figure 5.7). In comparison to PAAS, the major concentration of carbonate minerals is expressed by the lower contents of HFSE and ∑REE+Y on carbonate-silicate

rocks.

5.6.1.2.C and O Isotopes – Dolomitic Marbles

C and O isotopic data from the likely pristine carbonates (samples SS-091, SS-092 and SS-093) of BF presented restrict $\delta^{13}C$ and $\delta^{18}O$ variations (up to 2‰; Figure 5.9). Unlike $\delta^{13}C$, $\delta^{18}O$ values are prone to be disturbed by metamorphic decarbonisation and diagenetic re-equilibration reactions (calcite/dolomite and hot fluids interaction; Matthews and Kolodny 1978; Valley 1986; Banner et al. 1990; Sharp et al. 2003; Hood et al. 2018). This probably occurred in the Buritirama dolomitic marbles. Positive $\delta^{13}C$ values (+ 3.18‰ to + 4.96‰) are evaluated in the context of the Lomagundi isotopic excursion, as detailed below.

5.6.2. The Lomagundi Carbon Isotope Excursion

The Lomagundi Carbon Isotopic Excursion refers to the global increasing in $\delta^{13}C$ values of carbonatic rocks (8‰ on average) occurred between ca. 2.22 Ga and 2.06 Ga and likely as a consequence of the Great Oxygenation Event (GOE – ca. 2.4–2.3 Ga; Schidlowski et al. 1976; Holland 1999; Bekker et al. 2003; Canfield et al. 2013; Lyons et al. 2014). The Lomagundi Event has been worldwide recorded in Rhyacian platformal carbonates deposited coevally to the Buritirama dolomitic marbles (Maheshwari et al. 2010).

Dolomitic marbles $\delta^{13}C$ values (+ 3.18‰ to + 4.96‰) are correspondent to the rising or to the falling of the Lomagundi (Figure 5.9; Appendix 6) Excursion when confronted to distinct δ13C evolutionary curves (Shields and Veizer, 2002; Bekker et al. 2006; Maheshwari et al. 2010). However, fixing these rocks at any of those limits would be inaccurate, taking into account the absence of a precise age for the BF and the potential decresing of $\delta^{13}C$ values caused by decarbonisation reactions. For now, we assume that the $\delta^{13}C$ values detected on BF reflect the ocean waters carbon isotope signals during the Lomagundi Carbon Isotopic Excursion lifespan.

5.6.3. Mn-Carbonate Rocks

5.6.3.1.Nature and Origin

Mn-carbonate rocks are considered a metamorphic product of marine sediments (Mn-rich marls) bearing distinct modal concentrations of diagenetic Mn-carbonates and continental sediments (Dasgupta et al. 1992; Kleinschrot et al. 1994; Calvert and Pedersen, 1996; Salgado et al. 2019). They are marked by the absence of Mn-silicate phases (except braunite; Johnson et al. 2016), formed later during the metamorphic consumption of Mn-carbonates (Schreyer et al. 1992; Nyame, 2001; Nayak and Mohapatra,

1998; Salgado et al. 2019a). Such rocks consist of the main protore in Mn-sedimentary deposits as Nsuta (Ghana), Serra do Navio (Brazil), Molango (Mexico) and Kalahari (South Africa; Roy, 2006; Maynard, 2010).

The Buritirama Mn-carbonate rocks are formed by the ubiquitous metamorphic consumption of Mn-calcite and kutnohorite giving rise to Mn-diopside, rhodonite and spessartine (Salgado et al. 2019a). Minor phlogopite, plagioclase, K-feldspar and quartz are related to a continental source (Figure 5.3E and Figure 5.3F). Specifically, the zoned hyalophane present in these rocks has been reported in volcanogenic exhalative sediments, where it is formed by the interaction between detrital K-feldspar with hydrothermal and diagenetic Ba-rich fluids (Bjorlykke and Graffin, 1973; McSwiggen et al. 1994; Chang et al. 2018).

The major hydrothermal alteration recorded on BF Mn-carbonate rocks will be treated in further studies. Minerals like pyroxmangite and kanoite reported in a previous work (Salgado et al. 2019a) are now interpreted as the product of the post-metamorphic hydrothermal event, along part of the sulphides (e.g. chalcopyrite and pyrrhotite).

5.6.3.2. Geochemistry

The Mn-carbonate rocks of BF are distinguished from dolomitic marble by the increasing of MnO contents (e.g. kutnohorite) counterbalanced by the reduction of CaO-MgO concentrations (e.g. dolomite). Such exchange occurs while keeping almost the same contents of SiO_2, Al_2O_3, TiO_2 and HFSE (Figure 5.5 and Figure 5.6), for the equivalent pairs Mn-marbles/dolomitic marbles and Mn-carbonate-silicate rocks/carbonate-silicate rocks. The influence of hydrothermal vents on these rocks is suggested by the positive correlation between Eu/Eu*, BaO and MnO ($r > + 0.55$) and the negative correlation with crustal elements (Figure 5.8; Derry and Jacobsen, 1990; Von Damm, 1990; Bau and Möller, 1997; Kurian et al. 2008). The high Mn/Fe fractionation ratios (up to 25) detected on Mn-carbonate rocks and the low FeO content in most of the stratigraphic package can be interpreted in the context of a stratified ocean (Canfield, 1998), as will be later addressed.

Moving further into the understanding of Mn-carbonate rocks, the content of redox-sensitive proxies Ni, Zn, Mo, Cd, V, U and Co can be linked by two major pathways: i) scavenging from ocean water by Fe-Mn-oxyhydroxides particles (Fe-Mn ocean cycle); and ii) uptaking and sinking by organic compounds. The distinct redox gradients developed during diageneses can disturb both process and will be later evaluated (Froelich et al. 1979; Tribovillard et al. 2006; Morford et al. 1999; Morford et al. 2005; Roy, 2006; Maynard, 2010; Hein, 2013; Maynard, 2014).

In an attempt to detect trustful ocean-related signals of Ni, Zn, Mo, Cd, V, U and Co, we compare

the Mn-carbonates of Buritirama with Nsuta and Serra do Navio deposits, PAAS (Cd value from Li, 2000), pelagic clays (Li, 2000) and a Mn-sedimentary deposit standard proposed by Maynard (2010; Figure 5.6). As a result, BF Mn-carbonates rocks present the highest contents of Ni and Zn, slight Cd enrichment, and V and U depletion. Mo and Co values correspond to pelagic clays (Li, 2000) and PAAS, respectively (Figure 5.6). Ni, Zn and Cd exhibit no correspondence with HFSE, Al2O3 and TiO2.

The high Ni and Zn contents on Mn-carbonate rocks seem to be related to distinct processes. Ni exhibits a strong positive correlation with the hydrothermally-related Eu/Eu* (r = + 0.72; Figure 5.8B), MnO (r = + 0.69; Figure 5.6A) and negative correlation with the commonly organophile P2O5 (r = - 0.70), Zn (- 0.78) and Cd (r = - 0.69; Boyle, 1976; Bruland, 1990; Derry and Jacobsen, 1990; Föllmi, 1996; Benitez-Nelson, 2000; John et al. 2014; Roshan et al. 2017). In contrast, Zn present moderate negative correlations with Eu/Eu*(r = - 0.56; Figure 5.8F), MnO (r = - 0.57; Figure 5.6C) and strong positive correlations with P_2O_5 (r = + 0.93) and Cd (r = + 0.76).

The correlated Cd and Mo (r = + 0.79) shows a positive correspondence with P_2O_5 (r = + 0.75 and + 0.97, respectively) and Zn (r = + 0.76 and + 0.79, respectively). Instead, weak negative correlations are detected when confronting Cd, Mo, P_2O_5, Zn vs. MnO, SiO2, Zr, Sc, Eu, Ni and Eu/Eu*. Such patterns suggest a probably organic matter control on Cd and Mo values (i.e., micronutrients; Bruland et al. 1983; Roshan et al. 2017; Smedley et al. 2017). Moderate to strong positive correlation of Co with Zr (r = + 0.58), Al_2O_3 (r = + 0.73) and negative correlations with MnO (r = - 0.72) and Eu/Eu* (r = - 0.70) suggest a continental origin.

Normally, V sinking is associated with Mn-cycle and organic compounds (e.g. adsorbed and organometallic ligands) while U-enrichment patterns comes from its association with organic matter under anoxic/euxinic conditions (Calvert and Pedersen, 1993; Tribovillard et al. 2006). Both elements are depleted on Buritirama Mn-carbonate rocks and could have been diagenetically regenerated (Zheng et al. 2002a, 2002b; Algeo et al. 2020).

The Mn-carbonate rocks PAAS-normalized REE+Y patterns are flat and mainly product of its detrital fraction (Figure 5.7A). However, Ce/Ce* and Eu/Eu* show no correlation with typical upper-crust elements (e.g. HFSE and Al_2O_3) suggesting a seawater source for both. Negative Ce/Ce* anomalies contrast to the high concentrations of Ce present in Mn-nodules and seems to be derived from diagenetic remobilization (Pedersen et al. 1983; Dubinin et al. 1997).

5.6.3.3. C and O Isotopes – Mn-carbonates

The $\delta^{13}C$ values from Mn-carbonate deposits worldwide have been reported as a primordial evidence of microbially-mediated reduction of Mn-oxides by organic matter or methane oxidation

(Polgári et al. 1991; Lovley et al. 1991). Such reaction gives rise to organic-derived CO_3^{2-} that is recognized on the structure of rhodochrosite, kutnohorite and Mn-calcite by negative $\delta^{13}C$ signals (Okita et al. 1988; Calvert and Pedersen, 1993; Kuleshov, 2017). Mn-carbonate rocks of BF record predominantly negative $\delta^{13}C$ data that partially overlies the fields defined by the Molango and Nsuta deposits (Figure 5.9; Okita and Shanks, 1992; Nyame, 2006). However, most carbonate-hosted Mn-deposits exhibit even lower $\delta^{13}C$ values (ranging from - 2‰ to - 15‰) than Buritirama.

The relatively high $\delta^{13}C$ values (- 2.56‰ to + 0.15‰) detected on Buritirama Mn-carbonates are attributed to the mixing between two distinct CO_3^{2-} reservoir: i) provided by anaerobic organic matter degradation; and ii) furnished by calcite and dolomite dissolution (Okita et al. 1988; Polgári et al. 1991; Kuleshov, 2017). The influence of detrital marine carbonates is additionally supported by the high contents of MgO and CaO on Mn-carbonate rocks and the impact of such minerals in the overall $\delta^{13}C$ values would be rather significant.

The negative covariance between $\delta^{13}C$ and $\delta^{18}O$ (r = - 0.79) recorded on Mn-carbonate rocks could be related to two driving factors: i) the mentioned influence of detrital marine carbonates in increasing $\delta^{13}C$ values, or alternatively; ii) a product of distinct degrees of microbially-mediated Mn reduction, which culminate in lower values of $\delta^{13}C$ associated to high grades of Mn. The later process has been recognized in different deposits (Okita et al. 1988; Polgári et al.1991; Calvert and Pedersen 1993; Kuleshov, 2017) and is suggested by the negative correlation between the $\delta^{13}C$ and Mn (r = - 0.78) on Buritirama Mn-carbonates.

5.6.4. The Buritirama Basin

The metasedimentary rocks present at the Lower Unit, Intermediate Unit and Upper Unit of BF are here tentatively correlated to distinct sedimentary facies usually reported in a platformal depositional system (Figure 5.10). The thick orthoquartzite (Lower Unit) laying down over the Xingu Complex (local basement) is followed upward by platformal carbonates (dolomitic marbles) and marls (carbonate-silicate rocks), suggesting its probable deposition at the sea front. These rocks present a lateral compositional variability recorded by the increasing of muscovite and/or iron oxyhydroxides. Fluctuations in the primary sedimentary facies are indicated by the direct contact between orthoquartzites and Mn-carbonate rocks. The dolomitic marbles represent a platformal shelf and the samples SS-091, SS-092 and SS-093 record pristine carbonates with negative Ce/Ce* and positive Eu/Eu* anomalies pointing to an oxic depositional environment with the influence of sea-floor hydrothermal plumes (Derry and Jacobsen 1990; Von Damm 1990; Bau and Alexander, 2006). Moderate positive $\delta^{13}C$ values recorded (+ 3.18‰ to + 4.96‰) on these rocks are often recognized in Rhyacian shelves and attributed

to the Lomagundi Event as reported (Maheshwari et al. 2010). Carbonate-silicate rocks are the dominant lithotype in the Buritirama stratigraphy and consist of equivalents to marl. In contrast to dolomitic marbles, they record variable amounts of crustal contamination expressed by higher concentrations of HFSE and Al_2O_3 (Figure 5.5A and Figure 5.6G). Such rocks can gradually turn into calc-silicate rocks (Rosen et al. 2007; Salgado et al. 2019a). Quartz-biotite schist is possible equivalent to metamorphosed shales and apart from the Lower Unit, it is present in the Upper Unit. However, this lithotype has limited information and is going to be evaluated in further studies. Mn-marbles are detailed in the following metallogenetic model.

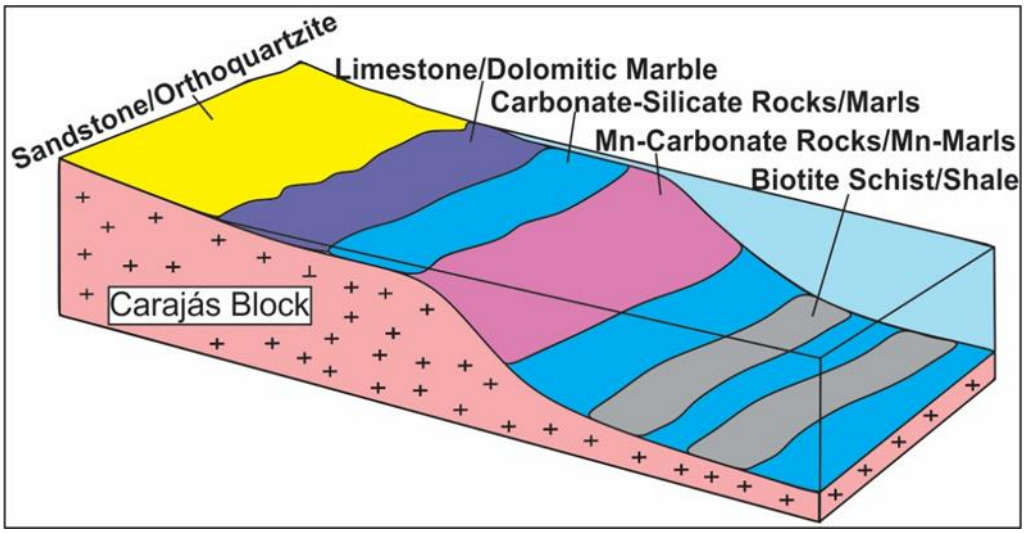

Figure 5.10 – General Model for the Buritirama Basin.

5.6.5. Metallogenetic Model

The classical multistage genetic model of Mn-carbonate deposits is primary redox-controlled and mostly involves the precipitation of Mn-nodules over the oxic-anoxic transition (redoxcline) follow by their deposition on the ocean bottom (Roy, 2006; Maynard, 2010). Mn-nodules are buried and submitted to sub-oxic/anoxic conditions just below the sediment-water surface, where bacterially mediated oxidation of organic matter can reduce Mn^{4+} to Mn^{+2}. The soluble Mn^{2+} diffuses reacting with CO_3^{2-} (major organic bicarbonate) to form diagenetic (Ca)Mn-carbonates (Okita et al. 1988; Polgári et al. 1991; Calvert and Pedersen, 1993). All of those processes culminate in the stratification and regeneration of chemical species along the sedimentary pile and the primary Mn-source is linked to hydrothermal plumes (Froelich et al. 1979; Tribovillard et al. 2006; Usui et al. 1997; Morford et al. 1999; Morford et al. 2005; Maynard, 2014; Hein, 2013). The Mn-carbonate rocks of BF are addressed in the light of this framework (Figure 5.11).

The geochemistry of BF Mn-rocks exhibits a positive correlation Eu/Eu* with Mn (Figure 5.8A),

Ba (Figure 5.8B) and Ni (Figure 5.8C), which indicate a direct influence of hydrothermal vents on these rocks. The high Mn/Fe ratios (up to 25; Appendix 5) are typical features of Mn-carbonates developed into stratified redox oceans with shallow oxic waters enriched in Ca^{2+} and Mg^{2+} and anoxic deep waters bearing high concentrations of Mn^{2+} and Fe^{2+}. In this scenario, Mn/Fe fractionation can be a product of Fe precipitation (oxides and sulphides) near ocean vents at lower Eh (- 0.2) and higher pH (c.a. 11) conditions, while Mn^{2+} is transported away from its hydrothermal source owing to its larger stability field under moderated reductive conditions (Krauskopf, 1957; Force and Cannon, 1988; Maynard, 2014). This process is envisaged for the BF considering the low concentrations of Fe recorded in the basin derived from a gradual Eh-pH transition established over hydrothermal vents during its pathway from anoxic to oxic ocean waters.

Mn-nodules (hydrogenic and diagenetic) and organic-matter sinking (primary production zones) are ultimately the metal sources of Mn-carbonate rocks (Okita and Shanks, 1992; Force and Cannon, 1988; Roy, 2006; Hein, 2013; Maynard, 2014). In this sense, the prominent concentrations of Ni and Zn on Buritirama Mn-carbonate rocks point out to two distinct configurations: i) Ni exhibit a positive correlation with the hydrothermal-related elements Mn, Eu and Ba, suggesting its scavenging by sorption on Mn-particles, while; ii) Zn presents a positive correlation with organophile elements Cd and P, indicating the uptake by organic complexes along the photic zone (Bruland, 1980; Frazer and Fisk, 1981; Derry and Jacobsen, 1990; Benitez-Nelson, 2000; John et al. 2014; Roshan et al. 2017). Any of these elements exhibited a possible detrital source (Figure 5.5 and Figure 5.6).

As a second stage, bacterially mediated solubilisation of Mn-nodules and organic-matter decomposition during diagenesis would release Mn^{2+}, Ni^{2+} and Zn^{2+} into the pore-water solution (Figure 5.11). Such elements can move upward regressing to the ocean water or be fixed in the sediment. In the Buritirama Mn-carbonate rocks, Mn^{2+} reacted with marine (dissolution detrital carbonates) and planktonic-derived (organic-matter oxidation) CO_3^{2-} as suggested by the slightly negative $\delta^{13}C$ (- 2.56‰ to + 0.15‰) values. The formed diagenetic carbonate could have incorporated Ni and Zn in its structure. The $\delta^{13}C$ range and its negative correlation with $\delta^{18}O$ is considered to be controlled by Mn-concentrations on carbonates (Okita et al. 1988; Polgári et al. 1991). In this sense, the prevalence of Mn-calcite and kutnohorite in the Buritirama Mn-rocks would reflect on the relatively high $\delta^{13}C$ values and significant concentration of Ca^{2+} in the pore-water. High Y/Ho ratios reinforce the influence of detrital calcite and dolomite over the Buritirama Mn-carbonates.

Low concentration of SO_4^{2-} during the diagenetic formation of Buritirama Mn-carbonates is suggested by the minor presence of sulphides and the primary incorporation of Ba by hyalophane rather than barite. The low concentration of Mo and V detected on these rocks suggests they were probably

driven out from sedimentary pile to the seawater, considering that both elements are readily adsorbed and enriched in Mn-nodules. In accordance with the "redox ladder", Mo and V are expected to be recycled under sub-oxic/anoxic environments and to be fixed in euxinic basins (e.g. Fe-Mo-S compound and V_2O_3; Helz et al. 1996; Bostick et al. 2003). U is prone to be associated with organic matter along euxinic basins and its signal is easily lost during episodic oxygenation (Zheng et al. 2002a). The slightly enrichment of Cd reflects the significant concentration of organic matter in the system while Co has a detrital source (Bruland, 1990; Derry and Jacobsen, 1990).

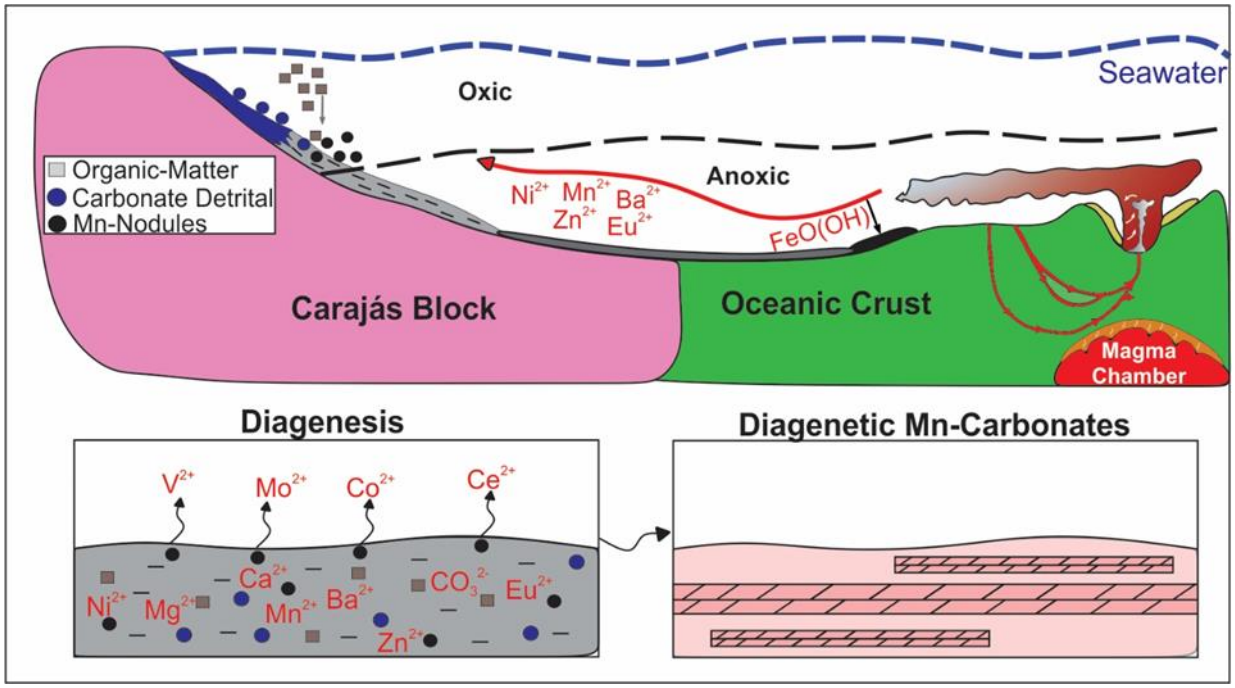

Figure 5.11 – Metallogenetic model for the Buritirama Mn-carbonate rocks.

The Buritirama Mn-carbonate deposit contrasts to the Serra do Navio and Nsuta deposits by: i) presence of pyroxene and the virtual absence of graphite, both linked to its higher metamorphic grade (amphibolite facies); ii) absence of rhodochrosite suggesting lower Mn^{2+}/Ca^{2+} ratios during diagenesis (Mucci, 2004; Kleinschrot et al. 1994; Chisonga et al. 2012); iii) slightly negative anomalies of Ce and the lower contents of V and Co, indicating partial regeneration of these elements during diagenesis (German et al. 1990; Dubinin and Sval'nov, 2003); iv) higher concentration of BaO linked to a hydrothermal source; v) higher Y/Ho ratios, $\delta^{13}C$ values and Ca and Mg concentrations attributed to the influence of detrital carbonates during diagenesis. Those distinct patterns are connected to the different tectonic environments and diagenetic pathways proposed to each of the deposits.

5.6.6. Implication for the Carajás Domain

Siderian and Rhyacian passive margin sediments set up over Archean domains are an outstanding feature of the São Francisco (Brazil), Superior (Canada), Kaapvaal (South Africa) and Pilbara (Australia) cratons and record the major depositional peak of Fe and Mn on Earth (Bradley, 2008; Condie and O'neill, 2010; Maynard, 2010). In the Carajás Province, supracrustal sequences and tectonic-metamorphic events have been mainly interpreted as Archean, however, recently studies are gradually uncovering the occurrence of large Paleoproterozoic units over the Carajás Archean nuclei. How the various Paleoproterozoic units are correlated is not clear, but Pereira (2009) has recognized a possible foreland basin (maximum depositional age at ca. 2.0 Ga) named Caninana Formation, while Araújo and Nogueira (2019) report glacial sedimentary rocks (2.58–2.06 Ga) along the Serra Sul ridge. Tavares et al. (2018) and Salgado et al. (2019a) drew attention to the effects of the Transamazonian orogeny on the northeastern border of the Carajás domain. Mougeot et al. (1996) carried out Pb–Pb dating on disseminated sulphides from sandstones of the controversial Águas Claras Formation, yielding an age of 2.06 Ga, while Fabre et al. (2011) recognized the lack of mass independent fractionation (MIF) in such minerals. Both suggest a Paleoproterozoic age for Águas Claras Formation (2.1 Ga) and its world-class Mn Azul deposit, despite Archean ages (c.a. 2.6 Ga) have also been propose based on detrital zircon and zircon from crosscutting gabbro dikes (Dias et al. 1996; Trendall et al. 1998). Bekker et al. (2017) reported positive $\delta^{13}C$ values (up to + 7.60‰) for dolomites located at the base of Águas Claras Formation (Serra Pelada area) and correlated these rocks with the Lomagundi Excursion and Sereno Mn-deposit. The BF fit in this scenario and the petrographic, geochemical and isotope data presented here reinforce the platformal nature of the basin.

In this paper, the novel positive $\delta^{13}C$ values (+ 3.18‰ to + 4.96‰) determined for dolomitic marbles of BF is another important piece of evidence in the Paleoproterozoic setting. Such values suggest a connection between the BF and the Águas Claras Formation located inward the Carajás domain (Bekker et al. 2017). Both units record $\delta^{13}C$ anomalies interpreted as an expression of the Lomagundi Carbon Isotopic Excursion in the Carajás Province. The Buritirama and Águas Claras basins were probably interconnected by a single ancient ocean sometime between 2.18-2.06 Ga. The Sereno Mn-deposit could also have been part of this system (Costa et al. 2016; Araújo and Sousa, 2018).

Evidences of an extensional phase associated with the deposition of Buritirama and probably of the Águas Claras Formation are not straightforward and coeval volcanic rocks have not been yet dated. Salgado et al. (2019b) suggested that the late Archean magmatic-hydrothermal event (ca. 2.50 Ga) related to the emplacement of A-type granites (Machado et al. 1991; Lindenmayer et al. 1994; Souza et al. 1996; Toledo et al. 2019) and IOCG mineralizations (Northern Copper Belt; Réquia et al. 2003;

Tallarico et al. 2005; Xavier et al. 2012; Moreto et al. 2015) could represent the early stages of a rift system at the northern border of the Carajás domain (Buritirama rift). Nevertheless, this scenario embraces an expressive lifespan for the Buritirama basin and needs to be better constrained, as well as the extent of such magmatic-hydrothermal event.

5.7. Conclusion

The Buritirama Formation along the Buritirama ridge represents part of a carbonatic platformal basin fringing the northern border of the Carajás block (2.18–2.06 Ga), which started probably after 2.55 Ga as indicated by the emplacement of anorogenic A-type granites and closed during the Transamazonian orogenic cycle (ca. 2.06 Ga). It is individualized in three main parts: Lower Unit, Intermediate Unit and Upper Unit.

Dolomitic marbles (limestones) samples collected at the Lower Unit (samples SS-091, SS-092 and SS-093) show a modern-seawater like geochemical pattern with high Y/Ho ratio (>48.39), low concentrations of ∑REE+Y, HREE+Y-enrichment, positive anomalies of La/La*, Eu/Eu* and slightly negative anomalies of Ce/Ce*. High $\delta^{13}C$ values (+ 3.18‰ to + 4.96‰ V-PDB) detected on these rocks are interpreted as an expression of the Lomagundi Carbon Isotopic Excursion. Carbonate-silicate rocks (marls) form by the increasing input of detrital sediments, primary expressed by the mineral assemblage (Ca, Dol, Di, Phl, K-Fds, Qz and Pl) and high concentration of continental-sourced elements (e.g. Zr, Th, Al_2O_3).

Mn-carbonate rocks of BF are considered a metamorphic product of marine sedimentary protoliths (Mn-marls) bearing different modal concentrations of diagenetic Mn-carbonates and continental sediments. They are formed by Mn-calcite, kutnohorite, rhodonite, spessartite, hyalophane and barite are associated with terrigenous related minerals such as plagioclase, quartz and K-feldspar. The metallogenesis of the Buritirama Mn-carbonate deposit involved a multistage process correlated to the classical Mn-sedimentary model that can individualized in: i) Mn-nodules precipitation over oxic conditions followed by their deposition on the ocean bottom; ii) bacterially mediated oxidation of organic matter coupled with Mn^{4+} to Mn^{2+} reduction under sub-oxic/anoxic conditions developed below the sediment-water interface; iii) soluble Mn^{2+} diffusion and reaction with CO_3^{2-} (organic and inorganic bicarbonate) to form diagenetic (Ca)Mn-carbonates. The contents of the correlated elements Mn, Ni, Ba and Eu on Mn-carbonate rocks are linked to a hydrothermal source while Zn, Cd and P_2O_5 present an organic affinity. The elements Ce, Mo, V, U and Co were probable remobilized during the diagenesis.

The novel positive $\delta^{13}C$ values (+ 3.18‰ to + 4.96‰ V-PDB) determined for dolomitic marbles

of BF connect this unit with the Águas Claras Formation located inward the Carajás domain. Both units record $\delta^{13}C$ typical of the Lomagundi Carbon Isotopic Excursion and were probably interconnected by a single ancient ocean sometime between 2.18-2.06 Ga. The Sereno Mn-deposit could have been part of this system.

5.8. Acknowledgements

This work was supported by Buritirama Mineração and the authors acknowledge João Araújo, Jorge Baptista and Michel Fontes, all members of this Company, for the support received. FAC is a Research Fellow of the CNPq, Brazil, and thanks for the ongoing support, especially through the project "Chemostratigraphy of Precambrian sedimentary successions of Brazil - fluctuations of atmospheric O" (303566/2019-1).

6. CONTRIBUIÇÕES PARA O CONHECIMENTO GEOLÓGICO

Acredita-se que as principais contribuições para o conhecimento geológico da presente tese foram:

i) A definição de uma seção-tipo para a Formação Buritirama apresentando os principais litotipos que compõem esta unidade bem como seu empilhamento tectônico. Acredita-se que o quartzito basal e de topo tenham se depositado em um mesmo momento sendo tectonicamente sobreposto durente a oroênese Transamazônas.

ii) As fases deformacionais registradas na Formação Buritirama e atribuídas ao evento Transamazônico;

iii) A idade máxima deposicional Paleoproterozóica para a Formação Buritirama, anteriormente intendida como uma unidade Arqueana;

iv) A identificação do Metagranito Buritirama e seu posterior detalhamento geoquímico e geocronológico. A idade de ~2,55 Ga obtida para o metagranito Buritirama está provavelmente vinculada a um evento tectono-magmático. Recentes dados geocronológicos sugerem idades entre 2.3-2.1 Ga para a Formação Águas Claras, desta forma, o metagranito Buritirama poderia representar estágios iniciais de um evento extensional. Tal evento, seria também precursor da bacia Buritirama;

v) O entendimento dos carbonatos presentes na Formação Buritirama como possivelmente depositados em um ambiente marinho plataformal;

vi) A proposição de um modelo metalogenético para os carbonatos manganesíferos.

7. ATIVIDADES COMPLEMENTARES

Os trabalhos desenvolvidos no âmbito desta tese, não se findam com a mesma. Uma sequência de estudos de natureza geocronológica e isotópica está planejada para a região da Serra de Buritirama, onde se pretende-se: i) avaliar o hidrotermalismo associado aos carbonatos manganesíferos; ii) determinar a idade do embasamento e da geração de diques/sills máficos e ácidos que cortam a Formação Buritirama e; iii) caracterizar os óxidos de manganês formados a partir da decomposição dos carbonatos manganesíferos. Existe ainda a possibilidade de se realizar estudos de natureza termobarométrica e petrocronológica.

8. REFERENCIAS BIBLIOGRÁFICAS

Ague, J.J., 2003. Fluid infiltration and transport of major, minor, and trace elements during regional metamorphism of carbonate rocks, Wepawaug Schist, Connecticut, USA. Am. J. Sci. 303, 753–816. https://doi.org/10.2475/ajs.303.9.753.

Algeo, T.J., Li, C., 2020. Redox classification and calibration of redox thresholds in sedimentary systems. Geochim. Cosmochim. Acta 1–19. https://doi.org/10.1016/j.gca.2020.01.055.

Almeida F.F., Brito Neves B.B., Carneiro C.D.R. 2000. The origin and evolution of the South American Platform. Earth Science Review, 50:77–111.

Almeida F.F., Hasui Y., Brito Neves B.B. 1976. The Upper Precambrian of South America. Boletim IG, Instituto de Geociências da USP, 7:45–80.

Almeida F.F., Hasui Y., Brito Neves B.B., Fuck R.A., 1981. Brazilian structural provinces: an introduction. Earth Science Review, 17:1-19.

Alvarenga C.J.S., Moura C.A.V., Gorayeb P.S., Abreu F.A.M., 2000. Paraguai and Araguaia belts. In: Cordani U.G., Milani E.J., Thomaz Filho A., Campos D.A., (ed.) Tectonic evolution of South America, Beca, Rio de Janeiro. p. 183-193.

Anderson W.L., Dyer R.C., Tores D.D. 1974. Ocorrências de manganês na bacia do Rio Itacaiúnas, centro-leste do Estado do Pará. In: 26° Congresso Brasileiro de Geologia. Porto Alegre, Anais, p. 149–164.

Andrade M.S., Nakashima J., Podestá P.R. 1986. Depósito de manganês da Serra de Buritirama, Pará. In: Schobbenhaus C. and Coelho C.E.S. (eds.). Principais Depósitos Minerais do Brasil, DNPN/Companhia Vale do Rio Doce, V. II, p. 153-166.

ANM, 2018. Anuário Mineral Brasileiro 2017. Brasília: ANM, 2018.

Araújo O.J.B., Maia R.G.N.M., João X.S.J., Costa J.B.S. 1988. A Megaestruturação Arqueana da Folha Serra dos Carajás. In: 7° Congresso Latino Americano de Geologia. Belém, V.1, Anais, p. 324-338.

Araújo, O.J.B., Maia, R.G.N., 1991. Programa Levantamentos Geológicos Básicos do Brasil (PLGB), Serra dos Carajás: folha SB.22-Z-A, Estado do Pará. Escala 1:250.000. Texto explicativo. Brasília: DNPM/CPRM, 164 p.

Araujo, R., Nogueira, A., 2019. Serra sul diamictite of the carajas basin (Brazil): A paleoproterozoic glaciation on the amazonian craton. Geology 47, 1166–1170. https://doi.org/10.1130/G46923.1.

Araújo, R.N.; Sousa, M.J., 2018. Áreas de Relevante Interesse Mineral – Província Mineral de Carajás, PA: Estratigrafia e Análise do Minério de Mn de Carajás – Área Azul, Sereno, Buritirama e Antônio Vicente. In: Informe de Recursos Minerais – Programa Geologia, Mineração e Transformação Mineral – 16° Série Províncias Minerais do Brasil – Áreas de Relevante Interesse Econômico. CPRM – Serviço Geológico do Brasil, pp. 198.

Avelar, V.G., Lafon J-M., Junior, F.C.C., Macambira, E.M.B., 1999. O Magmatismo Arqueano da Região de Tucumã-Província Mineral de Carajás: Novos Resultados Geocronológicos. Rev. Bras. Geociências 29, 453–460. https://doi.org/10.25249/0375-7536.1999294453460.

Banner, J.L., Hanson, G.N., 1990. Calculation of simultaneous isotopic and trace element variations during water-rock interaction with applications to carbonate diagenesis. Geochim. Cosmochim. Acta 54, 3123–3137. https://doi.org/10.1016/0016-7037(90)90128-8.

Barbosa, J.P.O., 2004. Geologia Estrutural, Geoquímica, Petrografia e Geocronologia de Granitóides da Região do Igarapé Gelado, Norte da Província Mineral de Carajás. Master's dissertation, Universidade Federal do Pará, Brazil, 112 p.

Barros, C.E.M., Macambira M.J.B., Barbey P., Scheller T., 2004. Dados Isotópicos Pb-Pb em zircão (evaporação) e Sm-Nd do Complexo Granítico Estrela, Província Mineral de Carajás, Brasil: Implicações Petrológicas e Tectônicas. Rev. Bras. de Geociências, 34, 531-538.

Barros, C.E.M., Sardinha A.S., Barbosa, J.P.O., Macambira M.J.B., Barbey P., Boullier A-M., 2009. Structure, Petrology, Geochemistry and Zircon U/Pb and Pb/Pb Geochronology of the Synkinematic Archean (2.7 ga) A-type granites from the carajás metallogenic province, Northern Brazil. The Canadian Mineralogist, 47, 1423-1440.

Bau, M., 2006. Preservation of primary REE patterns without Ce anomaly during dolomitization of Mid-Paleoproterozoic limestone and the potential re-establishment of marine anoxia immediately after the "Great Oxidation Event." South African J. Geol. 109, 81–86. https://doi.org/10.2113/gssajg.109.1-2.81.

Bau, M., Koschinsky, A., 2009. Oxidative scavenging of cerium on hydrous Fe oxide: Evidence from the distribution of rare earth elements and yttrium between Fe oxides and Mn oxides in hydrogenetic ferromanganese crusts. Geochem. J. 43, 37–47. https://doi.org/10.2343/geochemj.1.0005.

Bau, M., Möller, P., Dulski, P., 1997. Yttrium and lanthanides in eastern Mediterranean seawater and their fractionation during redox-cycling. Mar. Chem. 56, 123–131. https://doi.org/10.1016/S0304-4203(96)00091-6.

Beisiegel, V.R., Bernardelli, A.L., Drummond, N.F., Ruff, A.W., Tremaine, J.W., 1973. Geologia e Recursos Naturais da Serra dos Carajás. Rev. Bras. de Geociências, 3, 215-242.

Bekker, A., Berni, G.V., Cabrial, A.R., Davis, D., Karhu, J., 2017. Lomagundi Carbon-Isotope Excursion on the Amazonian Craton. https://doi.org/10.1130/abs/2017am-305433.

Bekker, A., Karhu, J.A., Eriksson, K.A., Kaufman, A.J., 2003. Chemostratigraphy of Paleoproterozoic carbonate successions of the Wyoming Craton: Tectonic forcing of biogeochemical change? Precambrian Res. 120, 279–325. https://doi.org/10.1016/S0301-9268(02)00164-X.

Bekker, A., Karhu, J.A., Kaufman, A.J., 2006. Carbon isotope record for the onset of the Lomagundi carbon isotope excursion in the Great Lakes area, North America. Precambrian Res. 148, 145–180. https://doi.org/10.1016/j.precamres.2006.03.008.

Bello, R.M.S. 1978. Condições de Metamorfismo de Buritirama, Pará e Serra do Navio, Amapá. Master's dissertation, Universidade de São Paulo, Brazil, 154 p.

Benitez-Nelson, C.R., 2000. The biogeochemical cycling of phosphorus in marine systems. Earth Sci. Rev. 51, 109–135. https://doi.org/10.1016/S0012-8252(00)00018-0.

Besser M. L. 2012. Origem e Evolução das Rochas Paleoproterozoicas da Área Rio Bacajá, Pará, Brasil. MS Dissertation, Setor de Geociências, Universidade Federal do Paraná, Curitiba, 136 p.

Bjorlykke, K. O., Griffin, W. L. 1973. Barium Feldspars in Ordovician Sediments, Oslo Region, Norway. SEPM J. Sediment. Res. Vol. 43, 461–465. https://doi.org/10.1306/74d7279d-2b21-11d7-8648000102c1865d.

Bonin, B., 2007. A-type granites and related rocks: Evolution of a concept, problems and prospects. Litohs 97, 1-29.

Bostick, B.C., Fendorf, S., Helz, G.R., 2003. Differential adsorption of molybdate and tetrathiomolybdate on pyrite (FeS2). Environ. Sci. Technol. 37, 285–291. https://doi.org/10.1021/es0257467.

Boyle, E.A., Sclater, F., Edmond, J.M., 1976. On the marine geochemistry of cadmium. Nature 263, 42–44. https://doi.org/10.1038/263042a0.

Bradley, D.C., 2008. Passive margins through earth history, Earth-Science Reviews, 91, 1–26.
Brito Neves, B.B. and Cordani, U.G. 1991. Tectonic evolution of South America during Late Proterozoic. Precambrian Research, 53:23-40.

Brown P.E., Essene E.J., Peacor D.R. 1980. Phase Relations Inferred from Field Data for Mn Pyroxenes and Pyroxenoids. Contrib. Mineral. Petrol. 74:417-425.

Bruland, K.W., 1980. Oceanographic distributions of cadmium, zinc, nickel, and copper in the North Pacific. Earth Planet. Sci. Lett. 47, 176–198. https://doi.org/10.1016/0012-821X(80)90035-7.

Bucher, K. and Grapes, R., 2011. Petrogenesis of Metamorphic Rocks. Berlin: Springer-Verlag, 428 p.

Buick, I.S., 1998. High-δ 13 C Paleoproterozoic carbonates from the Transvaal Supergroup, South Africa. Geology 26, 875–878. https://doi.org/10.1130/0091-7613(1998)026<0875:HCPCFT>2.3.CO;2.

Calvert, S.E., Pedersen, T.F., 1993. Geochemistry of Recent oxic and anoxic marine sediments:

Implications for the geological record. Mar. Geol. 113, 67–88. https://doi.org/10.1016/0025-3227(93)90150-T.

Calvert, S.E., Pedersen, T.F., 1996. Sedimentary geochemistry of manganese: implications for the environment of formation of manganiferous black shales. Econ. Geol. 91, 36–47.
Canfield, D.E., 1998. A new model for Proterozoic ocean chemistry. Nature 396, 450–453. https://doi.org/10.1038/24839.

Canfield, D.E., Ngombi-Pemba, L., Hammarlund, E.U., Bengtson, S., Chaussidon, M., Gauthier-Lafaye, F., Meunier, A., Riboulleau, A., Rollion-Bard, C., Rouxel, O., Asael, D., Pierson-Wickmann, A.C., El Albani, A., 2013. Oxygen dynamics in the aftermath of the Great Oxidation of Earth's atmosphere. Proc. Natl. Acad. Sci. U. S. A. 110, 16736–16741. https://doi.org/10.1073/pnas.1315570110.

Capitani, C. and Peters, T. 1981. The Solvus in the System $MnCO_3$-$CaCO_3$. Contrib. Mineral. Petrol. 76:394-400.

Chang, C., Hu, W.-X., Fu, Q., Cao, J., Wang, X.-L., Wan, Y., Yao, S.-P., 2018. Characteristics and formation processes of (Ba, K, NH 4)-feldspar and cymrite from a lower Cambrian black shale sequence in Anhui Province, South China . Mineral. Mag. 82, 1–21. https://doi.org/10.1180/minmag.2017.081.017.

Chisonga, B.C., Gutzmer, J., Beukes, N.J., Huizenga, J.M., 2012. Nature and origin of the protolith succession to the Paleoproterozoic Serra do Navio manganese deposit, Amapa Province, Brazil. Ore Geology Reviews 47, 59-76.

Condie, K.C. 2016. Earth as an Evolving Planetary System. Elsevier, United Kingdon, pp. 430.

Condie, K.C., O'Neill C., 2010. The Archean-Proterozoic boundary: 500 my of tectonic transition in earth history. American Journal of Science, 310, 775–790.

Coplen, T.B., 1996. New guidelines for reporting stable hydrogen, carbon, and oxygen isotope-ratio data. Geochem. Cosmochim. Acta 60, 3359–3360.

Coplen, T.B., Brand, W.A., Gehre, M., Groning, M., Meijer, H.A., Toman, B., et al. 2006. New guidelines for delta13C measurements. Anal. Chem. 78, 2439–2441.

Cordani U.G., Tassinari C.C.G., Kawashita K. 1984. A Serra dos Carajás como região limítrofe entre províncias tectônicas. Ciências da Terra, 9:6–11.

Cordani U.G., Tassinari C.C.G., Teixeira W., Basei M.A.S., 2000. Crustal evolution of the South América Platform. In: Cordani U.G., Milani E.J., Filho A.T., Campos D.A., (eds.) Tectonic Evolution of South America. Beca, Rio de Janeiro, p. 19-40.

Costa J.B.S., Hasui Y. 1997. O Pré-Cambriano da Região Amazônica no Brasil. In: Simpósio Nacional de Estudos Tectônicos. Pirenópolis, Anais, p. 39-41.

Costa, U.A.P, Paula, R.R., Silva, D.P.B., Barbosa, J.P.O., Silva, C.M.G., Tavares, F.M., Oliveira, J.K.M., Justo, A.P., 2016. Programa Geologia do Brasil. Mapa de Integração Geológico-Geofísica da ARIM Carajás, Escala 1:250.000. Estado do Pará. CPRM.

Dall'Agnol R., Oliveira D.C., Lamarão C.N. 2013. Magmatismo granitoide arqueano e evolução geológica do Subdomínio de Transição da Província Carajás, sudeste do Cráton Amazônico, Brasil. Boletim do Museu Paraense Emílio Goeldi. Ciências Naturais. Belém, v. 8, p. 251-256.

Dall'Agnol, R., Teixeira, N.P., Rämö, O.T., Moura, C.A.V., Macambira, M.J.B., de Oliveira, D.C., 2005. Petrogenesis of the Paleoproterozoic rapakivi A-type granites of the Archean Carajás metallogenic province, Brazil. Lithos 80, 101–129. https://doi.org/10.1016/j.lithos.2004.03.058.

Dasgupta S., Banerjee H., Fukuoka M., Bhattacharya, Roy S. 1990. Petrogenesis of Metamorphosed Manganese Deposits and the Nature of Precursor Sediments. Ore Geology Review, 5:359-384.

Dasgupta S., Roy S., Fukuoka M. 1992. Depositional Models for Manganese Oxide and Carbonate Deposits of Precambrian Sausar Group, India. Econ. Geol. 87, 1412-1418.

Deer W. A., Howie R. A., Zussman J. K. 1992. An introduction to the rock-forming minerals. England, Longman Group, 696 p.

Delinardo, M.A.S., 2014. Metatexitos e diatexitos do Complexo Xingu na região de Canaã dos Carajás: implicações para a evolução mesoarqueana do Domínio Carajás. Master's dissertation, Universidade Estadual de Campinas, Brazil, 119 p.

Derry, L.A., 1991. "The chemical evolution of Precambrian seawater: Evidence from REEs in banded iron formations". L. A. Derry and S. B. Jacobsen (1990) Geochim. Cosmochim. Acta 54, 2965-2977. Geochim. Cosmochim. Acta 55, 1181. https://doi.org/10.1016/0016-7037(91)90174-4.

Dias, G.S., Macambira, M.J.B., Dall'Agnol, R., Soares, A.D.V., and Barros, C.E.M., 1996, Datação de zircões de Sill de metagabro: Comprovação da idade arqueana da Formação Águas Claras, Carajás, Pará [ext. abs.]: Simpósio de Geologia da Amazônia, V, Belém, Sociedade Brasileira de Geologia, Extended Abstracts Bulletin, p. 376–379.

DOCEGEO. Rio Doce Geologia e Mineração S.A., 1988. Revisão litoestratigráfica da Província Mineral de Carajás - litoestratigrafia e principais depósitos minerais. In: 35° Congresso Brasileiro de Geologia, Belém, Anais, pp. 11-54.

Dubinin, A.V., Sval'nov, V.N. 2003. Geochemistry of the Manganese Ore Process in the Ocean: Evidence from Rare Earth Elements. Lithology and Mineral Resources, 38, 91–100.
Dyer, R.C. 1972. Relatório preliminar dos trabalhos de pesquisa de manganês na Serra de Buritirana, municípios de Marabá e Itupiranga, Estado do Para. DNPM, Belém.

Eby, N., 1992. Chemical subdivision of the A-type granitoids:Petrogenetic and tectonic implications. Geology, 20, 641-644.

Fabre, S., Nédélec, A., Poitrasson, F., Strauss, H., Thomazo, C., Nogueira, A., 2011. Iron and sulphur isotopes from the Carajás mining province (Pará, Brazil): Implications for the oxidation of the ocean and the atmosphere across the Archaean-Proterozoic transition. Chem. Geol. 289, 124–139. https://doi.org/10.1016/j.chemgeo.2011.07.019.

Fabre, S., Nédélec, A., Poitrasson, F., Strauss, H., Thomazo, C., Nogueira, A., 2011. Iron and sulphur isotopes from the Carajás mining province (Pará, Brazil): implications for the oxidation of the ocean and the atmosphere across the Archaean–Proterozoic transition. Chemical Geology, 289, 124–139.

Faraco M.T.L., Vale A.G., Santos J.O., Luzardo R., Ferreira A.L., Oliveira M. Marinho P.A.C. 2005. Levantamento geológico da região ao norte da Província Carajás: Noticias Preliminares. In: Simpósio de Geologia da Amazônia. Manaus, Short-Paper, 131-136.

Feio, G.R.L., Dall'Agnol, R., Dantas, E.L., Macambira, M.J.B., Santos, J.O.S., Althoff, F.J., Soares, J.E.B., 2013. Archean granitoid magmatism in the Canaã dos Carajás area: Implications for crustal evolution of the Carajás province, Amazonian craton, Brazil. Precambrian Res. 227, 157–185. https://doi.org/10.1016/j.precamres.2012.04.007.

Feio, G.R.L., Dall'Agnol, R., Dantas, E.L., Macambira, M.J.B., Gomes, A.C.B., Sardinha, A.S., Oliveira, D.C., Santos, R.D., Santos, P.A., 2012. Geochemistry, geochronology, and origin of the Neoarchean Planalto Granite suite, Carajás, Amazonian craton: A-type or hydrated charnockitic granites? Lithos, 151, 57-73.

Ferreira Filho, C.F., Cançado, F., Correa, C., Macambira, E.M.B., Siepierski, L., Junqueira-Brod, T.C., 2007. Mineralizações estratiformes de EGP-Ni associadas a complexos acamadados em Carajás: os exemplos de Luanga e Serra da Onça. In: Rosa-Costa L.T., Klein E.L., Viglio E.P. (Eds.). Contribuições à Geologia da Amazônia. Publitec Gráfica & Editora, Belém, pp. 1-14.

Ferry, J.M. 1976. Metamorphism of Calcareous Sediments in the Waterville-Vassalboro Area, South-Central Maine: Mineral Reactions and Graphical Analysis. American Journal of Science, 276:841-882.

Ferry, J.M. 1983. Regional metamorphism of the Vassalboro Formation, south-central Maine, USA: a case study of the role of fluid in metamorphic petrogenesis. Journal of Geological Society, 140:551-576.

Figueiredo e Silva, R. C., Hagemann, S., Lobato, L. M., Rosiere, C. A., Banks, D. A., Davidson, G. J., Vennemann, T., Hergt, J., 2013. Hydrothermal Fluid Processes and Evolution of the Giant Serra Norte Jaspilite-Hosted Iron Ore Deposits, Carajas Mineral Province, Brazil. Economic Geology and the Bulletin of the Society of Economic Geologists, 108, 739-779.

Föllmi, K.B., 1996. The phosphorus cycle, phosphogenesis and marine phosphate-rich deposits. Earth-Science Rev. 40, 55–124. https://doi.org/10.1016/0012-8252(95)00049-6.

Force, E.R., Cannon, W.F. 1988. A depositional model for shallow–marine manganese deposits around black-shale basins. Econ. Geol., 83, 83–117.

Frazer, J.Z., Fisk, M.B. 1981. Geological factors related to characteristics of sea-floor manganese nodule deposits. Deep-Sea Research, 28, 1533-1551.

Froelich, P.N., Klinkhammer, G.P., Bender, M.L., Luedtke, N.A., Heath, G.R., Cullen, D., Dauphin, P., Hammond, D., Hartman, B., Maynard, V., 1979. Early oxidation of organic matter in pelagic sediments of the eastern equatorial Atlantic: suboxic diagenesis. Geochim. Cosmochim. Acta 43, 1075–1090. https://doi.org/10.1016/0016-7037(79)90095-4.

Frost, B.R., Barnes, C.G., Collins, W.J., Arculus, R.J., Ellis, D.J., Frost, C.D., 2001. A geochemical classification for granitic rocks. Journal of Petrology, 42, 2033–2048.

Galarza, M.A. and Macambira M.J.B., 2002. Geocronologia e Evolução Crustal da Área do Depósito de Cu-Au Gameleira, Província Mineral de Carajás (Pará), Brasil. Revista do Instituto de Geociências –

USP, 2, 143-159.

German, C.R., Elderfield, H., 1990. Application of the Ce anomaly as a paleoredox indicator: The ground rules. Paleoceanography 5, 823–833. https://doi.org/10.1029/PA005i005p00823

Gibbs, A.K., Wirth, K.R., Hirata, W.K., Olszewski, JR., 1986. Age and composition of the Grão Pará Group volcanics, Serra dos Carajás. Rev. Bras. Geociências, 16, 201-211.

Goldsmith, J.R. and Graf, D. L. 1960. Subsolidus Relations in the System CaCO3-MgCO3-MnCO3. The Journal of Geology, 68:324-335.

Gomes C.B., Cordani U.G., Basei M.A.S. 1975. Radiometric ages from the Serra dos Carajás area, Northern Brazil. Geological Society of America Bulletin, 86:939-942.

Grainger C.J., Groves D.I., Tallarico F.H.B., Fletcher I.R. 2008. Metallogenesis of the Carajás Mineral Province, Southern Amazon Craton, Brazil: Varying styles of Archean through Paleoproterozoic to Neoproterozoic base- and precious-metal mineralisation. Ore Geology Reviews, 33:451-489.

Grenholm, M., 2019. The global tectonic context of the ca. 2.27-1.96 Ga Birimian Orogen – Insights from comparative studies, with implications for supercontinent cycles. Earth-Science Reviews, 193, 260-298.

Hasui Y. and Almeida F.F.M. 1985. The Central Brazil Shield Reviewed. Episodes, 8:29–37.

Helz, G.R., Miller, C.V., Charnock, J.M., Mosselmans, J.L.W., Pattrick, R.A.D., Garner, C.D., Vaughan, D.J., 1996. Mechanisms of molybdenum removal from the sea and its concentration in black shales: EXAFS evidences. Geochim. Cosmochim. Acta 60, 3631–3642.

Herz N., Hasui Y., Costa J.B.S., Matta M.A.S. 1989. The Araguaia Fold Belt, Brazil: a reactived Brasiliano/Pan-African Cycle (550Ma) geosuture. Precambrian Research, 42:371-386.

Hirata, W.K., et al. 1982. Geologia regional da Província Mineral de Carajás. In: 1° Simpósio de Geologia da Amazônia, Anais, pp. 100-110.

Hirdes, W. and Davis, D.W., 1998. First U-Pb zircon age of extrusive volcanism in the Birimian Super-group of Ghana/West Africa. Journal of African Earth Sciences, 27, 291-294.

Hood, A. v. S., Planavsky, N.J., Wallace, M.W., Wang, X., 2018. The effects of diagenesis on geochemical paleoredox proxies in sedimentary carbonates. Geochim. Cosmochim. Acta 232, 265–287. https://doi.org/10.1016/j.gca.2018.04.022.

Hoskin, P.W.O., Schaltegger, U., 2003. The Composition of Zircon and Igneous and Metamorphic Petrogenesis. Zircon 53, 27–62.

John, S.G., Conway, T.M., 2014. A role for scavenging in the marine biogeochemical cycling of zinc and zinc isotopes. Earth Planet. Sci. Lett. 394, 159–167. https://doi.org/10.1016/j.epsl.2014.02.053

Johnson, J. E., Webb, S. M., MA, C. and Fischer, W. W.2016. Manganese mineralogy and diagenesis in the sedimentary rock record. Geochim. Cosmochim. Acta, 173, 210–231.

Jorge João, X. da S., Vale, A.G., Lobato, T. de A.M., 1987. Programa Levantamentos Geológicos Básicos do Brasil. Texto Explicativo. Escala 1:250.000, Folha SA.22-Y-D, Altamira, Estado do Pará. Texto. DNPM/CPRM, 31 p.

Karhu, J.A. and Holland, H.D., 1996. Carbon isotopes and the rise of atmospheric oxygen. Geology 24, 867–870. https://doi.org/10.1130/00917613(1996)024<0867:CIATRO>2.3.CO;2.

Klein C. & Duthow B. (eds.) 2007. Manual of Mineral Science. Michigan, Willey, 716 p.

Kleinschrot, D., Klemd, Reiner., Brocker, M., Okrusch, M., Franz, L., Schmidt K., 1993. The Nsuta Manganese deposit, Ghana: Geological setting, ore-forming process and metamorphic evolution. Z. Anfew. Geol., 39, 48-50.

Kobayashi H. 1977. Kanoite (Mn2+, Mg)2 [Si2O6], a New Clinopyroxene in the Metamorphic Rock From Tatehira, Oshima Peninsula, Hokkaido, Japan. Journal of Geological Society of Japan, 83:537-542.

Krauskopf K. B. (1957) Separation of manganese from iron in sedimentary processes. Geochim. Cosmochim. Acta 12, 61–84.

Kretz, R. and Garrett, D. 1980. Occurence, Mineral Chemistry, and Metamorphism of Precambrian Carbonate Rocks in a Portion of Grenille Province. Journal of Petrology, 21:573-620.

Kuleshov, V.N., 2011. Manganese Deposits: Communication 2. Major Epochs and Phases of Manganese Accumulation in the Earth's History. Lithology and Mineral Resources, 46, 546-565.

Kuleshov, V.N., 2017. Isotope Geochemistry: The Origin and Formation of Manganese Rocks and Ores, Elsevier, India.

Kurian, S., Nath, B.N., Ramaswamy, V., Naman, D., Gnaneshwar Rao, T., Kamesh Raju, K.A., Selvaraj, K., Chen, C.T.A., 2008. Possible detrital, diagenetic and hydrothermal sources for Holocene sediments of the Andaman backarc basin. Mar. Geol. 247, 178–193. https://doi.org/10.1016/j.margeo.2007.09.006.

Lana, C., Farina, F., Gerdes A., Alkmim A., Gonçalves, G.O., Jardim, A.C., 2017. Characterization of zircon reference materials via high precision U-Pb LA-MC-ICP-MS. Journal of Analytical Atomic Spectrometry, 10, 1-13.

Lindenmayer, Z.G., 1990. Salobo Sequence, Carajás, Brazil: geology, geochemistry and metamorphism. Ph.D. thesis, University of Western Ontário, Canada, 407 p.

Lindenmayer, Z.G., Fyfe, W.S., Bocalon, V.L.S., 1994. Nota preliminar sobre as intrusões granitóides do depósito de cobre do Salobo, Carajás. Acta Geológica Leopoldensia, 17, 153–184.

Liu, X.M., Hardisty, D.S., Lyons, T.W., Swart, P.K., 2019. Evaluating the fidelity of the cerium paleoredox tracer during variable carbonate diagenesis on the Great Bahamas Bank. Geochim. Cosmochim. Acta 248, 25–42. https://doi.org/10.1016/j.gca.2018.12.028.

Ludwig, K.R., 2008. User's Manual for Isoplot 3.6. A Geochronological Toolkit for Microsoft Excel. Special Publication, No. 4. Berkeley Geochronologic Center, Berkeley, USA.

Lyons, T.W., Reinhard, C.T., Planavsky, N.J., 2014. The rise of oxygen in Earth's early ocean and atmosphere. Nature 506, 307–315. https://doi.org/10.1038/nature13068.

Macambira J.B 2003. O ambiente deposicional da Formação Carajás e uma proposta de modelo evolutivo para a Bacia Grão Pará. PhD Thesis, Universidade Estadual de Campinas, 217 p.

Macambira J.B., Macambira M.J.B., Scheller T., Gomes A.C.B. 1996. Geocronologia Pb/Pb e tipologia de zircões de rochas vulcânicas da Formação Carajás - Pará: Indicador da idade dos BIFs. In: 39° Congresso Brasileiro de Geologia. Salvador, Anais, v. 6, p. 516-518.

Macambira M.J.B., Pinheiro R.V.L., Armstrong R.A., 2007. A fronteira Arqueano-Paleoproterozóico no SE do Cráton Amazônico; abrupta no tempo, suave na tectônica? In: Simpósio de Geologia da Amazônia, V. 10, Anais, p. 105-108.

Macambira, M.J.B., Silva, D.C.C., Barros, C.E.M., Scheller, T., 2003. New isotope evidences confirming the existence of a Paleoproterozoic terrain in the region at north of the Carajás Mineral Province. In: 4° South American Symposium on Isotope Geology, Salvador, Anais, pp. 205-208.

Macambira, M.J.B., Silva, D.C.C., Vasquez, M.L., Barros, C.E.M., 2004. Investigação do Limite Arqueano-Paleoproterozóico ao Norte da Província de Carajás, Amazônia Oriental. In: 42° Congresso Brasileiro de Geologia, Anais, CD-ROM.

Macambira, M.J.B., Vasquez, M.L., Silva, D.C.C. da, Galarza, M.A., Barros, C.E. de M., Camelo, J. de F., 2009. Crustal growth of the central-eastern Paleoproterozoic domain, SW Amazonian craton: Juvenile accretion vs. reworking. J. South Am. Earth Sci. 27, 235–246. https://doi.org/10.1016/j.jsames.2009.02.001.

Machado, N., Lindenmayer, Z., Krogh, T.E., Lindenmayer, D., 1991. U-Pb geochronology of Archean magmatism and basement reactivation in the Carajás area, Amazon shield, Brazil. Precambrian Res. 49, 329–354. https://doi.org/10.1016/0301-9268(91)90040-H.

Maheshwari, A., Sial, A.N., Gaucher, C., Bossi, J., Bekker, A., Ferreira, V.P., Romano, A.W., 2010. Global nature of the Paleoproterozoic Lomagundi carbon isotope excursion: A review of occurrences in Brazil, India, and Uruguay. Precambrian Res. 182, 274–299. https://doi.org/10.1016/j.precamres.2010.06.017.

Maniar, P.D. and Piccoli, P.M., 1989. Tectonic discrimination of granitoids. Geol. Soc. Am. Bull., 101, 635-643.

Marangoanha, B., Oliveira, D.C. de, Oliveira, V.E.S. de, Galarza, M.A., Lamarão, C.N., 2019. Neoarchean A-type granitoids from Carajás province (Brazil): New insights from geochemistry, geochronology and microstructural analysis. Precambrian Res. 324, 86–108. https://doi.org/10.1016/j.precamres.2019.01.010.

Martins P.L.G. 2017. Petrologia e Geoquímica dos Basaltos da Formação Parauapebas: Implicações para O Ambiente Tectônico Da Bacia Grão Pará, Província De Carajás. MS Dissertation, Instituto de Geociências, Universidade de Brasília, Brasília, 93 p.

Martins, P.L.G., Toledo, C.L.B., Silva, A.M., Chemale, F., Santos, J.O.S., Assis, L.M., 2017. Neoarchean magmatism in the southeastern Amazonian Craton, Brazil: Petrography, geochemistry and

tectonic significance of basalts from the Carajás Basin. Precambrian Res. 302, 340–357. https://doi.org/10.1016/j.precamres.2017.10.013.

Matthews, A., Kolodny, Y., 1978. Oxygen isotope fractionation in decarbonation metamorphism: the Mottled Zone event. Earth Planet. Sci. Lett. 39, 179–192. https://doi.org/10.1016/0012-821X(78)90154-1.

Maynard J.B. 2010. The Chemistry of Manganese Ores through Time: A Signal of Increasing Diversity of Earth-Surface Environments. Economic Geology, 105:535–552.

Maynard, J.B. 2014. Manganiferous Sediments, Rocks, and Ores. Treatise on Geochemistry, Heinrich D. Holland & Karl K. Turekian (Eds.), Vol. 9, Sediments, Diagenesis and Sedimentary Rocks, 327-349.

McSwiggen, P.L., Morey, G.B. and Cleland, J.M. 1994. Occurrence and genetic-implications of hyalophane in manganese-rich iron-formation, Cuyuna-Iron-Range, Minnesota, USA. Mineralogical Magazine, 58, 387–399.

Meireles E.M., Hirata H.K., Amaral A.F., Medeiros Filho C.A., Gato W.C. 1984. Geologia das folhas Carajás e Rio Verde, Província Mineral dos Carajás, estado do Pará. In: 33° Congresso Brasileiro de Geologia. Rio de Janeiro, Anais, V.5, p. 2164-2170.

Melezhik, V.A., Roberts, D., Fallick, A.E., Gorokhov, I.M., Kusnetzov, A.B., 2005. Geochemical preservation potential of high-grade calcite marble versus dolomite marble: Implication for isotope chemostratigraphy. Chem. Geol. 216, 203–224. https://doi.org/10.1016/j.chemgeo.2004.11.020.

Melo, G.H.C., Monteiro, L.V.S., Xavier, R.P., Moreto, C.P.N., Santiago, E.B.S., Dufrane, S.A., Aires, B., Santos, A.F.F., 2016. Temporal evolution of the giant Salobo IOCG deposit, Carajás Province (Brazil): Constraints from paragenesis of hydrothermal alteration and U-Pb geochronology: Mineralium Deposita 52, 709–732.

Moreto, C.P.N., Monteiro, L.V.S., Xavier, R.P., Creaser, R.A., DuFrane, S.A., Melo, G.H.C., Delinardo da Silva, M.A., Tassinari, C.C.G., Sato, K., 2015. Timing of multiple hydrothermal events in the iron oxide–copper–gold deposits of the Southern Copper Belt, Carajás Province, Brazil. Miner. Depos. 50, 517–546. https://doi.org/10.1007/s00126-014-0549-9.

Moreto, C.P.N., Monteiro, L.V.S., Xavier, R.P., DuFrane, S.A., 2015. Neoarchean and Paleoproterozoic Iron Oxide-Copper-Gold Events at the Sossego Deposit, Carajás Province, Brazil: Re-Os and U-Pb Geochronological Evidence. Economic Geology, 110, 809-835.

Morford, J.L., Emerson, S., 1999. The geochemistry of redox sensitive trace metals in sediments. Geochim. Cosmochim. Acta 63, 1735–1750. https://doi.org/10.1016/S0016-7037(99)00126-X.

Morford, J.L., Emerson, S.R., Breckel, E.J., Kim, S.H., 2005. Diagenesis of oxyanions (V, U, Re, and Mo) in pore waters and sediments from a continental margin. Geochim. Cosmochim. Acta 69, 5021–5032. https://doi.org/10.1016/j.gca.2005.05.015.

Morimoto C.N. 1988. Nomenclature of Pyroxenes. American Mineralogist, 63:1137-1142.

Mougeot, R., Respaut, J.P., Briqueu, L., Ledru, P., Milesi, J.P., Macambira, M.J.B., Huhn, S.B., 1996. Geochronological constrains for the age of the Águas Claras Formation (Carajás province, Pará, Brazil).

In: 35° Congresso Brasileiro de Geologia, Salvador, Anais, pp. 579–581.

Moura C.A.V. & Souza S.H.P. 1996. Síntese dos dados Geocronológicos das rochas do Embasamento do Cinturão Araguaia e suas Implicações Estratigráficas. In: 39° Congresso Brasileiro de Geologia, Salvador, Anais, p. 31-34.

Moura C.A.V. and Gaudette H. 1993. Evidence of Brasiliano/ Panafrican deformation in the Araguaia Belt: Implication for Gondwana evolution. Revista Brasileira de Geociências, 23:117-123.

Mucci, A., 2004. The behavior of mixed Ca-Mn carbonates in water and seawater: Controls of manganese concentrations in marine porewaters. Aquat. Geochemistry 10, 139–169. https://doi.org/10.1023/B:AQUA.0000038958.56221.b4.

Mücke, A., Dzigbodi-Adjimah, K., Annor, A., 1999. Mineralogy, petrography, geochemistry and genesis the of the Paleoproterozoic Birimian manganese-formation of Nsuta/Ghana. Mineralium Deposita, 34, 297-311.

Mücke, A., Olobaniyi, S.B., 2017. Mineralogical, Geochemical and Genetic Investigations of the Algoma-type Manganese-Formation of Nsuta, Ghana: New Insight from Subsurface Samples. Journal of Mining and Geology, 53, 117–142.

Nagell, R.H., 1962. Geology of The Serra do Navio Manganese District, Brazil. Economic Geology, 57, 481-498.

Nascimento, R.S.C., Sial, A.N., Pimentel, M.M., 2007. C- and Sr-isotope systematics applied to Neoproterozoic marbles of the Seridó belt, northeastern Brazil. Chem. Geol. 237, 191–210. https://doi.org/10.1016/j.chemgeo.2006.06.017.

Nayak, B.R., Mohapatra, B.K., 1998. Mn-Piroxenoids from Gangpur Group of Rocks, Orissa, India. J. Min. Petr. Econ. Geol., 93, 380-388.

Nielsen, R.J. and Beard, J.S., 2000. Magnetite-melt HFSE partitioning. Chemical Geology, 164, 21-34.

Nogueira, A.F.C., 1995. Análise faciológica e aspectos estruturais da Formação Águas Claras, região central da Serra dos Carajás-PA. Marster's dissertation, Universidade Federal do Pará, Brazil, 167 p.

Nyame, F. K., 2001. Petrological significance of manganese carbonate inclusions in spessartine garnet and relation to the stability of spessartine in metamorphosed manganese-rich rocks. Contrib. to Mineral. Petrol. 141, 733–746. https://doi.org/10.1007/s004100100257.

Nyame, F. K., Beukes, N.J. 2006.The Genetic Significance Of Carbon And Oxygen Isotopic Variations In Mn-Bearing Carbonates From The Palaeo-Proterozoic (~2.2ga) Nsuta Deposit In The Birimian Of Ghana. Carbonates and Evaporites, 21, 21-32.

Okita P.M., Maynard J.B., Spiker E.C., Force E.R. 1988. Isotopic evidence for organic matter oxidation by manganese reduction in the formation of stratiform manganese carbonate ore. Geochimica et Cosmochimica Acta, 52:2679-2685.

Okita, P.M., Shanks, W.C., 1992. Origin of stratiform sediment-hosted manganese carbonate ore deposits: Examples from Molango, Mexico, and TaoJiang, China. Chem. Geol. 99, 139–163.

https://doi.org/10.1016/0009-2541(92)90036-5.

Oliveira J.R. 1994. Programa Levantamentos Geológicos Básicos do Brasil (PLGB), Carta Geológica, Carta Metalogenética, Escala 1:250.000, Folha SB.22-X-C, Serra Pelada, Estado do Pará. DNPM/CPRM, 220 p.

Oliveira, J.R., Neto, C.S.S., Costa, E.J.S., 1994. Programa Levantamentos Geológicos Básicos do Brasil (PLGB), Carta Geológica, Carta Metalogenética, Escala 1:250.000, Folha SB.22-X-C, Serra Pelada, Estado do Pará. DNPM/CPRM, 220 p.

Oliveira, R.G., Teixeira, N.A., Costa, I.S.L., Tavares, F.M., Domingos, N.R.R. 2017. Levantamento Aerogravimétrico Carajás – Contribuição à Tectônica e Metalogenia da Porção Leste do Cráton Amazonas. In: 15° Simpósio de Geologia da Amazônia, Belém.

Ordóñez-Calderón, J.C., Polat, A., Fryer, B.J., Gagnon, J.E., Raith, J.G., Appel, P.W.U., 2008. Evidence for HFSE and REE mobility during calc-silicate metasomatism, Mesoarchean (~3075 Ma) Ivisaartoq greenstone belt, southern West Greenland. Precambrian Res. 161, 317–340. https://doi.org/10.1016/j.precamres.2007.09.004.

Peacor D.R., Essene E.J., Brown P.E., Winter G.A. 1978. The Crystal Chemistry and Petrogenesis of a magnesian rhodonite. American Mineralogist, 63:1137-1142.

Pearce, J.A., Harris, B.W.N, Tindle, A.G., 1984. Trace Element Discrimination Diagrams for the Tectonic Interpretation of Granitic Rocks. Journal of Petrology 25, 956-983.

Pereira, R.M.P., 2009. Geologia da Região Sul da Serra Norte e Características do Minério de Ferro do Depósito N8, Província Mineral Carajás. Marster's dissertation, Universidade Federal de Minas Gerais, Brazil, 131 p.

Peters T.J., Valarelli J.V., Coutinho J.M.V., 1977. The manganese deposits of Buritirama (Pará, Brazil). Schweiz. Mineral. Petrogr. Mitt. 57:313-327.

Pidgeon, R.T., MacAmbira, M.J.B., Lafon, J.M., 2000. Th-U-Pb isotopic systems and internal structures of complex zircons from an enderbite from the Pium Complex, Carajas Province, Brazil: Evidence for the ages of granulite facies metamorphism and the protolith of the enderbite. Chem. Geol. 166, 159–171. https://doi.org/10.1016/S0009-2541(99)00190-4.

Pinheiro R.V.L. 1997. Reativation history of the Carajás and Cinzento strike-slip systems, Amazon, Brazil. PhD Thesis, University of Durham, Durham, p. 408.

Pinheiro V.L. and Holdsworth R.E. 2000. Evolução Tectonoestratigráfica dos Sistemas Transcorrentes Carajás e Cinzento, Cinturão Itacaiúnas, na Borda Leste do Cráton Amazônico, Pará. Revista Brasileira de Geociências, 30:597-606.

Polgari, M., Okita, P.M., Hein, J.R., 1991. Stable isotope evidence for the origin of the Úrkút manganese ore deposit, Hungary. Journal of Sedimentary Petrology, 61: 384–393.

Ramsay J.G. and Huber M.I. 1987. The Techniques of Modern Structural Geology, Vol. 2: Folds and Fractures. Pergamon Press, London.

Reis, P.M., 2017. A Sequência Meta-vulcanossedimentar do Circular, Carajás (PA): Geologia, Petrografia, Litoquímica e Geocronologia. Ph.D. thesis, Universidade de São Paulo, Brazil, 99 p.

Réquia, K., Stein, H., Fontboté, L., Chiaradia, M., 2003. Re-Os and Pb-Pb geochronology of the Archean Salobo iron oxide copper-gold deposit, Carajás Mineral Province, northern Brazil. Miner. Depos., 38, 727–738.

Ricci P.S.F., Costa E.J.S., Faria C.A.S., Oliveira J. R. 2003. The reanalysed Carajás Block is interposed between the Bacajá (the crustal reworking "lost link" now being predicted) and Rio Maria Archean terranes-Guaporé Craton. In: Simpósio de Geologia da Amazônia. Manaus, Short-Paper, 392-398.

Ricci, P.S.F 2006a. Unprecedented recognition of granulitefacies volcano-sedimentary sequences in the Bacajá High-Grade Block (Pará): major strips and disconnected remainders. In: 43° Congresso Brasileiro de Geologia, Aracajú, CD-ROM..

Ricci, P.S.F., 2006b. Mineralogically bizarre charnockitoids of the Bacajá High-Grade Block (Pará): discharnockitized and re-emplaced plutons mistakenly confused with granitoids crystallised at shallower crustal levels. In: 9° Simpósio de Geologia da Amazônia, Belém, CD-ROM.

Ricci, P.S.F., Costa, E.J.S., 2004. Orogenic charnockitoids previously mapped as granulitic basement of the Bacajá Terrane (Eastern-Central Pará). In: 42° Congresso Brasileiro de Geologia, Araxá, CD-ROM.

Rogers, J.J.W., 1996. A history of continents in the past three billion years. J. Geol., 104, 91–107.

Rosen O., Desmons J., Fettes D. 2007. Metacarbonate and related rocks. A systematic nomenclature for metamorphic rocks: 7 Metacarbonate and related rocks. A proposal on behalf of the IUGS Subcommission on the Systematics of Metamorphic Rocks. Recommendations. IUGS Subcommission on the Systematics of Metamorphic Rocks.

Roshan, S., Wu, J., & DeVries, T. 2017. Controls on the cadmium-phosphate relationship in the tropical South Pacific. Global Biogeochemical Cycles, 31, 1516–1527. https://doi.org/10.1002/2016GB005556. Roy S. 1972. Metamorphism of Sedimentary Manganese Deposits. Acta Mineralogica-Petrographica, 20:325-336.

Roy, S., 2006. Sedimentary manganese metallogenesis in response to the evolution of system earth. Earth Sci. Rev. 77, 273–305.

Rubatto, D., 2002. Zircon trace element geochemistry: partitioning with garnet and the link between U-Pb ages and metamorphism. Chemical Geology, 184, 123-138.

Salgado, S.S., Caxito, F.D.A., Queiroga, G.N., De Castro, M.P., 2019a. Stratigraphy, petrography and tectonics of the manganese-bearing Buritirama Formation, Northern Carajás Domain, Amazon Craton. Brazilian J. Geol. 49, 1–15. https://doi.org/10.1590/2317-4889201920180106.

Salgado, S.S., de Andrade Caxito, F., Figueiredo e Silva, R.C., Lana, C., 2019b. Provenance of the Buritirama Formation reveals the Paleoproterozoic assembly of the Bacajá and Carajás blocks (Amazon Craton) and the chronocorrelation of Mn-deposits in the Transamazonian/Birimian system of northern Brazil/West Africa. J. South Am. Earth Sci. 96, 1–14. https://doi.org/10.1016/j.jsames.2019.102364.

Sanford R. F. 1980. Textures and Mechanisms of Metamorphic Reactions in the Cockeysville Marble

near Texas, Maryland. American Mineralogist, 65:654-669.

Santos J.O.S, Hartmann L.A., Gaudette H.E., Groves D.I., McNaughton N.J., Fletcher I.R. 2000. A new understanding of the provinces of the Amazon Craton based on integration of field mapping and U-Pb and Sm-Nd geochronology. Gondwana Research, 3:453-488.

Santos, J.O.S., 2003. Geotectônica dos Escudos da Guiana e Brasil Central In: Bizzi, L.A., Schobbenhaus, C., Vidotti, R.M., Gonçalves, J.H. (Eds.), Geologia, tectônica e recursos minerais do Brasil. Texto, mapas e SIG. CPRM-Serviço Geológico do Brasil, pp. 169–226.

Sardinha, A.S., Barros, C.E.M., Krymsky, R., 2006. Geology, Geochemistry and U–Pb Geochronology of the Archean (2.74 Ga) Serra do Rabo Granite Stocks, Carajás Metallogenic Province, Northern Brazil. Journal of South American Earth Sciences, 20, 327-339.

Schidlowski, M., Eichmann, R., Junge, C.E., 1976. Carbon isotope geochemistry of the Precambrian Lomagundi carbonate province, Rhodesia. Geochim. Cosmochim. Acta 40, 449–455. https://doi.org/10.1016/0016-7037(76)90010-7.

Schreyer, W., Bernhardt, H.-J., Medenbach, O., 1992. Petrologic evidence for a rhodochrosite precursor of spessartine in coticules of the Venn-Stavelot Massif, Belgium. Mineral. Mag. 56, 527–532. https://doi.org/10.1180/minmag.1992.056.385.08.

Semblano F.R.D., Pereira N.C.S., Vasquez M.L., Macambira M.J.B. 2016. Novos dados geológicos e isotópicos para o Domínio Iriri-Xingu, Província Amazônia Central: implicações para a idade do Grupo Iriri. Revista do Instituto de Geociências – USP, 16:19-38.

Shand, S.J., 1947. Eruptive Rocks, thirded.Hafner Publishing Company, NewYork, pp. 488.

Sharp, Z.D., Papike, J.J., Durakiewicz, T., 2003. The effect of thermal decarbonation on stable isotope compositions of carbonates. Am. Mineral. 88, 87–92. https://doi.org/10.2138/am-2003-0111.
Shields, G., Veizer, J., 2002. Precambrian marine carbonate isotope database: Version 1.1. Geochemistry, Geophys. Geosystems 3. https://doi.org/10.1029/2001GC000266.

Silva G.G., Lima J.J.C., Andrade A.R.F., Issler R.S., Guimarães G. 1974. Folha SB. 22 - Araguaia e parte da folha SC. 22 - Tocantins: geologia, geomorfologia, solos, vegetação e uso potencial da terra. DNPM, Rio de Janeiro, p. 143.

Siqueira, J.B., 1996. Aspectos lito-estruturais e mineralizações do Depósito Salobo 3A (Serra dos Carajás – PA). Ph.D. thesis, Universidade Federal do Pará, Brazil, 157 p.

Souza, S.R.B., Macambira, M.J.B., Sheller, T., 1996. Novos dados geocronológicos para os granitos deformados do Rio Itacaiúnas (Serra dos Carajás, PA); implicações estratigráficas. In: 5° Simpósio de Geologia da Amazônia, Belém, Anais, pp. 380-383.

Suita M.T.F. 1988. Geologia da área Luanga com ênfase na petrologia do complexo básico-ultrabásico Luanga e depósitos de cromita associados, Pará. MS Dissertation, Instituto de Geociências, Universidade de Brasília, Brasília, 320 p.

Sun, S.-S., McDonough, W.F., 1989. Chemical and isotopic systematics of oceanic basalts: implications for mantle composition and processes. In: Saunders, A.D., Norris, M.J. (Eds.), Magmatism in the Ocean

Basins, Geological Society Special Publication, London, vol. 42, pp. 313-345.

Tallarico, F.H.B., Figueiredo, B.R., Groves, D.I., Kositcin, N., McNaughton, N.J., Fletcher, I.R., Rego, J.L., 2005. Geology and SHRIMP U-Pb geochronology of the Igarapé Bahia deposit, Carajás copper-gold belt, Brazil: An Archean (2.57 Ga) example of Iron-Oxide Cu-Au-(U-REE) mineralization. Econ. Geol. 100, 7–28. https://doi.org/10.2113/100.1.0007.

Tassinari C.C.G. and Macambira M.J.B. 1999. Geochronological provinces of the Amazonian Craton. Episodes, 22:174–182.

Tassinari C.C.G. and Macambira M.J.B. 2004. A evolução tectônica do Cráton Amazônico. In: Mantesso-Neto V., Bartorelli A., Carneiro C.D.R., Brito Neves B.B. (eds.), Geologia do continente Sul-americano: evolução da obra de Fernando Flávio Marques de Almeida. Beca, São Paulo, p. 471-485.

Tavares F.M. 2015. Evolução Geotectônica do Nordeste da Província Carajás. PhD Thesis, Universidade Federal do Rio de Janeiro, Rio de Janeiro, 115 p.

Tavares, F.M. and Silva, C.M.G., 2013. Folha, SB.22-X-C-VI, Serra Pelada. Mapa Geológico. CPRM.

Tavares, F.M., Trouw, R.A.J., da Silva, C.M.G., Justo, A.P., Oliveira, J.K.M., 2018. The multistage tectonic evolution of the northeastern Carajás Province, Amazonian Craton, Brazil: Revealing complex structural patterns. J. South Am. Earth Sci. 88, 238–252. https://doi.org/10.1016/j.jsames.2018.08.024.

Taylor, S.R., McLennan, S., 1985. The Continental Crust: Its Composition and Evolution. Blackwell, Oxford.

Thompson, A.B., 1975. Calc-silicate diffusion zones between marble and pelitic schist. J. Petrol. 16, 314–346. https://doi.org/10.1093/petrology/16.1.314.

Toledo, P.I.F., Moreto, C.P.N., Xavier, R.P., Gao, J., de Matos, J.H. da S.N., de Melo, G.H.C., 2019. Multistage evolution of the Neoarchean (ca. 2.7 Ga) Igarapé cinzento (GT-46) iron oxide copper-gold deposit, Cinzento shear zone, Carajás Province, Brazil. Econ. Geol. 114, 1–34. https://doi.org/10.5382/econgeo.2019.4617.

Trendall, A.F., Basei, M.A.S., De Laeter, J.R., Nelson, D.R., 1998. SHRIMP zircon U-Pb constraints on the age of the Carajás formation, Grão Pará Group, Amazon Craton. Journal of South American Earth Sciences, 11, 265-277.

Tribovillard, N., Algeo, T.J., Lyons, T., Riboulleau, A., 2006. Trace metals as paleoredox and paleoproductivity proxies: An update. Chem. Geol. 232, 12–32. https://doi.org/10.1016/j.chemgeo.2006.02.012.

Valarelli J.V., Coutinho J.M.V., Bello R.M.S., 1978. Metamorfismo de Buritirama, Pará. In: 30° Congresso Brasileiro de Geologia. Recife, Anais, V.30, p. 1357-1363.

Valley, J.W., 1986. Stable isotope geochemistry of metamorphic rocks. In: Valley JW, Taylor HP, O'Neil JR (Eds) Stable Isotopes in high temperature geological processes (Reviews in mineralogy, vol 16) Mineral Soc Am, Washington, DC, pp 445–490.

Vasquez M.L. 2006. Geocronologia em zircão, monazita e granada e isotópos de Nd das associações

litológicas da porção oeste do domínio Bacajá: evolução crustal da porção meridional da província Maroni-itacaiúnas – sudeste do cráton amazônico. PhD Thesis, Centro de Geociências, Universidade Federal do Pará, Belém, 212 p.

Vasquez, M.L. and Rosa-Costa L.T., 2008. Geologia e Recursos Minerais do Estado do Pará: Sistema de Informações Geográficas – SIG: texto explicativo dos mapas Geológico e Tectônico e de Recursos Minerais do Estado do Pará. Escala 1:1.000.000. Belém: CPRM, 328 p.

Vasquez, M.L., Macambira, M.J.B., Armstrong, R.A., 2008. Zircon geochronology of granitoids from the western Bacajá domain, southeastern Amazonian craton, Brazil: neoarchean to Orosirian evolution. Precambrian Research, 161, 279-302.

Von Damm, K., 1990. Seafloor Hydrothermal Activity: Black Smoker Chemistry And Chimneys. Annu. Rev. Earth Planet. Sci. 18, 173–204. https://doi.org/10.1146/annurev.earth.18.1.173.

Whalen, J.B., Currie, K.L., Chappell, B.W., 1987. A-type granites: Ceochemical characteristics, discrimination and petrogenesis. Contribution to Mineralogy and Petrology, 95, 407-419.

Whitney, D.L. and Evans, B.W. 2010. Abbreviations for names of rock-forming minerals. American Mineralogist, 95:185-187.

Winter, C.J., 1994. Geology and base-metal mineralisation associated with Archaean iron formation in the Pojuca Corpo Quatro Deposit, Carajás, Brazil. Ph.D thesis, University of Southampton, United Kingdom, 173 p.

Wirth, K.R., Gibbs, A.K., Olszewski, W., 1986. U-Pb zircon ages of the Grão-Pará Group and Serra dos Carajás Granite. Rev. Bras. Geociências. https://doi.org/10.25249/0375-7536.1986195200.

Xavier, R.P., Monteiro, L.V.S., Moreto, C.P., Pestilho, A.L.S., Melo, G.H.C., Delinardo, M.A.S., Aires, B., Ribeiro, C., Silva, F.H.F., 2012. The Iron Oxide Copper-Gold Systems of the Carajás Mineral Province, Brazil. Econ. Geol., Special Publication 16, 1-22.

Yardley W.D.B. 1989. An Introduction to Metamorphic Rocks. United Kingdom, Harlow, 248 p.

Zheng, Y., Anderson, R.F., Van Geen, A., Fleisher, M.Q., 2002a. Preservation of particulate non-lithogenic uranium in marine sediments. Geochim. Cosmochim. Acta 66, 3085–3092. https://doi.org/10.1016/S0016-7037(01)00632-9.

Zheng, Y., Anderson, R.F., Van Geen, A., Fleisher, M.Q., 2002b. Remobilization of authigenic uranium in marine sediments by bioturbation. Geochim. Cosmochim. Acta 66, 1759–1772. https://doi.org/10.1016/s0016-7037(01)00886-9.

ANEXOS (APPENDICES)

Anexo 1 (Appendix 1) – Mineral Chemistry

1A - Representative microprobe analyses of carbonates from Buritirama Formation.

1B - Representative microprobe analyses of pyroxene from Buritirama Formation.

1C - Representative microprobe analyses of garnets from Buritirama Formation.

1D - Representative microprobe analyses of feldspar from Buritirama Formation.

1E - Representative microprobe analyses of pyroxenoids from Buritirama Formation.

1F - Representative microprobe analyses of amphiboles from Buritirama Formation.

1G - Representative microprobe analyses of micas from Buritirama Formation.

Anexo 2 (Appendix 2) – Litogeochemistry data from Buritirama Metagranite.

Anexo 3 (Appendix 3) – U/Pb isotopes dataset of Buritirama Formation
3A - U/Pb Isotopic data from the sample BUR-1 (Buritirama Metagranite).

3B - U/Pb Isotopic data from the sample BUR-3 (Quartzite – Lower Unit).

3C - U/Pb Isotopic data from the sample BUR-2 (Quartzite – Upper Unit).

Anexo 4 (Appendix 4) – Mineral Chemistry
4A – Representative microprobe analyses of carbonates from Buritirama Formation.

4B – Representative microprobe analyses of pyroxenoids from Buritirama Formation.

4C – Representative microprobe analyses of garnets from Buritirama Formation.

4D - Representative microprobe analyses of feldspar from Buritirama Formation.

Anexo 5 (Appendix 5) – Lithogeochemistry of Carbonate-bearing Rocks of the Buritirama Formation

Anexo 6 (Appendix 6) – Isotopic analysis of Mn-Carbonate Rocks and Dolomitic Marbles of Buritirama Formation.

1A – Representative microprobe analyses of carbonates from Buritirama Formation

Sample no.	SS-010	SS-010	SS-010	SS-010	SS-010	SS-010	SS-010	SS-010	SS-010	SS-010	SS-010	SS-010	SS-032
Mineral	Dol	Dol	Dol	Cal	Cal	Cal	Dol	Dol	Dol	Cal	Cal	Cal	Mn-Cal
Crystal-Spot	1.5	1.6	1.7	2.8	2.9	2.10	3.15	3.16	3.17	4.18	4.19	4.20	1.10
End-Members - Molar (%)													
CaCO3	51.96	51.43	51.48	81.58	96.29	98.74	51.57	51.20	51.37	93.85	95.61	94.72	76.82
MgCO3	47.40	47.85	47.77	17.58	3.30	0.87	47.45	47.81	47.78	5.51	3.81	4.80	3.62
MnCO3	0.30	0.33	0.41	0.34	0.11	0.08	0.63	0.56	0.55	0.18	0.25	0.12	19.12
FeCO3	0.34	0.39	0.34	0.49	0.31	0.30	0.35	0.43	0.29	0.47	0.33	0.36	0.44
SrCO3	0.00	0.00	0.00	0.00	0.00	0.00	0.00	0.00	0.00	0.00	0.00	0.00	0.00
BaCO3	0.00	0.00	0.00	0.00	0.00	0.00	0.00	0.00	0.00	0.00	0.00	0.00	0.00
Ca	0.53	0.53	0.53	0.84	0.97	1.00	0.54	0.54	0.54	0.97	0.96	0.98	0.81
Mg	0.49	0.50	0.50	0.18	0.03	0.01	0.50	0.50	0.50	0.06	0.04	0.05	0.04
Mn	0.00	0.00	0.00	0.00	0.00	0.00	0.01	0.01	0.01	0.00	0.00	0.00	0.20
Fe	0.00	0.00	0.00	0.01	0.00	0.00	0.00	0.00	0.00	0.00	0.00	0.00	0.00

Sample no.	SS-010	SS-010	SS-010	SS-010	SS-010	SS-010	SS-010	SS-010	SS-010	SS-010	SS-010	SS-010	SS-032
Sr	0.00	0.00	0.00	0.00	0.00	0.00	0.00	0.00	0.00	0.00	0.00	0.00	0.00
Ba	0.00	0.00	0.00	0.00	0.00	0.00	0.00	0.00	0.00	0.00	0.00	0.00	0.00
Total-Cations	1.03	1.04	1.04	1.03	1.01	1.01	1.05	1.05	1.05	1.04	1.00	1.03	1.05
Total-Cabon	1.03	1.04	1.04	1.03	1.01	1.01	1.05	1.05	1.05	1.04	1.00	1.03	1.05
Total-Oxygen	3.09	3.11	3.11	3.08	3.03	3.04	3.14	3.14	3.14	3.11	3.01	3.10	3.16
Sample no.	SS-032	SS-032	SS-032	SS-032	SS-032	SS-032	SS-032	SS-032	SS-032	SS-032	SS-032	SS-032	SS-032
Mineral	Mn-Cal	Mn-Cal	Mn-Cal	Mn-Cal	Mn-Cal	Mn-Cal	Mn-Cal	Mn-Cal	Mn-Cal	Mn-Cal	Mn-Cal	Mn-Cal	Mn-Cal
Crystal-Spot	1.2	1.3	2.4	2.5	2.6	3.7	3.8	3.9	4.30	4.31	4.32	5.54	5.55
End-Members - Molar (%)													
CaCO3	77.41	75.76	76.72	76.47	76.66	77.53	76.76	77.08	79.48	79.36	78.20	77.19	77.95
MgCO3	3.56	3.61	3.40	3.56	2.77	2.79	3.06	3.08	2.64	2.69	2.55	2.70	2.64
MnCO3	18.69	20.18	19.42	19.60	20.22	19.38	19.85	19.53	17.57	17.68	18.89	19.82	19.12
FeCO3	0.35	0.45	0.46	0.36	0.35	0.30	0.33	0.31	0.31	0.27	0.36	0.30	0.29
SrCO3	0.00	0.00	0.00	0.00	0.00	0.00	0.00	0.00	0.00	0.00	0.00	0.00	0.00
BaCO3	0.00	0.00	0.00	0.00	0.00	0.00	0.00	0.00	0.00	0.00	0.00	0.00	0.00
Total	100.00	100.00	100.00	100.00	100.00	100.00	100.00	100.00	100.00	100.00	100.00	100.00	100.00
Ca	0.80	0.80	0.80	0.80	0.83	0.82	0.81	0.82	0.86	0.86	0.85	0.84	0.85
Mg	0.04	0.04	0.04	0.04	0.03	0.03	0.03	0.03	0.03	0.03	0.03	0.03	0.03
Mn	0.19	0.21	0.20	0.21	0.22	0.20	0.21	0.21	0.19	0.19	0.21	0.22	0.21
Fe	0.00	0.00	0.00	0.00	0.00	0.00	0.00	0.00	0.00	0.00	0.00	0.00	0.00
Sr	0.00	0.00	0.00	0.00	0.00	0.00	0.00	0.00	0.00	0.00	0.00	0.00	0.00
Ba	0.00	0.00	0.00	0.00	0.00	0.00	0.00	0.00	0.00	0.00	0.00	0.00	0.00
Total-Cations	1.03	1.06	1.05	1.05	1.08	1.05	1.06	1.07	1.08	1.08	1.09	1.09	1.09
Total-Carbon	1.03	1.06	1.05	1.05	1.08	1.05	1.06	1.07	1.08	1.08	1.09	1.09	1.09
Total-Oxygen	3.09	3.17	3.14	3.16	3.25	3.16	3.17	3.20	3.25	3.25	3.27	3.27	3.27
Sample no.	SS-032	SS-034	SS-034	SS-034	SS-034	SS-037	SS-037	SS-037	SS-037	SS-037	SS-037	SS-037	SS-037
Mineral	Mn-Cal	Cal	Cal	Cal	Cal	Cal	Cal	Cal	Dol	Dol	Dol	Cal	Cal
Crystal-Spot	5.56	1.19	1.20	1.21	1.22	1.1	1.2	1.3	2.4	2.5	2.6	3.16	3.17
End-Members - Molar (%)													
CaCO3	77.45	99.23	95.96	96.36	96.99	92.35	92.96	93.17	52.02	51.73	53.10	93.03	91.95
MgCO3	2.52	0.00	3.32	2.84	2.17	7.15	6.54	6.30	47.28	47.53	46.13	6.44	7.60
MnCO3	19.83	0.73	0.65	0.70	0.81	0.40	0.43	0.43	0.48	0.48	0.45	0.43	0.37
FeCO3	0.21	0.04	0.07	0.10	0.02	0.10	0.07	0.11	0.22	0.26	0.32	0.10	0.08
SrCO3	0.00	0.00	0.00	0.00	0.00	0.00	0.00	0.00	0.00	0.00	0.00	0.00	0.00
BaCO3	0.00	0.00	0.00	0.00	0.00	0.00	0.00	0.00	0.00	0.00	0.00	0.00	0.00
Total	100.00	100.00	100.00	100.00	100.00	100.00	100.00	100.00	100.00	100.00	100.00	100.00	100.00
Ca	0.84	1.01	1.01	1.01	1.02	0.97	0.98	0.97	0.54	0.53	0.55	0.97	0.98
Mg	0.03	0.00	0.03	0.03	0.02	0.08	0.07	0.07	0.49	0.49	0.48	0.07	0.08
Mn	0.22	0.01	0.01	0.01	0.01	0.00	0.00	0.00	0.00	0.00	0.00	0.00	0.00
Fe	0.00	0.00	0.00	0.00	0.00	0.00	0.00	0.00	0.00	0.00	0.00	0.00	0.00
Sr	0.00	0.00	0.00	0.00	0.00	0.00	0.00	0.00	0.00	0.00	0.00	0.00	0.00

Sample no.	SS-010	SS-010	SS-010	SS-010	SS-010	SS-010	SS-010	SS-010	SS-010	SS-010	SS-010	SS-010	SS-032
Ba	0.00	0.00	0.00	0.00	0.00	0.00	0.00	0.00	0.00	0.00	0.00	0.00	0.00
Total-Cations	1.09	1.02	1.05	1.05	1.05	1.05	1.05	1.04	1.03	1.02	1.04	1.04	1.07
Total-Carbon	1.09	1.02	1.05	1.05	1.05	1.05	1.05	1.04	1.03	1.02	1.04	1.04	1.07
Total-Oxygen	3.27	3.06	3.16	3.14	3.14	3.15	3.16	3.13	3.10	3.07	3.12	3.12	3.20
Sample no.	SS-037	SS-037	SS-037	SS-037	SS-037	SS-037	SS-037	SS-056	SS-056	SS-056	SS-056	SS-056	SS-056
Mineral	Cal	Dol	Dol	Dol	Cal	Cal	Cal	Kut	Kut	Kut	Kut	Kut	Kut
Crystal-Spot	3.18	4.25	4.26	4.27	5.28	5.29	5.30	1.18	1.19	1.2	2.31	2.32	2.33
End-Members - Molar (%)													
CaCO3	94.50	51.44	51.60	51.43	91.13	91.10	93.71	63.52	61.78	62.25	64.99	64.22	65.37
MgCO3	5.00	47.89	47.69	47.86	8.36	8.37	5.79	6.28	6.86	6.55	5.82	5.96	5.17
MnCO3	0.39	0.40	0.47	0.41	0.42	0.37	0.40	29.97	31.00	30.89	28.96	29.62	29.32
FeCO3	0.10	0.27	0.24	0.29	0.08	0.16	0.10	0.22	0.37	0.31	0.23	0.20	0.14
SrCO3	0.00	0.00	0.00	0.00	0.00	0.00	0.00	0.00	0.00	0.00	0.00	0.00	0.00
BaCO3	0.00	0.00	0.00	0.00	0.00	0.00	0.00	0.00	0.00	0.00	0.00	0.00	0.00
Total	100.00	100.00	100.00	100.00	100.00	100.00	100.00	100.00	100.00	100.00	100.00	100.00	100.00
Ca	0.99	0.53	0.54	0.54	0.94	0.95	0.99	0.59	0.56	0.56	0.62	0.61	0.62
Mg	0.05	0.50	0.50	0.50	0.09	0.09	0.06	0.06	0.06	0.06	0.06	0.06	0.05
Mn	0.00	0.00	0.00	0.00	0.00	0.00	0.00	0.28	0.28	0.28	0.28	0.28	0.28
Fe	0.00	0.00	0.00	0.00	0.00	0.00	0.00	0.00	0.00	0.00	0.00	0.00	0.00
Sr	0.00	0.00	0.00	0.00	0.00	0.00	0.00	0.00	0.00	0.00	0.00	0.00	0.00
Ba	0.00	0.00	0.00	0.00	0.00	0.00	0.00	0.00	0.00	0.00	0.00	0.00	0.00
Total-Cations	1.04	1.04	1.04	1.04	1.04	1.05	1.06	0.93	0.91	0.90	0.96	0.96	0.95
Total-Carbon	1.04	1.04	1.04	1.04	1.04	1.05	1.06	0.93	0.91	0.90	0.96	0.96	0.95
Total-Oxygen	3.13	3.12	3.12	3.13	3.11	3.14	3.17	2.79	2.74	2.71	2.88	2.87	2.86
Sample no.	SS-056	SS-056	SS-056	SS-056	SS-056	SS-057	SS-057	SS-057	SS-057	SS-057	SS-058	SS-058	SS-058
Mineral	Kut	Kut	Kut	Kut	Kut	Cal	Cal	Cal	Cal	Cal	Kut	Kut	Kut
Crystal-Spot	3.37	3.38	3.39	4.7	4.8	1.11	1.12	2.13	3.14	3.15	1.16	1.17	1.18
End-Members - Molar (%)													
CaCO3	66.57	66.82	66.41	60.08	60.35	98.96	98.73	99.11	98.83	99.82	20.67	21.01	20.47
MgCO3	5.02	4.78	4.25	4.35	4.02	1.02	1.16	0.78	1.06	0.15	16.85	16.46	16.44
MnCO3	28.15	28.20	29.12	35.33	35.41	0.00	0.04	0.05	0.08	0.03	60.90	60.96	61.45
FeCO3	0.26	0.20	0.22	0.24	0.23	0.02	0.07	0.05	0.03	0.00	1.58	1.58	1.64
SrCO3	0.00	0.00	0.00	0.00	0.00	0.00	0.00	0.00	0.00	0.00	0.00	0.00	0.00
BaCO3	0.00	0.00	0.00	0.00	0.00	0.00	0.00	0.00	0.00	0.00	0.00	0.00	0.00
Total	100.00	100.00	100.00	100.00	100.00	100.00	100.00	100.00	100.00	100.00	100.00	100.00	100.00
Ca	0.63	0.63	0.64	0.53	0.54	0.97	0.99	0.99	1.00	0.98	0.18	0.19	0.18
Mg	0.05	0.05	0.04	0.04	0.04	0.01	0.01	0.01	0.01	0.00	0.15	0.15	0.15
Mn	0.27	0.27	0.28	0.31	0.32	0.00	0.00	0.00	0.00	0.00	0.54	0.54	0.54
Fe	0.00	0.00	0.00	0.00	0.00	0.00	0.00	0.00	0.00	0.00	0.01	0.01	0.01
Sr	0.00	0.00	0.00	0.00	0.00	0.00	0.00	0.00	0.00	0.00	0.00	0.00	0.00
Ba	0.00	0.00	0.00	0.00	0.00	0.00	0.00	0.00	0.00	0.00	0.00	0.00	0.00

Sample no.	SS-010	SS-010	SS-010	SS-010	SS-010	SS-010	SS-010	SS-010	SS-010	SS-010	SS-010	SS-010	SS-032
Total-Cations	0.95	0.95	0.96	0.89	0.89	0.98	1.00	1.00	1.01	0.98	0.89	0.89	0.89
Total-Carbon	0.95	0.95	0.96	0.89	0.89	0.98	1.00	1.00	1.01	0.98	0.89	0.89	0.89
Total-Oxygen	2.84	2.84	2.87	2.66	2.67	2.94	3.00	3.01	3.03	2.95	2.67	2.66	2.66
Sample no.	SS-058	SS-058	SS-058	SS-058	SS-060	SS-060	SS-060	SS-060	SS-060	SS-060	SS-060	SS-060	SS-060
Mineral	Kut	Kut	Kut	Kut	Kut	Kut	Kut	Kut	Kut	Kut	Kut	Kut	Kut
Crystal-Spot	2.37	2.38	2.39	2.40	1.11	1.12	1.13	1.14	2.4	3.41	4.42	5.59	5.60
End-Members - Molar (%)													
CaCO3	14.33	22.48	22.56	22.18	43.37	42.94	43.91	43.56	43.56	43.35	44.46	41.74	43.14
MgCO3	16.07	16.40	17.03	16.97	11.13	12.11	10.67	10.71	12.08	11.70	10.56	10.97	10.68
MnCO3	67.88	59.54	58.78	59.30	44.97	44.38	44.96	45.25	43.79	44.40	44.47	46.71	45.65
FeCO3	1.72	1.58	1.63	1.56	0.53	0.57	0.47	0.48	0.57	0.55	0.51	0.58	0.53
SrCO3	0.00	0.00	0.00	0.00	0.00	0.00	0.00	0.00	0.00	0.00	0.00	0.00	0.00
BaCO3	0.00	0.00	0.00	0.00	0.00	0.00	0.00	0.00	0.00	0.00	0.00	0.00	0.00
Total	100.00	100.00	100.00	100.00	100.00	100.00	100.00	100.00	100.00	100.00	100.00	100.00	100.00
Ca	0.13	0.20	0.20	0.20	0.41	0.40	0.40	0.41	0.41	0.42	0.42	0.39	0.40
Mg	0.14	0.15	0.15	0.15	0.11	0.11	0.10	0.10	0.11	0.11	0.10	0.10	0.10
Mn	0.61	0.54	0.53	0.54	0.42	0.41	0.41	0.43	0.41	0.43	0.42	0.44	0.42
Fe	0.02	0.01	0.01	0.01	0.00	0.01	0.00	0.00	0.01	0.01	0.00	0.01	0.00
Sr	0.00	0.00	0.00	0.00	0.00	0.00	0.00	0.00	0.00	0.00	0.00	0.00	0.00
Ba	0.00	0.00	0.00	0.00	0.00	0.00	0.00	0.00	0.00	0.00	0.00	0.00	0.00
Total-Cations	0.90	0.90	0.91	0.91	0.94	0.93	0.92	0.95	0.93	0.96	0.94	0.94	0.92
Total-Carbon	0.90	0.90	0.91	0.91	0.94	0.93	0.92	0.95	0.93	0.96	0.94	0.94	0.92
Total-Oxygen	2.69	2.70	2.73	2.72	2.83	2.80	2.75	2.84	2.80	2.88	2.83	2.82	2.76

1B – Representative microprobe analyses of pyroxene from Buritirama Formation.

Sample no.	SS-032	SS-032	SS-032	SS-032	SS-032	SS-032	SS-032	SS-032	SS-032	SS-032	SS-032	SS-032
Mineral	Mn-Di	Mn-Di	Mn-Di	Mn-Di	Mn-Di	Mn-Di	Mn-Di	Mn-Di	Mn-Di	Mn-Di	Mn-Di	Mn-Di
Crystal-Spot	1.20	1.21	1.22	1.23	2.24	2.25	2.26	3.27	3.28	3.29	4.48	4.49
SiO2	51.85	52.90	53.07	53.99	54.00	52.45	53.62	53.24	52.83	53.37	53.40	52.88
TiO2	0.02	0.01	0.00	0.01	0.04	0.05	0.03	0.02	0.03	0.05	0.02	0.02
Al2O3	0.56	0.37	0.27	0.32	0.43	0.40	0.33	0.35	0.31	0.38	0.43	0.35
Cr2O3	0.02	0.02	0.01	0.00	0.01	0.03	0.01	0.00	0.04	0.00	0.06	0.02
FeO	1.56	1.63	1.83	1.54	1.71	1.56	1.55	1.48	1.52	1.65	1.62	1.55
MnO	14.02	16.13	15.33	11.39	11.82	12.42	12.83	11.31	10.52	13.70	12.80	12.65
MgO	14.13	14.27	14.47	15.06	16.01	14.06	14.77	14.67	14.42	14.75	14.29	14.33
CaO	15.68	14.21	15.01	18.27	14.37	17.34	17.10	18.39	18.90	16.69	17.04	17.41
Na2O	0.22	0.22	0.23	0.25	0.44	0.30	0.28	0.27	0.24	0.28	0.27	0.30
K2O	0.04	0.01	0.02	0.00	0.01	0.00	0.00	0.00	0.02	0.00	0.00	0.00
Total (W%)	98.09	99.76	100.23	100.82	98.82	98.60	100.53	99.73	98.82	100.88	99.92	99.51
Si	1.99	2.01	2.00	2.00	2.03	2.00	2.00	2.00	2.00	1.99	2.01	2.00
Ti	0.00	0.00	0.00	0.00	0.00	0.00	0.00	0.00	0.00	0.00	0.00	0.00
Al	0.03	0.02	0.01	0.01	0.02	0.02	0.01	0.02	0.01	0.02	0.02	0.02

Cr	0.00	0.00	0.00	0.00	0.00	0.00	0.00	0.00	0.00	0.00	0.00	0.00
Fe	0.05	0.05	0.06	0.05	0.05	0.05	0.05	0.05	0.05	0.05	0.05	0.05
Mn	0.46	0.52	0.49	0.36	0.38	0.40	0.41	0.36	0.34	0.43	0.41	0.40
Mg	0.81	0.81	0.81	0.83	0.90	0.80	0.82	0.82	0.81	0.82	0.80	0.81
Ca	0.65	0.58	0.61	0.73	0.58	0.71	0.68	0.74	0.77	0.67	0.69	0.70
Na	0.02	0.02	0.02	0.02	0.03	0.02	0.02	0.02	0.02	0.02	0.02	0.02
K	0.00	0.00	0.00	0.00	0.00	0.00	0.00	0.00	0.00	0.00	0.00	0.00
Total-Cations	4.00	3.99	4.00	4.00	3.98	4.00	4.00	4.00	4.00	4.01	3.99	4.00
Total-Oxygen	6.00	6.00	6.00	6.00	6.00	6.00	6.00	6.00	6.00	6.00	6.00	6.00
Sample no.	SS-032	SS-032	SS-032	SS-032	SS-034	SS-034	SS-034	SS-034	SS-034	SS-034	SS-034	SS-034
Mineral	Mn-Di	Mn-Di	Mn-Di	Mn-Di	Di	Di	Di	Di	Di	Di	Di	Di
Crystal-Spot	4.50	4.51	4.52	4.53	1.1	1.2	1.3	1.4	2.5	2.6	2.7	3.30
SiO2	52.88	53.19	52.82	53.08	53.31	53.55	53.64	53.39	53.25	53.62	53.58	53.36
TiO2	0.02	0.02	0.03	0.03	0.08	0.06	0.04	0.11	0.14	0.05	0.03	0.05
Al2O3	0.35	0.35	0.39	0.28	2.39	2.39	2.42	2.69	2.48	2.28	1.66	2.36
Cr2O3	0.02	0.02	0.00	0.02	0.04	0.02	0.00	0.04	0.00	0.00	0.04	0.00
FeO	1.55	1.66	1.48	1.50	2.30	2.28	2.10	2.42	2.48	2.20	2.09	2.25
MnO	12.65	13.15	13.28	12.06	0.20	0.26	0.23	0.25	0.29	0.19	0.31	0.34
MgO	14.33	14.54	14.42	14.62	16.12	16.31	16.49	16.09	16.13	16.24	16.71	16.37
CaO	17.41	16.84	16.70	17.90	23.59	23.85	23.63	23.46	23.57	23.67	24.04	23.49
Na2O	0.30	0.27	0.29	0.24	1.03	0.94	0.96	1.16	0.97	1.05	0.84	0.98
K2O	0.00	0.01	0.01	0.01	0.01	0.02	0.02	0.02	0.01	0.00	0.01	0.00
Total (W%)	99.51	100.04	99.42	99.73	99.08	99.67	99.54	99.63	99.31	99.31	99.32	99.19
Si	2.00	2.00	2.00	2.00	1.96	1.95	1.96	1.95	1.95	1.96	1.96	1.96
Ti	0.00	0.00	0.00	0.00	0.00	0.00	0.00	0.00	0.00	0.00	0.00	0.00
Al	0.02	0.02	0.02	0.01	0.10	0.10	0.10	0.12	0.11	0.10	0.07	0.10
Cr	0.00	0.00	0.00	0.00	0.00	0.00	0.00	0.00	0.00	0.00	0.00	0.00
Fe	0.05	0.05	0.05	0.05	0.07	0.07	0.06	0.07	0.08	0.07	0.06	0.07
Mn	0.42	0.42	0.43	0.38	0.01	0.01	0.01	0.01	0.01	0.01	0.01	0.01
Mg	0.82	0.82	0.81	0.82	0.88	0.89	0.90	0.88	0.88	0.89	0.91	0.89
Ca	0.68	0.68	0.68	0.72	0.93	0.93	0.92	0.92	0.93	0.93	0.94	0.92
Na	0.02	0.02	0.02	0.02	0.07	0.07	0.07	0.08	0.07	0.07	0.06	0.07
K	0.00	0.00	0.00	0.00	0.00	0.00	0.00	0.00	0.00	0.00	0.00	0.00
Total-Cations	4.00	4.00	4.00	4.00	4.03	4.03	4.02	4.03	4.03	4.02	4.03	4.03
Total-Oxygen	6.00	6.00	6.00	6.00	6.00	6.00	6.00	6.00	6.00	6.00	6.00	6.00
Sample no.	SS-034	SS-034	SS-034	SS-034	SS-034	SS-034	SS-034	SS-034	SS-057	SS-057	SS-058	SS-058
Mineral	Di	Di	Di	Di	Di	Di	Di	Di	Mn-Di	Mn-Di	Kan	Kan
Crystal-Spot	3.31	3.32	4.34	4.35	5.49	6.50	7.51	8.52	1.8	1.9	1.19	1.20
SiO2	53.69	53.35	53.99	53.71	54.23	51.95	53.61	52.97	52.78	52.67	50.62	51.43
TiO2	0.06	0.04	0.05	0.11	0.04	0.05	0.05	0.14	0.01	0.01	0.02	0.02
Al2O3	2.02	1.90	2.27	2.48	1.40	2.09	1.60	2.52	0.45	0.42	0.08	0.03
Cr2O3	0.02	0.03	0.04	0.02	0.01	0.05	0.00	0.01	0.06	0.00	0.00	0.00
FeO	2.26	2.09	2.16	2.42	1.96	2.27	1.79	2.62	2.17	2.22	2.18	2.33
MnO	0.30	0.22	0.25	0.22	0.31	0.29	0.31	0.16	15.48	16.22	30.75	31.08

MgO	16.49	16.38	16.61	15.84	16.67	15.70	17.13	15.87	13.73	13.66	14.64	14.81
CaO	23.81	23.88	23.89	23.49	23.87	24.84	24.41	23.58	14.56	14.15	0.90	0.88
Na2O	0.99	0.86	0.93	1.11	0.83	0.83	0.63	0.98	0.33	0.28	0.05	0.02
K2O	0.01	0.01	0.01	0.01	0.00	0.00	0.00	0.00	0.01	0.00	0.00	0.00
Total (W%)	99.63	98.77	100.18	99.40	99.30	98.05	99.52	98.84	99.58	99.63	99.26	100.60
Si	1.96	1.96	1.96	1.96	1.98	1.94	1.96	1.95	2.01	2.01	2.00	2.00
Ti	0.00	0.00	0.00	0.00	0.00	0.00	0.00	0.00	0.00	0.00	0.00	0.00
Al	0.09	0.08	0.10	0.11	0.06	0.09	0.07	0.11	0.02	0.02	0.00	0.00
Cr	0.00	0.00	0.00	0.00	0.00	0.00	0.00	0.00	0.00	0.00	0.00	0.00
Fe	0.07	0.06	0.07	0.07	0.06	0.07	0.05	0.08	0.07	0.07	0.07	0.08
Mn	0.01	0.01	0.01	0.01	0.01	0.01	0.01	0.01	0.50	0.52	1.03	1.02
Mg	0.90	0.90	0.90	0.86	0.91	0.87	0.93	0.87	0.78	0.78	0.86	0.86
Ca	0.93	0.94	0.93	0.92	0.93	0.99	0.96	0.93	0.59	0.58	0.04	0.04
Na	0.07	0.06	0.07	0.08	0.06	0.06	0.04	0.07	0.02	0.02	0.00	0.00
K	0.00	0.00	0.00	0.00	0.00	0.00	0.00	0.00	0.00	0.00	0.00	0.00
Total-Cations	4.03	4.02	4.02	4.02	4.02	4.04	4.03	4.02	3.99	3.99	4.00	4.00
Total-Oxygen	6.00	6.00	6.00	6.00	6.00	6.00	6.00	6.00	6.00	6.00	6.00	6.00
Sample no.	SS-058	SS-060	SS-060	SS-060	SS-060	SS-060	SS-060	SS-060	SS-060	SS-060	SS-060	SS-060
Mineral	Kan	Kan	Kan	Kan	Kan	Kan	Kan	Kan	Kan	Kan	Kan	Kan
Crystal-Spot	1.21	1.1	1.2	1.3	1.4	1.5	2.6	2.7	2.8	2.9	2.10	3.21
SiO2	50.45	51.40	51.11	50.69	50.70	50.98	50.86	50.68	50.86	50.89	50.85	50.17
TiO2	0.01	0.02	0.00	0.01	0.04	0.01	0.01	0.04	0.00	0.01	0.01	0.02
Al2O3	0.06	0.80	0.09	0.05	0.03	0.08	0.07	0.10	0.07	0.09	0.10	0.06
Cr2O3	0.00	0.03	0.00	0.00	0.00	0.00	0.00	0.01	0.00	0.02	0.00	0.01
FeO	2.29	1.36	1.31	1.28	1.26	1.36	1.19	1.26	1.23	1.25	1.26	1.27
MnO	31.04	26.59	30.58	30.83	30.40	30.49	30.62	30.51	30.81	30.70	31.06	30.79
MgO	14.29	16.12	14.13	14.08	14.33	14.15	14.51	14.36	14.29	14.33	14.53	14.37
CaO	0.87	1.72	1.58	1.63	1.59	1.60	1.64	1.62	1.63	1.64	1.63	1.69
Na2O	0.03	0.06	0.12	0.09	0.07	0.10	0.09	0.06	0.09	0.08	0.10	0.06
K2O	0.00	0.02	0.01	0.00	0.01	0.01	0.00	0.00	0.01	0.00	0.00	0.01
Total (W%)	99.04	98.11	98.92	98.65	98.43	98.77	99.00	98.65	98.98	99.01	99.55	98.44
Si	2.00	2.00	2.01	2.01	2.01	2.01	2.00	2.00	2.01	2.01	2.00	1.99
Ti	0.00	0.00	0.00	0.00	0.00	0.00	0.00	0.00	0.00	0.00	0.00	0.00
Al	0.00	0.04	0.00	0.00	0.00	0.00	0.00	0.00	0.00	0.00	0.00	0.00
Cr	0.00	0.00	0.00	0.00	0.00	0.00	0.00	0.00	0.00	0.00	0.00	0.00
Fe	0.08	0.04	0.04	0.04	0.04	0.04	0.04	0.04	0.04	0.04	0.04	0.04
Mn	1.04	0.88	1.02	1.03	1.02	1.02	1.02	1.02	1.03	1.02	1.03	1.04
Mg	0.84	0.94	0.83	0.83	0.85	0.83	0.85	0.85	0.84	0.84	0.85	0.85
Ca	0.04	0.07	0.07	0.07	0.07	0.07	0.07	0.07	0.07	0.07	0.07	0.07
Na	0.00	0.00	0.01	0.01	0.01	0.01	0.01	0.00	0.01	0.01	0.01	0.00
K	0.00	0.00	0.00	0.00	0.00	0.00	0.00	0.00	0.00	0.00	0.00	0.00
Total-Cations	4.00	3.98	3.99	0.00	0.00	0.00	0.00	0.00	0.00	0.00	0.00	0.00
Total-Oxygen	6.00	6.00	6.00	6.00	6.00	6.00	6.00	6.00	6.00	6.00	6.00	6.00
Sample no.	SS-060	SS-060	SS-060	SS-060	SS-060	SS-060	SS-060	SS-060	SS-060	SS-060		

Mineral	Kan	Kan	Kan	Kan	Kan	Kan	Kan	Kan	Kan	Kan
Crystal-Spot	3.22	3.23	4.47	4.48	4.49	4.62	4.63	4.64	4.65	4.66
SiO2	50.20	50.10	51.04	51.58	50.99	50.97	50.92	50.55	50.89	50.90
TiO2	0.00	0.01	0.01	0.03	0.03	0.00	0.01	0.02	0.00	0.02
Al2O3	0.06	0.11	0.09	0.05	0.08	0.06	0.07	0.09	0.01	0.06
Cr2O3	0.01	0.02	0.00	0.04	0.01	0.00	0.00	0.01	0.00	0.00
FeO	1.20	1.25	1.27	1.21	1.24	1.29	1.24	1.37	1.18	1.17
MnO	30.92	31.01	31.04	29.77	31.07	30.96	31.01	30.94	31.53	31.38
MgO	14.45	14.21	14.65	14.97	14.61	14.33	14.31	14.15	14.07	14.39
CaO	1.53	1.64	1.59	1.45	1.50	1.52	1.52	1.52	1.50	1.50
Na2O	0.08	0.10	0.11	0.09	0.08	0.05	0.11	0.08	0.09	0.06
K2O	0.01	0.03	0.01	0.01	0.00	0.02	0.02	0.01	0.01	0.01
Total (W%)	98.46	98.46	99.82	99.19	99.60	99.20	99.20	98.73	99.27	99.49
Si	2.00	1.99	2.00	2.02	2.00	2.01	2.01	2.00	2.01	2.00
Ti	0.00	0.00	0.00	0.00	0.00	0.00	0.00	0.00	0.00	0.00
Al	0.00	0.00	0.00	0.00	0.00	0.00	0.00	0.00	0.00	0.00
Cr	0.00	0.00	0.00	0.00	0.00	0.00	0.00	0.00	0.00	0.00
Fe	0.04	0.04	0.04	0.04	0.04	0.04	0.04	0.05	0.04	0.04
Mn	1.04	1.05	1.03	0.99	1.03	1.03	1.03	1.04	1.05	1.04
Mg	0.86	0.84	0.86	0.87	0.85	0.84	0.84	0.84	0.83	0.84
Ca	0.07	0.07	0.07	0.06	0.06	0.06	0.06	0.06	0.06	0.06
Na	0.01	0.01	0.01	0.01	0.01	0.00	0.01	0.01	0.01	0.00
K	0.00	0.00	0.00	0.00	0.00	0.00	0.00	0.00	0.00	0.00
Total-Cations	0.00	0.00	0.00	0.00	0.00	0.00	0.00	0.00	0.00	0.00
Total-Oxygen	6.00	6.00	6.00	6.00	6.00	6.00	6.00	6.00	6.00	6.00

1C – Representative microprobe analyses of garnets from Buritirama Formation.

Sample no.	SS-002	SS-002	SS-002	SS-002	SS-002	SS-002	SS-002	SS-002	SS-002	SS-002	SS-002	SS-002	SS-002
Spot-Position	Rim	Rim	Rim	Core	Core	Core	Rim	Rim	Rim	Core	Core	Rim	Rim
Crystal-Spot	1.22	1.23	1.24	1.25	1.26	1.27	1.28	1.29	2.43	2.44	2.45	2.46	2.47
SiO2	38.07	38.09	37.92	38.14	37.86	37.77	38.00	38.06	38.24	37.93	38.16	38.36	38.06
TiO2	0.07	0.05	0.01	0.04	0.09	0.03	0.02	0.01	0.03	0.01	0.01	0.06	0.01
Al2O3	21.35	21.13	21.29	21.13	21.01	21.12	21.24	21.38	21.56	21.32	21.28	21.47	21.47
FeO	26.93	26.57	25.95	25.20	24.97	25.48	26.16	25.30	27.31	25.80	27.55	27.99	28.83
MnO	2.54	2.90	2.77	3.58	3.48	3.69	2.96	2.95	2.16	2.97	2.00	2.01	2.32
MgO	5.97	5.37	4.90	4.49	4.33	4.18	5.29	5.18	5.68	5.17	5.90	6.29	5.76
CaO	4.34	4.97	6.19	6.60	6.85	6.67	5.36	6.41	5.23	6.20	4.63	4.09	3.63
Na2O	0.04	0.00	0.02	0.04	0.07	0.05	0.00	0.04	0.03	0.02	0.01	0.05	0.02
K2O	0.00	0.01	0.01	0.01	0.01	0.00	0.00	0.01	0.01	0.00	0.00	0.00	0.00
Total (W%)	99.31	99.08	99.06	99.21	98.65	98.98	99.03	99.34	100.25	99.42	99.54	100.32	100.10
Si	3.00	3.01	3.00	3.02	3.02	3.01	3.01	3.00	2.99	2.99	3.00	2.99	2.99
Ti	0.00	0.00	0.00	0.00	0.01	0.00	0.00	0.00	0.00	0.00	0.00	0.00	0.00
Al	1.98	1.97	1.99	1.97	1.97	1.98	1.98	1.99	1.99	1.98	1.97	1.97	1.99

Fe	1.77	1.75	1.71	1.66	1.66	1.69	1.72	1.66	1.77	1.68	1.79	1.80	1.88
Mn	0.17	0.19	0.19	0.24	0.23	0.25	0.20	0.20	0.14	0.20	0.13	0.13	0.15
Mg	0.70	0.63	0.58	0.53	0.51	0.50	0.62	0.61	0.66	0.61	0.69	0.73	0.67
Ca	0.37	0.42	0.53	0.56	0.58	0.57	0.45	0.54	0.44	0.52	0.39	0.34	0.31
Total-Cations	8.00	7.98	7.99	7.98	7.98	7.99	7.99	7.99	7.99	7.98	7.98	7.98	7.99
Total-Oxygen	12.00	12.00	12.00	12.00	12.00	12.00	12.00	12.00	12.00	12.00	12.00	12.00	12.00
End-Members - Mole (%)													
Almandine	58.63	58.00	56.90	55.22	55.08	56.01	57.26	55.07	58.42	55.54	59.40	59.70	62.06
Andradite	0.54	0.54	0.37	0.26	0.25	0.49	0.41	0.52	0.87	1.04	1.05	1.16	0.84
Grossular	11.68	13.52	17.12	18.53	19.40	18.55	14.71	17.46	13.66	16.44	11.92	10.18	9.24
Pyrope	23.46	21.30	19.34	17.84	17.33	16.62	20.87	20.29	22.14	20.31	23.11	24.45	22.56
Spessartine	5.67	6.53	6.21	8.09	7.91	8.32	6.65	6.58	4.78	6.63	4.46	4.43	5.15
Uvarovite	0.02	0.12	0.07	0.07	0.04	0.00	0.11	0.09	0.13	0.04	0.07	0.07	0.15
Sample no.	SS-032	SS-032	SS-032	SS-032	SS-032	SS-032	SS-032	SS-032	SS-032	SS-032	SS-032	SS-032	SS-032
Spot-Position	-	-	Rim	Core	Rim	Rim	Rim	Core	Core	Rim	Rim	Rim	Core
Crystal-Spot	1.15	1.16	2.17	2.18	2.19	3.62	3.63	3.64	3.65	3.66	3.67	4.68	4.69
SiO2	36.41	36.70	36.32	36.32	36.02	36.57	37.13	37.67	37.20	36.72	36.91	37.39	36.59
TiO2	0.04	0.31	0.00	0.07	0.07	0.29	0.30	0.12	0.11	0.15	0.17	0.13	0.19
Al2O3	19.60	19.95	19.96	20.03	20.45	19.86	20.70	21.06	20.43	20.22	20.58	20.52	20.33
FeO	1.69	1.40	1.81	1.67	1.50	1.51	1.41	1.50	1.61	1.36	1.38	1.73	1.43
MnO	34.75	34.96	34.32	34.98	35.05	33.55	32.53	30.43	30.69	35.20	35.07	33.48	32.34
MgO	1.16	1.27	2.14	1.66	1.47	1.41	1.54	1.73	1.79	1.15	1.14	1.94	1.65
CaO	4.36	4.52	3.81	3.71	3.51	5.24	6.32	7.50	7.57	4.90	5.26	4.98	5.82
Na2O	0.02	0.08	0.05	0.04	0.01	0.02	0.00	0.06	0.03	0.06	0.06	0.04	0.03
K2O	0.01	0.01	0.02	0.01	0.02	0.01	0.01	0.04	0.00	0.01	0.02	0.01	0.03
Total (W%)	98.03	99.21	98.43	98.47	98.08	98.46	99.94	100.11	99.42	99.77	100.58	100.21	98.42
Si	3.01	3.00	2.98	2.99	2.97	3.00	2.98	3.00	2.99	2.98	2.97	3.00	2.99
Ti	0.00	0.02	0.00	0.00	0.00	0.02	0.02	0.01	0.01	0.01	0.01	0.01	0.01
Al	1.91	1.92	1.92	1.93	1.97	1.92	1.95	1.98	1.94	1.92	1.93	1.94	1.95
Fe	0.12	0.10	0.12	0.11	0.10	0.10	0.09	0.10	0.11	0.09	0.09	0.12	0.10
Mn	2.43	2.42	2.39	2.44	2.45	2.33	2.21	2.06	2.09	2.42	2.39	2.28	2.24
Mg	0.14	0.15	0.26	0.20	0.18	0.17	0.18	0.21	0.21	0.14	0.14	0.23	0.20
Ca	0.39	0.40	0.33	0.33	0.31	0.46	0.54	0.64	0.65	0.43	0.45	0.43	0.51
Total-Cations	8.01	8.00	8.02	8.02	8.02	8.00	8.00	8.00	8.01	8.01	8.02	8.00	8.01
Total-Oxygen	12.00	12.00	12.00	12.00	12.00	12.00	12.00	12.00	12.00	12.00	12.00	12.00	12.00
End-Members - Mole (%)													
Almandine	0.00	0.00	0.00	0.67	1.05	0.00	1.39	2.59	0.81	0.00	0.00	1.32	1.35
Andradite	3.28	2.73	3.69	2.87	1.34	2.79	1.50	0.34	2.59	2.95	2.63	2.14	1.75
Grossular	9.73	10.40	7.51	8.06	9.09	12.71	16.73	21.17	19.28	11.20	12.30	12.24	15.30
Pyrope	4.81	5.23	8.78	6.81	6.08	5.81	6.18	6.91	7.21	4.66	4.59	7.81	6.72
Spessartine	82.18	81.65	80.03	81.59	82.44	78.68	74.19	68.99	70.12	81.20	80.48	76.50	74.87
Uvarovite	0.00	0.00	0.00	0.00	0.00	0.00	0.00	0.00	0.00	0.00	0.00	0.00	0.00
Sample no.	SS-032	SS-032	SS-032	SS-032	SS-032	SS-032	SS-032	SS-058	SS-058	SS-058	SS-058	SS-058	SS-058

Spot-Position	Rim	Core	Rim	Rim	Core	Core	Rim	-	-	-	-	-	-
Crystal-Spot	4.71	5.42	5.43	6.44	6.45	6.46	6.47	1.11	1.12	2.13	3.14	4.15	5.25
SiO2	37.41	36.67	37.17	36.88	37.32	37.68	36.99	36.89	35.66	36.39	35.02	36.62	36.29
TiO2	0.11	0.23	0.05	0.24	0.28	0.06	0.15	0.36	0.49	0.15	1.02	0.32	0.16
Al2O3	20.78	19.59	20.38	20.18	20.05	20.41	20.16	20.87	20.68	20.82	19.85	20.89	20.60
FeO	1.60	1.71	1.97	1.74	1.53	2.16	1.73	1.22	1.14	1.17	1.23	1.23	1.17
MnO	32.17	34.91	33.40	33.77	34.84	33.16	34.69	38.13	37.62	38.54	37.60	38.28	38.09
MgO	1.70	1.04	2.57	2.19	1.46	2.64	1.71	1.18	1.21	1.05	1.42	1.15	1.24
CaO	6.79	5.00	3.62	4.45	4.59	3.97	3.94	2.03	2.34	1.80	2.62	2.10	1.86
Na2O	0.02	0.01	0.01	0.01	0.00	0.03	0.00	0.07	0.00	0.05	0.02	0.06	0.01
K2O	0.01	0.01	0.01	0.00	0.00	0.00	0.01	0.01	0.00	0.00	0.01	0.00	0.01
Total (W%)	100.59	99.16	99.16	99.46	100.06	100.10	99.38	100.76	99.14	99.96	98.80	100.65	99.42
Si	2.98	3.00	3.01	2.98	3.01	3.02	3.00	2.98	2.93	2.97	2.90	2.97	2.97
Ti	0.01	0.01	0.00	0.01	0.02	0.00	0.01	0.02	0.03	0.01	0.06	0.02	0.01
Al	1.94	1.89	1.95	1.91	1.91	1.93	1.93	1.99	2.01	2.00	1.94	2.00	1.99
Fe	0.11	0.12	0.13	0.12	0.10	0.14	0.12	0.08	0.08	0.08	0.08	0.08	0.08
Mn	2.17	2.42	2.29	2.31	2.38	2.25	2.39	2.61	2.62	2.66	2.64	2.63	2.64
Mg	0.20	0.13	0.31	0.26	0.18	0.31	0.21	0.14	0.15	0.13	0.18	0.14	0.15
Ca	0.58	0.44	0.31	0.39	0.40	0.34	0.34	0.18	0.21	0.16	0.23	0.18	0.16
Total-Cations	8.01	8.01	8.00	8.01	8.00	8.00	8.00	8.00	8.00	8.00	8.00	8.00	8.00
End-Members - Mole (%)													
Almandine	0.96	0.00	2.04	0.57	0.00	1.74	0.95	1.79	0.00	0.68	0.00	0.63	0.51
Andradite	2.26	4.13	1.94	3.14	2.74	2.27	2.35	0.37	1.37	0.74	4.33	0.87	1.06
Grossular	17.19	9.73	8.61	9.80	10.32	9.25	9.21	5.40	4.21	4.56	0.00	5.27	4.24
Pyrope	6.76	4.28	10.42	8.85	5.96	10.66	6.98	4.77	5.07	4.30	6.05	4.69	5.07
Spessartine	72.83	81.86	77.00	77.64	80.97	76.09	80.50	87.55	89.35	89.72	89.59	88.54	88.91
Uvarovite	0.00	0.00	0.00	0.00	0.00	0.00	0.00	0.13	0.00	0.00	0.03	0.00	0.20
Sample no.	SS-058	SS-058	SS-058	SS-058	SS-056	SS-056	SS-056	SS-056	SS-056	SS-056	SS-057	SS-057	SS-057
Spot-Position	-	-	-	-	Rim	Core	Core	Rim	Rim	Core	Rim	Core	Rim
Crystal-Spot	6.26	7.27	8.28	9.29	1.1	1.2	1.3	1.4	2.15	2.16	1.1	1.2	1.3
SiO2	36.55	36.47	36.34	36.02	36.09	35.65	36.23	36.28	36.40	36.51	36.29	36.54	37.14
TiO2	0.46	0.08	0.12	0.82	0.07	0.10	0.21	0.21	0.18	0.24	0.33	0.38	0.29
Al2O3	20.59	20.79	20.51	20.33	20.35	19.84	20.00	20.29	19.83	19.62	20.61	20.76	20.88
FeO	1.24	1.37	1.40	1.18	1.14	1.15	1.20	1.07	1.73	1.76	1.94	2.03	1.94
MnO	37.95	38.85	39.13	37.74	36.55	37.39	37.11	38.01	38.53	37.68	36.27	35.63	36.21
MgO	1.25	1.25	1.24	1.25	0.95	0.93	0.94	0.97	0.92	0.89	1.25	1.17	1.34
CaO	2.15	1.29	1.36	2.04	2.83	2.88	2.96	2.89	2.73	3.22	2.22	2.22	2.21
Na2O	0.05	0.03	0.00	0.05	0.04	0.06	0.03	0.05	0.01	0.01	0.07	0.10	0.05
K2O	0.01	0.01	0.01	0.01	0.04	0.02	0.03	0.02	0.01	0.01	0.01	0.00	0.00
Total (W%)	100.25	100.13	100.10	99.43	98.07	98.01	98.70	99.78	100.33	99.95	98.99	98.84	100.05
Si	2.97	2.97	2.97	2.95	2.99	2.97	2.99	2.97	2.97	2.98	2.98	2.99	3.00
Ti	0.03	0.00	0.01	0.05	0.00	0.01	0.01	0.01	0.01	0.01	0.02	0.02	0.02
Al	1.97	2.00	1.98	1.97	1.99	1.95	1.95	1.96	1.91	1.90	1.99	2.01	1.99
Fe	0.08	0.09	0.10	0.08	0.08	0.08	0.08	0.07	0.12	0.12	0.13	0.17	0.15

Mn	2.61	2.68	2.70	2.62	2.57	2.64	2.59	2.63	2.66	2.61	2.52	2.47	2.48
Mg	0.15	0.15	0.15	0.15	0.12	0.12	0.12	0.12	0.11	0.11	0.15	0.14	0.16
Ca	0.19	0.11	0.12	0.18	0.25	0.26	0.26	0.25	0.24	0.28	0.20	0.19	0.19
Total-Cations	8.00	8.01	8.02	8.00	8.00	8.02	8.00	8.02	8.03	8.02	8.00	7.99	7.99
Total-Oxygen	12.00	12.00	12.00	12.00	12.00	12.00	12.00	12.00	12.00	12.00	12.00	12.00	12.00
End-Members - Mole (%)													
Almandine	0.66	0.89	0.00	0.00	1.87	0.00	0.47	0.00	0.00	0.00	3.67	5.58	4.91
Andradite	1.24	0.91	2.17	1.34	0.57	3.06	2.07	2.61	4.66	4.56	0.13	0.00	0.00
Grossular	4.98	2.43	1.41	4.65	7.85	4.11	6.51	4.62	1.92	3.98	6.30	6.36	6.37
Pyrope	5.08	5.09	5.09	5.17	3.92	3.89	3.86	3.97	3.75	3.65	5.13	4.81	5.43
Spessartine	87.95	90.22	91.20	88.76	85.79	88.84	86.89	88.76	89.67	87.72	84.64	83.07	83.25
Uvarovite	0.09	0.45	0.12	0.09	0.00	0.10	0.19	0.05	0.00	0.09	0.13	0.18	0.04
Sample no.	SS-057	SS-057	SS-057	SS-060	SS-060	SS-060	SS-060	SS-060	SS-060	SS-060	SS-060	SS-060	SS-060
Spot-Position	Rim	Core	Rim	Rim	Rim	Core	Rim	Rim	Rim	Core	Rim	Core	Rim
Crystal-Spot	2.21	2.22	2.23	1.31	1.32	1.33	1.34	2.36	2.37	2.38	2.39	3.75	4.77
SiO2	37.24	36.96	36.21	37.00	36.63	36.17	35.25	36.38	36.17	35.96	36.30	36.47	36.66
TiO2	0.36	0.38	0.25	0.38	0.20	0.35	0.19	0.26	0.31	0.09	0.12	0.22	0.11
Al2O3	21.20	20.96	20.67	20.67	20.96	20.26	19.93	20.67	20.30	20.22	20.29	20.72	20.92
FeO	2.02	2.08	1.93	0.80	0.80	0.84	0.77	0.77	0.79	0.69	0.82	0.84	0.78
MnO	37.63	37.26	37.14	38.27	38.50	38.77	38.76	38.85	38.49	39.02	38.93	38.60	38.56
MgO	1.16	1.04	1.30	1.22	1.22	1.27	1.11	1.31	1.26	1.22	1.14	1.08	1.13
CaO	2.25	2.12	2.25	2.18	2.16	2.21	2.30	2.06	2.14	1.98	1.89	2.10	1.99
Na2O	0.11	0.06	0.10	0.06	0.08	0.06	0.04	0.03	0.07	0.03	0.03	0.05	0.03
K2O	0.01	0.00	0.00	0.00	0.00	0.01	0.01	0.01	0.01	0.01	0.06	0.00	0.01
Total (W%)	101.97	100.85	99.84	100.58	100.55	99.93	98.37	100.34	99.54	99.24	99.58	100.07	100.19
Si	2.97	2.98	2.96	2.99	2.97	2.96	2.94	2.96	2.96	2.96	2.98	2.97	2.98
Ti	0.02	0.02	0.02	0.02	0.01	0.02	0.01	0.02	0.02	0.01	0.01	0.01	0.01
Al	2.00	1.99	1.99	1.97	2.00	1.96	1.96	1.98	1.96	1.97	1.96	1.99	2.00
Fe	0.14	0.14	0.13	0.05	0.05	0.06	0.05	0.05	0.05	0.05	0.06	0.06	0.05
Mn	2.55	2.55	2.57	2.62	2.64	2.68	2.74	2.67	2.67	2.72	2.70	2.66	2.65
Mg	0.14	0.13	0.16	0.15	0.15	0.15	0.14	0.16	0.15	0.15	0.14	0.13	0.14
Ca	0.19	0.18	0.20	0.19	0.19	0.19	0.21	0.18	0.19	0.17	0.17	0.18	0.17
Total-Cations	8.00	8.00	8.02	7.99	8.01	8.02	8.05	8.02	8.01	8.03	8.01	8.01	8.01
Total-Oxygen	12.00	12.00	12.00	12.00	12.00	12.00	12.00	12.00	12.00	12.00	12.00	12.00	12.00
End-Members - Mole (%)													
Almandine	3.32	4.24	1.13	0.67	0.00	0.00	0.00	0.00	0.00	0.00	0.00	0.00	0.48
Andradite	0.32	0.00	1.53	0.64	0.80	2.90	2.74	1.91	2.25	2.40	2.18	1.05	0.42
Grossular	6.06	6.15	4.93	5.58	5.19	1.07	0.00	2.13	2.21	0.36	2.08	4.79	5.39
Pyrope	4.63	4.21	5.34	4.95	4.97	5.22	4.68	5.36	5.19	5.07	4.70	4.42	4.60
Spessartine	85.59	85.39	86.87	88.05	89.04	90.80	92.49	90.46	90.16	91.91	90.84	89.67	89.11
Uvarovite	0.09	0.01	0.20	0.12	0.00	0.00	0.09	0.15	0.19	0.26	0.20	0.07	0.00

1D – Representative microprobe analyses of feldspar from Buritirama Formation.

Sample no.	SS-002	SS-002	SS-002	SS-002	SS-002	SS-002	SS-002	SS-002	SS-002	SS-032	SS-032	SS-032
Mineral	Pl	Pl	Pl	Pl	Pl	Pl	Pl	Pl	Pl	Mc	Mc	Mc
Crystal-Spot	1.13	1.14	1.15	1.16	1.17	2.18	2.19	2.20	2.21	1.58	1.59	2.60
SiO2	56.96	59.86	56.15	59.38	56.34	57.49	59.00	59.05	58.61	62.89	62.07	62.20
TiO2	0.00	0.00	0.00	0.00	0.01	0.00	0.00	0.00	0.00	0.00	0.00	0.00
Al2O3	26.53	26.19	24.27	26.57	26.16	26.54	25.63	25.38	25.60	18.38	18.55	18.25
Cr2O3	0.02	0.00	0.00	0.00	0.00	0.01	0.00	0.00	0.00	0.00	0.01	0.02
FeO	0.07	0.39	1.23	0.41	0.16	0.11	0.09	0.06	0.10	0.04	0.07	0.03
MnO	0.00	0.01	0.05	0.04	0.03	0.00	0.00	0.00	0.00	0.00	0.11	0.07
MgO	0.00	0.09	0.30	0.11	0.00	0.00	0.00	0.00	0.00	0.01	0.02	0.00
CaO	8.95	1.50	11.43	1.25	8.90	8.78	7.66	7.35	7.95	0.00	0.20	0.00
BaO	0.00	0.03	0.02	0.01	0.00	0.00	0.00	0.01	0.01	3.34	3.57	4.23
Na2O	6.47	7.29	4.89	6.93	6.56	6.78	7.42	7.57	7.17	1.33	1.33	1.31
K2O	0.05	3.41	1.34	3.74	0.06	0.05	0.06	0.06	0.06	13.29	12.30	12.74
Total (W%)	99.03	98.77	99.68	98.44	98.22	99.74	99.85	99.49	99.497	99.273	98.239	98.84
Si	2.58	2.70	2.57	2.69	2.57	2.58	2.64	2.65	2.63	2.97	2.96	2.96
Ti	0.00	0.00	0.00	0.00	0.00	0.00	0.00	0.00	0.00	0.00	0.00	0.00
Al	1.41	1.39	1.31	1.42	1.41	1.41	1.35	1.34	1.36	1.02	1.04	1.03
Cr	0.00	0.00	0.00	0.00	0.00	0.00	0.00	0.00	0.00	0.00	0.00	0.00
Fe	0.00	0.01	0.04	0.01	0.01	0.00	0.00	0.00	0.00	0.00	0.00	0.00
Mn	0.00	0.00	0.00	0.00	0.00	0.00	0.00	0.00	0.00	0.00	0.00	0.00
Mg	0.00	0.01	0.02	0.01	0.00	0.00	0.00	0.00	0.00	0.00	0.00	0.00
Ca	0.43	0.07	0.56	0.06	0.44	0.42	0.37	0.35	0.38	0.00	0.01	0.00
Ba	0.00	0.00	0.00	0.00	0.00	0.00	0.00	0.00	0.00	0.06	0.07	0.08
Na	0.57	0.64	0.43	0.61	0.58	0.59	0.64	0.66	0.62	0.12	0.12	0.12
K	0.00	0.20	0.08	0.22	0.00	0.00	0.00	0.00	0.00	0.80	0.75	0.77
Total-Cations	5.00	5.02	5.01	5.01	5.01	5.01	5.01	5.01	5.00	4.98	4.96	4.97
Total-Oxygen	8.00	8.00	8.00	8.00	8.00	8.00	8.00	8.00	8.00	8.00	8.00	8.00
End Member Mole (%)												
An	43.23	8.00	52.26	6.87	42.67	41.59	36.21	34.81	37.87	0.00	1.15	0.00
Ab	56.51	70.36	40.46	68.73	56.98	58.15	63.46	64.85	61.81	13.21	13.97	13.51
Or	0.26	21.64	7.28	24.40	0.35	0.25	0.33	0.34	0.31	86.79	84.89	86.49
Sample no.	SS-032	SS-032	SS-034	SS-034	SS-034	SS-034	SS-034	SS-034	SS-034	SS-034	SS-034	SS-056
Mineral	Mc	Mc	Mc	Mc	Mc	Mc	Mc	Mc	Mc	Mc	Mc	Mc
Crystal-Spot	3.61	1.8	1.9	1.10	2.44	2.45	2.46	3.53	3.54	4.55	5.56	1.21
SiO2	62.76	64.00	64.47	64.96	64.43	64.18	64.82	64.07	64.22	64.62	63.95	63.81
TiO2	0.00	0.00	0.00	0.00	0.00	0.00	0.00	0.00	0.00	0.00	0.00	0.00
Al2O3	18.24	19.42	19.88	19.60	19.51	19.33	18.31	19.79	19.48	19.68	18.64	18.91
Cr2O3	0.01	0.00	0.00	0.01	0.04	0.00	0.00	0.03	0.00	0.00	0.00	0.03
FeO	0.05	0.08	0.03	0.07	0.05	0.05	0.04	0.05	0.02	0.00	0.05	0.02
MnO	0.02	0.03	0.01	0.02	0.01	0.02	0.01	0.00	0.00	0.01	0.00	0.11
MgO	0.00	0.00	0.03	0.02	0.01	0.00	0.02	0.00	0.01	0.01	0.00	0.00
CaO	0.01	0.07	0.02	0.10	0.03	0.04	0.03	0.07	0.05	0.06	0.07	0.01
BaO	2.86	0.00	0.00	0.00	0.00	0.00	0.00	0.00	0.00	0.00	0.00	1.02

Sample no.	SS-002	SS-002	SS-002	SS-002	SS-002	SS-002	SS-002	SS-002	SS-002	SS-032	SS-032	SS-032
Mineral	Pl	Pl	Pl	Pl	Pl	Pl	Pl	Pl	Pl	Mc	Mc	Mc
Crystal-Spot	1.13	1.14	1.15	1.16	1.17	2.18	2.19	2.20	2.21	1.58	1.59	2.60
Na2O	1.31	0.97	1.28	0.70	1.08	1.51	1.21	0.97	0.74	1.19	0.92	0.61
K2O	13.29	14.94	14.43	15.19	14.82	14.31	14.56	15.12	15.31	14.96	15.19	15.02
Total (W%)	98.54	99.49	100.17	100.67	99.98	99.44	98.99	100.10	99.82	100.53	98.82	99.53
Si	2.98	2.96	2.95	2.97	2.96	2.96	3.00	2.95	2.96	2.96	2.98	2.98
Ti	0.00	0.00	0.00	0.00	0.00	0.00	0.00	0.00	0.00	0.00	0.00	0.00
Al	1.02	1.06	1.07	1.05	1.06	1.05	1.00	1.07	1.06	1.06	1.02	1.04
Cr	0.00	0.00	0.00	0.00	0.00	0.00	0.00	0.00	0.00	0.00	0.00	0.00
Fe	0.00	0.00	0.00	0.00	0.00	0.00	0.00	0.00	0.00	0.00	0.00	0.00
Mn	0.00	0.00	0.00	0.00	0.00	0.00	0.00	0.00	0.00	0.00	0.00	0.00
Mg	0.00	0.00	0.00	0.00	0.00	0.00	0.00	0.00	0.00	0.00	0.00	0.00
Ca	0.00	0.00	0.00	0.00	0.00	0.00	0.00	0.00	0.00	0.00	0.00	0.00
Ba	0.05	0.00	0.00	0.00	0.00	0.00	0.00	0.00	0.00	0.00	0.00	0.02
Na	0.12	0.09	0.11	0.06	0.10	0.13	0.11	0.09	0.07	0.11	0.08	0.05
K	0.80	0.88	0.84	0.88	0.87	0.84	0.86	0.89	0.90	0.87	0.90	0.90
Total-Cations	4.98	4.99	4.99	4.98	4.99	5.00	4.98	5.00	4.99	5.00	5.00	5.00
Total-Oxygen	8.00	8.00	8.00	8.00	8.00	8.00	8.00	8.00	8.00	8.00	8.00	8.00
End Member Mole (%)												
An	0.06	0.33	0.12	0.49	0.17	0.20	0.16	0.36	0.23	0.29	0.34	0.03
Ab	12.98	8.92	11.90	6.55	9.99	13.75	11.21	8.85	6.83	10.74	8.39	5.78
Or	86.96	90.75	87.98	92.96	89.84	86.05	88.62	90.79	92.94	88.97	91.27	94.19
Sample no.	SS-056	SS-057	SS-057	SS-057	SS-057	SS-057	SS-057	SS-057	SS-057	SS-060	SS-060	SS-060
Mineral	Mc	Mc	Mc	Mc	Mc	Mc	Mc	Mc	Mc	Mc	Mc	Mc
Crystal-Spot	1.22	1.4	2.5	3.16	3.17	4.18	4.19	4.20	5.10	1.16	1.17	1.18
SiO2	63.96	60.92	64.51	63.15	62.67	61.92	61.11	61.55	60.99	63.73	64.05	63.72
TiO2	0.00	0.00	0.00	0.00	0.00	0.00	0.00	0.00	0.00	0.00	0.00	0.00
Al2O3	18.62	19.57	19.79	19.33	19.21	19.71	19.85	19.81	19.89	18.84	18.85	18.86
Cr2O3	0.03	0.00	0.00	0.02	0.00	0.00	0.01	0.00	0.01	0.01	0.00	0.00
FeO	0.00	0.14	0.05	0.01	0.04	0.04	0.00	0.00	0.04	0.04	0.02	0.01
MnO	0.04	0.21	0.21	0.00	0.06	0.04	0.05	0.02	0.22	0.10	0.04	0.06
MgO	0.01	0.01	0.00	0.00	0.01	0.00	0.00	0.02	0.01	0.01	0.00	0.01
CaO	0.00	0.02	0.01	0.06	0.09	0.00	0.02	0.02	0.00	0.06	0.00	0.03
BaO	0.99	4.38	3.43	2.84	2.87	4.38	5.08	4.53	4.78	0.85	0.67	0.81
Na2O	0.23	0.89	4.82	1.62	1.26	1.07	1.15	1.30	0.67	0.23	0.39	0.41
K2O	15.70	12.89	7.82	12.75	13.31	12.99	12.70	12.92	13.24	15.21	15.28	15.65
Total (W%)	99.56	99.02	100.64	99.78	99.51	100.15	99.96	100.16	99.85	99.07	99.30	99.55
Si	2.99	2.92	2.97	2.96	2.96	2.93	2.91	2.91	2.91	3.00	3.00	2.97
Ti	0.00	0.00	0.00	0.00	0.00	0.00	0.00	0.00	0.00	0.00	0.00	0.00
Al	1.03	1.11	1.07	1.07	1.07	1.10	1.11	1.10	1.12	1.04	1.04	1.04
Cr	0.00	0.00	0.00	0.00	0.00	0.00	0.00	0.00	0.00	0.00	0.00	0.00
Fe	0.00	0.01	0.00	0.00	0.00	0.00	0.00	0.00	0.00	0.00	0.00	0.00
Mn	0.00	0.01	0.01	0.00	0.00	0.00	0.00	0.00	0.01	0.00	0.00	0.00

Sample no.	SS-002	SS-002	SS-002	SS-002	SS-002	SS-002	SS-002	SS-002	SS-002	SS-032	SS-032	SS-032
Mineral	Pl	Pl	Pl	Pl	Pl	Pl	Pl	Pl	Pl	Mc	Mc	Mc
Crystal-Spot	1.13	1.14	1.15	1.16	1.17	2.18	2.19	2.20	2.21	1.58	1.59	2.60
Mg	0.00	0.00	0.00	0.00	0.00	0.00	0.00	0.00	0.00	0.00	0.00	0.00
Ca	0.00	0.00	0.00	0.00	0.00	0.00	0.00	0.00	0.00	0.00	0.00	0.00
Ba	0.02	0.08	0.06	0.05	0.05	0.08	0.09	0.08	0.09	0.02	0.01	0.01
Na	0.02	0.08	0.43	0.15	0.11	0.10	0.11	0.12	0.06	0.02	0.04	0.04
K	0.94	0.79	0.46	0.76	0.80	0.78	0.77	0.78	0.81	0.91	0.91	0.93
Total-Cations	5.00	5.00	5.00	5.00	5.00	5.00	5.00	5.00	5.00	5.00	5.00	5.00
Total-Oxygen	8.00	8.00	8.00	8.00	8.00	8.00	8.00	8.00	8.00	8.00	8.00	8.00
End Member Mole (%)												
An	0.00	0.11	0.07	0.32	0.48	0.00	0.09	0.09	0.00	0.31	0.00	0.133959
Ab	2.13	9.49	48.33	16.12	12.49	11.10	12.05	13.26	7.14	2.27	3.73	3.850676
Or	97.87	90.40	51.60	83.56	87.03	88.90	87.86	86.65	92.86	97.42	96.27	96.01536

Sample no.	SS-060	SS-060	SS-060	SS-060	SS-060	SS-060
Mineral	Mc	Mc	Mc	Mc	Mc	Mc
Crystal-Spot	2.25	2.26	2.27	3.44	3.45	3.46
SiO2	64.03	64.59	64.47	63.09	62.17	63.94
TiO2	0.00	0.00	0.00	0.00	0.00	0.00
Al2O3	18.95	18.89	18.96	18.87	18.07	18.86
Cr2O3	0.01	0.00	0.02	0.00	0.01	0.03
FeO	0.03	0.02	0.06	0.04	0.40	0.06
MnO	0.01	0.03	0.08	0.14	1.92	0.18
MgO	0.00	0.00	0.01	0.00	2.37	0.02
CaO	0.00	0.00	0.00	0.02	0.18	0.01
BaO	0.65	0.60	0.56	1.33	0.56	0.76
Na2O	0.33	0.62	0.61	0.67	0.59	0.52
K2O	16.00	15.44	15.59	15.06	14.00	15.25
Total (W%)	100.00	100.19	100.34	99.22	100.28	99.62
Si	2.97	2.99	2.98	2.96	2.87	2.98
Ti	0.00	0.00	0.00	0.00	0.00	0.00
Al	1.04	1.03	1.03	1.04	0.98	1.04
Cr	0.00	0.00	0.00	0.00	0.00	0.00
Fe	0.00	0.00	0.00	0.00	0.02	0.00
Mn	0.00	0.00	0.00	0.01	0.07	0.01
Mg	0.00	0.00	0.00	0.00	0.16	0.00
Ca	0.00	0.00	0.00	0.00	0.01	0.00
Ba	0.01	0.01	0.01	0.02	0.01	0.01
Na	0.03	0.06	0.05	0.06	0.05	0.05
K	0.95	0.91	0.92	0.90	0.82	0.91
Total-Cations	5.00	5.00	5.00	5.00	5.00	5.00
Total-Oxygen	8.00	8.00	8.00	8.00	8.00	8.00
End Member Mole (%)						
An	0.00	0.00	0.00	0.08	1.02	0.04

Sample no.	SS-002	SS-002	SS-002	SS-002	SS-002	SS-002	SS-002	SS-002	SS-002	SS-032	SS-032	SS-032
Mineral	Pl	Pl	Pl	Pl	Pl	Pl	Pl	Pl	Pl	Mc	Mc	Mc
Crystal-Spot	1.13	1.14	1.15	1.16	1.17	2.18	2.19	2.20	2.21	1.58	1.59	2.60
Ab	3.00	5.74	5.60	6.34	5.96	4.94						
Or	97.00	94.26	94.40	93.57	93.02	95.02						

1E – Representative microprobe analyses of pyroxenoids from Buritirama Formation.

Sample no.	SS-056	SS-056	SS-056	SS-056	SS-056	SS-056	SS-056	SS-056	SS-056	SS-056	SS-058	SS-058	SS-058
Mineral	Rdn	Rdn	Rdn	Rdn	Rdn	Rdn	Rdn	Rdn	Rdn	Rdn	Rdn	Rdn	Rdn
Crystal-Spot	1.5	1.6	2.13	2.14	3.27	3.28	4.29	4.30	5.46	5.47	1.1	1.2	1.3
SiO2	46.98	47.10	47.78	47.97	47.56	47.22	47.07	47.04	46.78	46.40	48.24	48.14	47.58
TiO2	0.00	0.00	0.02	0.01	0.01	0.01	0.00	0.00	0.00	0.00	0.00	0.00	0.00
Al2O3	0.05	0.02	0.05	0.00	0.03	0.01	0.04	0.00	0.00	0.08	0.04	0.01	0.03
Cr2O3	0.02	0.01	0.00	0.05	0.00	0.00	0.00	0.00	0.02	0.04	0.00	0.00	0.01
FeO	0.85	0.86	1.09	1.09	0.80	0.89	0.76	0.89	0.58	0.56	2.39	2.41	2.33
MnO	44.03	43.94	41.69	42.83	43.23	44.21	43.68	43.73	45.46	44.12	40.81	40.54	41.23
MgO	3.25	3.23	5.93	5.71	3.93	3.71	3.46	3.52	2.99	2.84	7.37	6.99	7.22
CaO	4.13	4.07	2.57	2.13	4.22	4.25	4.31	4.30	4.44	4.66	1.07	1.09	1.14
Na2O	0.05	0.01	0.00	0.04	0.04	0.05	0.00	0.00	0.03	0.06	0.00	0.01	0.01
K2O	0.03	0.02	0.02	0.00	0.01	0.01	0.01	0.01	0.02	0.04	0.00	0.01	0.00
Total (W%)	99.39	99.26	99.13	99.82	99.81	100.35	99.33	99.50	100.32	98.79	99.93	99.19	99.55
Si	1.00	1.00	1.00	1.00	1.00	0.99	1.00	1.00	0.99	0.99	1.00	0.99	0.98
Ti	0.00	0.00	0.00	0.00	0.00	0.00	0.00	0.00	0.00	0.00	0.00	0.00	0.00
Al	0.00	0.00	0.00	0.00	0.00	0.00	0.00	0.00	0.00	0.00	0.00	0.00	0.00
Cr	0.00	0.00	0.00	0.00	0.00	0.00	0.00	0.00	0.00	0.00	0.00	0.00	0.00
Fe	0.02	0.02	0.02	0.02	0.01	0.02	0.01	0.02	0.01	0.01	0.04	0.04	0.04
Mn	0.79	0.79	0.74	0.76	0.77	0.79	0.78	0.78	0.81	0.80	0.71	0.71	0.72
Mg	0.10	0.10	0.18	0.18	0.12	0.12	0.11	0.11	0.09	0.09	0.23	0.22	0.22
Ca	0.09	0.09	0.06	0.05	0.09	0.10	0.10	0.10	0.10	0.11	0.02	0.02	0.03
Na	0.00	0.00	0.00	0.00	0.00	0.00	0.00	0.00	0.00	0.00	0.00	0.00	0.00
K	0.00	0.00	0.00	0.00	0.00	0.00	0.00	0.00	0.00	0.00	0.00	0.00	0.00
Total-Cations	2.00	2.00	2.00	2.00	2.00	2.01	2.00	2.00	2.01	2.01	2.00	1.99	1.99
Total-Oxygen	3.00	3.00	3.00	3.00	3.00	3.00	3.00	3.00	3.00	3.00	3.00	3.00	3.00

Sample no.	SS-058	SS-058	SS-058	SS-058	SS-058	SS-058	SS-058	SS-060	SS-060	SS-060
Mineral	Rdn	Rdn	Rdn	Rdn	Rdn	Rdn	Rdn	Rdn	Rdn	Rdn
Crystal-Spot	1.4	1.5	1.6	2.7	2.8	2.9	2.10	1.69	2.70	3.72
SiO2	48.64	47.81	47.96	47.94	47.90	47.67	47.94	46.31	45.66	47.49
TiO2	0.01	0.02	0.00	0.02	0.02	0.00	0.02	0.00	0.00	0.00
Al2O3	0.04	0.00	0.00	0.03	0.02	0.00	0.01	0.02	0.00	0.02
Cr2O3	0.00	0.02	0.03	0.00	0.03	0.01	0.00	0.00	0.00	0.00
FeO	2.36	2.36	2.38	2.52	2.36	2.40	2.27	0.65	0.79	0.77
MnO	40.68	40.58	41.47	41.35	40.13	41.10	41.39	47.78	46.91	44.52
MgO	7.50	7.35	6.93	7.12	7.33	7.27	6.82	2.90	3.14	5.08
CaO	1.13	1.14	1.10	1.05	1.05	1.10	1.11	1.34	1.57	1.09

Na2O	0.04	0.01	0.02	0.04	0.03	0.00	0.00	0.06	0.04	0.00
K2O	0.01	0.00	0.01	0.00	0.00	0.00	0.01	0.02	0.01	0.01
Total (W%)	100.39	99.29	99.90	100.08	98.86	99.55	99.57	99.07	98.11	98.99
Si	1.00	0.99	0.99	0.99	0.99	0.98	0.99	1.00	0.98	1.02
Ti	0.00	0.00	0.00	0.00	0.00	0.00	0.00	0.00	0.00	0.00
Al	0.00	0.00	0.00	0.00	0.00	0.00	0.00	0.00	0.00	0.00
Cr	0.00	0.00	0.00	0.00	0.00	0.00	0.00	0.00	0.00	0.00
Fe	0.04	0.04	0.04	0.04	0.04	0.04	0.04	0.01	0.01	0.01
Mn	0.71	0.71	0.73	0.72	0.70	0.72	0.72	0.87	0.85	0.81
Mg	0.23	0.23	0.21	0.22	0.23	0.22	0.21	0.09	0.10	0.16
Ca	0.02	0.03	0.02	0.02	0.02	0.02	0.02	0.03	0.04	0.03
Na	0.00	0.00	0.00	0.00	0.00	0.00	0.00	0.00	0.00	0.00
K	0.00	0.00	0.00	0.00	0.00	0.00	0.00	0.00	0.00	0.00
Total-Cations	2.02	1.99	2.00	2.00	1.98	1.99	1.99	2.01	1.99	2.04
Total-Oxygen	3.00	3.00	3.00	3.00	3.00	3.00	3.00	3.00	3.00	3.00

1F – Representative microprobe analyses of amphiboles from Buritirama Formation.

Sample no.	SS-002	SS-002	SS-002	SS-002	SS-002	SS-002	SS-002	SS-002	SS-010	SS-010	SS-010	SS-010	SS-037
Mineral	Cum	Cum	Cum	Cum	Cum	Cum	Cum	Cum	Tr	Tr	Tr	Tr	Tr
Crystal-Spot	1.1	1.2	1.3	2.4	2.5	2.6	2.7	2.8	1.11	1.12	1.13	1.14	1.19
SiO2	55.78	55.25	55.41	55.65	55.99	55.01	55.52	55.55	53.73	56.29	56.54	56.66	56.31
TiO2	0.06	0.09	0.06	0.07	0.06	0.03	0.04	0.04	0.11	0.08	0.07	0.07	0.08
Al2O3	1.09	1.44	0.94	1.33	1.00	0.93	1.15	1.04	4.51	2.29	2.44	2.27	2.48
FeO	19.60	19.59	19.84	19.66	19.46	19.62	19.48	19.80	2.24	1.59	1.76	1.61	1.86
MnO	0.49	0.49	0.50	0.48	0.45	0.46	0.48	0.48	0.12	0.08	0.10	0.09	0.05
MgO	19.12	18.51	19.68	18.95	19.19	20.02	19.14	19.44	21.93	23.68	23.82	23.58	22.76
CaO	1.28	1.50	1.10	1.28	1.11	1.01	1.41	1.03	12.89	13.03	12.34	12.57	12.62
Na2O	0.08	0.12	0.08	0.11	0.09	0.08	0.13	0.07	1.07	0.55	0.61	0.51	0.87
K2O	0.02	0.03	0.01	0.02	0.01	0.01	0.02	0.04	0.34	0.18	0.18	0.17	0.15
Total (W%)	97.53	97.00	97.61	97.55	97.36	97.18	97.35	97.49	96.95	97.77	97.87	97.53	97.18
Si	8.00	7.59	7.61	7.64	7.69	7.94	7.62	7.63	7.47	7.67	7.71	7.72	7.75
Ti	0.01	0.01	0.01	0.01	0.01	0.00	0.00	0.01	0.01	0.01	0.01	0.01	0.01
Al	0.18	0.23	0.15	0.21	0.16	0.16	0.19	0.17	0.74	0.37	0.39	0.36	0.40
Fe	2.35	2.25	2.28	2.26	2.24	2.37	2.24	2.27	0.26	0.18	0.20	0.18	0.21
Mn	0.06	0.06	0.06	0.06	0.05	0.06	0.06	0.06	0.01	0.01	0.01	0.01	0.01
Mg	4.09	3.79	4.03	3.88	3.93	4.31	3.92	3.98	4.55	4.81	4.84	4.79	4.67
Ca	0.20	0.22	0.16	0.19	0.16	0.16	0.21	0.15	1.92	1.90	1.80	1.84	1.86
Na	0.02	0.03	0.02	0.03	0.02	0.02	0.03	0.02	0.29	0.15	0.16	0.14	0.23
K	0.00	0.01	0.00	0.00	0.00	0.00	0.00	0.01	0.06	0.03	0.03	0.03	0.03
H	2.00	2.00	2.00	2.00	2.00	2.00	2.00	2.00	2.00	2.00	2.00	2.00	2.00
Total-Cations	16.91	16.18	16.32	16.28	16.26	17.02	16.27	16.29	17.32	17.13	17.16	17.08	17.17
Total-Oxygen	23.00	23.00	23.00	23.00	23.00	23.00	23.00	23.00	23.00	23.00	23.00	23.00	23.00
Sample no.	SS-037	SS-056	SS-056	SS-056	SS-056	SS-056							

Mineral	Tr	Mn-Cum	Mn-Cum	Mn-Cum	Mn-Cum	Mn-Cum
Crystal-Spot	1.20	1.9	1.11	2.34	2.35	2.36
SiO2	56.98	55.42	55.14	55.06	55.12	54.87
TiO2	0.03	0.01	0.01	0.01	0.00	0.00
Al2O3	2.13	0.10	0.11	0.10	0.06	0.08
FeO	1.55	1.30	1.30	1.23	1.24	1.16
MnO	0.14	18.11	17.72	16.75	17.39	17.12
MgO	23.07	19.92	20.05	20.06	20.48	20.24
CaO	12.92	1.42	1.44	1.91	1.67	1.77
Na2O	0.72	0.09	0.07	0.06	0.07	0.05
K2O	0.15	0.01	0.01	0.02	0.03	0.01
Total (W%)	97.70	96.37	95.85	95.20	96.05	95.29
Si	7.76	7.98	8.05	8.04	7.97	8.00
Ti	0.00	0.00	0.00	0.00	0.00	0.00
Al	0.34	0.02	0.02	0.02	0.01	0.01
Fe	0.18	0.16	0.16	0.15	0.15	0.14
Mn	0.02	2.21	2.19	2.07	2.13	2.11
Mg	4.68	4.28	4.36	4.37	4.41	4.40
Ca	1.89	0.22	0.23	0.30	0.26	0.28
Na	0.19	0.02	0.02	0.02	0.02	0.01
K	0.03	0.00	0.00	0.00	0.00	0.00
H	2.00	2.00	2.00	2.00	2.00	2.00
Total-Cations	17.08	16.89	17.02	16.96	16.96	16.96
Total-Oxygen	23.00	23.00	23.00	23.00	23.00	23.00

1G – Representative microprobe analyses of micas from Buritirama Formation.

Sample no.	SS-002	SS-002	SS-002	SS-002	SS-002	SS-002	SS-002	SS-002	SS-002	SS-002	SS-002	SS-002	SS-002
Mineral	Bt	Bt	Bt	Bt	Bt	Bt	Bt	Bt	Bt	Bt	Bt	Bt	Bt
Crystal-Spot	1.9	1.10	1.11	1.12	2.30	2.31	2.32	2.33	2.34	2.35	2.36	3.49	3.50
SiO2	39.84	39.25	39.30	39.26	39.55	39.36	38.69	39.71	39.39	39.22	39.96	39.10	39.51
TiO2	2.46	2.66	2.68	2.62	3.01	2.92	2.71	2.94	2.98	2.92	2.74	2.17	2.29
Al2O3	15.43	15.77	15.66	15.78	15.57	15.73	15.89	15.76	15.50	15.16	15.77	15.48	16.08
FeO	14.95	14.02	13.71	13.91	13.38	13.39	13.69	13.20	13.66	13.60	13.79	14.72	13.81
MnO	0.04	0.04	0.06	0.04	0.02	0.04	0.03	0.03	0.03	0.04	0.06	0.05	0.06
MgO	14.46	14.58	14.90	14.74	14.69	15.06	15.34	14.99	14.43	14.30	14.47	15.69	14.89
CaO	0.07	0.05	0.10	0.09	0.02	0.01	0.02	0.03	0.09	0.11	0.50	0.36	0.02
Na2O	0.23	0.21	0.21	0.20	0.31	0.37	0.32	0.29	0.31	0.32	0.24	0.16	0.29
K2O	8.34	8.77	8.92	8.74	8.85	8.75	7.90	8.87	8.65	8.36	6.84	7.45	8.77
F	0.00	0.00	0.00	0.00	0.00	0.00	0.00	0.00	0.00	0.00	0.00	0.00	0.00
Cl	0.00	0.00	0.00	0.00	0.00	0.00	0.00	0.00	0.00	0.00	0.00	0.00	0.00
H2O*	4.10	4.08	4.09	4.08	4.09	4.10	4.07	4.12	4.08	4.04	4.09	4.08	4.10
Total (W%)	99.92	99.43	99.62	99.46	99.49	99.72	98.65	99.93	99.13	98.06	98.46	99.27	99.82
Si	5.83	5.77	5.76	5.76	5.79	5.75	5.70	5.78	5.80	5.83	5.85	5.74	5.77

Al iv	2.17	2.23	2.24	2.24	2.21	2.25	2.30	2.22	2.21	2.17	2.15	2.26	2.23
Al vi	0.49	0.50	0.47	0.49	0.48	0.46	0.46	0.49	0.48	0.48	0.58	0.42	0.54
Ti	0.27	0.29	0.30	0.29	0.33	0.32	0.30	0.32	0.33	0.33	0.30	0.24	0.25
Cr	0.00	0.00	0.00	0.00	0.00	0.00	0.00	0.00	0.00	0.00	0.00	0.00	0.00
Fe	1.83	1.72	1.68	1.71	1.64	1.64	1.69	1.61	1.68	1.69	1.69	1.81	1.69
Mn	0.01	0.01	0.01	0.00	0.00	0.01	0.00	0.00	0.00	0.01	0.01	0.01	0.01
Mg	3.15	3.19	3.26	3.23	3.21	3.28	3.37	3.26	3.16	3.17	3.16	3.43	3.24
Ca	0.01	0.01	0.02	0.01	0.00	0.00	0.00	0.01	0.01	0.02	0.08	0.06	0.00
Na	0.07	0.06	0.06	0.06	0.09	0.10	0.09	0.08	0.09	0.09	0.07	0.05	0.08
K	1.56	1.64	1.67	1.64	1.65	1.63	1.49	1.65	1.62	1.58	1.28	1.40	1.63
OH*	4.00	4.00	4.00	4.00	4.00	4.00	4.00	4.00	4.00	4.00	4.00	4.00	0.00
Total-Cations	19.38	19.42	19.45	19.43	19.40	19.44	19.40	19.41	19.39	19.36	19.16	19.40	19.45
Sample no.	SS-002	SS-002	SS-010	SS-010	SS-010	SS-010	SS-010	SS-010	SS-010	SS-010	SS-012	SS-012	SS-012
Mineral	Bt	Bt	Phl	Phl	Phl	Phl	Phl	Phl	Phl	Phl	Phl	Phl	Phl
Crystal-Spot	3.51	3.52	1.1	1.2	1.3	1.4	2.21	2.22	2.23	2.24	1.7	2.20	2.22
SiO2	39.69	39.67	39.73	40.17	39.47	39.58	39.91	40.07	39.92	39.95	39.01	40.31	40.13
TiO2	2.16	2.19	0.67	0.67	0.64	0.63	0.60	0.61	0.63	0.64	1.36	1.27	1.25
Al2O3	15.60	15.91	15.98	15.39	16.04	15.78	15.70	15.98	15.84	15.64	16.59	15.98	16.09
FeO	13.69	13.37	2.62	2.42	2.60	2.67	2.37	2.40	2.29	2.29	4.20	4.58	4.75
MnO	0.05	0.02	0.00	0.03	0.03	0.03	0.04	0.02	0.05	0.02	0.05	0.04	0.07
MgO	14.82	15.27	24.25	24.62	24.08	24.36	24.60	25.14	24.62	24.78	22.10	22.23	22.45
CaO	0.06	0.02	0.03	0.02	0.02	0.04	0.06	0.04	0.05	0.03	0.09	0.02	0.02
Na2O	0.26	0.18	0.14	0.07	0.19	0.20	0.22	0.23	0.25	0.22	0.10	0.11	0.13
K2O	8.43	9.01	9.62	9.78	9.99	9.67	10.01	9.97	10.13	10.12	9.64	9.60	9.43
F	0.00	0.00	0.13	0.19	0.21	0.10	0.27	0.11	0.19	0.05	0.27	0.14	0.22
Cl	0.00	0.00	0.03	0.04	0.03	0.03	0.03	0.04	0.04	0.03	0.02	0.06	0.03
H2O*	4.07	4.11	4.18	4.19	4.17	4.17	4.19	4.24	4.20	4.20	4.02	4.12	4.09
Total (W%)	98.84	99.74	97.37	97.58	97.46	97.25	98.01	98.86	98.22	97.95	97.43	98.44	98.65
Si	5.84	5.79	5.70	5.75	5.68	5.69	5.71	5.67	5.69	5.70	5.64	5.76	5.72
Al iv	2.16	2.21	2.30	2.25	2.32	2.31	2.29	2.33	2.31	2.30	2.36	2.24	2.28
Al vi	0.55	0.53	0.40	0.35	0.40	0.37	0.35	0.34	0.36	0.33	0.46	0.45	0.43
Ti	0.24	0.24	0.07	0.07	0.07	0.07	0.06	0.07	0.07	0.07	0.15	0.14	0.13
Cr	0.00	0.00	0.00	0.00	0.00	0.00	0.00	0.00	0.00	0.00	0.00	0.00	0.00
Fe	1.69	1.63	0.31	0.29	0.31	0.32	0.28	0.28	0.27	0.27	0.51	0.55	0.57
Mn	0.01	0.00	0.00	0.00	0.00	0.00	0.00	0.00	0.01	0.00	0.01	0.00	0.01
Mg	3.25	3.32	5.18	5.25	5.16	5.22	5.24	5.30	5.24	5.27	4.76	4.73	4.77
Ca	0.01	0.00	0.00	0.00	0.00	0.01	0.01	0.01	0.01	0.00	0.01	0.00	0.00
Na	0.07	0.05	0.04	0.02	0.05	0.06	0.06	0.06	0.07	0.06	0.03	0.03	0.04
K	1.58	1.68	1.76	1.79	1.83	1.77	1.83	1.80	1.84	1.84	1.78	1.75	1.72
OH*	4.00	4.00	4.00	4.00	4.00	4.00	4.00	4.00	4.00	4.00	4.00	4.00	4.00
Total-Cations	19.39	19.46	19.78	19.78	19.84	19.82	19.85	19.86	19.86	19.86	19.71	19.65	19.67
Sample no.	SS-012	SS-012	SS-012	SS-012	SS-012	SS-012	SS-012	SS-012	SS-012	SS-012	SS-012	SS-012	SS-012
Mineral	Phl	Phl	Phl	Phl	Phl	Phl	Phl	Phl	Phl	Phl	Phl	Phl	Phl

Crystal-Spot	3.23	4.24	4.25	5.26	6.30	6.31	6.32	7.33	7.34	7.35	8.52	8.53	8.54
SiO2	40.33	40.98	40.30	40.85	40.80	40.27	40.66	40.47	40.20	40.57	40.79	39.09	40.15
TiO2	1.32	1.29	1.34	1.36	1.20	1.21	1.20	1.24	1.25	1.32	1.31	1.30	1.28
Al2O3	15.43	15.76	15.96	16.11	15.03	15.26	15.79	15.54	15.62	15.90	16.17	16.26	15.61
FeO	4.83	4.68	4.47	4.51	4.58	4.77	4.69	4.61	4.43	5.05	5.27	5.12	5.19
MnO	0.14	0.07	0.09	0.04	0.08	0.07	0.07	0.06	0.08	0.06	0.09	0.11	0.07
MgO	22.26	22.45	22.32	22.31	21.81	22.21	22.75	22.28	22.19	22.05	22.02	22.41	22.52
CaO	0.07	0.06	0.03	0.02	0.05	0.05	0.06	0.07	0.09	0.08	0.04	0.06	0.02
Na2O	0.07	0.13	0.11	0.10	0.13	0.11	0.12	0.09	0.10	0.13	0.15	0.16	0.14
K2O	9.58	9.74	9.61	9.46	9.81	9.84	9.43	9.57	9.56	9.46	9.44	9.46	9.33
F	0.23	0.16	0.20	0.26	0.43	0.29	0.18	0.32	0.17	0.15	0.08	0.29	0.14
Cl	0.04	0.04	0.04	0.04	0.04	0.04	0.06	0.05	0.04	0.05	0.05	0.04	0.05
H2O*	4.06	4.16	4.10	4.10	3.95	4.02	4.13	4.02	4.08	4.13	4.19	4.02	4.12
Total (W%)	98.36	99.52	98.55	99.16	97.91	98.14	99.13	98.34	97.82	98.95	99.60	98.32	98.61
Si	5.78	5.79	5.75	5.78	5.87	5.79	5.77	5.79	5.78	5.77	5.77	5.62	5.74
Al iv	2.22	2.21	2.25	2.22	2.13	2.21	2.23	2.21	2.22	2.23	2.23	2.38	2.26
Al vi	0.39	0.42	0.43	0.47	0.42	0.38	0.41	0.42	0.43	0.44	0.46	0.38	0.37
Ti	0.14	0.14	0.14	0.14	0.13	0.13	0.13	0.13	0.14	0.14	0.14	0.14	0.14
Cr	0.00	0.00	0.00	0.00	0.00	0.00	0.00	0.00	0.00	0.00	0.00	0.00	0.00
Fe	0.58	0.55	0.53	0.53	0.55	0.57	0.56	0.55	0.53	0.60	0.62	0.62	0.62
Mn	0.02	0.01	0.01	0.01	0.01	0.01	0.01	0.01	0.01	0.01	0.01	0.01	0.01
Mg	4.76	4.73	4.75	4.71	4.68	4.76	4.81	4.75	4.76	4.68	4.64	4.81	4.80
Ca	0.01	0.01	0.00	0.00	0.01	0.01	0.01	0.01	0.01	0.01	0.01	0.01	0.00
Na	0.02	0.04	0.03	0.03	0.04	0.03	0.03	0.03	0.03	0.04	0.04	0.04	0.04
K	1.75	1.76	1.75	1.71	1.80	1.81	1.70	1.75	1.75	1.72	1.70	1.74	1.70
OH*	4.00	4.00	4.00	4.00	4.00	4.00	4.00	4.00	4.00	4.00	4.00	4.00	4.00
Total-Cations	19.66	19.65	19.65	19.60	19.64	19.70	19.66	19.65	19.65	19.63	19.62	19.75	19.68
Sample no.	SS-012	SS-032	SS-032	SS-032	SS-032	SS-032	SS-032	SS-032	SS-032	SS-032	SS-032	SS-032	SS-032
Mineral	Phl	Mn-Phl	Mn-Phl	Mn-Phl	Mn-Phl	Mn-Phl	Mn-Phl	Mn-Phl	Mn-Phl	Mn-Phl	Mn-Phl	Mn-Phl	Mn-Phl
Crystal-Spot	8.55	1.14	2.33	2.34	2.35	2.36	3.37	3.38	3.39	3.40	4.72	4.73	4.74
SiO2	40.33	40.56	40.17	39.68	39.96	40.15	40.23	39.61	40.23	40.16	40.26	40.79	40.17
TiO2	1.32	1.04	1.32	1.34	1.37	1.33	1.32	1.31	1.29	1.36	1.81	1.77	2.05
Al2O3	15.63	14.11	14.68	15.67	15.39	15.54	15.19	15.24	15.09	15.40	15.80	15.12	14.99
FeO	5.12	3.23	3.25	3.25	3.32	3.19	3.19	3.22	3.06	3.20	3.55	3.14	3.44
MnO	0.07	3.19	3.31	3.40	3.31	3.40	3.30	3.31	3.20	3.39	2.91	3.09	3.13
MgO	21.85	23.00	22.20	22.14	22.01	21.97	22.16	21.97	22.14	21.94	21.99	21.26	22.16
CaO	0.03	0.07	0.11	0.06	0.06	0.05	0.09	0.18	0.13	0.21	0.01	0.22	0.00
Na2O	0.14	0.15	0.10	0.08	0.08	0.08	0.10	0.09	0.09	0.07	0.09	0.10	0.11
K2O	9.48	9.34	9.47	8.87	9.46	9.44	8.99	9.13	9.66	9.24	9.00	7.31	8.80
SrO	0.12	0.00	0.00	0.00	0.00	0.00	0.00	0.00	0.00	0.00	0.00	0.00	0.00
BaO	0.03	0.00	0.00	0.00	0.00	0.00	0.00	0.00	0.00	0.00	0.00	0.00	0.00
H2O*	4.12	4.18	4.17	4.18	4.19	4.20	4.19	4.16	4.19	4.31	4.34	4.29	4.31
Total (W%)	98.23	98.87	98.79	98.66	99.14	99.35	98.75	98.21	99.08	99.28	99.76	97.08	99.16
Si	5.78	5.81	5.77	5.69	5.72	5.73	5.76	5.72	5.76	5.59	5.56	5.71	5.59

Al iv	2.22	2.19	2.23	2.31	2.28	2.27	2.24	2.28	2.24	2.41	2.44	2.29	2.41
Al vi	0.43	0.20	0.26	0.34	0.31	0.34	0.32	0.31	0.30	0.12	0.13	0.20	0.04
Ti	0.14	0.11	0.14	0.14	0.15	0.14	0.14	0.14	0.14	0.14	0.19	0.19	0.21
Cr	0.00	0.00	0.00	0.00	0.00	0.00	0.00	0.00	0.00	0.00	0.00	0.00	0.00
Fe	0.61	0.39	0.39	0.39	0.40	0.38	0.38	0.39	0.37	0.37	0.41	0.37	0.40
Mn	0.01	0.39	0.40	0.41	0.40	0.41	0.40	0.40	0.39	0.40	0.34	0.37	0.37
Mg	4.67	4.91	4.75	4.73	4.69	4.67	4.73	4.73	4.72	4.55	4.53	4.43	4.59
Ca	0.01	0.01	0.02	0.01	0.01	0.01	0.01	0.03	0.02	0.03	0.00	0.03	0.00
Na	0.04	0.04	0.03	0.02	0.02	0.02	0.03	0.02	0.03	0.02	0.02	0.03	0.03
K	1.73	1.71	1.74	1.62	1.73	1.72	1.64	1.68	1.76	1.64	1.59	1.30	1.56
OH*	4.00	4.00	4.00	4.00	4.00	4.00	4.00	4.00	4.00	4.00	4.00	4.00	4.00
Total-Cations	19.64	19.76	19.73	19.67	19.71	19.69	19.65	19.70	19.73	19.28	19.21	18.92	19.21
Sample no.	SS-032	SS-034	SS-034	SS-034	SS-034	SS-034	SS-034	SS-034	SS-034	SS-034	SS-034	SS-034	SS-034
Mineral	Mn-Phl	Phl	Phl	Phl	Phl	Phl	Phl	Phl	Phl	Phl	Phl	Phl	Phl
Crystal-Spot	4.75	1.11	1.12	2.13	2.14	2.15	3.16	3.17	3.18	4.23	4.24	4.25	5.26
SiO2	40.21	40.01	40.85	41.00	40.86	40.11	40.57	40.93	40.79	40.62	40.89	40.97	40.82
TiO2	2.16	0.94	0.95	0.96	0.86	0.97	0.92	0.94	0.88	0.92	0.95	0.90	0.98
Al2O3	14.81	15.33	15.55	15.63	15.04	15.26	15.34	16.00	15.45	15.30	15.53	15.39	15.51
FeO	3.27	3.16	3.27	3.17	3.01	2.94	3.07	3.10	3.22	3.34	3.25	3.08	3.10
MnO	2.81	0.07	0.11	0.17	0.16	0.09	0.10	0.14	0.13	0.12	0.13	0.13	0.15
MgO	21.95	24.05	23.56	23.50	24.89	24.35	24.31	23.98	23.74	23.57	23.44	23.40	23.35
CaO	0.02	0.02	0.00	0.02	0.05	0.01	0.07	0.05	0.07	0.06	0.04	0.28	0.09
Na2O	0.06	0.10	0.09	0.07	0.11	0.08	0.09	0.10	0.08	0.09	0.07	0.10	0.09
K2O	8.58	10.08	10.13	10.11	8.93	10.18	9.95	10.35	9.97	9.93	9.98	9.84	10.15
F	0.00	0.15	0.14	0.22	0.11	0.19	0.32	0.27	0.31	0.18	0.25	0.23	0.18
Cl	0.00	0.08	0.06	0.06	0.05	0.06	0.07	0.07	0.05	0.07	0.07	0.05	0.07
H2O*	4.28	4.29	4.35	4.36	4.35	4.31	4.34	4.39	4.34	4.20	4.22	4.22	4.34
Total (W%)	98.13	98.28	99.05	99.26	98.43	98.55	99.15	100.30	99.01	98.38	98.83	98.58	98.81
Si	5.63	5.59	5.64	5.64	5.63	5.58	5.60	5.59	5.64	5.80	5.81	5.82	5.65
Al iv	2.37	2.41	2.36	2.36	2.37	2.42	2.40	2.41	2.36	2.20	2.19	2.18	2.35
Al vi	0.07	0.11	0.16	0.18	0.08	0.09	0.10	0.16	0.15	0.37	0.41	0.40	0.17
Ti	0.23	0.10	0.10	0.10	0.09	0.10	0.10	0.10	0.09	0.10	0.10	0.10	0.10
Cr	0.00	0.00	0.00	0.00	0.00	0.00	0.00	0.00	0.00	0.00	0.00	0.00	0.00
Fe	0.38	0.37	0.38	0.36	0.35	0.34	0.36	0.35	0.37	0.40	0.39	0.37	0.36
Mn	0.33	0.01	0.01	0.02	0.02	0.01	0.01	0.02	0.02	0.01	0.02	0.02	0.02
Mg	4.58	5.01	4.84	4.82	5.11	5.05	5.01	4.88	4.89	5.01	4.96	4.96	4.81
Ca	0.00	0.00	0.00	0.00	0.01	0.00	0.01	0.01	0.01	0.01	0.01	0.04	0.01
Na	0.02	0.03	0.02	0.02	0.03	0.02	0.02	0.03	0.02	0.03	0.02	0.03	0.02
K	1.53	1.79	1.78	1.77	1.57	1.81	1.75	1.80	1.76	1.81	1.81	1.79	1.79
OH*	4.00	4.00	4.00	4.00	4.00	4.00	4.00	4.00	4.00	4.00	4.00	4.00	4.00
Total-Cations	19.14	19.42	19.30	19.28	19.25	19.43	19.36	19.34	19.31	19.74	19.71	19.70	19.29
Sample no.	SS-034	SS-034	SS-034	SS-034	SS-034	SS-034	SS-034	SS-034	SS-034	SS-034	SS-034	SS-037	SS-037
Mineral	Phl	Phl	Phl	Phl	Phl	Phl	Phl	Phl	Phl	Phl	Phl	Phl	Phl

Crystal-Spot	6.27	7.28	7.29	8.36	8.37	8.38	9.39	9.40	10.41	10.42	10.43	1.7	1.8
SiO2	40.71	40.89	40.81	40.94	40.63	40.37	40.27	40.12	40.98	40.05	40.81	39.75	40.14
TiO2	0.93	0.93	0.95	0.98	0.96	0.99	0.92	0.92	0.91	0.92	0.95	0.45	0.46
Al2O3	15.52	15.36	15.47	15.37	15.97	15.12	15.23	15.23	15.43	15.76	15.31	15.58	15.41
FeO	3.21	3.35	3.33	3.14	2.99	3.17	3.30	3.23	3.15	3.13	3.12	2.64	2.63
MnO	0.15	0.16	0.13	0.15	0.10	0.12	0.16	0.11	0.14	0.17	0.13	0.03	0.05
MgO	23.56	23.55	23.66	23.78	24.09	24.03	24.32	24.56	23.49	23.54	24.39	24.30	24.67
CaO	0.02	0.10	0.08	0.06	0.06	0.11	0.11	0.05	0.04	0.02	0.02	0.07	0.07
Na2O	0.09	0.04	0.07	0.09	0.10	0.08	0.10	0.10	0.08	0.11	0.09	0.11	0.18
K2O	10.14	9.97	10.08	10.02	9.81	9.87	9.89	10.02	10.01	10.20	10.00	10.12	9.94
F	0.17	0.15	0.12	0.00	0.00	0.00	0.00	0.00	0.00	0.00	0.00	0.00	0.14
Cl	0.06	0.05	0.06	0.00	0.00	0.00	0.00	0.00	0.00	0.00	0.00	0.07	0.11
H2O*	4.34	4.14	4.16	4.23	4.25	4.20	4.21	4.21	4.22	4.19	4.24	4.15	4.10
Total (W%)	98.91	98.69	98.92	98.77	98.95	98.06	98.50	98.52	98.43	98.09	99.05	97.24	97.89
Si	5.63	5.81	5.79	5.80	5.73	5.77	5.73	5.71	5.82	5.73	5.77	5.72	5.74
Al iv	2.37	2.19	2.21	2.20	2.27	2.23	2.27	2.29	2.18	2.27	2.23	2.28	2.26
Al vi	0.16	0.38	0.37	0.37	0.39	0.31	0.29	0.27	0.40	0.38	0.32	0.37	0.34
Ti	0.10	0.10	0.10	0.10	0.10	0.11	0.10	0.10	0.10	0.10	0.10	0.05	0.05
Cr	0.00	0.00	0.00	0.00	0.00	0.00	0.00	0.00	0.00	0.00	0.00	0.00	0.00
Fe	0.37	0.40	0.39	0.37	0.35	0.38	0.39	0.38	0.37	0.37	0.37	0.32	0.31
Mn	0.02	0.02	0.02	0.02	0.01	0.02	0.02	0.01	0.02	0.02	0.02	0.00	0.01
Mg	4.86	4.99	5.00	5.02	5.07	5.12	5.16	5.21	4.97	5.02	5.14	5.22	5.26
Ca	0.00	0.02	0.01	0.01	0.01	0.02	0.02	0.01	0.01	0.00	0.00	0.01	0.01
Na	0.03	0.01	0.02	0.02	0.03	0.02	0.03	0.03	0.02	0.03	0.02	0.03	0.05
K	1.79	1.81	1.82	1.81	1.77	1.80	1.80	1.82	1.81	1.86	1.80	1.86	1.81
OH*	4.00	4.00	4.00	4.00	4.00	4.00	4.00	4.00	4.00	4.00	4.00	4.00	4.00
Total-Cations	19.32	19.71	19.74	19.73	19.73	19.77	19.80	19.83	19.71	19.79	19.77	19.85	19.84
Sample no.	SS-037	SS-037	SS-037	SS-037	SS-037	SS-037	SS-037	SS-037	SS-037	SS-037	SS-037	SS-060	SS-060
Mineral	Phl	Phl	Phl	Phl	Phl	Phl	Phl	Phl	Phl	Phl	Phl	Mn-Phl	Mn-Phl
Crystal-Spot	1.9	2.10	2.11	2.12	3.13	3.14	4.15	5.21	5.22	5.23	5.24	1.52	1.53
SiO2	39.68	40.08	39.86	39.58	39.96	40.97	41.90	40.43	40.39	40.83	40.21	41.11	40.73
TiO2	0.46	0.48	0.47	0.47	0.42	0.40	0.38	0.47	0.44	0.47	0.48	1.70	1.65
Al2O3	15.90	15.80	15.63	15.64	15.26	15.12	15.09	15.58	15.71	15.53	15.36	12.78	12.56
FeO	2.61	2.60	2.57	2.61	2.83	2.49	2.99	2.64	2.81	2.13	2.48	1.71	1.72
MnO	0.00	0.06	0.04	0.06	0.02	0.08	0.04	0.05	0.04	0.04	0.05	3.41	3.38
MgO	24.59	24.68	24.92	24.78	24.62	25.58	25.96	24.93	25.10	25.52	25.14	22.69	22.28
CaO	0.11	0.02	0.03	0.06	0.01	0.05	0.30	0.01	0.00	0.03	0.06	0.10	0.03
Na2O	0.12	0.13	0.10	0.15	0.13	0.04	0.11	0.09	0.11	0.09	0.07	0.05	0.10
K2O	10.21	10.11	10.04	9.97	10.20	9.80	6.87	10.25	10.23	10.37	10.22	9.46	9.69
F	0.08	0.19	0.16	0.18	0.01	0.05	0.05	0.09	0.16	0.14	0.08	1.82	1.82
Cl	0.07	0.08	0.05	0.07	0.07	0.05	0.10	0.06	0.07	0.05	0.05	0.05	0.04
H2O*	4.13	4.10	4.11	4.08	4.16	4.21	4.23	4.17	4.15	4.18	4.16	3.26	3.22
Total (W%)	97.96	98.30	97.96	97.63	97.67	98.85	98.04	98.78	99.19	99.39	98.35	98.13	97.21
Si	5.68	5.71	5.70	5.68	5.74	5.78	5.87	5.73	5.71	5.74	5.72	5.96	5.97

Al iv	2.32	2.29	2.30	2.32	2.26	2.22	2.13	2.27	2.29	2.26	2.28	2.04	2.03
Al vi	0.36	0.36	0.33	0.33	0.32	0.29	0.36	0.33	0.33	0.32	0.30	0.15	0.14
Ti	0.05	0.05	0.05	0.05	0.05	0.04	0.04	0.05	0.05	0.05	0.05	0.19	0.18
Cr	0.00	0.00	0.00	0.00	0.00	0.00	0.00	0.00	0.00	0.00	0.00	0.00	0.00
Fe	0.31	0.31	0.31	0.31	0.34	0.29	0.35	0.31	0.33	0.25	0.30	0.21	0.21
Mn	0.00	0.01	0.00	0.01	0.00	0.01	0.00	0.01	0.00	0.00	0.01	0.42	0.42
Mg	5.25	5.24	5.31	5.30	5.27	5.38	5.42	5.27	5.29	5.35	5.34	4.90	4.87
Ca	0.02	0.00	0.00	0.01	0.00	0.01	0.05	0.00	0.00	0.00	0.01	0.01	0.00
Na	0.03	0.03	0.03	0.04	0.04	0.01	0.03	0.03	0.03	0.03	0.02	0.01	0.03
K	1.86	1.84	1.83	1.82	1.87	1.76	1.23	1.85	1.85	1.86	1.86	1.75	1.81
OH*	4.00	4.00	4.00	4.00	4.00	4.00	4.00	4.00	4.00	4.00	4.00	4.00	4.00
Total-Cations	19.88	19.85	19.86	19.88	19.88	19.81	19.48	19.86	19.87	19.86	19.87	19.64	19.68

Sample no.	SS-060	SS-060	SS-060	SS-060
Mineral	Mn-Phl	Mn-Phl	Mn-Phl	Mn-Phl
Crystal-Spot	1.52	1.53	2.54	2.55
SiO2	41.11	40.73	40.67	41.66
TiO2	1.70	1.65	1.77	1.60
Al2O3	12.78	12.56	12.96	12.48
FeO	1.71	1.72	1.72	1.67
MnO	3.41	3.38	3.37	3.30
MgO	22.69	22.28	22.53	23.09
CaO	0.10	0.03	0.09	0.09
Na2O	0.05	0.10	0.07	0.08
K2O	9.46	9.69	9.37	9.24
F	1.82	1.82	1.68	1.74
Cl	0.05	0.04	0.04	0.04
H2O*	3.26	3.22	3.31	3.32
Total (W%)	98.13	97.21	97.57	98.30
Si	5.96	5.97	5.93	6.01
Al iv	2.04	2.03	2.07	1.99
Al vi	0.15	0.14	0.15	0.13
Ti	0.19	0.18	0.19	0.17
Cr	0.00	0.00	0.00	0.00
Fe	0.21	0.21	0.21	0.20
Mn	0.42	0.42	0.42	0.40
Mg	4.90	4.87	4.90	4.97
Ca	0.01	0.00	0.01	0.01
Na	0.01	0.03	0.02	0.02
K	1.75	1.81	1.74	1.70
OH*	4.00	4.00	4.00	4.00
Total-Cations	19.64	19.68	19.65	19.62

Anexo 2 (Appendix 2) – Litogeochemistry data from Buritirama Metagranite.

Sample	GRT-01	GRT-02	GRT-03	GRT-04
Elements	**Major Elements (%)**			
SiO2	71.02	73.49	70.84	71.83
TiO2	0.64	0.65	0.72	0.69
Al2O3	12.53	12.98	12.8	12.72
Cr2O3	<0,01	<0,01	<0,01	<0,01
Fe2O3	5.11	4.95	5.7	5.49
MnO	0.1	0.09	0.09	0.09
MgO	0.7	0.7	0.89	0.92
CaO	1.69	1.74	1.75	1.65
Na2O	2.82	3.05	2.9	2.87
K2O	4.75	5.12	5.18	5.17
P2O5	0.12	0.11	0.17	0.12
LOI	0.05	0.1	0.06	0.04
Elements	**Trace Elements (ppm)**			
Ba	1084	1135	1102	1125
Rb	137.3	139.6	150	148.6
Th	38.1	35.4	54.9	20.7
U	3.55	3.12	2.76	2.17
Nb	20.07	21.06	23.31	20.83
Ta	1.15	1.26	1.29	1.15
Sr	118	123	119	118
Nd	67.6	70.5	122.5	49
Zr	439	495	512	500
Hf	11.63	13.45	13.43	13.22
Yb	4.7	5	5.6	4.6
Zn	67	75	57	45
V	34	31	35	33
Ni	7	5	7	<5
Co	10.8	6.4	7.3	7
Cr	3	3	5	5
Cu	11	11	9	9
Ga	18.2	19.1	17	19.6
Mo	<2	<2	<2	2
Sn	3.6	3.6	4	3.9
Elements	**Rare Earth Elements (ppm)**			
La	98.2	104.8	237.2	46.6
Ce	185.1	198.1	413.8	104.2
Pr	19.1	20.62	38.59	12.63
Nd	67.6	70.5	122.5	49
Sm	10.9	12.3	17.6	10
Eu	1.26	1.41	1.7	1.23
Gd	9.79	10.08	12.99	9.28

Sample	GRT-01	GRT-02	GRT-03	GRT-04
Tb	1.4	1.51	1.87	1.36
Dy	8.11	8.88	10.37	8.33
Ho	1.65	1.79	2.07	1.64
Er	4.87	5.19	5.55	4.78
Tm	0.73	0.81	0.87	0.72
Yb	4.7	5	5.6	4.6
Lu	0.69	0.76	0.82	0.73
Y	44.29	46.59	54.5	42.97

Anexo 3 (Appendix 3)

3A – U/Pb Isotopic data from the sample BUR-1 (Buritirama metagranite).

	Sample BUR-1					Isotope Ratios ± 2σ (%)									Dates (Ma) ± 2σ (abs)								
Spot	f206c	206Pb	U (µg g-1) a	Th/U	206Pb/ 204Pb	207Pb/ 206Pb	2σ (%)	207Pb/ 235U	2σ (%)	206Pb/ 238U	2σ (%)	Rho	208Pb/ 232Th	2σ (%)	207Pb/ 206Pb	2σ	206Pb/ 238U	2σ	207Pb/ 235U	2σ	208Pb/ 232Th	2σ	% Conc
A113	0.000	63278	263	1.36	1054.6405	0.16891	1.03	11.1637	2.07	0.479343	1.80	0.87	0.13956	1.92	2547	17	2524	38	2537	19	2641	48	99.81
A130	0.000	31438	131	1.29	628.7640	0.16885	1.07	11.1604	2.17	0.479373	1.89	0.87	0.13805	2.09	2546	18	2525	40	2537	20	2614	51	99.83
A011	0.000	74812	311	1.26	74811.9680	0.16887	0.98	11.1624	2.04	0.479403	1.79	0.88	0.13183	1.76	2546	16	2525	38	2537	19	2503	41	99.83
A088	0.000	62203	258	1.15	62203.3290	0.16907	1.00	11.1884	2.07	0.479943	1.81	0.87	0.12862	1.85	2548	17	2527	38	2539	19	2446	43	99.83
A074	0.013	51888	216	1.28	2594.3765	0.16829	1.04	11.1518	2.03	0.480614	1.75	0.86	0.13245	1.95	2541	17	2530	37	2536	19	2514	46	99.93
A050	0.000	10366	43	1.52	370.2170	0.17013	1.18	11.2980	2.23	0.481626	1.89	0.85	0.13466	2.39	2559	20	2534	40	2548	21	2553	57	99.77
A108	0.000	74435	307	1.11	448.4016	0.16954	1.04	11.2683	2.05	0.482046	1.77	0.86	0.14320	1.96	2553	17	2536	37	2546	19	2705	49	99.93
A008	0.000	17961	74	1.57	17960.6480	0.16862	1.04	11.2107	2.10	0.482196	1.82	0.87	0.13336	1.95	2544	17	2537	38	2541	20	2530	46	99.85
A058	0.000	68019	279	1.21	430.5005	0.17016	1.01	11.3395	2.02	0.483308	1.74	0.86	0.13122	1.89	2559	17	2542	37	2551	19	2492	44	99.92
A048	0.020	38724	159	1.25	577.9730	0.16975	0.99	11.3255	2.08	0.483899	1.83	0.88	0.17710	1.77	2555	17	2544	39	2550	20	3296	54	99.93
A075	0.000	65053	268	0.99	65052.6838	0.16913	1.00	11.2882	2.06	0.484049	1.80	0.87	0.13769	1.86	2549	17	2545	38	2547	19	2607	45	99.79
A132	0.042	75009	307	1.44	1027.5200	0.16985	1.04	11.3544	2.08	0.484840	1.80	0.87	0.13395	1.96	2556	17	2548	38	2553	20	2541	47	99.87
A034	0.000	27520	113	1.77	1719.9869	0.16899	1.03	11.3095	2.20	0.485371	1.94	0.88	0.13429	1.91	2548	17	2551	41	2549	21	2547	46	99.63
A035	0.000	23338	96	1.68	23338.2877	0.16941	1.04	11.3529	2.21	0.486041	1.95	0.88	0.12418	1.95	2552	18	2554	41	2553	21	2366	44	99.66
A055	0.000	63340	259	1.23	527.8351	0.16951	0.98	11.3669	2.07	0.486352	1.82	0.88	0.13915	1.77	2553	16	2555	38	2554	19	2633	44	99.65
A054	0.018	72394	296	1.31	1508.2096	0.16956	0.98	11.3787	2.07	0.486712	1.82	0.88	0.13691	1.75	2553	16	2556	38	2555	19	2594	43	99.63
A012	0.000	22846	93	1.35	2284.6231	0.16985	1.02	11.4258	2.17	0.487884	1.91	0.88	0.12964	1.93	2556	17	2562	41	2559	20	2464	45	99.58
A049	0.000	29932	122	0.95	29932.3256	0.16969	1.01	11.4288	2.08	0.488475	1.82	0.88	0.13604	1.90	2555	17	2564	39	2559	20	2578	46	99.49
A057	0.000	37679	153	1.01	4186.5161	0.17031	1.00	11.4762	2.08	0.488725	1.82	0.88	0.13765	1.87	2561	17	2565	39	2563	20	2607	46	99.60
A030	0.000	48639	198	1.28	48639.2372	0.16932	0.99	11.4104	2.05	0.488765	1.80	0.88	0.13364	1.80	2551	17	2565	38	2557	19	2535	43	99.38
A071	0.000	67982	279	1.22	1133.0359	0.16788	1.02	11.3163	2.02	0.488875	1.75	0.86	0.13338	1.89	2537	17	2566	37	2550	19	2531	45	99.06
A150	0.000	70319	286	1.11	772.7334	0.16899	1.07	11.4269	2.16	0.490407	1.88	0.87	0.12798	2.09	2548	18	2572	40	2559	20	2434	48	99.15
A079	0.000	24220	99	1.78	24220.4111	0.16832	1.04	11.3913	2.09	0.490848	1.82	0.87	0.13787	1.93	2541	18	2574	39	2556	20	2611	47	98.97
A076 - Inherited	0.000	34248	112	1.08	34248.4300	0.19357	1.05	14.1954	2.16	0.531882	1.89	0.87	0.11710	2.15	2773	17	2749	42	2763	21	2238	45	99.79
A073 - Inherited	0.000	16644	48	1.45	49.6833	0.20751	1.04	16.0345	2.15	0.560410	1.88	0.88	0.40313	1.87	2886	17	2868	44	2879	21	6846	108	99.90

3B – U/Pb Isotopic data from the sample BUR-3 (Quartzite – Lower Unit).

	Sample BUR-3					Isotope Ratios ± 2σ (%)									Dates (Ma) ± 2σ (abs)								
Spot	f206c	206Pb	U (µg g-1) a	Th/U	206Pb/ 204Pb	207Pb/ 206Pb	2σ (%)	207Pb/ 235U	2σ (%)	206Pb/ 238U	2σ (%)	Rho	208Pb/ 232Th	2σ (%)	207Pb/ 206Pb	2σ	206Pb/ 238U	2σ	207Pb/ 235U	2σ	208Pb/ 232Th	2σ	% Conc
C009	0.000	42602	118	1.63	211.9521	0.20970	0.99	16.1411	2.12	0.558267	1.88	0.88	0.08754	1.92	2903	16	2859	44	2885	20	1696	31	99.91
D010	0.000	20462	72	0.99	6820.6049	0.19625	1.26	14.5398	2.36	0.537328	2.00	0.85	0.14742	3.01	2795	21	2772	45	2786	23	2780	78	99.98
C010	0.085	30207	127	3.58	387.2712	0.16589	1.14	10.6375	2.23	0.465064	1.92	0.86	0.02960	2.57	2517	19	2462	40	2492	21	590	15	99.61
D011	0.000	13213	19	2.62	30.1665	0.34227	1.34	35.8638	2.63	0.759955	2.26	0.86	0.29402	2.78	3673	20	3644	63	3663	26	5210	128	99.93
D012	0.000	29520	108	1.26	289.4090	0.19060	1.14	13.8363	2.37	0.526506	2.08	0.88	0.09753	2.48	2747	19	2727	46	2739	23	1881	45	99.92
C012	0.000	59613	299	1.83	246.3352	0.15012	0.98	8.9126	2.14	0.430601	1.90	0.89	0.05773	1.80	2347	17	2308	37	2329	20	1134	20	99.95
C013	0.043	59838	151	1.15	997.3046	0.23852	0.98	17.7509	2.06	0.539753	1.82	0.88	0.10060	1.89	3110	16	2782	41	2976	20	1938	35	94.25
C014	0.000	50257	192	0.82	4568.8255	0.17461	1.12	11.7249	2.11	0.487013	1.79	0.85	0.12884	2.44	2602	19	2558	38	2583	20	2450	56	99.85
D014	0.000	7646	28	1.16	7646.2770	0.18968	1.48	13.9132	2.68	0.531997	2.24	0.83	0.14598	3.71	2739	24	2750	50	2744	26	2754	96	99.27
D015	0.000	35857	145	1.61	35856.9716	0.18007	1.17	12.5340	2.42	0.504823	2.11	0.87	0.11282	2.45	2654	19	2634	46	2645	23	2161	50	99.89
D016	0.000	33496	150	1.42	389.4864	0.17049	1.07	11.3501	2.11	0.482840	1.82	0.86	0.11734	2.11	2562	18	2540	38	2552	20	2243	45	99.97
C016	0.000	43180	152	1.51	180.6701	0.20092	0.99	12.7160	2.07	0.459015	1.82	0.88	0.07928	1.87	2834	16	2435	37	2659	20	1542	28	92.35
C017	0.000	16220	43	1.20	16220.3409	0.21480	1.09	16.9105	2.18	0.570989	1.89	0.87	0.15269	2.38	2942	18	2912	45	2930	21	2872	64	99.81
D017	0.000	12363	42	1.57	12363.0883	0.19053	1.98	14.8864	3.27	0.566675	2.60	0.80	0.14044	4.77	2747	33	2894	61	2808	32	2656	119	96.41
C018	0.054	49624	241	1.56	463.7778	0.15318	1.06	9.2229	2.18	0.436670	1.90	0.87	0.09011	2.15	2382	18	2336	38	2360	20	1744	36	99.79
D019	0.000	22663	66	0.68	22662.9833	0.21618	1.40	17.3899	2.49	0.583416	2.06	0.83	0.15828	3.84	2952	23	2963	49	2957	24	2970	106	99.30
C019	0.000	31705	109	2.17	1093.2665	0.19390	1.06	12.9988	2.23	0.486211	1.97	0.88	0.05976	2.21	2776	17	2554	42	2680	21	1173	25	96.11
C029	0.000	13845	53	1.58	76.9165	0.17441	1.20	11.7482	2.50	0.488548	2.19	0.88	0.06345	2.93	2600	20	2564	47	2585	24	1244	35	99.96
D029	0.000	24127	101	1.71	513.3374	0.17754	1.16	12.1814	2.17	0.497628	1.84	0.85	0.11766	2.38	2630	19	2604	40	2618	21	2248	51	99.95
D030	0.000	41803	119	0.55	3800.2701	0.22047	1.48	17.9160	2.52	0.589365	2.04	0.81	0.13185	3.94	2984	24	2987	49	2985	25	2503	93	99.46
C030	0.000	56925	211	1.60	2475.0059	0.17681	1.09	12.0557	2.37	0.494518	2.10	0.89	0.09998	2.14	2623	18	2590	45	2609	22	1926	39	99.89
C031	0.000	28358	102	1.93	28357.6776	0.17958	1.04	12.3767	2.27	0.499864	2.01	0.89	0.03746	2.30	2649	17	2613	44	2633	22	743	17	99.95
D032	0.000	19087	50	0.53	19087.1303	0.22474	1.51	19.3851	2.56	0.625598	2.06	0.81	0.17511	4.23	3015	24	3132	52	3061	25	3262	127	97.19
C032	0.000	51123	185	2.60	51123.1430	0.18106	1.04	12.3847	2.12	0.496082	1.84	0.87	0.06599	2.09	2663	17	2597	40	2634	20	1292	26	99.41
D033	0.000	27543	81	0.86	27542.8691	0.21763	1.17	17.3358	2.20	0.577716	1.86	0.85	0.11694	2.63	2963	19	2939	44	2954	21	2235	56	99.99
C033	0.000	9821	34	1.02	577.7352	0.17403	1.05	13.1071	2.21	0.546228	1.94	0.88	0.14149	2.25	2597	18	2809	45	2687	21	2675	56	94.61
D034	0.000	21900	75	1.47	21899.8080	0.19230	1.21	14.8837	2.22	0.561334	1.86	0.84	0.14328	2.57	2762	20	2872	43	2808	21	2707	65	97.20
D035	0.054	16012	70	0.74	348.0780	0.17342	1.70	11.7137	2.74	0.489875	2.16	0.79	0.13364	4.38	2591	28	2570	46	2582	26	2535	105	99.93
D037	0.000	33441	143	1.30	33440.9004	0.17442	1.60	11.9184	2.55	0.495595	1.99	0.78	0.11910	3.68	2600	27	2595	43	2598	24	2274	79	99.60
D039	0.042	49873	121	1.73	615.7162	0.24404	1.18	20.9789	2.30	0.623465	1.97	0.86	0.07276	2.58	3147	19	3124	49	3138	23	1420	35	99.97
D040	0.000	33588	153	1.88	33587.8548	0.16948	1.57	11.1347	2.77	0.476503	2.29	0.82	0.05816	3.75	2552	26	2512	48	2534	26	1143	42	99.64

	Sample BUR-3					Isotope Ratios ± 2σ (%)									Dates (Ma) ± 2σ (abs)								
Spot	f206c	206Pb	U (µg g-1) a	Th/U	206Pb/ 204Pb	207Pb/ 206Pb	2σ (%)	207Pb/ 235U	2σ (%)	206Pb/ 238U	2σ (%)	Rho	208Pb/ 232Th	2σ (%)	207Pb/ 206Pb	2σ	206Pb/ 238U	2σ	207Pb/ 235U	2σ	208Pb/ 232Th	2σ	% Conc
D048	0.000	30958	108	2.96	30957.6780	0.19653	1.23	14.5791	2.25	0.538036	1.89	0.84	0.10099	2.59	2798	20	2775	43	2788	22	1945	48	99.96
C049	0.000	47659	157	1.64	340.4227	0.18944	1.07	13.5335	2.33	0.518140	2.07	0.89	0.04707	2.34	2737	18	2691	46	2718	22	930	21	99.84
C050	0.085	76825	289	1.32	413.0371	0.17615	1.16	11.8980	2.28	0.489865	1.96	0.86	0.12624	2.52	2617	19	2570	42	2596	22	2403	57	99.80
D050	0.000	17756	77	3.85	94.4452	0.18336	1.38	11.8009	2.51	0.466787	2.09	0.83	0.05074	3.04	2683	23	2469	43	2589	24	1000	30	95.89
D051	0.000	12841	42	1.71	188.8441	0.20471	1.65	15.6327	2.68	0.553860	2.12	0.79	0.14232	3.78	2864	27	2841	49	2855	26	2690	95	99.97
C052	0.000	10114	31	1.55	10113.9782	0.19708	1.26	14.5465	2.41	0.535318	2.05	0.85	0.11661	2.92	2802	21	2764	47	2786	23	2229	62	99.99
C053	0.000	7261	18	0.93	7260.9510	0.21267	1.11	18.1202	2.32	0.617967	2.03	0.88	0.16258	2.82	2926	18	3102	51	2996	23	3045	80	95.65
D053	0.000	23712	101	1.69	109.2714	0.17460	1.39	11.8903	2.50	0.493911	2.08	0.83	0.11473	3.10	2602	23	2588	45	2596	24	2195	65	99.80
D054	0.000	17968	67	0.85	408.3544	0.17964	1.26	13.5848	2.33	0.548469	1.96	0.84	0.13817	2.82	2650	21	2819	45	2721	22	2616	69	95.89
C056	0.000	40523	147	2.04	349.3347	0.18243	1.04	12.3499	2.13	0.490993	1.86	0.87	0.09279	2.05	2675	17	2575	40	2631	20	1794	35	98.66
D057	0.000	55984	127	0.74	55983.8846	0.25445	1.90	22.4582	2.87	0.640136	2.15	0.75	0.17503	4.67	3213	30	3190	55	3204	28	3260	141	99.97
C057	0.000	69035	257	1.65	387.8399	0.17589	1.06	12.0050	2.30	0.495013	2.04	0.89	0.08972	2.05	2615	18	2592	44	2605	22	1737	34	99.66
D058	0.000	30579	106	0.96	30578.8157	0.19683	1.44	14.6303	2.54	0.539092	2.09	0.82	0.10590	3.38	2800	24	2780	48	2792	24	2035	65	99.92
C058	0.000	11889	41	1.25	96.6618	0.18291	1.11	12.8209	2.20	0.508369	1.90	0.86	0.11178	2.45	2679	18	2650	42	2667	21	2142	50	99.82
D060	0.000	19571	80	0.70	161.7422	0.17875	1.85	12.3665	2.83	0.501764	2.13	0.75	0.13962	4.57	2641	31	2621	46	2633	27	2642	113	99.91
C069	0.061	59609	236	2.21	602.1142	0.17090	1.01	11.2861	2.16	0.478964	1.91	0.88	0.05913	1.89	2566	17	2523	40	2547	20	1161	22	99.87
C070	0.037	64386	216	0.67	748.6727	0.18699	0.98	13.3143	2.06	0.516408	1.81	0.88	0.14947	1.85	2716	16	2684	40	2702	20	2816	49	99.86
C071	0.000	71532	350	0.65	376.4838	0.15789	1.03	9.1331	2.08	0.419522	1.81	0.87	0.16097	2.07	2433	17	2258	35	2351	19	3017	58	96.85
C074	0.000	62524	251	1.72	500.1943	0.16978	1.04	11.1566	2.04	0.476588	1.75	0.86	0.11314	1.98	2555	17	2512	37	2536	19	2166	41	99.88
C076	0.000	67924	319	1.75	198.0293	0.16751	1.00	9.5110	2.18	0.411800	1.93	0.89	0.09828	1.81	2533	17	2223	37	2389	20	1895	33	93.86
C078	0.000	14684	51	2.25	14683.8081	0.18378	1.13	12.9952	2.21	0.512844	1.90	0.86	0.10501	2.27	2687	19	2669	42	2679	21	2018	44	99.58
C087	0.000	54916	182	1.94	1144.0781	0.19032	1.12	13.5284	2.29	0.515527	2.00	0.87	0.04329	2.49	2745	18	2680	44	2717	22	857	21	99.44
C088	0.000	24143	97	0.44	221.4936	0.16130	1.04	11.1126	2.08	0.499676	1.80	0.87	0.13542	2.45	2469	18	2612	39	2533	20	2567	59	96.00
C089	0.000	20303	59	1.29	48.6875	0.20380	1.05	15.4957	2.12	0.551455	1.84	0.87	0.18043	2.06	2857	17	2831	43	2846	20	3353	64	99.72
C090	0.000	13481	48	1.10	13481.2912	0.18067	1.27	12.5979	2.35	0.505725	1.98	0.84	0.14200	2.97	2659	21	2638	43	2650	22	2684	75	99.62
C091	0.000	51661	102	0.84	51661.2613	0.24118	0.99	22.5991	2.12	0.679597	1.87	0.88	0.13902	1.96	3128	16	3343	49	3210	21	2631	48	95.04
C092	0.000	79925	306	2.72	109.3363	0.19066	1.05	11.6983	2.25	0.445006	1.99	0.88	0.07630	1.97	2748	17	2373	40	2581	21	1486	28	92.73
C094	0.000	36375	137	1.23	713.2379	0.17555	1.20	11.8615	2.44	0.490053	2.13	0.87	0.09331	2.66	2611	20	2571	46	2594	23	1803	46	99.95
C095	0.000	48617	141	2.02	392.0746	0.19720	1.01	15.4554	2.06	0.568415	1.79	0.87	0.08186	1.95	2803	17	2901	42	2844	20	1590	30	97.15
C096	0.000	13297	48	0.55	114.6332	0.17128	1.11	12.4819	2.23	0.528546	1.94	0.87	0.13600	2.94	2570	19	2735	44	2641	21	2577	71	95.60
C098	0.000	88830	447	1.15	1325.8165	0.16445	0.99	8.8860	2.14	0.391900	1.90	0.89	0.06452	1.86	2502	17	2132	35	2326	20	1264	23	92.41
C099	0.000	52338	248	2.11	339.8570	0.16163	1.04	9.4320	2.14	0.423235	1.87	0.87	0.08912	2.00	2473	18	2275	36	2381	20	1726	33	96.36
C107	0.000	49023	156	2.88	653.6377	0.19338	1.09	14.0722	2.30	0.527764	2.03	0.88	0.03773	2.23	2771	18	2732	46	2755	22	749	16	99.99

	Sample BUR-3					Isotope Ratios ± 2σ (%)									Dates (Ma) ± 2σ (abs)								
Spot	f206c	206Pb	U (µg g-1) a	Th/U	206Pb/ 204Pb	207Pb/ 206Pb	2σ (%)	207Pb/ 235U	2σ (%)	206Pb/ 238U	2σ (%)	Rho	208Pb/ 232Th	2σ (%)	207Pb/ 206Pb	2σ	206Pb/ 238U	2σ	207Pb/ 235U	2σ	208Pb/ 232Th	2σ	% Conc
C109	0.000	95287	309	1.70	103.1243	0.20310	1.00	13.8033	2.16	0.492914	1.92	0.89	0.18025	1.82	2851	16	2583	41	2736	21	3350	56	95.19
C110	0.000	23539	86	0.89	534.9875	0.17827	1.11	12.1850	2.13	0.495746	1.82	0.85	0.13471	2.42	2637	18	2595	39	2619	20	2554	58	99.93
C111	0.000	31979	111	1.35	31979.2493	0.18425	1.11	12.8930	2.19	0.507497	1.88	0.86	0.07302	2.49	2692	18	2646	41	2672	21	1425	34	99.84
C117	0.084	64207	271	0.77	553.5047	0.16333	1.02	10.6019	2.11	0.470777	1.85	0.88	0.12938	1.96	2490	17	2487	39	2489	20	2459	45	99.25
C119	0.000	24631	91	1.08	24631.2272	0.17496	1.23	12.0691	2.29	0.500300	1.94	0.84	0.13505	2.78	2606	21	2615	42	2610	22	2560	67	98.97
C120	0.000	8900	23	1.21	128.9787	0.20802	1.28	17.2005	2.44	0.599700	2.07	0.85	0.16058	3.09	2890	21	3029	51	2946	24	3010	87	96.38
C127	0.000	40264	128	1.69	1750.5954	0.19252	1.26	14.0942	2.30	0.530971	1.92	0.83	0.05794	3.07	2764	21	2746	43	2756	22	1139	34	99.57
C130	0.048	96056	443	3.05	857.6398	0.15650	1.07	9.6852	2.25	0.448827	1.99	0.88	0.05309	2.00	2418	18	2390	40	2405	21	1046	21	99.80
C131	0.000	18431	68	1.02	18430.7308	0.16929	1.16	12.0688	2.25	0.517061	1.93	0.86	0.13531	2.57	2551	20	2687	43	2610	21	2565	62	96.21
C133	0.000	51495	125	0.62	408.6870	0.21572	1.00	18.4434	2.10	0.620095	1.85	0.88	0.14383	1.97	2949	16	3110	46	3013	20	2716	50	95.96
C136	0.000	10459	26	1.02	10459.2103	0.20823	1.19	17.9605	2.45	0.625560	2.14	0.87	0.10863	3.20	2892	19	3132	54	2988	24	2084	64	94.34
C137	0.000	28776	99	0.85	290.6650	0.17844	1.07	12.9799	2.23	0.527576	1.96	0.88	0.11048	2.26	2638	18	2731	44	2678	21	2118	46	97.19
C138	0.031	47474	177	0.46	719.3057	0.17224	1.03	11.9965	2.06	0.505141	1.79	0.87	0.13464	2.14	2580	17	2636	39	2604	20	2553	51	97.95
C139	0.000	17551	73	2.50	17550.8560	0.16704	1.37	10.7266	2.53	0.465727	2.12	0.84	0.04839	3.18	2528	23	2465	44	2500	24	955	30	99.42
C140	0.000	38026	118	1.57	6337.6744	0.19116	1.11	14.4296	2.32	0.547456	2.03	0.88	0.10718	2.24	2752	18	2815	47	2778	22	2058	44	97.87

3C – U/Pb Isotopic data from the sample BUR-2 (Quartzite – Upper Unit).

	Sample BUR-2					Isotope Ratios ± 2σ (%)									Dates (Ma) ± 2σ (abs)								
Spot	f206c	206Pb	U (µg g-1) a	Th/U	206Pb/ 204Pb	207Pb/ 206Pb	2σ (%)	207Pb/ 235U	2σ (%)	206Pb/ 238U	2σ (%)	Rho	208Pb/ 232Th	2σ (%)	207Pb/ 206Pb	2σ	206Pb/ 238U	2σ	207Pb/ 235U	2σ	208Pb/ 232Th	2σ	% Conc
B208	0.000	97082	456	0.76	257.5123	0.14371	1.10	8.5080	2.34	0.429369	2.07	0.88	0.14111	2.32	2272	19	2303	43	2287	20	1788	36	99.91
B217	0.059	103756	412	1.66	503.6698	0.14903	1.03	10.0697	2.16	0.490049	1.89	0.88	0.10516	2.05	2335	18	2571	11	2441	10	844	71	95.31
B257	0.000	73604	325	0.89	73604.1166	0.14907	1.11	9.0620	2.11	0.440894	1.80	0.85	0.09808	2.43	2335	19	2355	12	2344	13	706	68	99.84
B195	0.000	91936	367	0.94	425.6318	0.15721	0.96	10.0065	2.07	0.461643	1.83	0.89	0.15251	1.77	2426	16	2447	10	2435	9	576	12	99.87
B192	0.000	80326	356	1.46	147.6572	0.16116	0.99	9.0293	2.02	0.406350	1.77	0.87	0.10639	1.86	2468	17	2198	41	2341	21	3126	55	93.33
B200	0.000	88623	381	2.39	393.8778	0.16166	1.02	9.2968	2.20	0.417081	1.96	0.89	0.05210	1.96	2473	17	2247	6	2368	7	364	16	94.34
B216	0.000	39533	171	3.88	4941.6382	0.16307	1.01	9.2170	2.08	0.409937	1.82	0.88	0.02752	1.96	2488	17	2215	10	2360	9	567	12	93.28
B167	0.000	26856	100	2.69	1918.3004	0.16709	1.06	10.8883	2.16	0.472603	1.88	0.87	0.04115	2.24	2529	18	2495	39	2514	20	815	18	99.84
B260	0.000	87614	383	0.85	147.9974	0.16791	1.04	9.1536	2.10	0.395377	1.82	0.87	0.07953	2.19	2537	17	2148	6	2353	7	359	17	90.70

	Sample BUR-2					Isotope Ratios ± 2σ (%)									Dates (Ma) ± 2σ (abs)								
Spot	f206c	206Pb	U (µg g-1) a	Th/U	206Pb/ 204Pb	207Pb/ 206Pb	2σ (%)	207Pb/ 235U	2σ (%)	206Pb/ 238U	2σ (%)	Rho	208Pb/ 232Th	2σ (%)	207Pb/ 206Pb	2σ	206Pb/ 238U	2σ	207Pb/ 235U	2σ	208Pb/ 232Th	2σ	% Conc
B250	0.092	28328	100	1.36	422.8132	0.16839	1.16	11.3498	2.23	0.488843	1.91	0.85	0.11046	2.55	2542	19	2566	34	2552	19	549	11	99.94
B207	0.000	68843	290	1.83	894.0675	0.16966	1.03	9.4750	2.21	0.405033	1.96	0.89	0.08067	2.01	2554	17	2192	40	2385	20	2091	40	91.36
B252	0.008	122232	414	0.97	1697.6718	0.17251	1.11	11.8053	2.29	0.496319	2.01	0.88	0.09752	2.42	2582	18	2598	41	2589	20	2613	59	99.76
B240	0.063	113114	382	0.44	796.5781	0.17268	1.07	11.8406	2.25	0.497304	1.98	0.88	0.12380	2.36	2584	18	2602	6	2592	7	386	18	99.82
B227	0.000	44402	147	0.95	44402.0265	0.17376	1.04	12.1132	2.08	0.505593	1.80	0.87	0.11585	2.19	2594	17	2638	40	2613	20	1565	30	99.64
B153	0.000	81884	278	0.78	560.8500	0.17593	1.08	11.9192	2.37	0.491363	2.11	0.89	0.12548	2.25	2615	18	2577	45	2598	22	2389	51	99.75
B237	0.000	88996	286	1.18	559.7254	0.17712	1.06	12.4534	2.22	0.509944	1.95	0.88	0.11336	2.21	2626	18	2656	11	2639	10	788	52	99.93
B210	0.000	32893	105	1.21	1644.6528	0.17783	1.11	12.5030	2.35	0.509924	2.07	0.88	0.10615	2.43	2633	18	2656	28	2643	22	3807	63	99.93
B193	0.000	59323	187	4.61	270.8810	0.17945	1.02	12.6705	2.09	0.512104	1.82	0.87	0.08052	1.96	2648	17	2666	30	2655	19	2366	39	99.81
B228	0.055	77152	240	0.74	714.3740	0.18001	1.01	12.8651	2.08	0.518344	1.82	0.87	0.13692	2.02	2653	17	2692	20	2670	25	863	16	99.74
B187	0.000	72156	223	0.94	1311.9206	0.18065	0.97	12.9309	2.11	0.519138	1.88	0.89	0.11715	1.84	2659	16	2696	45	2675	22	2389	51	99.79
B172	0.000	50730	164	2.28	685.5404	0.18111	0.97	12.5190	2.12	0.501326	1.89	0.89	0.06156	1.82	2663	16	2619	41	2644	20	1207	21	99.64
B247	0.000	88200	271	1.60	88200.3760	0.18168	1.09	12.9968	2.27	0.518826	1.99	0.88	0.14230	2.29	2668	18	2694	49	2679	21	3257	60	99.98
B151	0.000	73910	234	2.72	73910.0604	0.18220	1.00	12.7790	2.15	0.508670	1.90	0.88	0.07853	1.86	2673	17	2651	42	2663	20	1528	27	99.90
B155	0.000	134280	425	0.51	1002.0921	0.18233	1.00	12.7735	2.22	0.508113	1.98	0.89	0.08575	2.05	2674	17	2649	43	2663	21	1663	33	99.97
B180	0.000	97315	305	1.28	653.1211	0.18332	1.01	12.8818	2.22	0.509656	1.98	0.89	0.06456	2.01	2683	17	2655	43	2671	21	1264	25	99.98
B238	0.032	82219	246	0.92	714.9455	0.18442	1.22	13.3776	2.28	0.526111	1.92	0.84	0.13454	2.84	2693	20	2725	11	2707	10	708	53	99.89
B254	0.000	37506	112	1.79	269.8309	0.18498	1.04	13.4467	2.13	0.527216	1.86	0.87	0.11405	2.12	2698	17	2730	38	2712	24	93	2	99.90
B218	0.000	45621	135	0.85	45620.6611	0.18550	1.09	13.4938	2.13	0.527568	1.84	0.86	0.13799	2.41	2703	18	2731	11	2715	11	774	77	99.97
B248	0.000	67681	193	0.35	727.7477	0.18576	1.16	14.0383	2.28	0.548096	1.96	0.86	0.15064	2.92	2705	19	2817	56	2752	23	3363	73	98.22
B157	0.000	69896	213	1.99	69895.6964	0.18666	1.10	13.2755	2.13	0.515826	1.82	0.86	0.05786	2.42	2713	18	2681	40	2699	20	1137	27	99.90
B170	0.000	44962	126	1.02	44961.7230	0.18863	1.04	14.4170	2.28	0.554331	2.02	0.89	0.13913	2.13	2730	17	2843	47	2778	22	2633	52	97.06
B158	0.000	94806	297	1.34	238.8059	0.18989	1.01	12.8826	2.17	0.492040	1.92	0.89	0.16724	1.89	2741	17	2579	41	2671	21	3126	55	97.13
B178	0.000	52261	154	2.48	706.2263	0.18994	1.02	13.6701	2.04	0.521977	1.77	0.87	0.09676	1.94	2742	17	2708	39	2727	20	1867	35	99.85
B148	0.000	53694	152	1.15	53694.0205	0.19445	0.97	14.2854	2.07	0.532835	1.83	0.88	0.13381	1.76	2780	16	2753	41	2769	20	2538	42	99.99
B212	0.000	12462	34	1.24	183.2586	0.19528	1.11	14.8386	2.24	0.551110	1.94	0.87	0.15164	2.44	2787	18	2830	39	2805	20	1867	35	99.68
B152	0.000	41086	111	0.06	41085.7239	0.19987	1.04	14.9907	2.05	0.543971	1.77	0.86	0.17200	5.48	2825	17	2800	41	2815	20	3208	162	99.96
B236	0.000	72395	186	0.96	72394.5300	0.20079	1.00	15.5199	2.11	0.560586	1.86	0.88	0.11845	1.98	2833	16	2869	10	2848	9	540	12	99.81

	Sample BUR-2					Isotope Ratios ± 2σ (%)									Dates (Ma) ± 2σ (abs)								
Spot	f206c	206Pb	U (µg g-1) a	Th/U	206Pb/ 204Pb	207Pb/ 206Pb	2σ (%)	207Pb/ 235U	2σ (%)	206Pb/ 238U	2σ (%)	Rho	208Pb/ 232Th	2σ (%)	207Pb/ 206Pb	2σ	206Pb/ 238U	2σ	207Pb/ 235U	2σ	208Pb/ 232Th	2σ	% Conc
B154	0.000	25694	67	1.23	25694.0174	0.20279	1.16	15.3997	2.19	0.550769	1.86	0.85	0.15255	2.53	2849	19	2828	43	2840	21	2870	68	99.86
B149	0.000	50928	131	1.97	565.8659	0.20420	0.97	15.6449	2.12	0.555665	1.88	0.89	0.04276	1.92	2860	16	2849	44	2855	20	846	16	99.67
B188	0.033	32904	81	0.76	1265.5444	0.20715	1.01	16.2586	2.08	0.569247	1.81	0.87	0.09556	2.30	2883	16	2905	43	2892	21	2870	68	99.88
B174	0.000	29587	73	2.73	356.4694	0.21149	1.06	16.4648	2.12	0.564622	1.83	0.87	0.09248	2.10	2917	17	2886	43	2904	20	1788	36	99.92
B231	0.000	110352	223	0.79	1050.9714	0.23246	1.01	19.7534	2.17	0.616312	1.92	0.88	0.13371	2.08	3069	16	3095	26	3079	21	1419	25	99.97
B256	0.000	51302	78	1.75	26.3356	0.25510	1.16	26.3656	2.38	0.749598	2.08	0.87	0.48763	2.50	3217	18	3606	10	3360	9	547	12	93.24
B213	0.000	60028	83	1.17	706.2121	0.29478	1.00	29.0018	2.09	0.713546	1.84	0.88	0.17482	2.00	3443	16	3472	35	3454	20	2141	37	99.99
B214	0.000	99834	127	0.76	99833.5072	0.31082	1.07	31.4660	2.29	0.734224	2.03	0.89	0.18104	2.36	3525	16	3549	43	3534	21	1264	25	99.92

4A – Representative microprobe analyses of carbonates from Buritirama Formation.

Crystal-Spot	Sample	End-Members - Molar (%)				Cations			
		CaCO3	MnCO3	FeCO3	MgCO3	Ca	Mn	Fe	Mg
185	SS-082	80.698	17.077	1.311	0.914	0.76	0.22	0.02	0.01
155	SS-082	79.809	18.911	0.136	1.145	0.75	0.24	0.00	0.01
155	SS-082	79.809	18.911	0.136	1.145	0.75	0.24	0.00	0.01
184	SS-082	79.357	18.743	0.752	1.147	0.75	0.24	0.01	0.01
132	SS-068	78.040	19.655	0.411	1.894	0.73	0.25	0.01	0.01
134	SS-082	77.252	20.119	0.474	2.155	0.73	0.25	0.01	0.01
186	SS-081	79.624	18.743	0.436	1.196	0.75	0.24	0.01	0.01
135	SS-082	77.180	20.272	0.540	2.007	0.73	0.26	0.01	0.01
187	SS-068	77.701	20.329	0.508	1.462	0.73	0.26	0.01	0.01
189	SS-068	76.473	20.542	0.958	2.028	0.72	0.26	0.01	0.01
133	SS-081	76.249	21.250	0.408	2.093	0.71	0.27	0.01	0.01
145	SS-082	76.645	21.232	0.416	1.707	0.72	0.27	0.01	0.01
190	SS-068	76.356	20.388	1.216	2.040	0.72	0.26	0.02	0.01
81	SS-082	77.059	20.681	0.370	1.890	0.72	0.26	0.00	0.01
191	SS-082	77.310	20.755	0.082	1.852	0.73	0.26	0.00	0.01
146	SS-081	76.039	21.851	0.433	1.677	0.71	0.27	0.01	0.01
154	SS-081	75.229	22.406	0.369	1.995	0.70	0.28	0.00	0.01
154	SS-089	75.229	22.406	0.369	1.995	0.70	0.28	0.00	0.01
188	SS-068	77.163	20.981	0.000	1.856	0.72	0.27	0.00	0.01
79	SS-082	75.176	22.529	0.502	1.793	0.70	0.28	0.01	0.01
80	SS-068	75.440	22.402	0.398	1.760	0.70	0.28	0.01	0.01
88	SS-068	74.620	22.877	0.552	1.951	0.70	0.29	0.01	0.01
107	SS-081	75.086	23.410	0.258	1.246	0.70	0.29	0.00	0.01
89	SS-089	74.075	23.502	0.462	1.962	0.69	0.29	0.01	0.01
106	SS-068	74.238	24.029	0.377	1.357	0.69	0.30	0.00	0.01
91	SS-068	73.740	24.051	0.461	1.747	0.68	0.30	0.01	0.01
92	SS-068	74.080	23.814	0.406	1.701	0.69	0.30	0.01	0.01
90	SS-089	73.344	24.080	0.448	2.128	0.68	0.30	0.01	0.01
110	SS-089	73.656	24.478	0.319	1.547	0.68	0.31	0.00	0.01
109	SS-068	72.828	25.335	0.367	1.470	0.67	0.32	0.00	0.01
108	SS-081	72.840	25.275	0.332	1.553	0.67	0.31	0.00	0.01
93	SS-089	71.699	26.194	0.374	1.733	0.66	0.33	0.00	0.01
202	SS-068	50.908	43.156	0.261	5.675	0.45	0.52	0.00	0.03
215	SS-068	50.599	43.298	0.578	5.525	0.45	0.52	0.01	0.03
293	SS-089	50.973	44.957	0.367	3.702	0.45	0.53	0.00	0.02
201	SS-089	50.084	43.966	0.450	5.500	0.44	0.52	0.01	0.03
213	SS-081	49.638	44.106	0.528	5.728	0.44	0.52	0.01	0.03
163	SS-081	47.472	45.374	0.420	6.734	0.42	0.54	0.01	0.04
214	SS-089	48.906	44.694	0.633	5.767	0.43	0.53	0.01	0.03
294	SS-068	50.226	45.815	0.291	3.668	0.44	0.54	0.00	0.02
166	SS-081	46.704	46.317	0.293	6.686	0.41	0.55	0.00	0.04
211	SS-082	48.795	44.941	0.738	5.526	0.43	0.53	0.01	0.03

Crystal-Spot	Sample	End-Members - Molar (%)				Cations			
		CaCO3	MnCO3	FeCO3	MgCO3	Ca	Mn	Fe	Mg
164	SS-082	46.864	45.985	0.425	6.726	0.41	0.55	0.01	0.04
295	SS-089	50.717	45.153	0.412	3.719	0.44	0.53	0.00	0.02
292	SS-081	50.422	45.574	0.290	3.713	0.44	0.54	0.00	0.02
291	SS-082	49.858	46.215	0.200	3.726	0.44	0.54	0.00	0.02
167	SS-082	46.963	45.768	0.157	7.112	0.42	0.55	0.00	0.04
210	SS-089	48.626	45.583	0.302	5.488	0.43	0.54	0.00	0.03
212	SS-082	46.373	47.505	0.332	5.790	0.41	0.56	0.00	0.03
165	SS-089	47.007	46.008	0.304	6.681	0.41	0.55	0.00	0.04
286	SS-081	46.337	48.833	0.386	4.443	0.40	0.57	0.00	0.02
283	SS-082	45.917	49.120	0.366	4.597	0.40	0.57	0.00	0.02
284	SS-089	48.150	47.126	0.320	4.404	0.42	0.55	0.00	0.02
282	SS-082	46.373	49.062	0.260	4.305	0.40	0.57	0.00	0.02
265	SS-089	46.546	48.415	0.460	4.579	0.40	0.57	0.01	0.02

4B – Representative microprobe analyses of pyroxenoids from Buritirama Formation.

Sample no.	SS-082	SS-082	SS-082	SS-082	SS-082	SS-082	SS-082	SS-083	SS-083	SS-083	SS-083	SS-089	SS-089	SS-089	SS-089
Mineral	Rdn	Rdn	Rdn	Rdn	Rdn	Rdn	Rdn	Rdn	Rdn	Rdn	Rdn	Rdn	Rdn	Rdn	Rdn
Crystal-Spot	141	142	150	151	156	157	161	160	162	163	173	174	178	179	180
SiO2	46.28	46.41	48.42	48.19	47.11	47.05	47.07	48.81	48.70	47.76	48.50	48.51	48.07	48.28	48.76
TiO2	0.06	0.00	0.03	0.00	0.00	0.05	0.00	0.05	0.00	0.05	0.07	0.09	0.00	0.02	0.05
Al2O3	0.00	0.00	0.00	0.00	0.00	0.00	0.04	0.00	0.00	0.40	0.00	0.00	0.00	0.00	0.00
Cr2O3	0.01	0.02	0.00	0.03	0.03	0.03	0.00	0.00	0.02	0.01	0.00	0.01	0.04	0.05	0.00
FeO	0.86	0.64	2.21	1.83	1.81	1.58	0.76	2.03	2.83	1.84	2.05	1.75	1.46	1.54	2.72
MnO	47.01	45.11	40.69	40.38	41.49	42.50	43.68	39.76	40.42	38.70	39.65	40.07	40.80	40.08	40.20
MgO	0.78	0.31	3.83	4.03	3.44	2.73	3.46	3.80	3.88	4.05	4.04	3.84	2.74	3.56	4.08
CaO	3.91	6.27	5.64	5.62	5.55	5.67	4.31	5.88	5.92	5.67	5.73	6.04	6.42	6.06	5.45
Na2O	0.06	0.04	0.05	0.00	0.02	0.02	0.00	0.05	0.07	0.04	0.01	0.00	0.04	0.02	0.03
K2O	0.01	0.03	0.03	0.03	0.01	0.02	0.01	0.00	0.01	0.05	0.00	0.01	0.02	0.00	0.00
Total (W%)	98.96	98.82	100.89	100.10	99.46	99.64	99.33	100.37	101.85	98.55	100.05	100.32	99.57	99.61	101.30
Si	0.97	0.97	1.01	1.01	0.99	0.99	1.00	1.02	1.02	1.00	1.00	1.02	1.01	1.01	1.02
Ti	0.00	0.00	0.00	0.00	0.00	0.00	0.00	0.00	0.00	0.00	0.00	0.00	0.00	0.00	0.00
Al	0.00	0.00	0.00	0.00	0.00	0.00	0.00	0.00	0.00	0.01	0.00	0.00	0.00	0.00	0.00
Cr	0.00	0.00	0.00	0.00	0.00	0.00	0.00	0.00	0.00	0.00	0.00	0.00	0.00	0.00	0.00
Fe	0.01	0.01	0.04	0.03	0.03	0.03	0.01	0.04	0.05	0.03	0.04	0.03	0.03	0.03	0.05
Mn	0.83	0.80	0.72	0.72	0.74	0.75	0.78	0.71	0.72	0.69	0.71	0.71	0.72	0.71	0.71
Mg	0.02	0.01	0.12	0.13	0.11	0.09	0.11	0.12	0.12	0.13	0.23	0.12	0.09	0.11	0.13
Ca	0.09	0.14	0.13	0.13	0.12	0.13	0.10	0.13	0.13	0.13	0.02	0.14	0.14	0.14	0.12
Na	0.00	0.00	0.00	0.00	0.00	0.00	0.00	0.00	0.00	0.00	0.00	0.00	0.00	0.00	0.00
K	0.00	0.00	0.00	0.00	0.00	0.00	0.00	0.00	0.00	0.00	0.00	0.00	0.00	0.00	0.00
Total-Cations	1.93	1.94	2.02	2.01	1.99	1.98	2.00	2.02	2.04	1.99	2.00	2.02	1.99	2.00	2.03
Total-Oxygen	3.00	3.00	3.00	3.00	3.00	3.00	3.00	3.00	3.00	3.00	3.00	3.00	3.00	3.00	3.00

4C – Representative microprobe analyses of garnets from Buritirama Formation.

Sample no.	SS-082	SS-082	SS-082	SS-082	SS-082	SS-083	SS-083	SS-083	SS-083	SS-084	SS-084
Spot-Position	127.0	128.0	129.0	131.0	139.0	140.0	137.0	138.0	139.0	140.0	141.0
SiO2	37.1	37.7	37.8	36.7	37.8	37.7	38.3	37.8	37.8	37.8	37.7
TiO2	0.1	0.3	0.2	0.2	0.1	0.2	0.2	0.2	0.2	0.2	0.2
Al2O3	21.8	21.7	21.7	21.7	21.7	21.5	21.9	21.6	21.7	21.4	21.6
FeO	2.7	2.6	2.5	2.4	2.2	1.4	1.8	2.3	2.3	2.4	2.0
MnO	34.4	35.1	35.3	35.4	35.3	34.7	35.5	35.4	35.2	35.4	34.9
MgO	2.2	1.5	1.9	1.7	1.6	0.9	1.8	1.8	1.5	1.6	1.6
CaO	2.2	2.3	2.2	2.3	2.3	5.3	2.1	2.3	2.3	2.3	2.3
Na2O	0.1	0.1	0.1	0.1	0.1	0.0	0.1	0.1	0.0	0.1	0.0
K2O	0.0	0.0	0.0	0.0	0.0	0.0	0.0	0.0	0.0	0.0	0.0
Total (W%)	100.7	101.3	101.8	100.4	101.1	101.7	101.8	101.5	101.0	101.3	100.3
Si	3.0	3.0	3.0	3.0	3.0	3.0	3.0	3.0	3.0	3.0	3.0
Ti	0.0	0.0	0.0	0.0	0.0	0.0	0.0	0.0	0.0	0.0	0.0
Al	2.1	2.0	2.0	2.1	2.0	2.0	2.0	2.0	2.0	2.0	2.0
Fe	0.2	0.2	0.2	0.2	0.1	0.1	0.1	0.2	0.2	0.2	0.1
Mn	2.3	2.4	2.4	2.4	2.4	2.3	2.4	2.4	2.4	2.4	2.4
Mg	0.3	0.2	0.2	0.2	0.2	0.1	0.2	0.2	0.2	0.2	0.2
Ca	0.2	0.2	0.2	0.2	0.2	0.4	0.2	0.2	0.2	0.2	0.2
Total-Cations	8.0	8.0	8.0	8.0	8.0	8.0	8.0	8.0	8.0	8.0	8.0
Total-Oxygen	12.0	12.0	12.0	12.0	12.0	12.0	12.0	12.0	12.0	12.0	12.0
Sample no.	SS-084	SS-084	SS-084	SS-084	SS-089	SS-089	SS-089	SS-089	SS-089	SS-089	SS-089
Spot-Position	142.0	143.0	144.0	145.0	157.0	158.0	160.0	167.0	168.0	169.0	170.0
SiO2	37.9	35.9	36.3	36.2	37.8	38.0	37.1	37.4	37.3	37.2	37.7
TiO2	0.1	0.2	0.4	0.3	0.1	0.3	0.3	0.4	0.2	0.3	0.1
Al2O3	21.8	21.2	21.0	20.8	21.9	21.9	21.5	21.2	21.6	21.8	21.9
FeO	1.7	1.8	1.2	2.2	2.8	1.9	1.4	1.1	2.2	2.6	1.9
MnO	35.5	35.7	35.5	34.8	35.0	35.3	35.0	33.9	35.0	35.3	35.2
MgO	2.0	1.5	0.9	1.8	1.6	1.6	1.7	1.0	1.8	1.7	1.9
CaO	2.3	2.2	2.8	2.3	2.4	2.5	2.4	5.3	2.4	2.3	2.3
Na2O	0.1	0.1	0.0	0.1	0.0	0.1	0.0	0.0	0.0	0.0	0.0
K2O	0.0	0.0	0.0	0.0	0.0	0.0	0.0	0.0	0.0	0.0	0.0
Total (W%)	101.4	98.6	98.2	98.5	101.6	101.5	99.5	100.4	100.5	101.3	101.0
Si	3.0	2.9	3.0	3.0	3.0	3.0	3.0	3.0	3.0	3.0	3.0
Ti	0.0	0.0	0.0	0.0	0.0	0.0	0.0	0.0	0.0	0.0	0.0
Al	2.0	2.1	2.0	2.0	2.0	2.0	2.0	2.0	2.0	2.0	2.1
Fe	0.1	0.1	0.1	0.2	0.2	0.1	0.1	0.1	0.1	0.2	0.1
Mn	2.4	2.5	2.5	2.4	2.4	2.4	2.4	2.3	2.4	2.4	2.4
Mg	0.2	0.2	0.1	0.2	0.2	0.2	0.2	0.1	0.2	0.2	0.2
Ca	0.2	0.2	0.2	0.2	0.2	0.2	0.2	0.5	0.2	0.2	0.2
Total-Cations	8.0	8.0	8.0	8.0	8.0	8.0	8.0	8.0	8.0	8.0	8.0
Total-Oxygen	12.0	12.0	12.0	12.0	12.0	12.0	12.0	12.0	12.0	12.0	12.0

4D - Representative microprobe analyses of feldspar from Buritirama Formation.

Sample no.	SS-082	SS-082	SS-082	SS-082	SS-082	SS-082	SS-089	SS-089	SS-089	SS-089	SS-089	SS-089	SS-089	SS-089
Mineral	hyl	hyl	hyl	hyl	hyl	hyl	hyl	hyl	hyl	hyl	hyl	hyl	hyl	hyl
Crystal-Spot	166	165	164	162	161	160	155	154	153	149	124	122	121	120
SiO2	58.1	58.3	57.1	58.0	58.6	60.5	55.6	55.5	56.4	56.4	61.9	59.8	59.8	60.4
TiO2	0.0	0.0	0.0	0.1	0.1	0.0	0.0	0.0	0.0	0.0	0.0	0.0	0.0	0.0
Al2O3	21.1	21.4	21.2	20.9	20.6	19.9	21.8	21.8	21.6	20.7	19.8	20.1	19.9	19.3
Cr2O3	0.0	0.0	0.0	0.0	0.0	0.0	0.0	0.0	0.0	0.0	0.0	0.0	0.1	0.0
FeO	0.5	0.0	0.0	0.0	0.1	0.1	0.0	0.0	0.0	0.7	0.0	0.0	0.0	0.1
MnO	0.1	0.1	0.2	0.0	0.0	0.1	0.1	0.0	0.0	0.2	0.0	0.0	0.0	0.0
MgO	0.0	0.0	0.0	0.0	0.0	0.0	0.0	0.0	0.0	0.0	0.0	0.0	0.0	0.0
CaO	0.8	0.7	0.5	1.1	1.4	1.3	1.2	0.5	1.2	1.2	0.3	1.1	0.6	0.6
BaO	9.6	10.2	10.3	9.3	8.1	6.1	10.7	10.9	10.2	8.1	4.9	5.7	6.5	4.6
K2O	11.1	11.1	11.1	12.0	11.9	12.6	10.4	11.6	11.1	12.5	14.6	13.1	13.7	14.4
Na2O	0.4	0.7	0.5	0.3	0.6	0.3	0.8	0.5	0.6	1.0	0.1	1.1	0.8	0.5
Total (W%)	101.8	102.6	101.0	101.8	101.4	100.9	100.4	100.8	101.2	100.8	101.7	100.9	101.4	99.9
Si	2.8	2.8	2.8	2.8	2.8	2.9	2.7	2.7	2.8	2.8	2.9	2.9	2.9	2.9
Ti	0.0	0.0	0.0	0.0	0.0	0.0	0.0	0.0	0.0	0.0	0.0	0.0	0.0	0.0
Al	1.2	1.2	1.2	1.2	1.2	1.1	1.3	1.3	1.2	1.2	1.1	1.1	1.1	1.1
Cr	0.0	0.0	0.0	0.0	0.0	0.0	0.0	0.0	0.0	0.0	0.0	0.0	0.0	0.0
Fe	0.0	0.0	0.0	0.0	0.0	0.0	0.0	0.0	0.0	0.0	0.0	0.0	0.0	0.0
Mn	0.0	0.0	0.0	0.0	0.0	0.0	0.0	0.0	0.0	0.0	0.0	0.0	0.0	0.0
Mg	0.0	0.0	0.0	0.0	0.0	0.0	0.0	0.0	0.0	0.0	0.0	0.0	0.0	0.0
Ca	0.0	0.0	0.0	0.1	0.1	0.1	0.1	0.0	0.1	0.1	0.0	0.1	0.0	0.0
Ba	0.4	0.4	0.4	0.4	0.3	0.2	0.4	0.4	0.4	0.3	0.2	0.2	0.2	0.2
K	0.7	0.7	0.7	0.7	0.7	0.8	0.7	0.7	0.7	0.8	0.9	0.8	0.8	0.9
Na	0.1	0.1	0.1	0.0	0.1	0.0	0.1	0.1	0.1	0.1	0.0	0.0	0.1	0.1
Total-Cations	5.2	5.2	5.2	5.2	5.2	5.1	5.2	5.2	5.2	5.3	5.1	5.1	5.2	5.1
Total-Oxygen	8.0	8.0	8.0	8.0	8.0	8.0	8.0	8.0	8.0	8.0	8.0	8.0	8.0	8.0

Anexo 5 (Appendix 5) – Lithogeochemistry of Carbonate-bearing Rocks of the Buritirama Formation

Elements/ Unit		Mn-Carbonate Rocks						Mn-Carbonate-Silicate Rocks		Dolomitic Marble									Carbonate-Silicate Rocks					
MnO	Wt%	29.30	25.30	20.90	32.10	32.80	22.40	9.05	9.16	0.35	0.21	0.29	0.27	1.26	1.12	1.05	1.10	1.03	0.15	0.12	0.15	0.35	0.24	0.23
Mn	Wt%	22.69	19.59	16.18	24.86	25.40	17.35	7.01	7.09	0.27	0.16	0.22	0.21	0.98	0.87	0.81	0.85	0.80	0.12	0.09	0.12	0.27	0.19	0.18
Mn/Fe	Wt%	24.03	20.01	6.87	25.21	19.63	4.05	3.43	4.04	0.36	0.24	0.31	0.25	1.33	1.27	2.33	2.49	2.43	0.07	0.05	0.09	0.12	0.12	0.09
SiO2	Wt%	27.10	27.40	32.20	16.00	21.30	16.00	49.10	45.50	20.02	19.76	22.23	21.84	23.20	21.90	8.78	7.76	9.43	40.71	47.07	39.39	51.30	47.81	50.90
Al2O3	Wt%	2.74	4.00	7.65	2.76	4.42	2.80	8.23	7.05	3.72	3.72	3.51	3.63	1.63	1.22	0.90	0.96	0.89	7.04	8.38	6.37	9.26	7.89	9.23
Fe2O3	Wt%	1.35	1.40	3.37	1.41	1.85	6.12	2.92	2.51	1.08	0.97	1.05	1.20	1.05	0.98	0.50	0.49	0.47	2.53	2.76	1.83	3.17	2.23	2.72
CaO	Wt%	11.80	12.90	12.70	11.20	11.50	15.90	12.60	15.50	28.83	26.07	28.33	27.11	27.10	27.80	29.10	30.10	29.10	20.86	17.06	21.25	15.10	18.22	15.20
MgO	Wt%	8.38	7.31	9.29	8.96	8.05	6.96	8.87	10.40	16.87	17.30	16.07	15.63	19.60	19.60	19.90	19.70	19.80	15.15	12.38	15.04	11.10	13.34	11.30
TiO2	Wt%	0.08	0.13	0.16	0.11	0.10	0.12	0.30	0.28	0.15	0.14	0.13	0.15	0.11	0.07	0.01	0.03	0.03	0.28	0.33	0.23	0.34	0.28	0.29
P2O5	Wt%	0.13	0.10	0.09	0.15	0.09	0.40	<0,01	0.11	0.06	0.07	0.09	0.10	0.09	0.06	0.05	0.04	0.05	0.05	0.09	0.09	0.10	0.08	0.08
Na2O	Wt%	<0,1	<0,1	0.11	<0,1	<0,1	<0,1	0.90	0.70	0.08	0.04	0.03	0.04	<0,1	<0,1	<0,1	<0,1	0.10	0.34	0.53	0.37	0.71	0.65	0.63
K2O	Wt%	1.37	2.33	1.93	1.17	1.26	0.47	3.14	2.69	1.40	2.14	1.77	2.13	0.61	0.31	0.43	0.48	0.43	3.87	5.16	3.83	5.40	4.83	5.82
BaO	Wt%	1.12	0.60	0.15	0.46	1.01	0.09	0.70	0.66	0.01	0.02	0.01	0.03	0.02	0.01	0.01	0.01	0.01	0.03	0.06	0.04	0.07	0.06	0.05
LOI	Wt%	16.09	13.26	10.30	18.84	14.00	14.45	2.90	5.02	29.80	29.92	28.23	27.59	26.76	28.24	39.01	39.76	38.37	10.66	5.84	11.96	3.80	6.86	3.73
Ni	ppm	541.4	684.0	651.5	1048.0	861.0	230.4	294.8	357.0	14.9	12.9	12.7	14.4	49.0	36.0	22.4	21.5	21.1	20.6	23.8	18.9	30.4	22.9	22.7
Zn	ppm	1495.0	892.0	3231.0	1272.0	1659.0	>10000	2457.0	1842.0	51.0	34.0	27.0	45.0	75.0	37.0	41.0	40.0	41.0	84.0	65.0	57.0	53.0	75.0	140.0
Mo	ppm	3.79	3.96	35.04	5.00	4.00	1530.73	50.36	35.00	0.21	0.26	0.28	0.23	0.31	0.26	0.58	0.26	0.33	0.32	0.78	0.68	2.50	0.53	0.58
Co	ppm	6.10	9.90	21.30	11.40	10.30	15.60	17.50	21.20	5.80	3.90	4.40	4.20	4.30	4.00	3.20	3.10	3.00	7.80	7.30	6.20	7.80	6.40	6.70
V	ppm	29.00	22.00	90.00	13.00	16.00	86.00	79.00	22.00	12.00	13.00	15.00	13.00	13.00	12.00	15.00	16.00	13.00	31.00	29.00	21.00	24.00	25.00	21.00
Cu	ppm	4.40	4.00	63.20	11.00	24.00	812.20	148.60	87.00	5.80	<0,5	0.60	2.10	57.00	7.00	<0,5	<0,5	<0,5	11.50	3.70	15.20	4.30	1.20	6.30
Cr	ppm	16.00	19.00	39.00	22.00	28.00	23.00	50.00	22.00	11.00	10.00	8.00	10.00	6.00	7.00	8.00	5.00	5.00	13.00	24.00	14.00	24.00	39.00	22.00
Zr	ppm	9.90	54.00	68.50	45.00	51.00	24.90	90.30	107.00	41.30	55.20	54.10	32.80	183.00	122.00	10.40	8.90	9.10	83.20	138.20	95.80	116.50	119.30	129.00
Th	ppm	2.60	1.70	11.20	3.20	3.40	2.40	8.40	6.20	3.30	3.50	3.40	3.50	4.60	3.80	1.30	0.90	1.30	6.10	8.20	6.10	9.50	7.60	9.20
Hf	ppm	0.28	1.74	2.30	1.50	1.81	0.60	2.81	3.26	1.26	1.67	1.64	0.96	5.50	3.87	0.29	0.25	0.26	2.53	4.24	2.79	3.20	3.48	3.72
Ta	ppm	1.61	1.07	0.52	0.72	0.54	0.13	1.22	0.95	0.26	0.27	0.21	0.23	0.54	2.38	0.40	0.35	<0,05	0.33	0.48	0.36	0.48	0.41	0.53
U	ppm	0.20	0.30	4.91	0.91	0.96	1.80	3.51	3.69	0.29	0.41	0.55	0.13	0.44	0.68	0.07	0.07	<0,05	0.51	0.75	0.62	0.91	0.63	0.87

Elements/ Unit		Mn-Carbonate Rocks						Mn-Carbonate-Silicate Rocks		Dolomitic Marble									Carbonate-Silicate Rocks					
Sc	ppm	1.70	3.50	6.00	4.10	5.30	2.30	5.80	6.70	3.20	2.50	2.90	3.20	1.30	1.90	0.70	0.60	0.60	6.70	6.80	5.00	6.80	5.90	6.40
Cd	ppm	1.30	15.41	10.96	16.22	15.12	29.59	11.63	5.30	0.31	0.12	0.07	0.12	0.18	0.14	0.25	0.22	0.22	0.18	0.23	0.17	0.07	0.36	0.30
Sr	ppm	303.4	193.0	176.7	183.0	183.0	255.0	189.9	207.0	91.9	71.3	83.1	87.9	40.0	40.0	68.5	70.9	65.4	68.0	101.9	49.4	105.0	76.5	82.9
Ga	ppm	15.80	19.50	10.40	22.00	22.00	6.00	14.00	14.40	4.90	5.20	4.50	4.90	3.10	2.40	1.70	1.80	1.80	8.70	11.60	7.80	11.10	9.30	12.50
La	ppm	19.00	24.10	15.90	24.90	25.60	12.30	29.50	31.60	9.80	9.80	11.60	8.90	10.70	10.30	8.80	8.50	8.20	15.60	16.50	11.50	18.80	16.70	16.60
Ce	ppm	16.30	24.90	27.10	21.40	33.30	17.40	46.70	43.90	15.60	14.30	15.60	14.20	12.80	12.30	10.30	10.30	9.60	24.70	30.20	20.80	30.00	27.60	29.40
Pr	ppm	2.56	3.90	3.05	3.03	4.69	2.18	5.75	5.29	1.73	1.75	1.85	1.70	1.83	1.86	1.70	1.60	1.57	2.93	3.50	2.29	3.40	3.30	3.26
Nd	ppm	9.40	13.90	12.10	11.20	17.10	9.40	20.20	20.20	6.80	6.10	6.90	6.10	7.40	6.80	6.40	5.70	6.00	10.40	12.80	8.30	14.00	11.80	13.40
Sm	ppm	1.60	2.30	2.10	1.90	2.90	1.70	3.50	4.00	1.30	1.20	1.30	1.10	1.40	1.10	1.30	1.10	1.10	2.10	2.40	1.70	2.50	2.30	2.30
Eu	ppm	0.61	0.91	0.50	0.91	1.29	0.53	0.96	1.31	0.37	0.22	0.35	0.25	0.38	0.35	0.29	0.27	0.33	0.49	0.54	0.37	0.64	0.44	0.57
Gd	ppm	1.99	2.51	1.86	2.39	3.20	1.92	3.51	4.28	1.26	0.94	1.17	1.07	1.83	1.72	1.35	0.98	1.39	1.80	2.14	1.55	2.30	2.04	1.96
Tb	ppm	0.29	0.38	0.25	0.35	0.47	0.28	0.53	0.65	0.17	0.13	0.15	0.14	0.26	0.24	0.19	0.14	0.20	0.29	0.29	0.19	0.31	0.27	0.27
Dy	ppm	1.83	2.29	1.50	2.09	2.57	1.86	3.52	3.78	0.97	0.82	0.86	0.95	1.81	1.53	1.22	1.02	1.25	1.75	1.74	1.26	1.95	1.66	1.65
Y	ppm	13.59	15.85	10.74	14.61	18.93	15.60	23.27	25.03	7.13	6.45	6.72	6.33	17.68	15.57	13.55	10.73	14.29	11.09	10.65	8.59	12.93	10.48	10.87
Ho	ppm	0.40	0.47	0.30	0.45	0.57	0.37	0.76	0.77	0.24	0.19	0.18	0.17	0.39	0.33	0.28	0.20	0.29	0.35	0.30	0.31	0.40	0.31	0.34
Er	ppm	1.19	1.36	0.95	1.25	1.70	1.08	2.39	2.24	0.64	0.54	0.57	0.45	1.17	1.02	0.74	0.61	0.83	1.17	1.12	0.74	1.18	0.87	1.02
Tm	ppm	0.15	0.20	0.14	0.18	0.26	0.13	0.35	0.31	0.10	0.07	0.09	0.08	0.17	0.14	0.11	0.08	0.11	0.16	0.15	0.09	0.18	0.15	0.14
Yb	ppm	0.90	1.30	1.00	1.00	1.60	0.80	2.30	2.00	0.50	0.50	0.50	0.50	1.10	0.90	0.60	0.50	0.60	0.90	1.10	0.80	1.20	1.00	1.00
Lu	ppm	0.13	0.21	0.14	0.12	0.21	0.10	0.34	0.27	0.08	0.07	0.07	0.08	0.15	0.13	0.08	0.06	0.08	0.16	0.16	0.12	0.18	0.13	0.14
∑REE	ppm	69.9	94.6	77.6	85.8	114.4	65.7	143.6	145.6	46.7	43.1	47.9	42.0	59.1	54.3	46.9	41.8	45.8	73.9	83.6	58.6	90.0	79.1	82.9
Y/Ho		33.98	33.72	35.80	32.47	33.21	42.16	30.62	32.51	29.71	33.95	37.33	37.24	45.33	47.18	48.39	53.65	49.28	31.69	35.50	27.71	32.33	33.81	31.97
Eu/Eu*		1.76	1.88	1.26	2.20	2.13	1.49	1.34	1.57	1.46	1.00	1.44	1.18	1.24	1.38	1.11	1.27	1.38	1.18	1.19	1.18	1.34	1.02	1.32
Ce/Ce*		0.71	0.69	1.07	0.79	0.79	1.05	0.87	0.96	1.08	0.87	0.96	0.91	0.86	0.74	0.69	0.70	0.71	0.91	0.96	1.00	1.10	0.91	1.13
La/La*		1.69	1.49	1.01	1.84	1.26	0.93	1.27	1.25	1.12	1.41	1.38	1.25	1.09	1.27	1.12	1.28	1.10	1.29	1.08	1.17	1.00	1.21	0.92

Anexo 6 (Appendix 6) – Isotopic analysis of Mn-Carbonate Rocks and Dolomitic Marbles of Buritirama Formation.

Sample	Lithology	δ13C	δ18O	δ18O
		VPDB	VPDB	VSMOW
SS-082	Mn-carbonate Rocks	-0.75	-14.04	16.43
SS-082	Mn-carbonate Rocks	-0.78	-13.74	16.74
SS-082	Mn-carbonate Rocks	-0.27	-13.78	16.70
SS-082	Mn-carbonate Rocks	0.15	-13.66	16.82
SS-082	Mn-carbonate Rocks	-1.15	-13.11	17.39
SS-082	Mn-carbonate Rocks	-0.17	-13.38	17.11
SS-089	Mn-carbonate Rocks	-0.04	-14.74	15.71
SS-089	Mn-carbonate Rocks	-1.15	-13.91	16.57
SS-089	Mn-carbonate Rocks	-0.27	-14.35	16.11
SS-089	Mn-carbonate Rocks	0.06	-14.32	16.15
SS-083	Mn-carbonate Rocks	-0.77	-12.64	17.88
SS-083	Mn-carbonate Rocks	-0.90	-13.30	17.19
SS-083	Mn-carbonate Rocks	-0.86	-13.21	17.28
SS-084	Mn-carbonate Rocks	-2.56	-12.91	17.60
SS-068	Mn-carbonate Rocks	-1.61	-12.10	18.43
SS-068	Mn-carbonate Rocks	-1.36	-12.39	18.13
SS-068	Mn-carbonate Rocks	-1.39	-12.17	18.37
SS-084	Mn-carbonate Rocks	-1.46	-12.08	18.45
SS-084	Mn-carbonate Rocks	-1.64	-11.96	18.57
SS-084	Mn-carbonate Rocks	-2.64	-10.79	19.78
SS-091	Dolomitic Marbles	3.88	-13.54	16.94
SS-091	Dolomitic Marbles	3.61	-13.98	16.50
SS-091	Dolomitic Marbles	3.51	-14.06	16.41
SS-091	Dolomitic Marbles	3.98	-13.98	16.50
SS-091	Dolomitic Marbles	3.40	-14.12	16.35
SS-091	Dolomitic Marbles	3.48	-14.32	16.15
SS-091	Dolomitic Marbles	3.43	-14.57	15.88
SS-091	Dolomitic Marbles	3.36	-14.37	16.10
SS-092	Dolomitic Marbles	3.43	-14.80	15.65
SS-092	Dolomitic Marbles	3.50	-14.68	15.77
SS-092	Dolomitic Marbles	4.82	-14.08	16.39
SS-092	Dolomitic Marbles	4.77	-14.05	16.43
SS-092	Dolomitic Marbles	4.61	-14.44	16.02
SS-092	Dolomitic Marbles	3.94	-14.54	15.92
SS-092	Dolomitic Marbles	3.59	-14.82	15.63
SS-093	Dolomitic Marbles	3.61	-14.93	15.51
SS-093	Dolomitic Marbles	3.56	-14.90	15.55
SS-093	Dolomitic Marbles	3.18	-15.52	14.91
SS-093	Dolomitic Marbles	4.79	-14.06	16.41
SS-093	Dolomitic Marbles	4.85	-14.25	16.22
SS-093	Dolomitic Marbles	4.97	-14.18	16.29
SS-093	Dolomitic Marbles	4.04	-14.78	15.67

Sample	Lithology	δ13C	δ18O	δ18O
		VPDB	VPDB	VSMOW
SS-093	Dolomitic Marbles	4.12	-14.67	15.78
SS-093	Dolomitic Marbles	4.72	-14.30	16.16